Functional analysis of a high fidelity cerebellar synapse

Dissertation
for obtaining the academic degree
PhD (Dr. rer. nat.)
at the Medical faculty of the University of Leipzig

submitted by:
Abdelmoneim Eshra

born on 17. October 1988 in Alexandria, Egypt

Carl Ludwig Institute of Physiology
Medical faculty
University of Leipzig

supervised by:
Prof. Dr. med. Stefan Hallermann

Decision on the award of the doctoral degree: 19.07.2022

Table of contents

Abbreviations

AP	Action potential
Ca^{2+}	Calcium
cMFB	Cerebellar mossy fiber bouton
CNS	Central nervous system
GC	Granule cell
K^+	Potassium
Na^+	Sodium
RRP	Release-ready pool of vesicles
VGCC	Voltage-gated Ca^{2+} channel

List of figures

1. Introduction

The speed of information processing in the central nervous system (CNS) critically depends on several parameters including the frequency of neuronal signaling. Synapses represent the main functional units where signals of various frequencies are conveyed between neurons. The cerebellum is optimized for fast information processing of sensory inputs (Eccles et al., 1967). Rate-coded broad-bandwidth signals are reliably transmitted by the cerebellar mossy fibers to the cerebellar cortex via the cerebellar mossy fiber boutons (cMFB), which are capable of firing action potentials (APs) at kilohertz frequencies (Garwicz et al., 1998; Jörntell & Ekerot, 2006; Rancz et al., 2007; Ritzau-Jost et al., 2014). Granule cells (GCs) represent the first stage of information processing of the mossy fiber input and efficiently transfer information to the Purkinje cells. Therefore, the cMFB-GC synapse represents a model for high fidelity synaptic transmission at the mammalian CNS (Delvendahl & Hallermann, 2016). In the present work, the biophysical properties of synaptic release and postsynaptic firing were studied at this synapse. The following sections give an overview on neuronal firing, synaptic release, cMFB-GC synapse, enriched environment, and the aims of this work.

1.1. Neuronal firing

Due to their excitability, neurons are capable of communicating and transmitting information in the form of APs. The plasma membrane surrounding the nerve cell acts as an insulator separating the inside of the cell from the extracellular matrix. The presence of channels in this excitable membrane allows neurons to respond to electrical signals through the exchange of different ions between the neuron and its surrounding.

At resting conditions, the neuronal membrane is polarized such that the voltage difference across the cell membrane is around 70 mV. An AP is fired when electrical signals lead to a membrane depolarization exceeding the threshold of voltage gated sodium (Na^+) channels of approximately -50 mV. When the critical threshold of membrane depolarization is reached, an increase in Na^+ permeability occurs due to the activation of voltage gated Na^+ channels. This leads to a rapid self-amplifying Na^+ influx, occurring as positive feedback known as the Hodgkin cycle (Hodgkin & Huxley, 1952), that leads to the rapid rising phase of the AP towards the Na^+ reversal potential (Figure 1A). The depolarizing phase is ended by the fast

inactivation of Na$^+$ channels and the delayed activation of potassium (K$^+$) channels, which leads to a rapid repolarization phase towards the reversal potential of K$^+$ close to the resting membrane potential (Figure 1A). This is followed by a relative refractory period during which neuronal firing is not possible due to the inactivation of Na$^+$ channels. Therefore, the expression level and activation kinetics of various types of voltage-dependent Na$^+$ and K$^+$ channels control the AP waveform and, in addition, the timing of AP firing including the refractory period. The frequency of AP firing is a critical parameter which directly affects the function of the CNS. For example, in the cerebellum, the position of the limb has been shown to be directly correlated to the AP firing frequency of mossy fibers (Figure 1B).

APs are transferred from one neuron to another through the process of synaptic transmission. Synaptic signals, reaching a certain threshold at the axon initial segment of the postsynaptic neuron, trigger the firing of new APs. Therefore, neuronal signals continue to flow and carry information through the biological network. Information processing depends on the rate and the timing at which synaptic signals are transmitted and how those signals are integrated in the postsynaptic neurons.
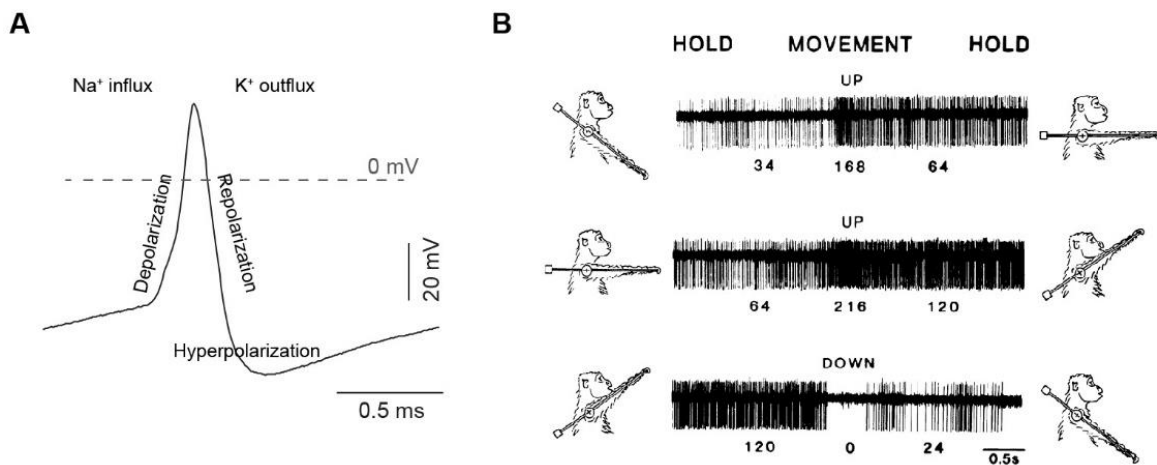
Figure 1: Action potential firing

(A) Example of an AP recorded from a cerebellar GC showing the different phases of the spike waveform. Inward Na$^+$ current leads to the rising phase of the AP until reaching the overshoot phase. The repolarizing phase occurs due to the inactivation of Na$^+$ channels and the activation of an outward K$^+$ current, which is followed by a hyperpolarized state in which AP firing is not possible (modified from Eshra et al., 2019). (B) *In vivo* extracellular recordings showing the relation between the AP firing frequency of the mossy fiber and the position of the monkey's limb. Note the correlation of the sustained firing rate to the limb position during the holding phase (Adopted from van Kan et al., 1993).

1.2. Synaptic release

In presynaptic terminals, APs leads to the opening of VGCCs. This generates a local calcium (Ca^{2+}) signal of high concentration, which triggers the exocytosis of synaptic vesicles (Figure 2). Based on their molecular maturation and proximity to the voltage-gated Ca^{2+} channels (VGCCs), two main functional pools of synaptic vesicles have been differentiated, the reserve pool and release-ready pool of vesicles (RRP) (Kaeser & Regehr, 2017; Neher & Sakaba, 2008). The AP-evoked local Ca^{2+} signals reach a concentration in the micromolar range which is three orders of magnitude higher than the Ca^{2+} concentration under resting conditions (Llinás et al., 1992; Simon & Llinás, 1985) (Figure 2B). However, these micromolar Ca^{2+} signals decay very fast via several mechanisms including extrusion (DiPolo & Beaugé, 1983), diffusion (Tran & Stricker, 2018), and buffering (Schwaller, 2020).

The exocytosis of synaptic vesicles induces a transient increase in the surface area of the presynaptic membrane which is counterbalanced by membrane retrieval through endocytosis (Heuser & Reese, 1973; Südhof, 2004; Sun et al., 2002). The retrieved membrane is used in the formation of new synaptic vesicles, which are then loaded with the neurotransmitter, and eventually mobilized to the reserve pool of vesicles (Figure 2A). During activity, synaptic vesicles from the reserve pool are used to refill the RRP via a process referred to as replenishment, reloading, or recruitment. These vesicles achieve fusion competence through further positional and molecular maturation steps known as priming (Imig et al., 2014; Neher & Sakaba, 2008).

The Ca^{2+} sensors which trigger vesicle fusion have been extensively studied. Classical work by Dodge and Rahamimoff has shown that Ca^{2+} ions exert a cooperative function while triggering vesicle fusion (Dodge & Rahamimoff, 1967). Further detailed analysis of the Ca^{2+} dependence of neurotransmitter release showed that synchronous vesicle fusion occurs via the cooperative binding of Ca^{2+} to the Ca^{2+} sensor (Brose et al., 1992) (Figure 2C).

Studying the Ca^{2+} sensitivity of these fusion sensors is challenging due to the difficulty to experimentally capture the concentration of the fast decaying microdomain Ca^{2+} signal at the vicinity of VGCCs (Figure 2B). Ca^{2+} uncaging technique allows the homogenous elevation of the Ca^{2+} concentration all over the presynaptic terminal, therefore bypassing the issue of the occurrence of extreme spatial Ca^{2+} gradients during the AP-triggered opening of the VGCCs. Using this technique, the Ca^{2+} sensitivity of the fusion sensors has been studied at several

synaptic terminals and different results were obtained which were dependent on the age and the type of the studied synapse (Beutner et al., 2001; Fukaya et al., 2021; Heidelberger et al., 1994; Sakaba, 2008; Schneggenburger & Neher, 2000; Thoreson et al., 2004; Wang et al., 2008). This discrepancy is likely to be functionally significant since presynaptic boutons show type-specific functional and structural differences (Atwood & Karunanithi, 2002; Nusser, 2018; Zhai & Bellen, 2004). For example, the size of the ready-releasable pool of vesicles, the release probability, the vesicle recruitment rates, and the occupancy of the release site varies between different types of neurons (Bornschein & Schmidt, 2019; Silva et al., 2021).

Due to the discrepancy in results obtained from different terminals, the previously described mechanistic release schemes cannot be directly applied to the cMFBs. Furthermore, cMFBs show ultrafast signaling properties (Ritzau-Jost et al., 2014) with prominent faster vesicle replenishment than other central synapses (Hallermann et al., 2010; Miki et al., 2020; Saviane & Silver, 2006), therefore, a release scheme explaining the fast functional aspects of this synapse is required. A precise description of the Ca^{2+} sensitivity of vesicle fusion critically impacts our mechanistic analysis of synaptic function. For example, studying the coupling distance between the VGCCs and the RRP requires a precise knowledge of the Ca^{2+} affinity of the fusion sensors of synaptic vesicles.
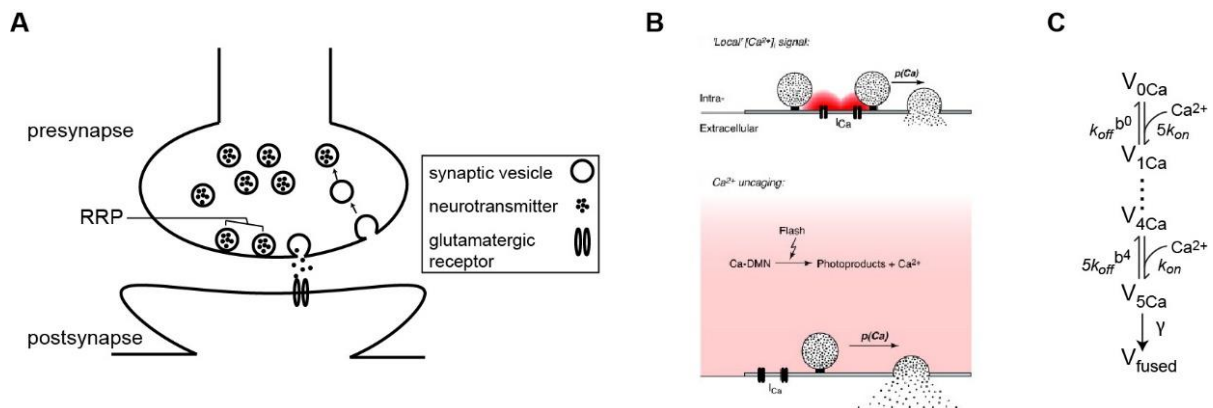
Figure 2: Synaptic vesicle cycle and neurotransmitter release

(A) Schematic diagram of a glutamatergic synapse. When an AP depolarizes the presynaptic membrane, voltage gated Ca^{2+} channels open and lead to Ca^{2+} influx which triggers the exocytosis of vesicles from the release-ready pool of vesicles (RRP). The release of glutamate and its subsequent binding to postsynaptic glutamatergic receptors generates an excitatory postsynaptic current. (B) *Top:* Illustration of the extreme Ca^{2+} gradients which occur due to the opening of the voltage-gated Ca^{2+} channels (VGCCs). Large local Ca^{2+} domains build up in the vicinity of the VGCCs but drop off very fast with distance from the VGCCs. Therefore, the experimental analysis of these local Ca^{2+} signals is very challenging. *Bottom:* illustration of the Ca^{2+} uncaging method which is used to induce a homogenous elevation of the Ca^{2+} concentration that is experimentally quantifiable. This technique overcomes the issue of different Ca^{2+} domains occurring due to the opening of the VGCCs (adopted from Kochubey et al., 2011). (C) Example of a reaction scheme describing the cooperative Ca^{2+} sensor which triggers

the fusion of synaptic vesicles with different rates via five Ca^{2+} steps. k_{on}, k_{off}, and γ represent the binding, unbinding, and fusion rates, respectively (modified from Eshra et al., 2021).

1.3. cMFB-GC synapse

cMFBs were described in detail by Ramon Cajal in the 19th century in his drawings of the cerebellar neurons (Ramón y Cajal, 1894, 1911; Figure 3A). Cerebellar mossy fibers represent one of the major inputs of information to the cerebellum. Cerebellar mossy fibers rise from the cerebellar white matter where they branch in the granule layer of the cerebellar cortex (Figure 3B). Each mossy fiber forms several rosette-like en-passant boutons along its axon at intervals of 20-80 μm (Krieger et al., 1985). In each of these rosettes, the cMFB forms synapses with the dendrites of approximately 10 - 100 GCs (Figure 3A, C, and D). Therefore, the cMFB-GC is a highly divergent synapse. Despite its divergence, the cMFB has a comparably small size with a diameter of about 3-12 μm (Jakab & Hámori, 1988). Accordingly, the cMFB-GC synapse has been described as a "device to secure a high mossy fiber to GC divergence with minimal physical structure" (Eccles et al., 1967).

GCs are the most abundant neurons in the human brain (Williams & Herrup, 1988). In most cerebellar network models, GCs have been considered as one population of neurons with homogenous functional properties (Albus, 1971; Ito, 1970; Marr, 1969). On the other hand, GCs' soma and parallel fibers show differences in their spatial arrangement as described since the early stainings of Ramon Cajal (Eccles et al., 1967; Ramón y Cajal, 1911, but see Espinosa & Luo, 2008; Wilms & Häusser, 2015).

Functionally, cerebellar mossy fibers send broad-bandwidth signals to the cerebellar cortex. The cMFB-GC synapse can reliably covey high frequency signals from the cerebellar mossy fiber to the GCs (Chadderton et al., 2004; Gabbiani et al., 1994; Rancz et al., 2007). It has been shown that the cMFB can fire APs at high frequencies up to 1 kHz (Ritzau-Jost et al., 2014) and can ensure neurotransmitter release with high fidelity (Figure 3C – 3F), which is mediated by fast replenishment of synaptic vesicles (Hallermann et al., 2010; Miki et al., 2020; Saviane & Silver, 2006).
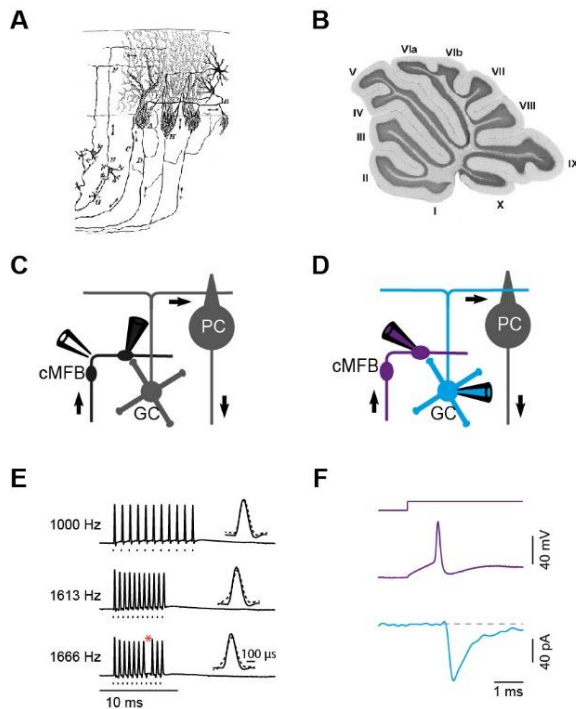
Figure 3: Signaling at the cMFB-GC synapse

(A) Early drawings of the cerebellar architecture from Ramon Cajal (adopted from Ramón y Cajal, 1911). (B) Scheme of a parasagittal slice from the cerebellar cortex showing the different cerebellar lobules (adopted from Straub et al., 2020). (C) Scheme of the cellular connectivity in the cerebellar cortex. Arrows represent the flow of information from the mossy fiber to the cerebellar cortex where the presynaptic cMFBs transmit signals to postsynaptic GCs. Axons of the GCs bifurcates to form the parallel fibers which excite the Purkinje cells. Axons of the Purkinje cells represent the sole output of the cerebellar cortex. The two pipettes represent the configuration for the extracellular stimulation of the mossy fiber axon (left pipette) and recording the AP firing at the cMFB (right patch-clamp pipette; modified from Delvendahl et al., 2015). (D) Same as in (C) but the two pipettes represent the configuration for the simultaneous pre- and postsynaptic patch-clamp recordings (modified from Delvendahl et al., 2015). (E) Examples of AP firing recorded at the cMFB with different stimulation frequencies elicited by the recording configuration described in (C). Note that the AP firing could be maintained at high frequencies up to 1.6 kHz (adopted from Ritzau-Jost et al., 2014). (F) Example of a simultaneous pre- and postsynaptic whole-cell recording. *Top:* represent the current injected in the cMFB. *Middle:* represent the presynaptic AP. *Bottom:* represent the postsynaptic current recorded at the GC (modified from Eshra et al., 2021).

1.4. Enriched environment

Enriched environment refers to refined housing conditions in which the complexity and novelty of the environment are enhanced. Enriched environment of lab animals includes social grouping as well as other complex inanimate objects, therefore, promoting the behavioral, motor, and cognitive stimulation (Rosenzweig et al., 1978). The idea that the brain is influenced by the environment goes back to at least the 19th century when Ramon Cajal described the neurons' ability to adapt to the environment (DeFelipe, 2006; Ramón y Cajal, 1911). However, the concept of enriched environment was introduced in an experimental scientific context by Donald Hebb in 1940s. Hebb observed that, compared to laboratory animals, animals that were raised at his home as pets had superior behavioral and problem-solving abilities (Hebb, 1947, 1949). This laid the foundation for research studies on enriched environment and its role on various brain functions. Nowadays, controlled experimental paradigms are used to establish environmental enrichment while housing laboratory animals. These housing paradigms include, for example, adding extra objects in the animal cage like climbing ladders, plastic tubes, tunnels and small boxes as well as a variety of other toys like igloos and saucer wheels (Figure 4A). In order to provide novelty and more chances for learning, the configuration of the enriched environment cage is regularly changed by rearranging the position of the toys and

by adding and removing different elements. Social interaction is promoted by housing the animals in larger groups compared to standard housing conditions.

Environmental enrichment has been shown to induce several alterations in the brain at the structural level (Diamond et al., 1966; Ehninger & Kempermann, 2003; Kempermann et al., 1997; Restivo et al., 2005; Volkmar & Greenough, 1972) and molecular level (Barak et al., 2013; Rampon et al., 2000; Rossi et al., 2006; Torasdotter et al., 1998). For example, dendritic spinogenesis has been shown to be enhanced upon environmental enrichment (Leggio et al., 2005) (Figure 4B). Moreover, establishing an enriched environment for animals with toys that stimulate motor performance (like saucer wheels and others), is considered to be a powerful tool to induce voluntary motor learning (Horvath et al., 2013; Lee et al., 2013; Madroñal et al., 2010). Interestingly, motor learning has been shown to induce structural plasticity at the cerebellar glomeruli (Ruediger et al., 2011) (Figure 4C), although in that study, enriched environment in itself did not induce structural alterations at the presynaptic terminal. However, it remains unanswered if the observed structural plasticity in the cerebellar cortex, in response to enhanced motor functions, has a functional correlate.
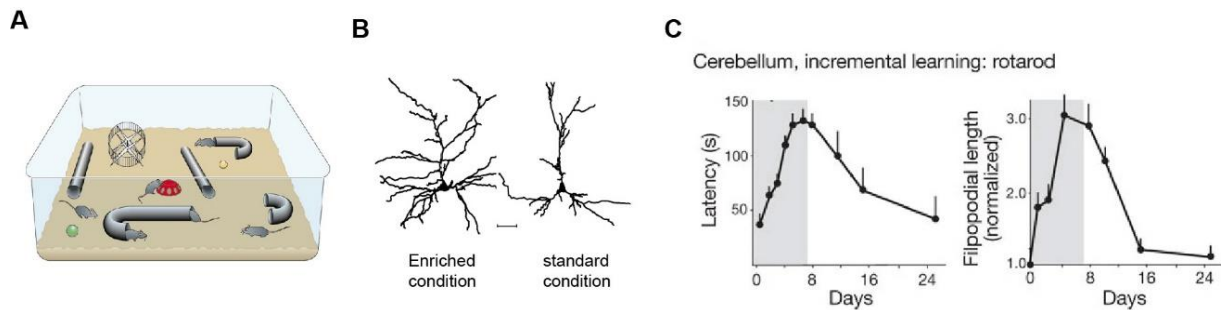
Figure 4: Structural changes induced by enriched environment and motor learning

(A) Illustration of a cage with the different tools used to implement the enriched environment (adopted from van Praag et al., 2000). (B) Illustration of the effect of environmental enrichment on the branching of the apical dendrites of cortical neurons. Scale bar: 30 μm (adopted from Leggio et al., 2005). (C) *Left:* motor learning curve obtained from training the animal on a rotarod. *Right:* the corresponding structural changes occurring in the mossy fiber terminals manifested in an increased number of filopodia (adopted from Ruediger et al., 2011).

1.5. Aims

Information transfer at the cMFB-GC synapse represents one of the major inputs to the cerebellum. Mossy fiber axons are able to send broad-bandwidth signals via ultrafast neuronal signaling with high frequencies up to 1 kHz. In this work, I studied high frequency signaling at the cMFB-GC synapse from the synaptic, the neuronal network, and the behavioral perspectives.

High fidelity neurotransmission occurs at the cMFB-GC synapse and is mediated by a fast cycle of synaptic vesicles (Miki et al., 2020; Ritzau-Jost et al., 2014; Saviane & Silver, 2006). However, the biophysical tuning of the release machinery to perform fast synaptic release remains unknown. Therefore, the first aim of this work was to study the Ca^{2+} dependence of the different steps of the vesicle cycle mediating synaptic transmission at this synapse. In order to do this, I used a range of methods to address the Ca^{2+} sensitivity of the three central steps in the vesicle cycle: priming, fusion, and replenishment. By combining tools to directly manipulate the presynaptic Ca^{2+} concentration, pre- and postsynaptic recordings, and two-photon Ca^{2+} imaging, I was able to describe the Ca^{2+} sensitivity of synaptic release at the cMFB.

GCs represent major information processing units in the cerebellar network and are the most abundant neurons in the whole brain (Williams & Herrup, 1988). How do fast mossy fiber signals propagate along the cerebellar network? In most cerebellar network models, GCs have been considered as a homogenous population of neurons with similar functional properties. However, the spatial arrangement of these cells has been shown to be quite distinct since the early stainings of Ramon Cajal (Eccles et al., 1967; Ramón y Cajal, 1911). A better understanding of the biophysical and firing properties of GCs based on their spatial arrangement would provide more insights into the cerebellar information processing. Therefore, the second aim of this work was to study the spatio-functional differences between different populations of cerebellar GCs based on their depth and rostro-caudal organization. Using somatic recordings of different GC populations, I described gradients in the firing frequencies of GCs based on their spatial properties.

It remains unclear, whether the neuronal ability to perform high frequency firing can be considered a plastic phenomenon that could be directly modulated via experiences. Structural plasticity has been shown to occur in the cerebellar cortex in response to enhancing the motor

performance. These alterations were manifested as an increase in the number of filopodia per mossy fiber terminal in lobule IX of the cerebellum (Ruediger et al., 2011). However, if the observed structural plasticity has a functional correlate remains largely unknown. Therefore, the third aim of this work was to investigate the influence of the environmental enrichment and the consequent improvement in motor performance on the firing properties of cerebellar neurons. In order to do this, I focused on mice raised under control conditions or enriched environment, assessed their motor performance, and then performed somatic recordings of GCs of the vestibular cerebellum. This analysis described the adaptations of the firing frequencies of GCs in response to environmental enrichment.

2. Publication 1

Title: **Calcium dependence of neurotransmitter release at a high fidelity synapse**

Calcium dependence of neurotransmitter release at a high fidelity synapse

Abdelmoneim Eshra, Hartmut Schmidt, Jens Eilers, Stefan Hallermann*

Carl-Ludwig-Institute for Physiology, Medical Faculty, University of Leipzig, Leipzig, Germany

Abstract The Ca^{2+}-dependence of the priming, fusion, and replenishment of synaptic vesicles are fundamental parameters controlling neurotransmitter release and synaptic plasticity. Despite intense efforts, these important steps in the synaptic vesicles' cycle remain poorly understood due to the technical challenge in disentangling vesicle priming, fusion, and replenishment. Here, we investigated the Ca^{2+}-sensitivity of these steps at mossy fiber synapses in the rodent cerebellum, which are characterized by fast vesicle replenishment mediating high-frequency signaling. We found that the basal free Ca^{2+} concentration (<200 nM) critically controls action potential-evoked release, indicating a high-affinity Ca^{2+} sensor for vesicle priming. Ca^{2+} uncaging experiments revealed a surprisingly shallow and non-saturating relationship between release rate and intracellular Ca^{2+} concentration up to 50 μM. The rate of vesicle replenishment during sustained elevated intracellular Ca^{2+} concentration exhibited little Ca^{2+}-dependence. Finally, quantitative mechanistic release schemes with five Ca^{2+} binding steps incorporating rapid vesicle replenishment via parallel or sequential vesicle pools could explain our data. We thus show that co-existing high- and low-affinity Ca^{2+} sensors mediate priming, fusion, and replenishment of synaptic vesicles at a high-fidelity synapse.

Introduction

Neurotransmitter release is mediated by the presynaptic vesicle cycle (*Südhof, 2004*) including (1) the priming of neurotransmitter-filled vesicles, (2) the fusion of primed vesicles, and (3) the replenishment of new vesicles after fusion. The Ca^{2+}-sensitivity of these steps is difficult to determine due to the large spatial gradients of the Ca^{2+} concentration, which occur during Ca^{2+} influx through the Ca^{2+} channels. While the basal free intracellular Ca^{2+} concentration is ~50 nM, thousandfold higher local microdomains of Ca^{2+} build and decay very fast around the Ca^{2+} channels (*Simon and Llinás, 1985*; *Yamada and Zucker, 1992*). The small size and the rapid kinetics of the microdomain signals complicate the quantification of the local Ca^{2+} signals with the imaging techniques (*Neher, 1998*). Ca^{2+} uncaging circumvented this problem by allowing for the homogenous elevation of Ca^{2+} concentration throughout the whole presynaptic compartment via UV-photolysis of caged Ca^{2+} compounds (*Kaplan and Ellis-Davies, 1988*) and thus the direct measurement of the Ca^{2+}-concentration immediately relevant for vesicle fusion (reviewed by *Neher, 1998*; *Kochubey et al., 2011*).

Among the steps of the presynaptic vesicle cycle, the Ca^{2+}-sensitivity of vesicle fusion is best studied. First experiments with Ca^{2+} uncaging at retinal bipolar cells of goldfish found a very low sensitivity of the release sensors with a half saturation at ~100 μM Ca^{2+} concentration and a fourth to fifth power relationship between Ca^{2+} concentration and neurotransmitter release (*Heidelberger et al., 1994*), similar to previous estimates at the squid giant synapse (*Adler et al., 1991*; *Llinás et al., 1992*). Subsequent work at other preparations showed different dose-response curves. For example, analysis of a central excitatory synapse, the calyx of Held (*Forsythe, 1994*) at a young pre-hearing age, found a much higher affinity with significant release below 5 μM intracellular Ca^{2+} concentration and a steep dose-response curve (*Bollmann et al., 2000*; *Lou et al., 2005*;

Schneggenburger and Neher, 2000; *Sun et al., 2007*). Further analysis of the calyx of Held during neuronal development comparing the Ca^{2+}-sensitivity of the release sensors at the age of P9 to P12-P15 (*Kochubey et al., 2009*) and P9 to P16-P19 (*Wang et al., 2008*) showed a developmental decrease in the Ca^{2+}-sensitivity of vesicle fusion. Studies at two other central synapses, the hippocampal mossy fiber boutons of rats (P18–30; *Fukaya et al., 2021*) and the boutons of cerebellar basket cells of mice (P11-16; *Sakaba, 2008*), also described a high Ca^{2+}-sensitivity of vesicle fusion with a steep dose-response curve. In contrast, the dose-response curve of sensory neurons of the rod photoreceptors was more shallow (*Duncan et al., 2010*; *Thoreson et al., 2004*) and vesicle fusion below 7 μM Ca^{2+} concentration was absent at the cochlear inner hair cells (*Beutner et al., 2001*).

The steps preceding the fusion of synaptic vesicles are in general still poorly understood (*Südhof, 2013*). We refer to vesicle priming as the molecular and positional preparation of vesicles for fusion near Ca^{2+} channels (*Neher and Sakaba, 2008*). Molecular priming has recently been shown to be the functional correlate of vesicle docking (*Imig et al., 2014*; *Maus et al., 2020*). Vesicle replenishment refers to the delivery of new vesicles during sustained activity. The effect of the residual Ca^{2+} on the strength of synapses particularly during synaptic facilitation has been studied for decades with a particular focus on the release probability of vesicles (see Discussion). Here, we investigate the Ca^{2+}-dependence of priming and replenishment, which increases the number of release-ready vesicles. Previous work provided evidence that priming and replenishment are strongly Ca^{2+}-dependent (reviewed by *Silva et al., 2021*, and *Neher and Sakaba, 2008*). The following findings demostrate the Ca^{2+}-dependence of vesicle priming and replenishment. First, the size of the pool of fast-releasing vesicles linearly depends on the intracellular Ca^{2+} concentration at the calyx of Held synapse (*Hosoi et al., 2007*; see also *Awatramani et al., 2005*; *Wang and Kaczmarek, 1998*). Second, the sustained component of release, presumably reflecting vesicle replenishment, linearly depends on the intracellular Ca^{2+} concentration at cerebellar basket cell synapses (*Sakaba, 2008*). Third, the number of docked vesicles assessed by electron microscopic techniques is rapidly and reversibly regulated depending on the resting Ca^{2+} levels and neuronal activity at hippocampal neurons (*Chang et al., 2018*; *Imig et al., 2020*; *Kusick et al., 2020*; *Vandael et al., 2020*; *Vevea et al., 2021*). Fourth, the occupancy of the docking sites increases upon elevating extracellular Ca^{2+} levels at cerebellar synapses (*Blanchard et al., 2020*; *Malagon et al., 2020*). Finally, in several studies on chromaffin cells and synapses of vertebrates and invertebrates, the assumption of Ca^{2+}-dependent priming was required to explain the experimental data (*Doussau et al., 2017*; *Kobbersmed et al., 2020*; *Millar et al., 2005*; *Pan and Zucker, 2009*; *Voets, 2000*; *Walter et al., 2013*). In contrast, previous studies at cerebellar mossy fiber synapses could explain release during trains of action potentials or prolonged depolarizations with Ca^{2+}-independent vesicle priming and replenishment (*Hallermann et al., 2010*; *Ritzau-Jost et al., 2014*; *Ritzau-Jost et al., 2018*; *Saviane and Silver, 2006*).

The discrepant findings of the Ca^{2+}-sensitivity of vesicle priming, fusion, and replenishment could be due to methodological errors. However, synapses show type-specific functional and structural differences (*Atwood and Karunanithi, 2002*; *Nusser, 2018*; *Zhai and Bellen, 2004*). The rate at which vesicles are replenished to empty release sites seems to be particularly different between types of synapses. The cerebellar mossy fiber bouton (cMFB) conveys high-frequency sensory information to the cerebellar cortex and relies on extremely fast vesicle replenishment (*Miki et al., 2020*; *Ritzau-Jost et al., 2014*; *Saviane and Silver, 2006*). The aim of this study was therefore to determine the Ca^{2+}-sensitivity of vesicle priming, fusion, and replenishment at mature cMFBs synapses at physiological temperature, and to test whether and how the prominent fast vesicle replenishment affects the Ca^{2+}-dependence of the vesicle priming, fusion, and replenishment at this synapse. To measure the Ca^{2+}-dependence of vesicle priming, we first directly manipulated the free basal intracellular Ca^{2+} concentration and measured the amount of action potential-evoked release. To meaure the Ca^{2+}-dependence of vesicle fusion, we focused the initial release kinetics of the fusion of the primed vesicles upon Ca^{2+} uncaging (with time constants mostly << 10 ms). To finally measure the Ca^{2+}-dependence of vesicle replenishment, we focused on the sustained component of release occurring during 100 ms of flash-evoked Ca^{2+} increase.

Our data revealed a strong dependence of the number of release-ready vesicles on basal Ca^{2+} concentrations between 30 and 180 nM, a significant release below 5 μM, an apparent shallow dose-response curve in the studied Ca^{2+} concentration range of 1 to 50 μM, and little Ca^{2+}-dependence of vesicle replenishment during sustained elevated intracellular Ca^{2+} concentrations.

Computational simulations incorporating mechanistic release schemes with five Ca^{2+} binding steps and fast vesicle replenishment via sequential or parallel pools of vesicles could explain our data. Our results show the co-existence of Ca^{2+} sensors with high- and low-affinities that cover a large range of intracellular Ca^{2+} concentrations and mediate fast signaling at this synapse.

Results

Action potential-evoked synaptic release critically depends on basal intracellular Ca^{2+} concentration

To investigate the impact of the basal intracellular Ca^{2+} concentration on synaptic release, we performed simultaneous patch-clamp recordings from presynaptic cerebellar mossy fiber boutons (cMFB) and postsynaptic granule cells (GC) of 5- to 6-week-old mice at physiological temperatures (*Figure 1A and B*). We aimed at clamping the free Ca^{2+} concentration in the presynaptic patch solution to either low or high basal Ca^{2+} concentrations by adding different concentrations of Ca^{2+} and the Ca^{2+} chelator EGTA (see Materials and methods). Two-photon quantitative Ca^{2+} imaging with the dual-indicator method using Fluo-5F as the Ca^{2+} indicator (*Delvendahl et al., 2015*; *Sabatini et al., 2002*) revealed the free Ca^{2+} concentration of the presynaptic intracellular solution to be 28 ± 3 and 183 ± 8 nM, for the low and high basal Ca^{2+} conditions (n = 4 and 4), respectively (*Figure 1A*). In both solutions, the free EGTA concentration was 4.47 mM (see Materials and methods). In response to triggering a single action potential in the presynaptic
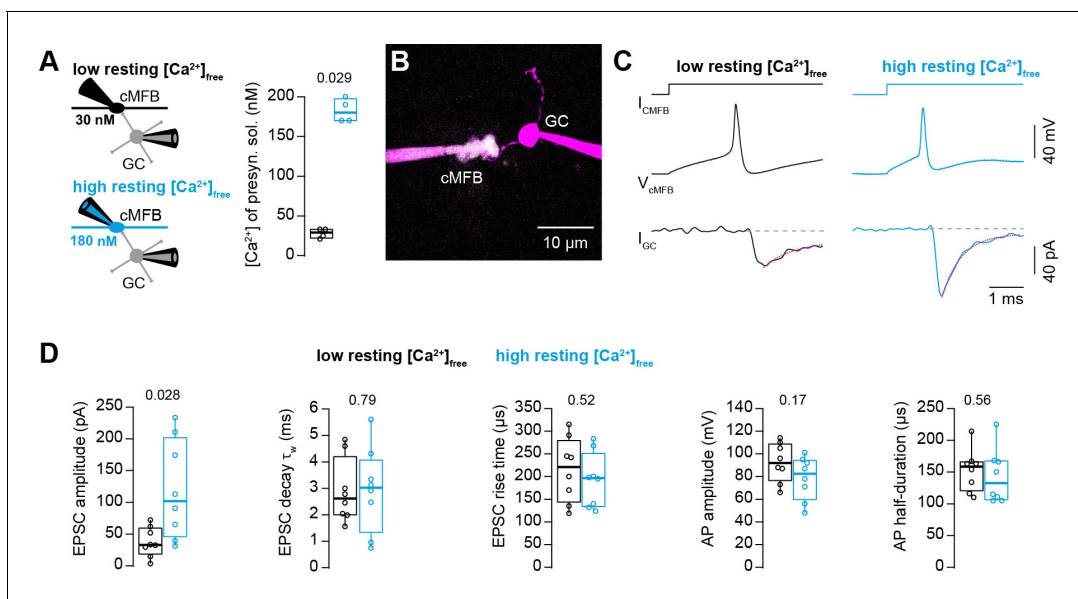

Figure 1. Action potential-evoked synaptic release critically depends on basal intracellular Ca^{2+} concentration. (**A**) *Left:* Illustration of the cellular connectivity of the cMFB to GC synapse during simultaneous pre- and postsynaptic patch-clamp recording. The presynaptic terminal was loaded with an intracellular solution having either low or high free basal Ca^{2+} concentration (top and bottom, respectively). *Right:* Comparison of the average free Ca^{2+} concentration in the presynaptic patch pipette (quantified by two-photon Ca^{2+} imaging) for the intracellular solutions with low and high basal Ca^{2+} (n = 4 each). (**B**) Example two-photon microscopic image of a cMFB and a GC in the paired whole-cell configuration. (**C**) Example traces of a paired cMFB-GC recording with current injection (I_{cMFB}) (*top*) eliciting an action potential in the cMFB (*middle*) and an EPSC in the postsynaptic GC (*bottom*). Black and blue color code corresponds to low and high free basal Ca^{2+} concentration in the presynaptic solution, respectively. The decay of the EPSC was fitted with a bi-exponential function (magenta line). (**D**) Comparison of the properties of presynaptic action potentials and EPSCs evoked after eliciting an action potential in the presynaptic terminal using solutions having either low (black) or high (blue) free Ca^{2+} concentration. From left to right: peak amplitude of the EPSC, weighted decay time constant of the EPSC, 10-to-90% rise time of the EPSC, amplitude of the presynaptic action potential, and action potential half-duration (n = 8 and 8 paired cells for the conditions with low and high resting Ca^{2+} concentration, respectively). Boxplots show median and 1st/3rd quartiles with whiskers indicating the whole data range. Values of individual experiments are superimposed as circles. The numbers above the boxplots represent p-values of Mann-Whitney *U* tests.

The online version of this article includes the following source data for figure 1:

Source data 1. Action potential-evoked synaptic release critically depends on basal intracellular Ca^{2+} concentration.

13

terminal, the recorded excitatory postsynaptic current (EPSC) depended strongly on the presynaptic resting Ca^{2+} concentration (*Figure 1C*). We found an almost threefold increase in the EPSC amplitude when elevating the resting Ca^{2+} concentration in the presynaptic terminals from 30 to 180 nM. On average, the EPSC amplitudes were 39 ± 8 and 117 ± 28 pA for the low and high basal Ca^{2+} conditions, respectively (n = 8 and 8; $P_{Mann-Whitney}$ = 0.028; *Figure 1D*). Interestingly, the frequency of miniature currents in-between the current injections used to elicit action potentials had a tendency to increase with elevated basal Ca^{2+} concentration (median 1.1 and 3.5 Hz for the low and high basal Ca^{2+} conditions, respectively, n = 8 and 8; $P_{Mann-Whitney}$ = 0.13; data not shown). The EPSC rise and decay kinetics were not significantly different (*Figure 1D*). No significant differences were observed in the action potential waveform including amplitude and half duration (*Figure 1D*) indicating that the altered synaptic strength was not caused by changes in the shape of the presynaptic action potential. These data indicate that moderate changes in the presynaptic basal Ca^{2+} concentration can alter synaptic strength up to threefold.

Ca^{2+} uncaging dose-response curve measured with presynaptic capacitance measurements

To gain a better understanding of the profound sensitivity of AP-evoked release on presynaptic basal Ca^{2+} concentration, we established presynaptic Ca^{2+} uncaging and measured the release kinetics upon step-wise elevation of Ca^{2+} concentration. We combined wide-field illumination using a high-power UV laser with previously established quantitative two-photon Ca^{2+} imaging (*Delvendahl et al., 2015*) to quantify the post-flash Ca^{2+} concentration (*Figure 2A*). This approach offers sub-millisecond control of the UV flashes and a high signal to noise ratio of the two-photon Ca^{2+} imaging deep within the brain slice. The flash-evoked artefacts in the two-photon signals, presumably due to luminescence in the light path, could be reduced to a minimum with an optimal set of spectral filters and gate-able photomultipliers (PMTs). Subtraction of the remaining artefact in the background region of the two-photon line scan resulted in artefact-free fluorescence signals (*Figure 2B and C*).

To obtain a large range of post-flash Ca^{2+} concentrations within the bouton, we varied the concentration of the Ca^{2+}-cage DMn (1–10 mM) and the intensity (10–100%) and the duration (100 or 200 μs) of the UV laser pulse (*Table 1*). The spatial homogeneity of the Ca^{2+} elevation was assessed by UV illumination of caged fluorescein mixed with glycerol (*Figure 2—figure supplement 1*; *Schneggenburger and Neher, 2000*; *Bollmann et al., 2000*). The resulting post-flash Ca^{2+} concentration was quantified with either high- or low-affinity Ca^{2+} indicator (Fluo-5F or OGB-5N). To measure the kinetics of neurotransmitter release independent of dendritic filtering or postsynaptic receptor saturation, vesicular fusion was quantified by measuring the presynaptic capacitance with a 5 kHz-sinusoidal stimulation (*Hallermann et al., 2003*). The first 10 ms of the flash-evoked capacitance increase was fitted with functions containing a baseline and mono- or bi-exponential components (magenta line in *Figure 2D and E*; see *Equation 1* in the Materials and methods section). With increasing post-flash Ca^{2+} concentration the fast time constant decreased (τ in case of mono- and τ_1 in case of bi-exponential fits; *Figure 2D*). The inverse of the fast time constant represents a direct readout of the fusion kinetics of the release-ready vesicles. When plotting the inverse of the time constant as a function of post-flash Ca^{2+} concentration, we obtained a shallow dose-response curve that showed a continuous increase in the release rate with increasing post-flash Ca^{2+} concentration up to 50 μM (*Figure 2F*). In some experiments with high Ca^{2+} concentrations, the release was too fast to be resolved with 5 kHz capacitance sampling (i.e. time constants were smaller than 200 μs; *Figure 2E*). We therefore increased the frequency of the sinusoidal stimulation in a subset of experiments to 10 kHz (15 out of 80 experiments). Such high-frequency capacitance sampling is to our knowledge unprecedented at central synapses and technically challenging because exceptionally low access resistances are required (<~15 MΩ) to obtain an acceptable signal-to-noise ratio (*Gillis, 1995*; *Hallermann et al., 2003*). Despite these efforts, the time constants were sometimes faster than 100 μs, representing the resolution limit of 10 kHz capacitance sampling (*Figure 2E*). These results indicate that the entire pool of release-ready vesicles can fuse within less than 100 μs. Fitting a Hill equation on both 5- and 10 kHz data resulted in a best-fit K_D of >50 μM with a best-fit Hill coefficient, *n*, of 1.2 (*Figure 2F*).

In addition to the speed of vesicle fusion, we analyzed the delay from the onset of the UV-illumination to the onset of the rise of membrane capacitance, which was a free parameter in our fitting
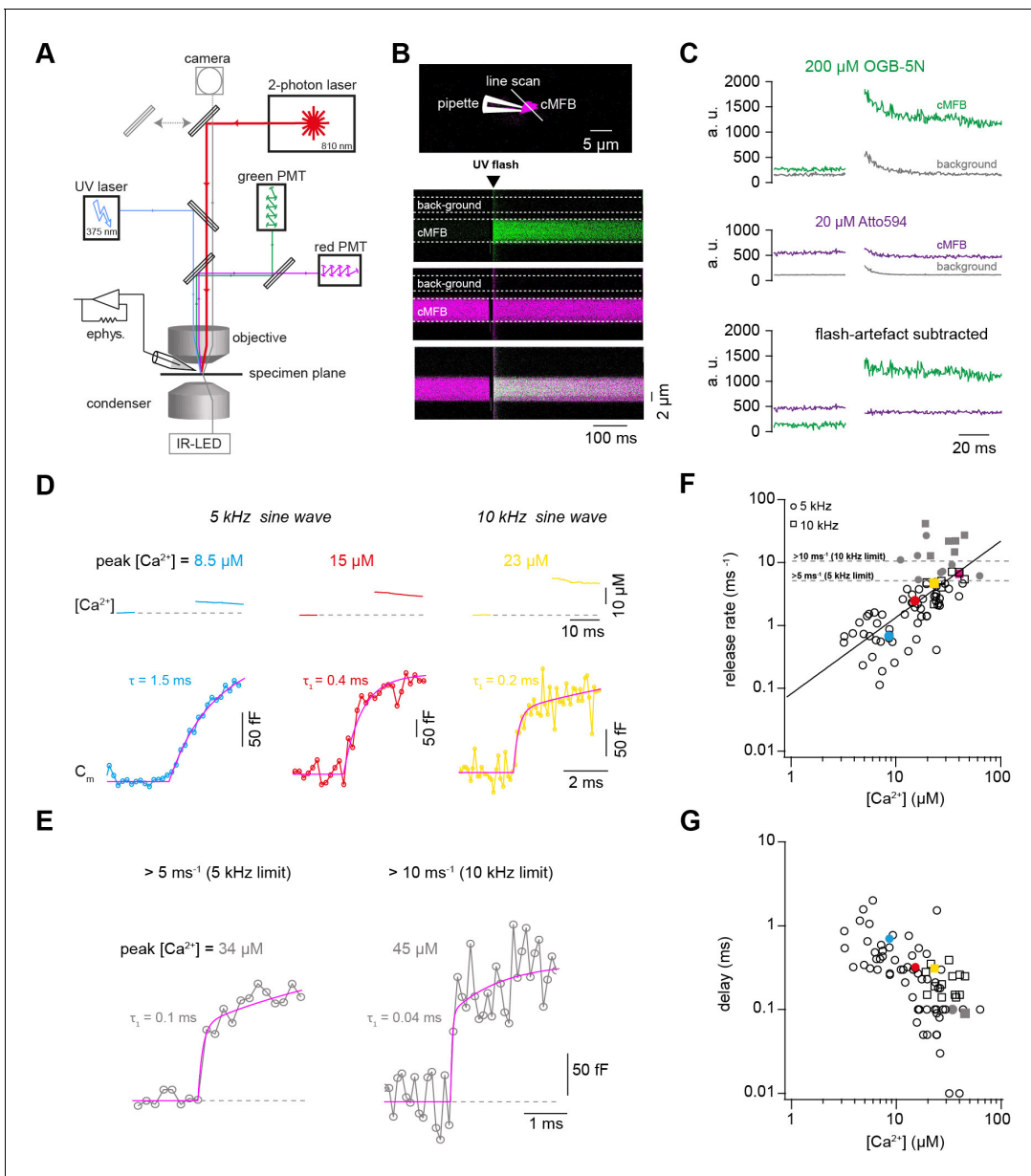
14

Figure 2. Ca^{2+} uncaging dose-response curve measured with presynaptic capacitance measurements. (**A**) Illustration of the experimental setup showing the light path of the two-photon laser illumination (red line), the UV laser illumination (blue line), the electrophysiology amplifier ('ephys.'), the red and green gate-able photomultiplier tubes (PMTs), and infrared LED illumination with oblique illumination via the condenser for visualization of the cells at the specimen plane by the camera (gray line) when the upper mirror is moved out of the light path (gray arrow). (**B**) *Top:* Two-photon microscopic image of a cMFB in the whole-cell configuration loaded with OGB-5N, Atto594, and DMn/ Ca^{2+}. Positions of the patch pipette and line scan are indicated. *Bottom:* Two-photon line scan showing the fluorescence signal as measured through the green PMT, red PMT, and an overlay of the green and red channels. Arrow indicates the onset of the UV flash and dashed lines represent the flash-induced luminescence artefact as detected outside the cMFB. The lookup tables for the green and red channel were arbitrarily adjusted independent of the absolute values in C. (**C**) *Top:* change in fluorescence intensity within the cMFB for the green channel along with the corresponding flash-induced green artefact measured in the background. *Middle:* change in fluorescence intensity within the cMFB for the red channel along with the corresponding flash-induced red artefact. *Bottom:* green and red fluorescence signal after subtracting the flash-induced artefacts. (**D**) *Top:* Ca^{2+} signals of different concentrations elicited through Ca^{2+} uncaging in three different cells, the flash was blanked. *Bottom:* corresponding traces of capacitance recordings measured using a 5 kHz (left and middle) or 10 kHz sinusoidal stimulation (right). τ represents the time constant from a mono-exponential fit, τ_1 represents the time constant of the fast component of a bi-exponential fit. (**E**) Traces of capacitance recordings showing the resolution limit in detecting fast release rates of >5 ms^{-1} using 5 kHz sinusoidal stimulation or >10 ms^{-1} using 10 kHz sinusoidal stimulation. (**F**) Plot of release rate versus post-flash Ca^{2+} concentration (n = 65 from 5-kHz- and from 15 10-kHz-recordings obtained from 80 cMFBs). The line represents a fit with a Hill equation (*Equation 2*) with best-fit values V_{max} = $1.7*10^7$ ms^{-1}, K_D = $7.2*10^6$ µM, and *n* = 1.2. Color coded symbols correspond to traces in (**D** – **E**). Gray symbols represent values above the resolution

Figure 2 continued on next page

15

Figure 2 continued

limit. (**G**) Plot of synaptic delay versus post-flash Ca^{2+} concentration (n = 64 from 5-kHz- and 15 from 10-kHz-recordings obtained from 79 cells). Note that one recording was removed from the analysis because the exponential fit led to a negative value of the delay. Color coded symbols correspond to traces in (**D** – **E**).

The online version of this article includes the following source data and figure supplement(s) for figure 2:

Source data 1. Ca^{2+} uncaging dose-response curve measured with presynaptic capacitance measurements.

Figure supplement 1. Measurement of the UV energy profile with caged fluorescein.

functions (see *Equation 1*). The delay was strongly dependent on the post-flash Ca^{2+} concentration and the dose-response curve showed no signs of saturation at high Ca^{2+} concentrations (*Figure 2G*), which is consistent with the non-saturating release rates. These data reveal that the fusion kinetics of synaptic vesicles increased up to a Ca^{2+} concentration of 50 µM without signs of saturation, suggesting a surprisingly low apparent affinity of the fusion sensor at mature cMFBs under physiological temperature conditions ($K_D > 50$ µM).

Ca^{2+} uncaging dose-response curve measured with deconvolution of EPSCs

Capacitance recordings are not very sensitive in detecting low release rates. We therefore performed simultaneous pre- and postsynaptic recordings and used established deconvolution techniques to calculate the presynaptic release rate by analyzing the EPSC as previously applied at this synapse (*Figure 3A,B*; *Ritzau-Jost et al., 2014*). Kynurenic acid (2 mM) and cyclothiazide (100 µM) were added to the extracellular solution in order to prevent the saturation and desensitization of postsynaptic AMPA receptors, respectively. Ca^{2+} uncaging in the presynaptic terminal evoked EPSCs with kinetics, which strongly depended on the post-flash Ca^{2+} concentration. The cumulative release obtained from deconvolution analysis of the recorded EPSCs was fitted as previously done for capacitance traces (*Equation 1*). At low Ca^{2+} concentrations (<5 µM), a significant amount of neurotransmitter release could be measured, which is consistent with previous reports from central synapses (*Bollmann et al., 2000*; *Fukaya et al., 2021*; *Sakaba, 2008*; *Schneggenburger and Neher, 2000*). The presynaptic release rates increased with increasing post-flash Ca^{2+} concentration and no saturation in the release rate occurred in the dose-response curve (*Figure 3D*). The dose-response curve for the delay from the onset of the UV illumination to the onset of the rise of the cumulative release trace (*Equation 1*) did not show signs of saturation of the release kinetics in the

Table 1. Parameters for weak, middle, and strong post-flash Ca^{2+} elevations.

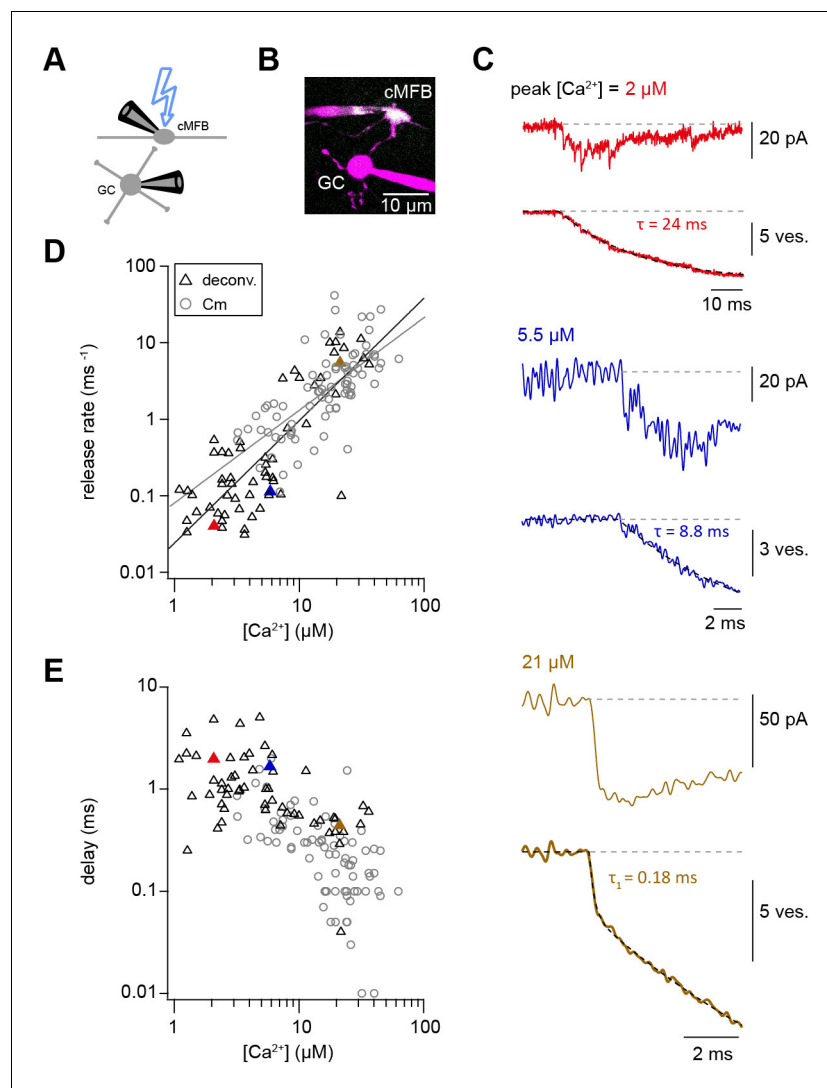|	weak Ca^{2+} elevation	middle Ca^{2+} elevation	strong Ca^{2+} elevation
UV illumination			
Duration (ms)	0.1 or 1	0.1	0.1 or 0.2
Intensity (%)	10–100	20–100	100
Concentration in intracellular solution (mM)			
ATTO 594	0.010	0.020	0.020
Fluo 5F	0.050	0	0
OGB 5N	0	0.200	0.200
CaCl2	0.500	2.000	10.000
DM-N	0.500	2.000	10.000
Obtained peak post-flash Ca^{2+} (µM)			
Min	1.1	2.7	15.7
Max	7.1	36.0	62.6
Median	2.4	8.8	25.1
Simulated uncaging fraction of DMn			
α	0.08–0.5	0.15–0.55	0.14–0.25

16

Figure 3. Ca^{2+} uncaging dose-response curve measured with deconvolution of EPSCs. (**A**) Illustration of the cellular connectivity in the cerebellar cortex showing the pre- and postsynaptic compartments during paired whole-cell patch-clamp recordings and Ca^{2+} uncaging with UV-illumination. (**B**) Two-photon microscopic image of a cMFB and a GC in the paired whole-cell patch-clamp configuration. (**C**) Three different recordings showing UV-flash evoked EPSC (*top trace*) and cumulative release rate measured by deconvolution analysis of the EPSCs (*bottom trace*). The peak Ca^{2+} concentration, quantified with two-photon Ca^{2+} imaging, is indicated in each panel. τ represents the time constant from mono-exponential fit, τ_1 represents the time constant of the fast component of bi-exponential fit. Note the different lengths of the baselines in the three recordings. (**D**) Plot of release rate versus post-flash Ca^{2+} concentration. Gray open circles represent data from capacitance measurements (*Figure 2*) and black triangles represent data from deconvolution analysis of EPSC (n = 57 recordings obtained from 42 paired cells). Gray and black lines represent fits with a Hill equation of the capacitance (as shown in *Figure 1F*) and the deconvolution data, respectively. The best-fit parameters for the fit on the deconvolution data were V_{max} = 6*10^7 ms^{-1}, K_D = 7.6*10^5 μM, and n = 1.6. Red, blue, and brown symbols correspond to the traces in (**C**). (**E**) Plot of synaptic delay versus post-flash Ca^{2+} concentration (n = 59 recordings obtained from 43 paired cells). Note that two recordings was removed from the analysis because the exponential fit led to a negative value of the delay Gray open circles represent data from capacitance measurements, and black triangles represent data from deconvolution analysis of EPSC. Red, blue, and brown symbols correspond to the traces in (**C**).

The online version of this article includes the following source data and figure supplement(s) for figure 3:

Source data 1. Ca^{2+} uncaging dose-response curve measured with deconvolution of EPSCs.
Figure supplement 1. Measuring the K_D of the Ca^{2+} sensitive dyes.
Figure supplement 2. Comparison of brief versus long UV illumination to rule out fast Ca^{2+} overshoots.
Figure 3 continued on next page

---

investigated range. Thus, consistent with capacitance measurements, deconvolution analysis of post-synaptic currents revealed a shallow Ca^{2+}-dependence of neurotransmitter release kinetics (*Figure 3D and E*). Fitting a Hill equation to the deconvolution data resulted in a best-fit K_D >50 µM and a Hill coefficient of 1.6 (*Figure 3D*). Therefore, two independent measures of synaptic release (presynaptic capacitance measurements and postsynaptic deconvolution analysis) indicate a non-saturating shallow dose-response curve up to ~50 µM.

To rule out methodical errors that might influence the dose-response curve, we carefully determined the K_D of the Ca^{2+} indicator OGB-5N using several independent approaches including direct potentiometry (*Figure 3—figure supplement 1*), because this value influences the estimate of the Ca^{2+} affinity of the fusion sensors linearly. We estimated a K_D of OGB-5N of ~30 µM being at the lower range of previous estimates ranging from 20 to 180 µM (*Delvendahl et al., 2015*; *DiGregorio and Vergara, 1997*; *Neef et al., 2018*), arguing against an erroneously high K_D of the Ca^{2+} indicator as a cause for the non-saturation.

In addition, we used the two following independent approaches to rule out a previously described Ca^{2+} overshoot immediately following the UV illumination. Such a Ca^{2+} overshoot would be too fast to be detected by the Ca^{2+} indicators (*Bollmann et al., 2000*) but could trigger strong release with weak UV illumination which would predict a shallow dose-response curve. First, the time course of Ca^{2+} release from DMn was simulated (see below; Figure 6A) and no significant overshoots were observed (see below). Secondly, we experimentally compared strong and short UV illumination (100% intensity; 0.1 ms) with weak and long UV illumination (10% intensity; 1 ms), because a Ca^{2+} overshoot is expected to primarily occur with strong and short UV illumination. Comparison of these two groups of UV illumination resulted in similar post-flash concentrations but did not reveal a significant difference in the corresponding release rate indicating that undetectable Ca^{2+} overshoots did not affect the measured release rate (*Figure 3—figure supplement 2*). Therefore, both approaches argue against a Ca^{2+} overshoot as an explanation for the shallow dose-response curve.

Presynaptic and postsynaptic measurements reveal two kinetic processes of neurotransmitter release

In some Ca^{2+} uncaging experiments, synaptic release appeared to have two components, which could be due to heterogeneity amongst release-ready vesicles. We therefore systematically compared mono- and bi-exponential fits to the capacitance and deconvolution data (*Figure 4A B*). Several criteria were used to justify a bi-exponential fit (see Materials and methods). One criterion was at least a 4% increase in the quality of bi- compared with mono-exponential fits as measured by the sum of squared differences between the fit and the experimental data (χ^2; *Figure 4D*). Consistent with a visual impression, this standardized procedure resulted in the classification of ~40% of all recordings as bi-exponential (38 out of 80 capacitance measurements and 17 out of 59 deconvolution experiments; *Figure 4C D*). The release rate of the fast component ($1/\tau_1$) of the merged capacitance and deconvolution data showed no signs of saturation consistent with our previous analyses of each data set separately. Fitting a Hill equation to the merged data indicated a K_D >50 µM and a Hill coefficient of 1.6 (*Figure 4C*). The release rate of the slow component ($1/\tau_2$; if existing) was on average more than 10 times smaller (black symbols, *Figure 4C*). These data indicate that there are at least two distinct kinetic steps contributing to release within the first 10 ms.

Fast sustained release with very weak Ca^{2+}-dependence

To gain more insights into the mechanisms of sustained vesicle release, we focused on the synaptic release within the first 100 ms after Ca^{2+} uncaging, presumably reflecting vesicle replenishment (*Sakaba, 2008*). Using capacitance measurements, we investigated the Ca^{2+}-dependence of sustained release by estimating the number of vesicles (N_v) released between 10 and 100 ms after flash onset (*Figure 5A*), assuming a single vesicle capacitance of 70 aF (*Hallermann et al., 2003*). There
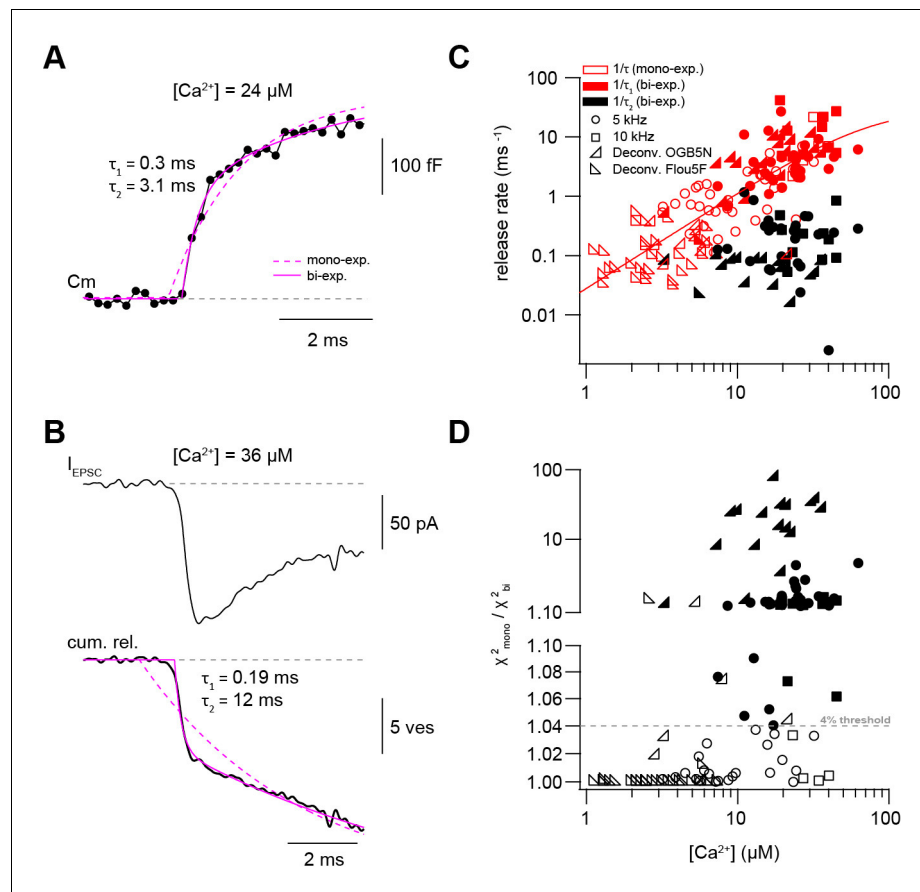
Figure 4. Presynaptic and postsynaptic measurements reveal two kinetic processes of neurotransmitter release. (A) Example of a capacitance trace showing the two components of release observed within the first 10 ms in response to UV-flash-evoked increase in Ca^{2+} concentration to 24 µM. The solid magenta line represents the bi-exponential fit and the dashed magenta line represents mono-exponential fit (see *Equation 1*). (B) *Top:* example trace of an EPSC recording in response to UV-flash evoked increase in Ca^{2+} concentration to 36 µM. *Bottom:* the corresponding cumulative release trace obtained from deconvolution analysis, showing the two components of release observed within the first 10 ms. The solid magenta line represents the bi-exponential fit and the dashed magenta line represents mono-exponential fit (see *Equation 1*). (C) Top: plot of neurotransmitter release rates as a function of peak Ca^{2+} concentration (n = 80 and 59 capacitance measurements and deconvolution analysis, respectively). Data obtained from capacitance measurements with sinusoidal frequency of 5 kHz are shown as circles, data from 10 kHz capacitance measurements are shown as squares, and cumulative release data obtained from deconvolution analysis are shown as lower left- and lower right- triangles for recordings with OGB-5N and Fluo5F, respectively. Open symbols correspond to data from the mono-exponential fits and filled symbols correspond to data from the bi-exponential fits. Red symbols represent merged data of the release rates obtained from mono-exponential fit and the fast component of the bi-exponential fit, and black symbols represent the second component of the bi-exponential fit. The line represents a fit with a Hill equation with best-fit parameters $V_{max} = 29.9$ ms^{-1}, $K_D = 75.5$ µM, and $n = 1.61$. (D) χ^2 ratio for the mono-exponential compared to the bi-exponential fits. Dashed line represents the threshold of the χ^2 ratio used to judge the fit quality of double compared to mono-exponential fits (as one criterion for selection). 5 kHz capacitance data are shown as circles, 10 kHz capacitance data are shown as squares, and cumulative release data (obtained from deconvolution analysis) are shown as lower left- and lower right- triangles for recordings with OGB-5N and Fluo5F, respectively. Open symbols correspond to data points judged as mono-exponential and filled symbols correspond to data points judged as bi-exponential.

The online version of this article includes the following source data for figure 4:

Source data 1. Presynaptic and postsynaptic measurements reveal two kinetic processes of neurotransmitter release.
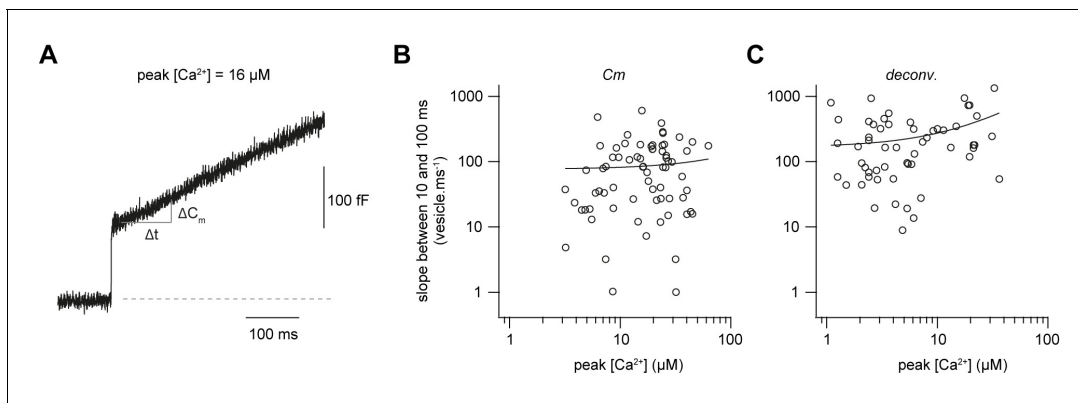
Figure 5. Fast sustained release with very weak Ca^{2+}-dependence. (**A**) Examples of a capacitance trace showing a sustained component of release. (**B**) Plot of the number of vesicles released between 10 and 100 ms as estimated from capacitance measurements divided by the time interval (90 ms) versus the post-flash Ca^{2+} concentration (n = 71 cMFBs). The line represents a linear fit to the data with a slope of 6 vesicles ms^{-1} μM^{-1} (Pearson correlation coefficient = 0.06, r^2 = 0.003; $P_{Pearson\ correlation}$ = 0.6). (**C**) Plot of the number of vesicles released between 10 and 100 ms as estimated from deconvolution analysis divided by the time interval (90 ms) versus the post-flash Ca^{2+} concentration (n = 51 cMFB-GC pairs). The line represents a linear fit to the data with a slope of 10 vesicles ms^{-1} μM^{-1} (Pearson correlation coefficient = 0.3, r^2 = 0.1; $P_{Pearson\ correlation}$ = 0.01).

The online version of this article includes the following source data for figure 5:

Source data 1. Fast sustained release with very weak Ca^{2+}-dependence.

was considerable variability in the release rate between 10 and 100 ms, which could be due to differences in bouton size and wash-out of proteins during whole-cell recordings. However, the release rate showed no obvious dependence on the post-flash Ca^{2+} concentration (*Figure 5B*). A comparable dose-response curve was obtained when investigating the rate of release between 10 and 100 ms using deconvolution analysis of postsynaptic currents, however, with a weak but significant correlation (*Figure 5C*). These data indicate that the slope of the sustained component of release is, if anything, weakly dependent on the intracellular Ca^{2+} concentration in the range of 1–50 µM, consistent with previously observed Ca^{2+}-independent vesicle replenishment as assessed by depolarizing cMFBs to 0 mV in the absence or presence of intracellular EGTA (*Ritzau-Jost et al., 2014*).

Release schemes with five Ca^{2+} steps and fast replenishment via parallel or sequential models can explain Ca^{2+}-dependence of release

To investigate the mechanisms that could explain a non-saturating and shallow dose-response curve and rapid sustained release, we performed modeling with various release schemes. First, we simulated the exact time course of the concentration of free Ca^{2+}. The Ca^{2+} release from DMn and subsequent binding to other buffers and the Ca^{2+} indicator were simulated based on previously described binding and unbinding rates (*Faas et al., 2005*; *Faas et al., 2007*; *Figure 6A*; *Table 2*; see Materials and methods). In contrast to previous results, which predicted a significant overshoot of Ca^{2+} following UV illumination with short laser pulses (*Bollmann et al., 2000*), our simulations predict little overshoot compared to the Ca^{2+} concentration measured by the Ca^{2+} indicator (*Figure 6B*). The discrepancy is readily described by recent improvements in the quantification of Ca^{2+} binding and unbinding kinetics (*Faas et al., 2005*; *Faas et al., 2007*). The calculations predict an almost step-like increase in the free Ca^{2+} concentration with a 10–90% rise time below 50 µs. These simulated UV illumination-induced transients of free Ca^{2+} concentrations were subsequently used to drive the release schemes. Realistic noise was added to the resulting simulated cumulative release rate and the traces were fit with exponential functions (*Equation 1*) as the experimental data (*Figure 6C*).

We compared three different release schemes in their ability to reproduce our experimental data. In model 1, a single pool of vesicles with two Ca^{2+} binding steps was used as previously established, for example for chromaffin cells and rod photoreceptors (*Duncan et al., 2010*; *Voets, 2000*). Such an assumption would readily explain the shallow dose-response curve (*Bornschein and Schmidt, 2018*). The 2nd component of release could be replicated by assuming rapid vesicle replenishment from a reserve pool (V_R; *Figure 6D*). However, adjusting the free parameters did not allow
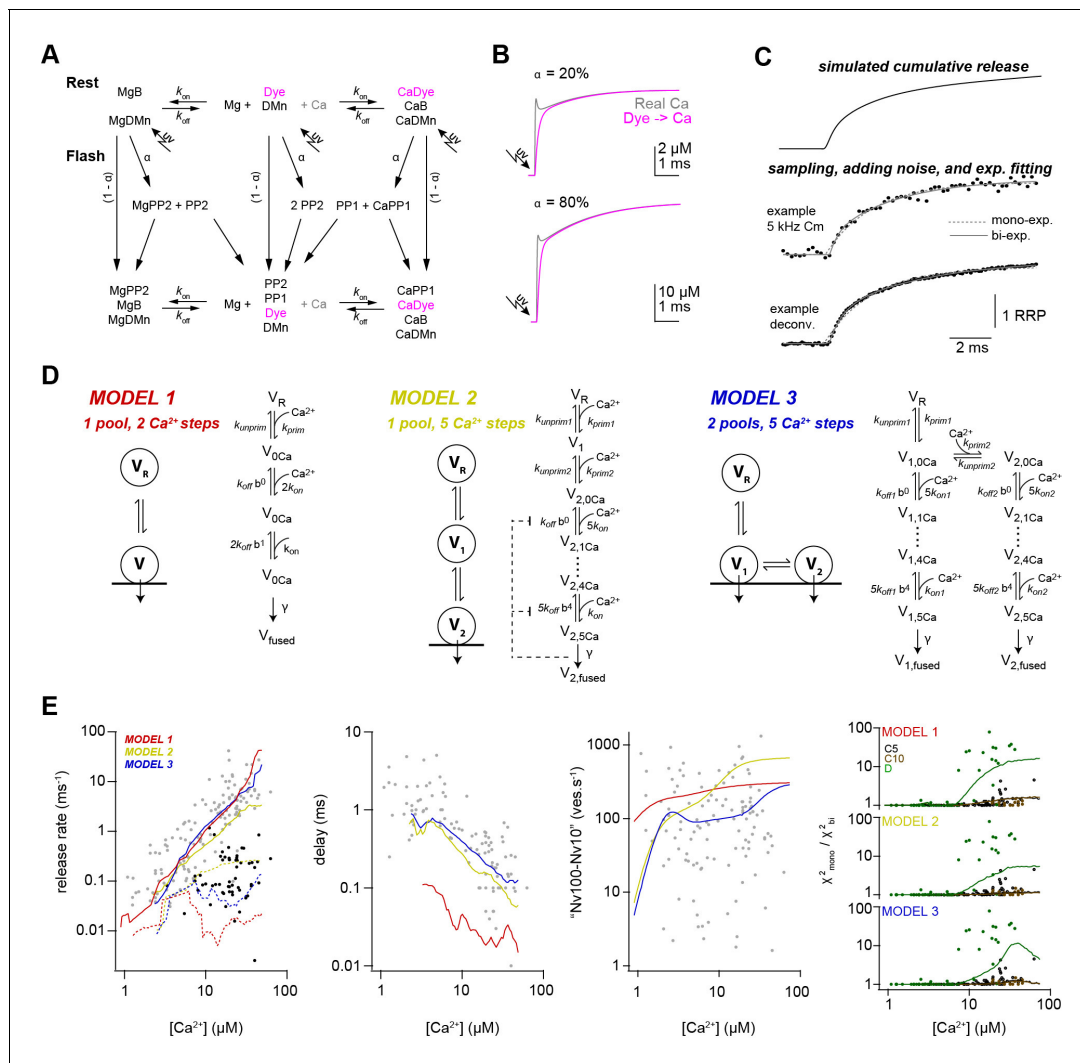
20

Figure 6. Release schemes with five Ca^{2+} steps and fast replenishment via parallel or sequential models can explain Ca^{2+}-dependence of release. (**A**) Scheme of the chemical reactions that were implemented in the model to calulate the UV-illumination-evoked increase in the free Ca^{2+} concentration. The model considered Ca^{2+} (Ca) and Mg^{2+} (Mg) binding to the indicator dye (OGB-5N or Fluo-5F), to DM-nitrophen (DMn), and to buffers (ATP and/or an endogenous buffer). The forward (k_{on}) and backward (k_{off}) rate constants differ between chemical species. Upon photolysis, a fraction α of metal bound and free DMn made a transition to different photoproducts (PP1 and PP2; **Faas et al., 2005**). For model parameters see **Table 2**. (**B**) The scheme in (**A**) was converted to a system of differential equations and the time courses of the 'real' free Ca^{2+} (magenta) and the free Ca^{2+} reported by Ca^{2+} dye were simulated for the indicated uncaging fractions α. Note that after less than 1 ms the dye reliably reflects the time course of Ca^{2+}. (**C**) Traces showing the steps used in the simulation of the kinetic model of release. (**D**) Graphical illustration of the three models used during the simulations. For model parameters see **Table 3**. (**E**) From left to right, predictions of each model and the experimental data for the inverse of τ_1 (gray symbols, solid lines) and inverse of τ_2 (black symbols, dashed lines), delay, vesicle replenishment rate between 10 and 100 ms, and the increase in the χ^2 ratio for the single- compared to the bi-exponential fits. Red, yellow, and blue lines correspond to simulations of models 1, 2, and 3, respectively. For the χ^2 ratio (*right plot*), the experimental data and the simulations are shown separately for 5-kHz- and 10-kHz-capacitance data (C5 and C10; black and brown, respectively) and the deconvolution data (D; green).

reproducing the synaptic delay (**Figure 6E**). We therefore tested two more sophisticated models in which vesicle fusion is triggered via five Ca^{2+} binding steps (**Schneggenburger and Neher, 2000**). In model 2, onevesicle pool represents the docked vesicles (V_2) and the other pool represents a replacement pool (V_1), which can undergo rapid docking and fusion (**Miki et al., 2016**; **Miki et al., 2018**), therefore representing two kinetic steps occurring in sequence. In model 3, two pools of vesicles (V_1, V_2) with different Ca^{2+}-sensitivity exist, where both types of vesicles can fuse with different Ca^{2+} affinity (**Voets, 2000**; **Walter et al., 2013**; **Wölfel et al., 2007**; **Hallermann et al., 2010**) therefore representing two kinetic steps occurring in parallel. Model 3 reproduced the data

Table 2. Parameters for simulations of Ca^{2+} release from DMN cage.

Parameters		Values	References number / Notes
Resting Ca^{2+}	$[Ca^{2+}]_{rest}$	$227*10^{-9}$ M	Measured
Total magnesium	$[Mg^{2+}]_T$	$0.5*10^{-3}$ M	Pipette concentration
Fluo-5F	[Fluo]	0 or 50 $*10^{-6}$ M (see *Table 1*)	Pipette concentration
	K_D	$0.83 *10^{-6}$ M	*Delvendahl et al., 2015*
	k_{off}	249 s-1	ibid
	k_{on}	$3*10^8$ $M^{-1}s^{-1}$	*Yasuda et al., 2004*
OGB-5N	[OGB]	0 or $200*10^{-6}$ M (see *Table 1*)	Pipette concentration
	K_D	$31.4*10^{-6}$ M	Measured (*Figure 3—figure supplement 1A*)
	k_{off}	6000 s^{-1}	ibid.
	k_{on}	$2.5*10^8$ $M^{-1}s^{-1}$	*DiGregorio and Vergara, 1997*
ATP	[ATP]	$5 *10^{-3}$ M	Pipette concentration
Ca^{2+} binding	K_D	$2*10^{-4}$ M	*Meinrenken et al., 2002*
	k_{off}	100 000 s^{-1}	ibid.
	k_{on}	$5*10^8$ $M^{-1}s^{-1}$	ibid.
Mg^{2+} binding	K_D	$100*10^{-6}$ M	*Bollmann et al., 2000*; MaxC
	k_{off}	1000 s^{-1}	ibid.
	k_{on}	$1*10^7$ $M^{-1}s^{-1}$	ibid.
Endogenous buffer	[EB]	$480 *10^{-6}$ M	*Delvendahl et al., 2015*
	K_D	$32*10^{-6}$ M	ibid
	k_{off}	16 000 s^{-1}	ibid.
	k_{on}	$5*10^8$ $M^{-1}s^{-1}$	ibid.
Total DM nitrophen	$[DMn]_T$	$500*10^{-6} – 10*10^{-3}$ M (see *Table 1*)	Pipette concentration
Ca^{2+} binding	K_D	$6.5*10^{-9}$ M	*Faas et al., 2005*
	k_{off}	0.19 s^{-1}	ibid.
	k_{on}	$2.9*10^7$ $M^{-1}s^{-1}$	ibid.
Mg^{2+} binding	K_D	$1.5*10^{-6}$ M	ibid.
	k_{off}	0.2 s^{-1}	ibid.
Uncaging fraction	α	See *Table 1*	
Fast uncaging fraction	af	0.67	*Faas et al., 2005*
Photoproduct 1	[PP1]		
Ca^{2+} binding	K_D	$2.38*10^{-3}$ M	*Faas et al., 2005*
	k_{off}	69 000 s^{-1}	ibid.
	k_{on}	$2.9*10^7$ $M^{-1}s^{-1}$	ibid.
Mg^{2+} binding	K_D	$1.5*10^{-6}$ M	ibid.
	k_{off}	300 s^{-1}	ibid.
	k_{on}	$1.3*10^5$ $M^{-1}s^{-1}$	ibid.
Photoproduct 2	[PP2]		
Ca^{2+} binding	K_D	$124.1*10^{-6}$ M	Ibid.
	k_{off}	3600 s^{-1}	ibid.
	k_{on}	$2.9*10^7$ $M^{-1}s^{-1}$	ibid.
Mg^{2+} binding	K_D	$1.5*10^{-6}$ M	ibid.
	k_{off}	300 s^{-1}	ibid.
	k_{on}	$1.3*10^5$ $M^{-1}s^{-1}$	ibid.

22

Table 3. Parameters for release scheme models.

Model1		Model2		Model3	
k_{on}	$2.95*10^9$ Ca^{2+}(t) M^{-1} s^{-1}	$k_{on,init}$	$5.10*10^8$ Ca^{2+}(t) M^{-1} s^{-1}	k_{on1}	$0.5\ k_{on2}$
		$k_{on,plug}$	$0.1\ k_{on,init}$	k_{on2}	$5.10*10^8$ Ca^{2+}(t) M^{-1} s^{-1}
k_{off}	$4.42*10^5$ s^{-1}	$k_{off,init}$	$2.55*10^4$ s^{-1}	k_{off1}	$10\ k_{off2}$
		$k_{off,plug}$	$0.4\ k_{off,init}$	k_{off2}	$2.55*10^4$ s^{-1}
b	0.25	b	0.25	b	0.25
γ	$1.77*10^4$ s^{-1}	γ	$1.77*10^4$ s^{-1}	γ	$1.77*10^4$ s^{-1}
k_{prim}	$0.6+30*(Ca^{2+}(t)/(K_{D,prim}+Ca^{2+}(t)))$ s^{-1}	k_{prim1}	$2.5+60*(Ca^{2+}(t)/(K_{D,prim1}+Ca^{2+}(t)))$ s^{-1}	k_{prim1}	30 s^{-1}
k_{unprim}	$0.6+30*(Ca^{2+}_{Rest}/(K_{D,prim}+Ca^{2+}_{Rest}))$ s^{-1}	$k_{unprim1}$	$2.5+60*(Ca^{2+}_{Rest}/(K_{D,prim1}+Ca^{2+}_{Rest}))$ s^{-1}	$k_{unprim1}$	30 s^{-1}
$K_{D,prim}$	2 μM	$K_{D,prim1}$	2 μM		
		k_{prim2}	$100+800*(Ca^{2+}(t)/(K_{D,prim2}+Ca^{2+}(t)))$ s^{-1}	k_{prim2}	$0.5+30*(Ca^{2+}(t)/(K_{D,prim2}+Ca^{2+}(t)))$ s^{-1}
		$k_{unprim2}$	$100+800*(Ca^{2+}_{Rest}/(K_{D,prim2}+Ca^{2+}_{Rest}))$ s^{-1}	$k_{unprim2}$	$0.5+30*(Ca^{2+}_{Rest}/(K_{D,prim2}+Ca^{2+}_{Rest}))$ s^{-1}
		$K_{D,prim2}$	2 μM	$K_{D,prim2}$	2 μM

as good as model 2; however, the non-saturation up to 50 μM could be reproduced somewhat better in model 3. Interestingly, models 2 and 3 both replicated the observed shallow dose-response curve despite the presence of five Ca^{2+} binding steps. These results indicate that established models with five Ca^{2+}-steps incorporating fast vesicle replenishment via sequential or parallel vesicle pools can replicate our data fairly well.

Ca^{2+} uncaging with different pre-flash Ca^{2+} concentrations indicates Ca^{2+}-dependent vesicle priming

Finally, we aimed to obtain a mechanistic understanding that could explain both the strong dependence of action potential-evoked release on basal Ca^{2+} concentration (*Figure 1*) and the Ca^{2+}-dependence of vesicle fusion (*Figures 2–6*). In principle, the action potential-evoked data in *Figure 1* could be explained by an acceleration of vesicle fusion kinetics or, alternatively, an increase in the number of release-ready vesicles upon elevated basal Ca^{2+}. To differentiate between these two mechanistic possibilities, we investigated the effect of basal Ca^{2+} concentration preceding the UV illumination (pre-flash Ca^{2+}) on flash-evoked release. The pre-flash Ca^{2+} concentration can only be reliably determined with the Ca^{2+} indicator Fluo5F used in the experiments with weak flashes (see *Table 1*). We therefore grouped the deconvolution experiments with weak flashes, which elevated the Ca^{2+} concentration to less than 7 μM, into two equally sized groups of low and high pre-flash Ca^{2+} (below and above a value of 200 nM, respectively). Due to the presence of the Ca^{2+} loaded DMn cage, the pre-flash Ca^{2+} concentrations were on average higher than the resting Ca^{2+} concentration in physiological conditions of around 50 nM (*Delvendahl et al., 2015*). In both groups, the post-flash Ca^{2+} concentration was on average similar (~3 μM; *Figure 7B*). The peak EPSC amplitude of postsynaptic current was significantly larger with high compared to low pre-flash Ca^{2+} concentration (38 ± 10 and 91 ± 16 pA, n = 18 and 13, respectively, P$_{Mann-Whitney}$ = 0.001; *Figure 7A and C*). Correspondingly, the amplitude of the fast component of release as measured from deconvolution analysis was larger with high compared to low pre-flash Ca^{2+} (18 ± 5 and 49 ± 10, n = 18 and 13, respectively, P$_{Mann-Whitney}$ = 0.005; *Figure 7C*). However, the kinetics of vesicle fusion, measured as the inverse of the time constant of the fast component of release, were not significantly different for both conditions (0.15 ± 0.04 and 0.12 ± 0.03 ms^{-1} for the low and high pre-flash Ca^{2+} conditions, n = 18 and 13, respectively, P$_{Mann-Whitney}$ = 0.74; *Figure 7C*). The delay was also not significantly different (P$_{Mann-Whitney}$ = 0.54; *Figure 7C*). These data indicate that the number of release-ready vesicles were increased upon elevating the basal Ca^{2+} concentration but the fusion kinetics were unaltered. We therefore added an additional Ca^{2+}-dependent maturation step to the initial vesicle priming of the release schemes (see Materials and methods; note that this was already present in the above-described simulations of *Figure 6* but it has little impact on these data). This allowed replicating the
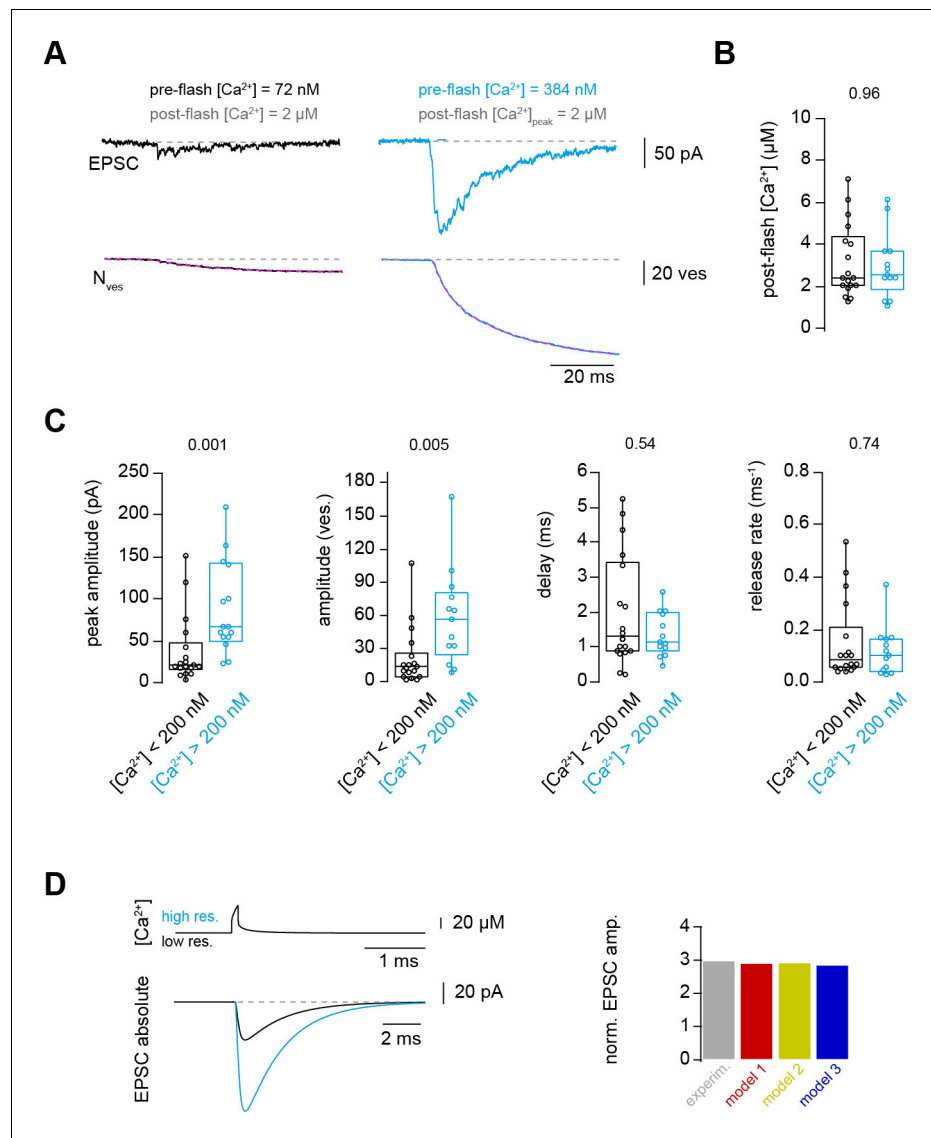
Figure 7. Ca^{2+} uncaging with different pre-flash Ca^{2+} concentrations indicates Ca^{2+}-dependent vesicle priming. (A) Two consecutive recordings from the same cell pair, with the same post-flash Ca^{2+} concentration but different pre-flash Ca^{2+} concentration in the presynaptic terminal. *Top:* postsynaptic current. *Bottom:* cumulative release of synaptic vesicles measured by deconvolution analysis of EPSCs superposed with a mono-exponential fit (magenta). Black and blue color represent low and high pre-flash Ca^{2+} concentration, respectively. The pre- and post-flash Ca^{2+} concentrations are indicated in each panel. (B) Comparison of the average post-flash Ca^{2+} concentration between both groups of either low (black) or high (blue) pre-flash Ca^{2+} concentration (n = 18 and 13 pairs, respectively). (C) From left to right: comparisons of the peak amplitude, the number of released vesicles measured as obtained from deconvolution analysis of EPSC, the delay of the release onset, and the release rate. Boxplots show median and 1st/3rd quartiles with whiskers indicating the whole data range. The values above the boxplots represent P-values of Mann-Whitney *U* tests. (D)*Top left:* simulated local action potential-evoked Ca^{2+}concentrations at 20 nm from a Ca^{2+} channel taken from ***Delvendahl et al., 2015***. Note the almost complete overlap of the two Ca^{2+} concertation traces with low and high basal Ca^{2+} concertation. *Bottom left:* predicted action potential-evoked EPSCs with low and high basal Ca^{2+} concertations. *Right:* ratio of the action potential-evoked EPSC amplitude with high and low basal Ca^{2+} concentrations for the experimental data and the model predictions.

The online version of this article includes the following source data for figure 7:

Source data 1. Ca^{2+} uncaging with different pre-flash Ca^{2+} concentrations indicates Ca^{2+}-dependent vesicle priming.

24

three-fold increase in the action potential-evoked release when driving the release scheme with a previously estimated local Ca^{2+} concentration during an action potential (*Figure 7D*; *Delvendahl et al., 2015*). Thus, the release schemes 2 and 3 describe all our experimental data and therefore represent to our knowledge the only release scheme explaining the priming, fusion, and replenishment of vesicles at a mature excitatory synapse in the CNS at physiological temperature.

Discussion

Here, we provided insights into the Ca^{2+}-dependence of vesicle priming, fusion, and replenishment at cMFBs. The results obtained at this synapse show prominent Ca^{2+}-dependent priming steps, a shallow non-saturating dose-response curve up to 50 µM, and little Ca^{2+}-dependence of sustained vesicle replenishment. Our computational analysis indicates that the peculiar dose-response curve can be explained by well-established release schemes having five Ca^{2+} steps and rapid vesicle replenishment via sequential or parallel vesicle pools. Thus, we established quantitative scheme of synaptic release for a mature high-fidelity synapse, exhibiting both high- and low-affinity Ca^{2+} sensors.

Ca^{2+} affinity of the vesicle fusion sensor

The Ca^{2+}-sensitivity of vesicle fusion seems to be synapse-specific. In contrast to the estimated Ca^{2+} affinity for vesicle fusion of ~100 µM at the bipolar cell of goldfish (*Heidelberger et al., 1994*) and the squid giant synapse (*Adler et al., 1991*; *Llinás et al., 1992*), recent studies showed that the affinity is much higher at three types of mammalian central synapses: the calyx of Held (*Bollmann et al., 2000*; *Lou et al., 2005*; *Schneggenburger and Neher, 2000*; *Sun et al., 2007*; *Wang et al., 2008*), the inhibitory cerebellar basket cell to Purkinje cell synapse (*Sakaba, 2008*), and the hippocampal mossy fiber boutons (*Fukaya et al., 2021*). Consistent with reports from mammalian central synapses, our data revealed prominent vesicle fusion at concentrations below 5 µM arguing for a high-affinity fusion sensor (*Figures 2–4*). However, the non-saturation of the dose-response curve (*Figures 2–4*) argues for the presence of a rather low-affinity fusion sensor at cMFBs. In our simulations, both models 2 and 3 exhibit vesicles with a Ca^{2+}-affinity similar to the calyx of Held. Nevertheless, with high intracellular Ca^{2+} concentrations (>20 µM) these vesicles will fuse very rapidly and the further increase in the release kinetics (causing the non-saturating dose-response curve) can be explained by rapid vesicle replenishment from a sequential pool of vesicles exhibiting use-dependent lowering of the Ca^{2+}-affinity (V_1 in model 2; *Miki et al., 2018*) or from a parallel pool of vesicles with lower Ca^{2+} affinity (V_1 in model 3; *Hallermann et al., 2010*). Our data therefore indicate that the shallow and non-saturating dose-response curve is the consequence of rapid replenishment of vesicles that still exhibit a lower Ca^{2+}-affinity compared to fully recovered vesicles. Consistent with this interpretation, a lowering in the Ca^{2+}-affinity of the vesicle fusion sensor has been observed at the calyx of Held with Ca^{2+} uncaging following vesicle depletion (*Müller et al., 2010*; *Wadel et al., 2007*). These newly replenished vesicles might contribute particularly to the dose-response curve at the cMFB because the cMFB has a much faster rate of vesicle replenishment compared with the calyx of Held synapse (*Miki et al., 2020*) providing a possible explanation why the here-reported dose-response curve differs from previous results at the calyx of Held. Furthermore, cMFBs seem to have functional similarities with ribbon-type synapses because it has recently been shown that the vesicle mobility in cMFBs is comparable to ribbon-type synapses (*Rothman et al., 2016*). The hallmark of ribbon-type synapses is their rapid vesicle replenishment (*Lenzi and von Gersdorff, 2001*; *Matthews, 2000*) and indeed more shallow dose-response curves were obtained at the ribbon photoreceptors and inner hair cell synapses (*Duncan et al., 2010*; *Heil and Neubauer, 2010*; *Johnson et al., 2010*; *Thoreson et al., 2004*, but see *Beutner et al., 2001*). The newly replenished vesicles might be molecularly immature and resemble vesicles that have only a near-linear remaining Ca^{2+} sensor when the fast Ca^{2+} sensor synaptotagmin II is lacking (*Kochubey and Schneggenburger, 2011*).

The here obtained dose-response curve has the following three caveats. First, the cMFB to GC synapses in lobule IX are functionally distinct based on the origin of the mossy fibers (*Chabrol et al., 2015*). Therefore, the here-recorded boutons in lobule IV/V could be molecularly and functionally distinct leading to the observed scatter in the dose-response curve, which could cause an apparent shallowing. Yet, the degree of scatter in the vesicular release rate at the cMFB seems comparable to

studies at other synapses (*Fukaya et al., 2021*; *Heidelberger et al., 1994*; *Sakaba, 2008*) including the calyx of Held (*Bollmann et al., 2000*; *Schneggenburger and Neher, 2000*), although the functional heterogeneity between different types of calyces (*Grande and Wang, 2011*) could be explained by differences in the coupling distance (*Fekete et al., 2019*). Second, we could not investigate allosteric or two-sensor models (*Lou et al., 2005*; *Sun et al., 2007*; *Li et al., 2021*) because we did not address the release rates in the low Ca^{2+} range (<1 µM), therefore, these questions remain to be investigated at the cMFBs. Third, currently available techniques to estimate fast release rates at near-physiological temperatures in the Ca^{2+} range above 50 µM are limited by the sampling frequency of capacitance measurements and dendritic filtering, which could prevent the detection of saturation at the upper end of the dose-response curve.

Ca^{2+}-sensitivity of vesicle priming

In previous reports, the Ca^{2+}-dependence of vesicle priming and replenishment at cMFBs was analyzed more indirectly with the Ca^{2+} chelator EGTA (*Ritzau-Jost et al., 2014*; *Ritzau-Jost et al., 2018*) and the obtained results could be explained by Ca^{2+}-dependent models but surprisingly also by Ca^{2+}-independent models (*Hallermann et al., 2010*; *Ritzau-Jost et al., 2018*). Furthermore, the analysis of molecular pathways showed that the recovery from depression is independent of the Ca^{2+}/calmodulin/Munc13 pathway at cMFBs (*Ritzau-Jost et al., 2018*). Our paired recordings and uncaging experiments (*Figures 1* and *7*) clearly demonstrate pronounced Ca^{2+}-dependence of vesicle priming at cMFBs. Taken together, these data indicate that some priming steps are mediated by Ca^{2+}-dependent mechanisms, which do not involve the Ca^{2+}/calmodulin/Munc13 pathway. A potential candidate for such a Ca^{2+}-dependent mechanism are the interaction of diacylgylcerol/phospholipase C or Ca^{2+}/phospholipids with Munc13s (*Lee et al., 2013*; *Lou et al., 2008*; *Rhee et al., 2002*; *Shin et al., 2010*). Another candidate for a high-affinity Ca^{2+} sensor is Synaptotamin 7 (see below).

Synaptic vesicles that fuse upon single action potentials (*Figure 1*) and weak uncaging stimuli (post-flash Ca^{2+} concentration of ~3 µM; *Figure 7*) are particularly fusogenic and thus might represent the superprimed vesicles with a particular high release probability (*Hanse and Gustafsson, 2001*; *Ishiyama et al., 2014*; *Kusch et al., 2018*; *Lee et al., 2013*; *Schlüter et al., 2006*; *Taschenberger et al., 2016*) suggesting that the process of superpriming is Ca^{2+}-dependent. This interpretation would also provide an explanation why in a recent report, triggering an action potential in the range of 10–50 ms before another action potential restored the synchronicity of synaptic vesicle fusion in mutant synapses which had an impaired synchronous release (*Chang et al., 2018*). It would be furthermore consistent with a proposed rapid, dynamic, and Ca^{2+}-dependent equilibrium between primed and superprimed vesicles (*Neher and Brose, 2018*). However, further investigations are needed for the dissection between the Ca^{2+}-dependence of priming and superpriming. Yet, our data show that some priming steps are strongly Ca^{2+}-dependent with a high-affinity Ca^{2+} sensor that allow detecting changes between 30 and 180 nM at cMFBs.

Ca^{2+}-sensitivity of vesicle replenishment

The upstream steps of vesicle priming, referred to as replenishment, recruitment, refilling, or reloading, remain controversial in particular with respect to their speed. The slow component of release (during prolonged depolarizations or Ca^{2+} elevations with uncaging) was initially interpreted as a sub-pool of release-ready vesicles that fuse with slower kinetics (see e.g. *Sakaba and Neher, 2001a*). However, recent studies indicate very fast vesicle replenishment steps (*Blanchard et al., 2020*; *Chang et al., 2018*; *Doussau et al., 2017*; *Hallermann et al., 2010*; *Lee et al., 2012*; *Malagon et al., 2020*; *Miki et al., 2016*; *Miki et al., 2018*; *Saviane and Silver, 2006*; *Valera et al., 2012*). These findings further complicate the dissection between fusion, priming, and replenishment steps. Therefore, the differentiation between 'parallel' release schemes with fast and slowly fusing vesicles and 'sequential' release schemes with fast vesicle replenishment and subsequent fusion is technically challenging at central synapses. Our data could be described by both sequential and parallel release schemes (models 2 and 3; *Figure 6*). The non-saturation of the release rate could be described somewhat better by the parallel model 3. However, further adjustment of the use-dependent slowing of the rates in model 2 (see $k_{on,plug}$, $k_{off,plug}$, *Equations 3 and 4*; *Miki et al., 2018*) can result in a sequential model exhibiting both fast and slowly fusing vesicles with different Ca^{2+}-sensitivity (see *Mahfooz et al., 2016*, for an alternative description of use-dependence of vesicle fusion).

Such use-dependent sequential models ultimately complicate the semantic definitions of 'sequential' and 'parallel', because the replenished vesicles of such sequential models will fuse in a molecularly different state, which could also be viewed as a parallel pathway to reach fusion. Independent of the difficulty to differentiate between sequential and parallel release schemes, the sustained component of release exhibited little Ca^{2+}-dependence in the here-tested range between 1 and 50 μM (*Figure 5*). However, it should be mentioned that measuring the sustained release rate is prone to errors with both presynaptic capacitance and postsynaptic current recordings, because the former cannot differentiate between exo- and endocytosis occurring simultaneously, and the latter can fail to dissect direct release from spill-over current, which is prominent at this synapse (*DiGregorio et al., 2002*). Nevertheless, the Ca^{2+}-independence of vesicle replenishment observed with capacitance measurements and the very weak Ca^{2+}-dependence observed with postsynaptic techniques seem consistent with the previously observed EGTA-independent slope of the sustained release during prolonged depolarizations (*Ritzau-Jost et al., 2014*). Our data cannot differentiate if replenishment is mediated by a saturated Ca^{2+} sensor for priming (model 2; assumed K_{dD} of 2 μM; *Miki et al., 2018*) or a parallel Ca^{2+}-independent step (model 3). Thus, during sustained activity at cMFBs, vesicle replenishment is mediated by either an apparently Ca^{2+}-independent process because of a saturated high-affinity Ca^{2+} sensor or a Ca^{2+}-independent process.

Implications for coupling distance

The Ca^{2+}-sensitivity of vesicle fusion critically impacts the estimates of the coupling distance between Ca^{2+} channels and synaptic vesicles, mainly those obtained based on functional approaches (*Neher, 1998*; *Eggermann et al., 2011*; but not on structural approaches, see e.g. *Éltes et al., 2017*; *Rebola et al., 2019*). Our previous estimate of the coupling distance at the cMFB of 20 nm (*Delvendahl et al., 2015*) was based on the release scheme of *Wang et al., 2008* obtained at the calyx of Held synapse at an age of (P16-P19) at room temperature and assuming a Q_{10} factor of 2.5. The now estimated k_{on} and k_{off} rates at mature cMFBs at physiological temperature were slightly larger and smaller than the temperature-corrected values from the calyx, respectively, resulting in a slightly higher affinity of the fast releasing vesicles (V_2 in models 2 and 3). Therefore, at the cMFB, the coupling distance of the vesicles released by a single action potential is if anything even smaller than the previous estimate of 20 nm.

Implications for synaptic facilitation

Our data might contribute to a better understanding of the mechanisms of the 'residual Ca^{2+} hypothesis' explaining synaptic facilitation (*Jackman and Regehr, 2017*; *Katz and Miledi, 1968*; *Magleby, 1987*; *Zucker and Regehr, 2002*). The strong dependence of the action potential-evoked release on basal Ca^{2+} (*Figure 1*) supports the critical effect of residual Ca^{2+} on synaptic strength. Our mechanistic analysis (particularly *Figure 7*) indicates that the number of release-ready vesicles rather than the vesicular release probability is regulated by residual Ca^{2+}. The high-affinity Ca^{2+} sensor Synaptotagmin-7 (*Sugita et al., 2002*) could be a sensor for the changes in basal Ca^{2+} levels and mediate the here-reported three-fold increase in synaptic strength (*Figures 1* and *7*). Synaptotagmin-7 has been shown to mediate vesicle recruitment (*Liu et al., 2014*), asynchronous release (*Luo and Südhof, 2017*), and synaptic facilitation (*Chen et al., 2017*; *Jackman et al., 2016*). If the recruitment and priming steps are fast enough they could provide a powerful mechanism for synaptic facilitation. Indeed, there is increasing evidence for ultra-fast Ca^{2+}-dependent recruitment and priming (reviewed in *Neher and Brose, 2018*) as well as facilitation mediated by an increase in the number of release-ready vesicles rather than the vesicular release probability (*Jackman et al., 2016*; *Kobbersmed et al., 2020*; *Vevea et al., 2021*). Our data are therefore consistent with the emerging view that facilitation is mediated by rapid Synaptotagmin-7/Ca^{2+}-dependent recruitment and priming of vesicles.

Implications for high-frequency transmission

Synaptic fidelity has been shown to increase with age at cMFBs (*Cathala et al., 2003*), neocortical synapses (*Bornschein et al., 2019*), and the calyx of Held (*Fedchyshyn and Wang, 2005*; *Nakamura et al., 2015*; *Taschenberger and von Gersdorff, 2000*). During high-frequency transmission, the residual Ca^{2+} concentration increases up to a few μM at cMFBs (*Delvendahl et al., 2015*)

but mature cMFBs can still sustain synchronous release (*Hallermann et al., 2010*; *Saviane and Silver, 2006*). The developmental decrease in the affinity of the release sensors observed at the calyx of Held (*Wang et al., 2008*) and the here-reported shallow-dose-response curve at mature cMFBs could be an evolutionary adaptation of synapses to prevent the depletion of the release-ready vesicles at medium Ca^{2+} concentrations and therefore allow maintaining sustained synchronous neurotransmission with high fidelity (*Matthews, 2000*).

Materials and methods

Key resources table

Reagent type (species) or resource	Designation	Source or reference	Identifiers	Additional information
Chemical compound, drug	NaCl	Sigma-Aldrich	Cat. # S9888	
Chemical compound, drug	$NaHCO_3$	Sigma-Aldrich	Cat. # S6297	
Chemical compound, drug	Glucose	Sigma-Aldrich	Cat. # G8270	
Chemical compound, drug	AP 5	Sigma-Aldrich	Cat. # A78403	
Chemical compound, drug	KCl	Sigma-Aldrich	Cat. # P9333	
Chemical compound, drug	$CaCl_2$	Sigma-Aldrich	Cat. # C5080	For extracellular solution
Chemical compound, drug	$CaCl_2$	Sigma-Aldrich	Cat. # 21115	For intracellular solution
Chemical compound, drug	EGTA	Sigma-Aldrich	Cat. # E0396	
Chemical compound, drug	NaH_2PO_4	Merck	Cat. # 106342	
Chemical compound, drug	Tetrodotoxin	Tocris	Cat. # 1078	
Chemical compound, drug	$MgCl_2$	Sigma-Aldrich	Cat. # M2670	
Chemical compound, drug	TEA-Cl	Sigma-Aldrich	Cat. # T2265	
Chemical compound, drug	HEPES	Sigma-Aldrich	Cat. # H3375	
Chemical compound, drug	NaGTP	Sigma-Aldrich	Cat. # G8877	
Chemical compound, drug	Na_2ATP	Sigma-Aldrich	Cat. # A2383	
Chemical compound, drug	DMnitrophen	Synptic systems	Cat. # 510016	
Chemical compound, drug	CsOH	Sigma-Aldrich	Cat. # C8518	
Chemical compound, drug	Atto594	ATTO-TEC	Cat. # AD 594	
Chemical compound, drug	OGB1	Thermo Fisher Scientific	Cat. # 06806	
Chemical compound, drug	OGB-5N	Thermo Fisher Scientific	Cat. # 944034	
Chemical compound, drug	Fluo-5F	Thermo Fisher Scientific	Cat. # F14221	

Continued on next page

Continued

Reagent type (species) or resource	Designation	Source or reference	Identifiers	Additional information
Chemical compound, drug	KOH solution	Roth	Cat. # K017.1	
Chemical compound, drug	Kynurenic acid	Sigma-Aldrich	Cat. # K3375	
Chemical compound, drug	Cyclothiazide	Sigma-Aldrich	Cat. # C9847	
Chemical compound, drug	Ca^{2+} Calibration Buffer Kit	Thermo Fisher Scientific	Cat. # C3008MP	
Chemical compound, drug	Caged fluorescein	Sigma-Aldrich	Cat. # F7103	
Chemical compound, drug	Glycerol	Sigma-Aldrich	Cat. # G5516	
Chemical compound, drug	Isoflourane	Baxter	Cat. # Hdg9623	
Chemical compound, drug	Aqua B. Braun	Braun	Cat. # 00882479E	For extracellular solution
Chemical compound, drug	Sterile Water	Sigma-Aldrich	W Cat. # 3500	For intracellular solution
Strain, strain background (mouse C57BL/6N)	Female, male C57BL/6N	Charles river	https://www.criver.com/	
Other	Vibratome	LEICA VT 1200	https://www.leica-microsystems.com/	
Other	Femto2D laser-scanning microscope	Femtonics	https://femtonics.eu/	
Other	UV laser source	Rapp OptoElectronic	https://rapp-opto.com/	375 nm, 200 mW
Other	DMZ Zeitz Puller	Zeitz	https://www.zeitz-puller.com/	
Other	Borocilicate glass	Science Products	https://science-products.com/en/	GB200F-10 With filament
Other	HEKA EPC10/2 amplifier	HEKA Elektronik	https://www.heka.com/	
Other	Ti:Sapphire laser	MaiTai, SpectraPhysics	https://www.spectra-physics.com/	
Other	Ca^{2+} sensitive electrode (ELIT 8041 PVC membrane)	NICO 2000	http://www.nico2000.net/index.htm	
Other	Single junction silver chloride reference electrode (ELIT 001 n)	NICO 2000	http://www.nico2000.net/index.htm	
Other	PH/Voltmeter	Metler toledo	https://www.mt.com/de/en/home.html	
Other	Osmomat 3000	Gonotec	http://www.gonotec.com/de	
Other	TC-324B perfusion heat controller	Warner Instruments	https://www.warneronline.com/	
Software, algorithm	MES	Femtonics	https://femtonics.eu/	
Software, algorithm	Igor Pro	Wavemetrics	https://www.wavemetrics.com/	
Software, algorithm	Patchmaster	HEKA Elektronik	https://www.heka.com/	
Software, algorithm	Adobe illustrator	Adobe	https://www.adobe.com/products/illustrator.html	
Software, algorithm	Mathematica	Wolfram	https://www.wolfram.com/mathematica/	
Software, algorithm	Maxchelator	Stanford University	https://somapp.ucdmc.ucdavis.edu/pharmacology/bers/maxchelator/	

Preparation

Animals were treated in accordance with the German Protection of Animals Act and with the guidelines for the welfare of experimental animals issued by the European Communities Council Directive. Acute cerebellar slices were prepared from mature P35–P42 C57BL/6 mice of either sex as previously described (*Hallermann et al., 2010*). Isoflurane was used to anesthetize the mice, which were then sacrificed by decapitation. The cerebellar vermis was quickly removed and mounted in a chamber filled with chilled extracellular solution. 300-µm-thick parasagittal slices were cut using a Leica VT1200 microtome (Leica Microsystems), transferred to an incubation chamber at 35°C for ~30 min, and then stored at room temperature until use. The extracellular solution for slice cutting and storage contained (in mM) the following: NaCl 125, NaHCO$_3$ 25, glucose 20, KCl 2.5, CaCl$_2$ 2, NaH$_2$PO$_4$ 1.25, MgCl$_2$1 (310 mOsm, pH 7.3 when bubbled with Carbogen [5% (vol/vol) O$_2$/95% (vol/vol) CO$_2$]). All recordings were restricted to lobules IV/V of the cerebellar vermis to reduce potential functional heterogeneity among different lobules (*Straub et al., 2020*).

Presynaptic recordings and flash photolysis

All recordings were performed at near-physiological temperature by adjusting the set temperature of the TC-324B perfusion heat controller (Warner Instruments, Hamden, CT, United States) until the temperature in the center of the recording chamber with immersed objective was between 36.0°C and 36.3°C. This process was repeated before using a new brain slice. During recordings, the thermometer was put at the side of the recording chamber and the readout was monitored to avoid potential drifts in temperature (the readout was between 32°C and 34°C, critically depending on the position of the thermometer, and changed during recording from one brain slice by less than 0.5°C). The room temperature was controlled using an air conditioner set to 24°C. Presynaptic patch-pipettes were from pulled borosilicate glass (2.0/1.0 mm outer/inner diameter; Science Products) to open-tip resistances of 3–5 MΩ (when filled with intracellular solution) using a DMZ Puller (Zeitz-Instruments, Munich, Germany). Slices were superfused with artificial cerebrospinal fluid (ACSF) containing (in mM): NaCl 105, NaHCO$_3$ 25, glucose 25, TEA 20, 4-AP 5, KCl 2.5, CaCl$_2$ 2, NaH$_2$PO4 1.25, MgCl$_2$ 1, and tetrodotoxin (TTX) 0.001, equilibrated with 95% O$_2$ and 5% CO$_2$. Cerebellar mossy fiber boutons (cMFBs) were visualized with oblique illumination and infrared optics (*Ritzau-Jost et al., 2014*). Whole-cell patch-clamp recordings of cMFBs were performed using a HEKA EPC10/2 amplifier controlled by Patchmaster software (HEKA Elektronik, Lambrecht, Germany). The intracellular solution contained (in mM): CsCl 130, MgCl$_2$ 0.5, TEA-Cl 20, HEPES 20, Na$_2$ATP 5, NaGTP 0.3. For Ca^{2+} uncaging experiments, equal concentrations of DM-nitrophen (DMn) and CaCl$_2$ were added depending on the aimed post-flash Ca^{2+} concentration, such that either 0.5, 2, or 10 mM was used for low, middle, or high target range of post-flash Ca^{2+} concentration, respectively (*Table 1*). To quantify post-flash Ca^{2+} concentration with a previously established dual indicator method (see below; *Delvendahl et al., 2015*; *Sabatini et al., 2002*), Atto594, OGB-5N, and Fluo-5F were used at concentrations as shown in (*Table 1*).

A 50 mM solution stock of DMn was prepared by neutralizing 50 mM DMn in H$_2$O with 200 mM CsOH in H$_2$O. The purity of each DMn batch was determined in the intracellular solution used for patching through titration with sequential addition of Ca^{2+} as previously described (*Schneggenburger, 2005*) and by measuring the Ca^{2+} concentration using the dual indicator method with 10 µM Atto594 and 50 µM OGB1 (*Delvendahl et al., 2015*).

After waiting for at least one minute in whole-cell mode to homogenously load the terminal with intracellular solution, capacitance measurements were performed at a holding potential of −100 mV with sine-wave stimulation (5 kHz or 10 kHz frequency and ±50 mV amplitude; *Hallermann et al., 2003*). Distant mossy fiber boutons on the same axon are unlikely to contaminate capacitance measurements because investigations at hippocampal mossy fiber buttons indicate that the high-frequency sine-wave techniques as used in our study are hardly affected by release from neighboring boutons on the same axon (*Hallermann et al., 2003*). During the ongoing sine-wave stimulation, a UV laser source (375 nm, 200 mW, Rapp OptoElectronic) was used to illuminate the whole presynaptic terminal. According to a critical illumination, the end of the light guide of the UV laser was imaged into the focal plan resulting in a homogeneous illumination in a circular area of ~30 µm diameter (*Figure 2—figure supplement 1*). The duration of the UV illumination was 100 µs controlled with sub-microsecond precision by external triggering of the laser source. In capacitance

measurements with 10 kHz sine wave frequency, longer pulses of 200 µs were used to reach high Ca²⁺ levels. In a subset of experiments, UV pulses of 1 ms were used to rule out fast undetectable Ca²⁺ overshoots (*Bollmann et al., 2000*; *Figure 3—figure supplement 2*). The UV flash intensity was set to 100% and reduced in some experiments (10–100%) to obtain small elevations in Ca²⁺ concentrations (*Table 1*). To avoid photoproducts-induced cell toxicity, we applied only one flash per recording. In a subset of the paired recordings with weak UV illumination (post-flash Ca²⁺ concentration < 5 µM), we used consecutive flashes on the same cell (from 43 paired cells, 16 consecutive recordings were used).

Paired recordings between cMFBs and GCs

For paired pre- and postsynaptic recordings, granule cells (GCs) were whole-cell voltage-clamped with intracellular solution containing the following (in mM): K-gluconate 150, NaCl 10, K-HEPES 10, MgATP three and Na-GTP 0.3 (300–305 mOsm, pH adjusted to 7.3 with KOH). 10 µM Atto594 was included to visualize the dendrites of the GCs (*Ritzau-Jost et al., 2014*). After waiting sufficient time to allow for the loading of the dye, the GC dendritic claws were visualized through two-photon microscopy, and subsequently, cMFBs near the dendrites were identified by infrared oblique illumination and were patched and loaded with caged Ca²⁺ and fluorescent indicators as previously described. The reliable induction of an EPSC in the GC was used to unequivocally confirm a cMFB-GC synaptic connection. In a subset of the Ca²⁺ uncaging experiments, simultaneous presynaptic capacitance and postsynaptic EPSC recordings were performed from cMFBs and GCs, respectively.

Clamping intracellular basal Ca²⁺ concentrations

The intracellular solution for presynaptic recordings of the data shown in *Figure 1* contained the following in mM: K-gluconate 150, NaCl 10, K-HEPES 10, MgATP 3, Na-GTP 0.3. With a combination of EGTA and CaCl₂ (5 mM EGTA / 0.412 mM CaCl₂ or 6.24 mM EGTA / 1.65 mM CaCl₂), we aimed to clamp the free Ca²⁺ concentration to low and high resting Ca²⁺ concentrations of ~50 or ~200 nM, respectively, while maintaining a free EGTA concentration constant at 4.47 mM. The underlying calculations were based on a Ca²⁺ affinity of EGTA of 543 nM (*Lin et al., 2017*). The resulting free Ca²⁺ concentration was quantified with the dual indicator method (see below) and was found to be to ~30 or ~180 nM, respectively (*Figure 1A*).

Quantitative two-photon Ca²⁺ imaging

For the quantification of Ca²⁺ signals elicited through UV-illumination-induced uncaging, two-photon Ca²⁺ imaging was performed as previously described (*Delvendahl et al., 2015*) using a Femto2D laser-scanning microscope (Femtonics) equipped with a pulsed Ti:Sapphire laser (MaiTai, Spectra-Physics) adjusted to 810 nm, a 60×/1.0 NA objective (Olympus), and a 1.4 NA oil-immersion condenser (Olympus). Data were acquired by doing line-scans through the cMFB. To correct for the flash-evoked luminescence from the optics, the average of the fluorescence from the line-scan in an area outside of the bouton was subtracted from the average of the fluorescence within the bouton (*Figure 2B*). Imaging data were acquired and processed using MES software (Femtonics). Upon releasing Ca²⁺ from the cage, we measured the increase in the green fluorescence signal of the Ca²⁺-sensitive indicator (OGB-5N or Fluo-5F) and divided it by the fluorescence of the Ca²⁺-insensitive Atto594 (red signal). The ratio (R) of green-over-red fluorescence was translated into a Ca²⁺ concentration through the following calculation (*Yasuda et al., 2004*).

$$[Ca^{2+}] = K_D \frac{(R - R_{min})}{(R_{max} - R)}$$

To avoid pipetting irregularities, which might influence the quantification of the fluorescence signals, pre-stocks of Ca²⁺-sensitive and Ca²⁺-insensitive indicators were used. For each pre-stock and each intracellular solution, 10 mM EGTA or 10 mM CaCl₂ were added to measure minimum (R_min) and maximum (R_max) fluorescence ratios, respectively. We performed these measurements in cMFBs and GCs as well as in cuvettes. Consistent with a previous report (*Delvendahl et al., 2015*), both R_min and R_max were higher when measured in cells than in cuvettes (by a factor of 1.73 ± 0.05; n = 83 and 63 measurements in situ and in cuvette; *Figure 3—figure supplement 3A*). The values in cMFBs and GCs were similar (*Figure 3—figure supplement 3B*). OGB-5N is not sensitive in detecting Ca²⁺

concentrations less than 1 µM. Therefore, we deliberately adjusted R_{min} of OGB-5N in the recordings where the pre-flash Ca^{2+} had negative values, to a value resulting in a pre-flash Ca^{2+} concentration of 60 nM, which corresponds to the average resting Ca^{2+} concentration in these boutons (*Delvendahl et al., 2015*). This adjustment of R_{min} resulted in a reduction of post-flash Ca^{2+} amplitudes of on average $7.5 \pm 0.4\%$ (n = 37).

The fluorescence properties of DMn change after flash photolysis, and the Ca^{2+} sensitive and insensitive dyes can differentially bleach during UV flash (*Schneggenburger, 2005*; *Zucker, 1992*). We assumed no effect of the UV flash on the K_D of the Ca^{2+}-sensitive dyes (*Escobar et al., 1997*), and measured R_{min} and R_{max} before and after the flash for each used UV flash intensity and duration in each of the three solutions (*Table 1*; *Schneggenburger and Neher, 2000*). The flash-induced change was strongest for R_{max} of solutions with OGB-5N, but reached only ~20% with the strongest flashes (*Figure 3—figure supplement 3F*).

Deconvolution

Deconvolution of postsynaptic currents was performed essentially as described by *Ritzau-Jost et al., 2014*, based on routines developed by *Sakaba and Neher, 2001b*. The principle of this method is that the EPSC comprises currents induced by synchronous release and residual glutamate in the synaptic cleft due to delayed glutamate clearance and glutamate spill-over from neighboring synapses, which is prominent at the cMFB to GC synapses (*DiGregorio et al., 2002*). Kynurenic acid (2 mM) and Cyclothiazide (100 µM) were added to the extracellular solution to reduce postsynaptic receptor saturation and desensitization, respectively. The amplitude of the miniature EPSC (mEPSC) was set to the mean value of 10.1 pA (10.1 ± 0.2 pA; n = 8) as measured in 2 mM kynurenic acid and 100 µM cyclothiazide. Kynurenic acid has been reported to absorb UV light resulting in a reduction of the uncaging efficiency (*Sakaba et al., 2005*; *Wölfel et al., 2007*). However, kynurenic acid particularly absorbs UV light at wavelength below 370 nm (*Wölfel et al., 2007*) suggesting that the reduction in the uncaging efficiency at the wavelength used in this study (375 nm) might be small. In agreement with this, we were able to increase the post-flash Ca^{2+} concentrations to ~50 µM.

The deconvolution kernel had the following free parameters: the mEPSC early slope τ_0, the fractional amplitude of the slow mEPSC decay phase α, the time constant of the slow component of the decay τ_2 of the mEPSC, the residual current weighting factor β, and the diffusional coefficient d. Applying the 'fitting protocol' described by *Sakaba and Neher, 2001b* before flash experiments might affect the number of vesicles released by subsequent Ca^{2+} uncaging. On the other hand, applying the 'fitting protocol' after Ca^{2+} uncaging might underestimate the measured number of vesicles due to flash-induced toxicity and synaptic fatigue especially when applying strong Ca^{2+} uncaging. Therefore, we used the experiments with weak and strong flashes to extract the mini-parameters and the parameters for the residual current of the deconvolution kernel, respectively, as described in the following in more detail. To obtain the mini parameters (early slope, α, and τ_2) using weak flashes, deconvolution was first performed with a set of trial parameters for each cell pair. The mini-parameters of the deconvolution were optimized in each individual recording to yield low (but non-negative) step-like elevations in the cumulative release corresponding to small EPSCs measured from the postsynaptic terminal (the parameters for the residual current had little impact on the early phase of the cumulative release rate within the first 5 ms, therefore, some reasonable default values for the parameters of the residual current were used while iteratively adjusting the fast mini parameters for each individual recording). Next, using the average of the mini-parameters obtained from weak flashes, the deconvolution parameters for the residual current (β and d) were optimized in each recording with strong flashes until no drops occurred in the cumulative release in the range of 5–50 ms after the stimulus (while iteratively readjusting the mini parameters, if needed, to avoid any drops in the cumulative release in the window of 5–10 ms that might arise when adjusting the slow parameters based on the cumulative release in the range of 5–50 ms). Finally, we averaged the values of each parameter and the deconvolution analysis of all recordings was re-done using the average parameters values. To test the validity of this approach, cumulative release from deconvolution of EPSCs and presynaptic capacitance recordings were compared in a subset of paired recordings (n = 9 pairs) similarly as done in previous investigations (*Ritzau-Jost et al., 2014*). Exponential fits to the cumulative release and the presynaptic capacitance traces provided very similar time constants. On a paired-wise comparison, the difference in the time constant was always less than 40%

(*Figure 3—figure supplement 4*). Therefore, both approaches yielded similar exponential time constants.

To combine the sustained release rate estimated from capacitance measurements (*Figure 5B*) and deconvolution analysis of EPSC (*Figure 5C*) for the modeling with release schemes (*Figure 6E*), we estimated the number of GCs per cMFB by comparing the product of the amplitude and the inverse of the time constant of the exponential fit of the presynaptic capacitance trace and the simultaneously measured cumulative release trace obtained by deconvolution analysis. Assuming a capacitance of 70 aF per vesicle (*Hallermann et al., 2003*), we obtained an average value of 90.1 GCs per MFB in close agreement with previous estimates using a similar approach (*Ritzau-Jost et al., 2014*). This connectivity ratio is larger than previous estimates (~10, *Billings et al., 2014*; ~50, *Jakab and Hamori, 1988*) which could be due to a bias toward larger terminals, ectopic vesicle release, postsynaptic rundown, or release onto Golgi cells.

Measurement of Ca²⁺ concentration using a Ca²⁺-sensitive electrode

A precise estimation of the binding affinity of the Ca²⁺-sensitive dyes is critical in translating the fluorescence signals into Ca^2 concentration. It has been reported that the K_D of fluorescent indicators differs significantly depending on the solution in which it is measured (*Tran et al., 2018*) due to potential differences in ionic strength, pH, and concentration of other cations. Accordingly, different studies have reported different estimates of the K_D of OGB-5N having an up to eight-fold variability (*Delvendahl et al., 2015*; *DiGregorio and Vergara, 1997*; *Neef et al., 2018*). In these studies, the estimation of the K_D of the Ca²⁺ sensitive dyes depended on the estimated K_D of the used Ca²⁺ chelator, which differs based on the ionic strength, pH, and temperature of the solution used for calibration. So, we set out to measure the K_D of OGB-5N, in the exact solution and temperature, which we used during patching, through direct potentiometry using an ion-selective electrode combined with two-photon Ca²⁺ imaging. An ion-selective electrode for Ca²⁺ ions provides a direct readout of the free Ca²⁺ concentration independent of the K_D of the used Ca²⁺ chelator. Using the same intracellular solution and temperature as used during experiments, the potential difference between the Ca²⁺-sensitive electrode (ELIT 8041 PVC membrane, NICO 2000) and a single junction silver chloride reference electrode (ELIT 001 n, NIC0 2000) was read out with a pH meter in voltage mode. A series of standard solutions, with defined Ca²⁺ concentration (Thermo Fisher Scientific) covering the whole range of our samples, were used to plot a calibration curve of the potential (mV) versus Ca²⁺ concentration (μM). Then, the potential of several sample solutions containing the same intracellular solution used for patching, but with different Ca²⁺ concentrations buffered with EGTA, was determined. This way, we got a direct measure of the free Ca²⁺ concentration of several sample solutions, which were later used after the addition of Ca²⁺-sensitive fluorometric indicators to plot the fluorescence signal of each solution versus the corresponding free Ca²⁺ concentration verified by the Ca²⁺-sensitive electrode, and accordingly the K_D of the Ca²⁺ indicators were obtained from fits with a Hill equation. The estimated K_D was two-fold higher than the estimate obtained using only the Ca²⁺ Calibration Buffer Kit (Thermo Fisher Scientific) without including intracellular patching solution (*Figure 3—figure supplement 1*). Comparable results were obtained when estimating the free Ca²⁺ concentration using Maxchelator software (https://somapp.ucdmc.ucdavis.edu/pharmacology/bers/maxchelator/). Therefore, we used two independent approaches to confirm the K_D of OGB-5N. We found that TEA increased the potential of the solutions measured through the Ca²⁺-sensitive electrode, which is consistent with a previous report showing a similar effect of quaternary ammonium ions on potassium sensitive microelectrodes (*Neher and Lux, 1973*). We compared the fluorescence signals of our samples with or without TEA, to check if this effect of TEA is due to an interaction with the electrode or due to an effect on the free Ca²⁺ concentration, and found no difference. Therefore, TEA had an effect on the electrode read-out without affecting the free Ca²⁺, and accordingly, TEA was removed during the potentiometric measurements (*Figure 3—figure supplement 1*). This resulted in a good agreement of the estimates of the free Ca²⁺ concentration measured using a Ca²⁺-sensitive electrode and those calculated via Maxchelator.

Assessment of the UV energy profile

The homogeneity of the UV laser illumination at the specimen plane was assessed in vitro by uncaging fluorescein (CMNB-caged fluorescein, Thermo Fisher Scientific). Caged fluorescein (2 mM) was

33

mixed with glycerol (5% caged fluorescein/ 95% glycerol) to limit the mobility of the released dye (*Bollmann et al., 2000*). We did the measurements at the same plane as we put the slice during an experiment. The fluorescence profile of the dye after being released from the cage was measured at different z-positions over a range of 20 μm. The intensity of fluorescein was homogenous over an area of 10 μm x 10 μm x 10 μm which encompasses the cMFB.

Data analysis

The increase in membrane capacitance and in cumulative release based on deconvolution analysis was fitted with the following single or bi-exponential functions using Igor Pro (WaveMetrics) including a baseline and a variable onset.

$$f_{mono}(t) = \begin{cases} 0 & \text{if } t < d, \\ a\left(1 - exp\left[-\frac{(t-d)}{\tau}\right]\right) & \text{if } t \geq d \end{cases}$$

$$f_{bi}(t) = \begin{cases} 0 & \text{if } t < d, \\ a\left(1 - a_1 exp\left[-\frac{(t-d)}{\tau_1}\right] - (1-a_1) exp\left[-\frac{(t-d)}{\tau_2}\right]\right) & \text{if } t \geq d \end{cases}$$

(1)

where d defines the delay, a the amplitude, τ the time constant of the mono-exponetial fit, τ_1 and τ_2 the time constants of the fast and slow components of the bi-exponential fit, respectively, and a_1 the relative contribution of the fast component of the bi-exponential fit. The fitting of the release traces was always done with a time window of 5 ms before and 10 ms after flash onset. If the time constant of the mono-exponential fit exceeded 10 ms, a longer fitting duration of 60 ms after flash onset was used for both the experimental and the simulated data.

The acceptance of a bi-exponential fit was based on the fulfillment of the following three criteria: (1) at least 4% decrease in the sum of squared differences between the experimental trace and the fit compared with a mono-exponential fit ($\chi^2_{mono}/\chi^2_{bi} > 1.04$), (2) the time constants of the fast and the slow components differed by a factor >3, and (3) the relative contribution of each component was >10% (i.e. $0.1 < a_1 < 0.9$). If any of these criteria was not met, a mono-exponential function was used instead. In the case of weak flashes, where we could observe single quantal events within the initial part of the EPSC, mono-exponential fits were applied. In *Figure 1*, bi-exponential functions were used to fit the decay of the EPSC and the amplitude-weighted time constants were used (*Hallermann et al., 2010*).

Hill equations were used to fit the release rate versus intracellular Ca^{2+} concentration on a double logarithmic plot according to the following equation:

$$H(x) = Log\left[V_{max}\frac{1}{1 + \left(\frac{K_D}{10^x}\right)^n}\right]$$

(2)

where Log is the decadic logarithm, V_{max} the maximal release rate, K_D the Ca^{2+} concentration at the half-maximal release rate, and n the Hill coefficient. H(x) was fit on the decadic logarithm of the release rates and x was the decadic logarithm of the intracellular Ca^{2+} concentration.

Modeling of intra-bouton Ca^{2+} dynamics

We simulated the intra-bouton Ca^{2+} dynamics using a single compartment model. The kinetic reaction schemes for Ca^{2+} and Mg^{2+}-uncaging and -binding (*Figure 6A*) were converted to a system of ordinary differential equations (ODEs) that was numerically solved using the NDSolve function in Mathematica 12 (Wolfram) as described previously (*Bornschein et al., 2019*). The initial conditions for the uncaging simulation were derived by first solving the system of ODEs for the steady state using total concentrations of all species and the experimentally determined $[Ca^{2+}]_{rest}$ as starting values. Subsequently, the values obtained for all free and bound species were used as initial conditions for the uncaging simulation. The kinetic properties of DMn were simulated according to *Faas et al., 2005*, *Faas et al., 2007*. The total DMn concentration ($[DMn]_T$) includes the free form ($[DMn]$), the Ca^{2+}-bound form ($[CaDMn]$), and the Mg^{2+}-bound form ($[MgDMn]$). Each of these forms is subdivided into an uncaging fraction (α) and a non-uncaging fraction ($1-\alpha$). The uncaging fractions were further subdivided into a fast (af) and a slow (1-af) uncaging fraction:

$$[DMn]_T = [DMn]_f + [DMn]_s + [CaDMn]_f + [CaDMn]_s + [MgDMn]_f + [MgDMn]_s$$

[DMn] = [DMn]$_f$ + [DMn]$_s$
[DMn]$_f$ = α af [DMn]
[DMn]$_s$ = α (1-af) [DMn]
[CaDMn] = [CaDMn]$_f$ + [CaDMn]$_s$
[CaDMn]$_f$ = α af [CaDMn]
[CaDMn]$_s$ = α (1-af) [CaDMn]
[MgDMn] = [MgDMn]$_f$ + [MgDMn]$_s$
[MgDMn]$_f$ = α af [MgDMn]
[MgDMn]$_s$ = α (1-af) [MgDMn]

The suffixes 'T', 'f', and 's' indicate total, fast or slow, respectively. The transition of fast and slow uncaging fractions into low-affinity photoproducts (PP) occurred with fast ($τ_f$) or slow ($τ_s$) time constants, respectively. Free Ca^{2+} or Mg^{2+}-bound DMn decomposed into two photoproducts (PP1, PP2) differing with respect to their binding kinetics. The binding kinetics of all species were governed by the corresponding forward (k_{on}) and backward (k_{off}) rate constants

$$\frac{d[CaDMn]}{dt}_x = k_{on}[Ca][DMn]_x - k_{off}[CaDMn]_x - \frac{[CaDMn]_x}{\tau_x} H(t - t_{flash}) \quad x = f, s$$

$$\frac{d[MgDMn]}{dt}_x = k_{on}[Mg][DMn]_x - k_{off}[MgDMn]_x - \frac{[MgDMn]_x}{\tau_x} H(t - t_{flash}) \quad x = f, s$$

$$\frac{d[DMn]}{dt}_x = -k_{on}[Ca][DMn]_x + k_{off}[CaDMn]_x - k_{on}[Mg][DMn]_x + k_{off}[MgDMn]_x$$
$$cc$$
$$- \frac{[DMn]_x}{\tau_x} H(t - t_{flash}) \quad x = f, s$$

$$\frac{d[CaPP1]}{dt} = k_{on}[Ca][PP1] - k_{off}[CaPP1] + \frac{[CaDMn]_f}{\tau_f} H(t - t_{flash}) + \frac{[CaDMn]_s}{\tau_s} H(t - t_{flash})$$

$$\frac{d[MgPP1]}{dt} = k_{on}[Mg][PP1] - k_{off}[MgPP1]$$

$$\frac{d[PP1]}{dt} = -k_{on}[Ca][PP1] + k_{off}[CaPP1] - k_{on}[Mg][PP1] + k_{off}[MgPP1]$$
$$+ \frac{[CaDMn]_f}{\tau_f} H(t - t_{flash}) + \frac{[CaDMn]_s}{\tau_s} H(t - t_{flash})$$

$$\frac{d[CaPP2]}{dt} = k_{on}[Ca][PP2] - k_{off}[CaPP2]$$

$$\frac{d[MgPP2]}{dt} = k_{on}[Mg][PP2] - k_{off}[MgPP2] + \frac{[MgDMn]_f}{\tau_f} H(t - t_{flash})$$
$$+ \frac{[MgDMn]_s}{\tau_s} H(t - t_{flash})$$

$$\frac{d[PP2]}{dt} = -k_{on}[Ca][PP2] + k_{off}[CaPP2] - k_{on}[Mg][PP2] + k_{off}[MgPP2]$$

$$+2 \frac{[DMn]_f}{\tau_f} H(t - t_{flash}) + \frac{[DMn]_s}{\tau_s} H(t - t_{flash})$$

$$+ \frac{[MgDMn]_f}{\tau_f} H(t - t_{flash}) + \frac{[MgDMn]_s}{\tau_s} H(t - t_{flash})$$

where H is the Heaviside step function and t_{flash} the time of the UV flash. Ca^{2+} and Mg^{2+}-binding to the dye, ATP, and an endogenous buffer (EB) were simulated by second-order kinetics:

$$\frac{d[Ca]}{dt}_{buffer} = -k_{on,j}[Ca][B] + k_{off,j}[CaB] \quad j = dye, ATP, EB$$

35

$$\frac{d[Mg]}{dt} = -k_{on,j}[Mg][B] + k_{off,j}[MgB] \quad j = ATP$$

$$\frac{d[B]}{dt} = -\frac{d[CaB]}{dt} - \frac{d[MgB]}{dt} \quad B = dye, ATP, EB$$

The time course of the total change in Ca^{2+} concentration or Mg^{2+} concentration is given by the sum of all the above equations involving changes in Ca^{2+} concentration or Mg^{2+} concentration, respectively. Ca^{2+} concentration as reported by the dye was calculated from the concentration of the Ca^{2+}-dye complex assuming equilibrium conditions (*Markram et al., 1998*). The clearing of Ca^{2+} from the cytosol was not implemented in these simulations. Instead, the Ca^{2+} concentration was simulated only for 10 ms after the flash. The experimentally observed subsequent decay of the Ca^{2+} concentration was implemented by an exponential decay to the resting Ca^{2+} concentration with a time constant of 400 ms. The parameters of the model are given in *Table 2*.

These simulations were used to obtain Ca^{2+} transients with peak amplitudes covering the entire range of post-flash Ca^{2+} concentrations. To this end, the uncaging efficiency α was varied in each of the three experimentally used combinations of concentrations of DMn and Ca^{2+} indicators (see *Table 1* for details).

Modeling of release schemes

Model one with two Ca^{2+} binding steps mediating fusion and one Ca^{2+}-dependent priming step was defined according to the following differential equation

$$\begin{pmatrix} dV_{0Ca}(t)/dt \\ dV_{1Ca}(t)/dt \\ dV_{2Ca}(t)/dt \\ dV_{fused}(t)/dt \end{pmatrix} = M \begin{pmatrix} V_{0Ca}(t) \\ V_{1Ca}(t) \\ V_{2Ca}(t) \\ V_{fused}(t) \end{pmatrix}$$

V_{0Ca}, V_{1Ca}, and V_{2Ca} denote the fraction of vesicles with a fusion sensor with 0 to 2 bound Ca^{2+} ions, respectively, and V_{fused} denotes the fused vesicles as illustrated in *Figure 6D*. The reserve pool V_R is considered to be infinite. M denotes the following 4x4 matrix:

$$\begin{pmatrix} -2k_{on}-k_{unprim}+k_{prim}/V_{0Ca}(t) & k_{off} & 0 & 0 \\ 2k_{on} & -k_{off}-k_{on} & 2k_{off}b & 0 \\ 0 & k_{on} & -y-2k_{off}b & 0 \\ 0 & 0 & y & 0 \end{pmatrix}$$

See *Table 3* for the values and Ca^{2+}-dependence of the rate constants in the matrix.

The initial condition was defined as $V_{0Ca}(0) = k_{prim}/k_{unprim}$ and $V_{1Ca}(0)$, $V_{2Ca}(0)$, and $V_{fused}(0)$ was zero. k_{prim} was the sum of a Ca^{2+}-dependent and Ca^{2+}-independent rate constants. The Ca^{2+}-dependence was implemented as a Michaelis-Menten kinetic with a maximum rate constant of 30 s^{-1} (*Ritzau-Jost et al., 2014*) and a K_D of 2 μM (*Miki et al., 2018*). The Ca^{2+}-independent rate constant was 0.6 s^{-1}, adjusted to reproduce the factor of 3 upon elevating Ca^{2+} from 30 to 180 nM (*Figures 1D* and *7D*). k_{unprim} was defined such that the occupancy $V_{0Ca}(0) = 1$ for the default pre-flash resting Ca^{2+} concentration of 227 nM (*Tables 2* and *3*). The occupancy was set to 1 for simplicity in all models because our data did not allow determining the occupancy (but for evidence of occupancy < 1 see *Pulido and Marty, 2017*).

The differential equations were solved with the NDSolve function of Mathematica. The Ca^{2+} concentration, $Ca^{2+}(t)$, was obtained from the simulations as described in the previous paragraph. $V_{fused}(t)$ represents the cumulative release normalized to the pool of release-ready vesicles per cMFB to GC connection. To reproduce the absolute sustained release rate (*Figures 5*, *6D*), $V_{fused}(t)$ was multiplied by a pool of release-ready vesicles per connection of 10 vesicles. The cumulative release, $V_{fused}(t)$, including a pre-flash baseline was sampled with 5 or 10 kHz. Realistic noise for 5- or 10-kHz-capacitance or deconvolution measurements was added and the data, in the 10 ms-window after the flash, were fit with mono- and bi- exponential functions (*Equation 1*). The selection of a bi- over a mono-exponential fit was based on identical criteria as in the analysis of the experimental data including the prolongation of the fitting duration from 10 to 60 ms if the time constant of the mono-exponential fit was >10 ms (see section Data analysis). For each peak post-flash Ca^{2+} concentration

(i.e. simulated $Ca^{2+}(t)$ transient) the sampling, addition of noise, and exponential fitting were repeated 50 times. The median of these values represents the prediction of the model for each peak post flash Ca^{2+} concentration. The parameters of the r were manually adjusted to obtain best-fit results.

Model 2 was a sequential two-pool model based on *Miki et al., 2018* with five Ca^{2+} binding steps mediating fusion and two Ca^{2+}-dependent priming steps defined according to the following differential equations

$$\begin{pmatrix} dV_{2,0Ca}(t)/dt \\ dV_{2,1Ca}(t)/dt \\ dV_{2,2Ca}(t)/dt \\ dV_{2,3Ca}(t)/dt \\ dV_{2,4a}(t)/dt \\ dV_{2,5Ca}(t)/dt \\ dV_{2,fused}(t)/dt \end{pmatrix} = M \begin{pmatrix} V_{2,0Ca}(t) \\ V_{2,1Ca}(t) \\ V_{2,2Ca}(t) \\ V_{2,3Ca}(t) \\ V_{2,4Ca}(t) \\ V_{2,5Ca}(t) \\ V_{2,fused}(t) \end{pmatrix}$$

$V_{2,0Ca}$, $V_{2,1Ca}$, ..., and $V_{2,5Ca}$ denote the fraction of vesicles with a fusion sensor with 0 to 5 bound Ca^{2+} ions, respectively, and $V_{2,fused}$ denotes fused vesicles as illustrated in *Figure 6D*. The fraction of vesicles in state V_1 is calculated according to the following differential equation

$$\frac{dV_1(t)}{dt} = k_{prim1} - k_{unprim1} \, V_1(t) - k_{prim2} \, V_1(t) + k_{unprim2} \, V_{2,0Ca}(t)$$

M denotes the following 7x7 matrix:

$$\begin{pmatrix} -5k_{on}-k_{unprim2}+k_{prim2}/V_1(t)/V_{2,0Ca}(t) & k_{off} & 0 & 0 & 0 & 0 & 0 \\ 5k_{on} & -k_{off}-4k_{on} & 2k_{off}b & 0 & 0 & 0 & 0 \\ 0 & 4k_{on} & -2k_{off}b-3k_{on} & 3k_{off}b^2 & 0 & 0 & 0 \\ 0 & 0 & 3k_{on} & -3k_{off}b^2-2k_{on} & 4k_{off}b^3 & 0 & 0 \\ 0 & 0 & 0 & 2k_{on} & -4k_{off}b^3-k_{on} & 5k_{off}b4 & 0 \\ 0 & 0 & 0 & 0 & k_{on} & -y-5k_{off}b^4 & 0 \\ 0 & 0 & 0 & 0 & 0 & y & 0 \end{pmatrix}$$

To implement the use-dependent slowing of the release rate constants of this model (*Miki et al., 2018*) in a deterministic way, a site-plugging state, $P(t)$, was defined according to

$$\frac{dP(t)}{dt} = (1 - P(t))\frac{dV_{2,fused}}{dt}(t) - 40ms \, P(t) \tag{3}$$

$P(t)$ is approaching one during strong release and decays with a time constant of 40 ms back to zero. Similar to the implementation by *Miki et al., 2018*, the rate constants k_{on} and k_{off} were linearly interpolated between two values depending on $P(t)$ as

$$k_{on}(t) = k_{on,init} + (k_{on,plugged} - k_{on,init}) \, P(t) \tag{4}$$

$$k_{off}(t) = k_{off,init} + (k_{off,plugged} - k_{off,init}) \, P(t)$$

The reserve pool V_R is considered to be infinite. See *Table 3* for the values and Ca^{2+}-dependence of the rate constants in these differential equations.

The initial condition is defined as $V_1(0) = k_{prim1}/k_{unprim1}$ and $V_{2,0Ca}(0) = (k_{prim1}/k_{unprim1})*(k_{prim2}/k_{unprim2})$. The initial condition of the other state $V_{2,1Ca}(0)$ to $V_{5,0Ca}(0)$, $V_{fused}(0)$, and $P(0)$ were zero. k_{prim1} and k_{prim2} were the sum of a Ca^{2+}-dependent and Ca^{2+}-independent rate constant defined similarly as described in *Miki et al., 2018* and adjusted as described for model 1. $k_{unprim1}$ and $k_{unprim2}$ were defined such that the occupancy $V_1(0) = 1$ and $V_{2,0Ca}(0) = 1$ for the default pre-flash resting Ca^{2+} concentration of 227 nM (*Tables 2* and *3*).

Model 3 was a parallel two-pool model similar as described by *Voets, 2000* and *Walter et al., 2013* but with five Ca^{2+} binding steps mediating fusion of both types of vesicles and a Ca^{2+}-independent priming step for V_1 vesicles and a Ca^{2+}-dependent transition step from V_1 to V_2 vesicles defined according to the following differential equations

37

$$\begin{pmatrix} dV_{1,0Ca}(t)/dt \\ dV_{1,1Ca}(t)/dt \\ dV_{1,2Ca}(t)/dt \\ dV_{1,3Ca}(t)/dt \\ dV_{1,4a}(t)/dt \\ dV_{1,5Ca}(t)/dt \\ dV_{1,fused}(t)/dt \end{pmatrix} = M_1 \begin{pmatrix} V_{1,0Ca}(t) \\ V_{1,1Ca}(t) \\ V_{1,2Ca}(t) \\ V_{1,3Ca}(t) \\ V_{1,4Ca}(t) \\ V_{1,5Ca}(t) \\ V_{1,fused}(t) \end{pmatrix}$$

$$\begin{pmatrix} dV_{2,0Ca}(t)/dt \\ dV_{2,1Ca}(t)/dt \\ dV_{2,2Ca}(t)/dt \\ dV_{2,3Ca}(t)/dt \\ dV_{2,4a}(t)/dt \\ dV_{2,5Ca}(t)/dt \\ dV_{2,fused}(t)/dt \end{pmatrix} = M_2 \begin{pmatrix} V_{2,0Ca}(t) \\ V_{2,1Ca}(t) \\ V_{2,2Ca}(t) \\ V_{2,3Ca}(t) \\ V_{2,4Ca}(t) \\ V_{2,5Ca}(t) \\ V_{2,fused}(t) \end{pmatrix}$$

$V_{1,0Ca}, V_{1,1Ca}, \ldots$ and $V_{1,5Ca}$ denote the fraction of vesicles with a low-affinity fusion sensor with 0 to 5 bound Ca^{2+} ions, respectively, and $V_{2,0Ca}, V_{2,1Ca}, \ldots$ and $V_{2,5Ca}$ denote the fraction of vesicles with a high-affinity fusion sensor with 0 to 5 bound Ca^{2+} ions, respectively. $V_{1,fused}$ and $V_{2,fused}$ denote fused vesicles as illustrated in *Figure 6D*.

M_1 denotes the following 7x7 matrix:

$$\begin{pmatrix} -5k_{on1}-k_{unprim1}-k_{prim2}+k_{prim1}/V_{1,0Ca}(t)+k_{unprim2}/V_{2,0Ca}(t)/V_{1,0Ca}(t) & k_{off1} & 0 & 0 & 0 & 0 & 0 \\ 5k_{on1} & -k_{off1}-4k_{on1} & 2k_{off1}b & 0 & 0 & 0 & 0 \\ 0 & 4k_{on1} & -2k_{off1}b-3k_{on1} & 3k_{off1}b^2 & 0 & 0 & 0 \\ 0 & 0 & 3k_{on1} & -3k_{off1}b^2-2k_{on1} & 4k_{off1}b^3 & 0 & 0 \\ 0 & 0 & 0 & 2k_{on1} & -4k_{off1}b^3-k_{on1} & 5k_{off1}b4 & 0 \\ 0 & 0 & 0 & 0 & k_{on1} & -y-5k_{off1}b^4 & 0 \\ 0 & 0 & 0 & 0 & 0 & y & 0 \end{pmatrix}$$

M_2 denotes the following 7x7 matrix:

$$\begin{pmatrix} -5k_{on1}-k_{unprim2}+k_{prim2}V_{1,0Ca}(t)/V_{2,0Ca}(t) & k_{off2} & 0 & 0 & 0 & 0 & 0 \\ 5k_{on2} & -k_{off2}-4k_{on2} & 2k_{off2}b & 0 & 0 & 0 & 0 \\ 0 & 4k_{on2} & -2k_{off2}b-3k_{on2} & 3k_{off2}b^2 & 0 & 0 & 0 \\ 0 & 0 & 3k_{on2} & -3k_{off2}b^2-2k_{on2} & 4k_{off2}b^3 & 0 & 0 \\ 0 & 0 & 0 & 2k_{on2} & -4k_{off2}b^3-k_{on2} & 5k_{off2}b4 & 0 \\ 0 & 0 & 0 & 0 & k_{on2} & -y-5k_{off2}b^4 & 0 \\ 0 & 0 & 0 & 0 & 0 & y & 0 \end{pmatrix}$$

The initial condition is defined as $V_{2,0Ca}(0) = k_{prim1}/k_{unprim1}$ and $V_{2,0Ca}(0) = (k_{prim1}/k_{unprim1})*(k_{prim2}/k_{unprim2})$. The initial condition of the other state $V_{1,1Ca}(0)$ to $V_{1,0Ca}(0)$, $V_{1,fused}(0)$, and $V_{2,1Ca}(0)$ to $V_{2,0Ca}(0)$, $V_{2,fused}(0)$ were zero. k_{prim1} was a Ca^{2+}-independent rate constant and k_{prim2} was the sum of a Ca^{2+}-dependent and Ca^{2+}-independent rate constants defined similarly as described in *Hallermann et al., 2010* and adjusted as described for model 1. $k_{unprim1}$ and $k_{unprim2}$ were defined such that the occupancy $V_{1,0Ca}(0) =$ one and $V_{2,0Ca}(0) =$ one for the default pre-flash resting Ca^{2+} concentration of 227 nM (*Tables 2* and *3*).

Statistical analysis

Boxplots show median and 1st/3rd quartiles with whiskers indicating the whole data range (*Figures 1* and *7*). For statistical comparison, Mann-Whitney *U* tests were used, and the p-values are indicated above the boxplots.

Acknowledgements

Additional information

Author contributions

Abdelmoneim Eshra, Conceptualization, Data curation, Investigation, Visualization, Methodology, Writing - original draft, Writing - review and editing; Hartmut Schmidt, Investigation, Visualization, Methodology, Writing - original draft, Writing - review and editing; Jens Eilers, Methodology, Writing - review and editing; Stefan Hallermann, Conceptualization, Software, Investigation, Methodology, Writing - original draft, Writing - review and editing

Author ORCIDs

Abdelmoneim Eshra https://orcid.org/0000-0002-6579-3000
Hartmut Schmidt http://orcid.org/0000-0002-9516-423X
Stefan Hallermann https://orcid.org/0000-0001-9376-7048

Ethics

Animal experimentation: All animals were treated in accordance with the German Protection of Animals Act and with the guidelines for the welfare of experimental animals issued by the European Communities Council Directive (EU Directive 2010/63/EU). The animal killing report number is T41/16 (gov. ID: DD24-5131/347/44).

Decision letter and Author response

Decision letter https://doi.org/10.7554/eLife.70408.sa1
Author response https://doi.org/10.7554/eLife.70408.sa2

Additional files

Supplementary files

• Transparent reporting form

Data availability

The code of the simulations of the release schemes (models 1 to 3) is available at https://github.com/HallermannLab/2021_eLife (copy archived at https://archive.softwareheritage.org/swh:1:rev:4cd31058945a8f1c8364d8fc21f0a2902de33365).

References

Adler EM, Augustine GJ, Duffy SN, Charlton MP. 1991. Alien intracellular calcium chelators attenuate neurotransmitter release at the squid giant synapse. *The Journal of Neuroscience* **11**:1496–1507. PMID: 1675264

Atwood HL, Karunanithi S. 2002. Diversification of synaptic strength: presynaptic elements. *Nature Reviews. Neuroscience* **3**:497–516. DOI: https://doi.org/10.1038/nrn876, PMID: 12094207

Awatramani GB, Price GD, Trussell LO. 2005. Modulation of transmitter release by presynaptic resting potential and background calcium levels. *Neuron* **48**:109–121. DOI: https://doi.org/10.1016/j.neuron.2005.08.038, PMID: 16202712

Beutner D, Voets T, Neher E, Moser T. 2001. Calcium dependence of exocytosis and endocytosis at the cochlear inner hair cell afferent synapse. *Neuron* **29**:681–690. DOI: https://doi.org/10.1016/s0896-6273(01)00243-4, PMID: 11301027

Billings G, Piasini E, Lőrincz A, Nusser Z, Silver RA. 2014. Network structure within the cerebellar input layer enables lossless sparse encoding. *Neuron* **83**:960–974. DOI: https://doi.org/10.1016/j.neuron.2014.07.020, PMID: 25123311

Blanchard K, Zorrilla de San Martín J, Marty A, Llano I, Trigo FF. 2020. Differentially poised vesicles underlie fast and slow components of release at single synapses. *Journal of General Physiology* **152**:201912523. DOI: https://doi.org/10.1085/jgp.201912523

Bollmann JH, Sakmann B, Borst JG. 2000. Calcium sensitivity of glutamate release in a calyx-type terminal. *Science* **289**:953–957. DOI: https://doi.org/10.1126/science.289.5481.953, PMID: 10937999

Bornschein G, Eilers J, Schmidt H. 2019. Neocortical high probability release sites are formed by distinct Ca^{2+} Channel-to-Release Sensor Topographies during Development. *Cell Reports* **28**:1410–1418. DOI: https://doi.org/10.1016/j.celrep.2019.07.008, PMID: 31390556

Bornschein G, Schmidt H. 2018. Synaptotagmin Ca^{2+} sensors and their spatial coupling to presynaptic Ca_vChannels in Central Cortical Synapses. *Frontiers in Molecular Neuroscience* **11**:494. DOI: https://doi.org/10.3389/fnmol.2018.00494, PMID: 30697148

Cathala L, Brickley S, Cull-Candy S, Farrant M. 2003. Maturation of EPSCs and intrinsic membrane properties enhances precision at a cerebellar synapse. *The Journal of Neuroscience* **23**:6074–6085. PMID: 12853426

Chabrol FP, Arenz A, Wiechert MT, Margrie TW, DiGregorio DA. 2015. Synaptic diversity enables temporal coding of coincident multisensory inputs in single neurons. *Nature Neuroscience* **18**:718–727. DOI: https://doi.org/10.1038/nn.3974, PMID: 25821914

Chang S, Trimbuch T, Rosenmund C. 2018. Synaptotagmin-1 drives synchronous Ca^{2+}-triggered fusion by C_2B-domain-mediated synaptic-vesicle-membrane attachment. *Nature Neuroscience* **21**:33–40. DOI: https://doi.org/10.1038/s41593-017-0037-5, PMID: 29230057

Chen C, Satterfield R, Young SM, Jonas P. 2017. Triple function of synaptotagmin 7 ensures efficiency of High-Frequency transmission at central GABAergic synapses. *Cell Reports* **21**:2082–2089. DOI: https://doi.org/10.1016/j.celrep.2017.10.122, PMID: 29166601

Delvendahl I, Jablonski L, Baade C, Matveev V, Neher E, Hallermann S. 2015. Reduced endogenous Ca^{2+} buffering speeds active zone $^{Ca2+}$ signaling. *PNAS* **112**:3075–3084. DOI: https://doi.org/10.1073/pnas.1508419112, PMID: 26015575

DiGregorio DA, Nusser Z, Silver RA. 2002. Spillover of glutamate onto synaptic AMPA receptors enhances fast transmission at a cerebellar synapse. *Neuron* **35**:521–533. DOI: https://doi.org/10.1016/s0896-6273(02)00787-0, PMID: 12165473

DiGregorio DA, Vergara JL. 1997. Localized detection of action potential-induced presynaptic calcium transients at a *Xenopus* neuromuscular junction. *The Journal of Physiology* **505**:585–592. DOI: https://doi.org/10.1111/j.1469-7793.1997.585ba.x, PMID: 9457637

Doussau F, Schmidt H, Dorgans K, Valera AM, Poulain B, Isope P. 2017. Frequency-dependent mobilization of heterogeneous pools of synaptic vesicles shapes presynaptic plasticity. *eLife* **6**:e28935. DOI: https://doi.org/10.7554/eLife.28935, PMID: 28990927

Duncan G, Rabl K, Gemp I, Heidelberger R, Thoreson WB. 2010. Quantitative analysis of synaptic release at the photoreceptor synapse. *Biophysical Journal* **98**:2102–2110. DOI: https://doi.org/10.1016/j.bpj.2010.02.003, PMID: 20483317

Eggermann E, Bucurenciu I, Goswami SP, Jonas P. 2011. Nanodomain coupling between Ca^{2+} channels and sensors of exocytosis at fast mammalian synapses. *Nature Reviews. Neuroscience* **13**:7–21. DOI: https://doi.org/10.1038/nrn3125, PMID: 22183436

Éltes T, Kirizs T, Nusser Z, Holderith N. 2017. Target cell Type-Dependent differences in Ca^{2+} Channel Function Underlie Distinct Release Probabilities at Hippocampal Glutamatergic Terminals. *The Journal of Neuroscience* **37**:1910–1924. DOI: https://doi.org/10.1523/JNEUROSCI.2024-16.2017, PMID: 28115484

Escobar AL, Velez P, Kim AM, Cifuentes F, Fill M, Vergara JL. 1997. Kinetic properties of DM-nitrophen and calcium indicators: rapid transient response to flash photolysis. *PflüGers Archiv European Journal of Physiology* **434**:615–631. DOI: https://doi.org/10.1007/s004240050444

Faas GC, Karacs K, Vergara JL, Mody I. 2005. Kinetic properties of DM-nitrophen binding to calcium and magnesium. *Biophysical Journal* **88**:4421–4433. DOI: https://doi.org/10.1529/biophysj.104.057745, PMID: 15778435

Faas GC, Schwaller B, Vergara JL, Mody I. 2007. Resolving the fast kinetics of cooperative binding: $^{ca2+}$ buffering by calretinin. *PLOS Biology* **5**:e311. DOI: https://doi.org/10.1371/journal.pbio.0050311, PMID: 18044987

Fedchyshyn MJ, Wang LY. 2005. Developmental transformation of the release modality at the Calyx of held synapse. *The Journal of Neuroscience* **25**:4131–4140. DOI: https://doi.org/10.1523/JNEUROSCI.0350-05.2005, PMID: 15843616

Fekete A, Nakamura Y, Yang YM, Herlitze S, Mark MD, DiGregorio DA, Wang LY. 2019. Underpinning heterogeneity in synaptic transmission by presynaptic ensembles of distinct morphological modules. *Nature Communications* **10**:826. DOI: https://doi.org/10.1038/s41467-019-08452-2, PMID: 30778063

Forsythe ID. 1994. Direct patch recording from identified presynaptic terminals mediating glutamatergic EPSCs in the rat CNS, in vitro. *The Journal of Physiology* **479**:381–387. DOI: https://doi.org/10.1113/jphysiol.1994.sp020303, PMID: 7837096

Fukaya R, Maglione M, Sigrist SJ, Sakaba T. 2021. Rapid Ca²⁺ channel accumulation contributes to cAMP-mediated increase in transmission at hippocampal mossy fiber synapses. *PNAS* **118**:e2016754118. DOI: https://doi.org/10.1073/pnas.2016754118, PMID: 33622791

Gillis KD. 1995. Membrane Capacitance Measurement. In: Sakmann B, Neher E (Eds). *Single-Channel Recording*. New York: Plenum Press. p. 155–198.

Grande G, Wang LY. 2011. Morphological and functional continuum underlying heterogeneity in the spiking fidelity at the Calyx of held synapse in vitro. *The Journal of Neuroscience* **31**:13386–13399. DOI: https://doi.org/10.1523/JNEUROSCI.0400-11.2011, PMID: 21940432

Hallermann S, Pawlu C, Jonas P, Heckmann M. 2003. A large pool of releasable vesicles in a cortical glutamatergic synapse. *PNAS* **100**:8975–8980. DOI: https://doi.org/10.1073/pnas.1432836100, PMID: 12815098

Hallermann S, Fejtova A, Schmidt H, Weyhersmüller A, Silver RA, Gundelfinger ED, Eilers J. 2010. Bassoon speeds vesicle reloading at a central excitatory synapse. *Neuron* **68**:710–723. DOI: https://doi.org/10.1016/j.neuron.2010.10.026

Hanse E, Gustafsson B. 2001. Vesicle release probability and pre-primed pool at Glutamatergic synapses in area CA1 of the rat neonatal Hippocampus. *The Journal of Physiology* **531**:481–493. DOI: https://doi.org/10.1111/j.1469-7793.2001.0481i.x

Heidelberger R, Heinemann C, Neher E, Matthews G. 1994. Calcium dependence of the rate of exocytosis in a synaptic terminal. *Nature* **371**:513–515. DOI: https://doi.org/10.1038/371513a0, PMID: 7935764

Heil P, Neubauer H. 2010. Summing across different active zones can explain the Quasi-Linear Ca-Dependencies of exocytosis by receptor cells. *Frontiers in Synaptic Neuroscience* **2**:148. DOI: https://doi.org/10.3389/fnsyn.2010.00148, PMID: 21423534

Hosoi N, Sakaba T, Neher E. 2007. Quantitative analysis of calcium-dependent vesicle recruitment and its functional role at the Calyx of held synapse. *The Journal of Neuroscience* **27**:14286–14298. DOI: https://doi.org/10.1523/JNEUROSCI.4122-07.2007, PMID: 18160636

Imig C, Min SW, Krinner S, Arancillo M, Rosenmund C, Südhof TC, Rhee J, Brose N, Cooper BH. 2014. The morphological and molecular nature of synaptic vesicle priming at Presynaptic active zones. *Neuron* **84**:416–431. DOI: https://doi.org/10.1016/j.neuron.2014.10.009, PMID: 25374362

Imig C, López-Murcia FJ, Maus L, García-Plaza IH, Mortensen LS, Schwark M, Schwarze V, Angibaud J, Nägerl UV, Taschenberger H, Brose N, Cooper BH. 2020. Ultrastructural imaging of Activity-Dependent synaptic Membrane-Trafficking events in cultured brain slices. *Neuron* **108**:843–860. DOI: https://doi.org/10.1016/j.neuron.2020.09.004, PMID: 32991831

Ishiyama S, Schmidt H, Cooper BH, Brose N, Eilers J. 2014. Munc13-3 superprimes synaptic vesicles at granule cell-to-basket cell synapses in the mouse cerebellum. *The Journal of Neuroscience* **34**:14687–14696. DOI: https://doi.org/10.1523/JNEUROSCI.2060-14.2014, PMID: 25355221

Jackman SL, Turecek J, Belinsky JE, Regehr WG. 2016. The calcium sensor synaptotagmin 7 is required for synaptic facilitation. *Nature* **529**:88–91. DOI: https://doi.org/10.1038/nature16507, PMID: 26738595

Jackman SL, Regehr WG. 2017. The mechanisms and functions of synaptic facilitation. *Neuron* **94**:447–464. DOI: https://doi.org/10.1016/j.neuron.2017.02.047, PMID: 28472650

Jakab RL, Hamori J. 1988. Quantitative morphology and synaptology of cerebellar glomeruli in the rat. *Anatomy and Embryology* **179**:81–88. DOI: https://doi.org/10.1007/BF00305102

Johnson SL, Franz C, Kuhn S, Furness DN, Rüttiger L, Münkner S, Rivolta MN, Seward EP, Herschman HR, Engel J, Knipper M, Marcotti W. 2010. Synaptotagmin IV determines the linear Ca²⁺ dependence of vesicle fusion at auditory ribbon synapses. *Nature Neuroscience* **13**:45–52. DOI: https://doi.org/10.1038/nn.2456, PMID: 20010821

Kaplan JH, Ellis-Davies GC. 1988. Photolabile chelators for the rapid photorelease of divalent cations. *PNAS* **85**:6571–6575. DOI: https://doi.org/10.1073/pnas.85.17.6571, PMID: 3137570

Katz B, Miledi R. 1968. The role of calcium in neuromuscular facilitation. *The Journal of Physiology* **195**:481–492. DOI: https://doi.org/10.1113/jphysiol.1968.sp008469

Kobbersmed JR, Grasskamp AT, Jusyte M, Böhme MA, Ditlevsen S, Sørensen JB, Walter AM. 2020. Rapid regulation of vesicle priming explains synaptic facilitation despite heterogeneous vesicle:Ca²⁺ channel distances. *eLife* **9**:e51032. DOI: https://doi.org/10.7554/eLife.51032, PMID: 32077852

Kochubey O, Han Y, Schneggenburger R. 2009. Developmental regulation of the intracellular Ca²⁺ sensitivity of vesicle fusion and ᶜᵃ²⁺-secretion coupling at the rat Calyx of held. *The Journal of Physiology* **587**:3009–3023. DOI: https://doi.org/10.1113/jphysiol.2009.172387, PMID: 19403608

Kochubey O, Lou X, Schneggenburger R. 2011. Regulation of transmitter release by Ca²⁺ and synaptotagmin: insights from a large CNS synapse. *Trends in Neurosciences* **34**:237–246. DOI: https://doi.org/10.1016/j.tins.2011.02.006, PMID: 21439657

Kochubey O, Schneggenburger R. 2011. Synaptotagmin increases the dynamic range of synapses by driving Ca²⁺-evoked release and by clamping a near-linear remaining Ca²⁺ sensor. *Neuron* **69**:736–748. DOI: https://doi.org/10.1016/j.neuron.2011.01.013, PMID: 21338883

Kusch V, Bornschein G, Loreth D, Bank J, Jordan J, Baur D, Watanabe M, Kulik A, Heckmann M, Eilers J, Schmidt H. 2018. Munc13-3 is required for the developmental localization of Ca²⁺ Channels to Active Zones and the

Nanopositioning of Ca$_V$2.1 Near Release Sensors. *Cell Reports* **22**:1965–1973. DOI: https://doi.org/10.1016/j.celrep.2018.02.010, PMID: 29466725

Kusick GF, Chin M, Raychaudhuri S, Lippmann K, Adula KP, Hujber EJ, Vu T, Davis MW, Jorgensen EM, Watanabe S. 2020. Synaptic vesicles transiently dock to refill release sites. *Nature Neuroscience* **23**:1329–1338. DOI: https://doi.org/10.1038/s41593-020-00716-1, PMID: 32989294

Lee JS, Ho WK, Lee SH. 2012. Actin-dependent rapid recruitment of reluctant synaptic vesicles into a fast-releasing vesicle pool. *PNAS* **109**:765–774. DOI: https://doi.org/10.1073/pnas.1114072109, PMID: 22393020

Lee JS, Ho WK, Neher E, Lee SH. 2013. Superpriming of synaptic vesicles after their recruitment to the readily releasable pool. *PNAS* **110**:15079–15084. DOI: https://doi.org/10.1073/pnas.1314427110, PMID: 23980146

Lenzi D, von Gersdorff H. 2001. Structure suggests function: the case for synaptic ribbons as exocytotic nanomachines. *BioEssays : News and Reviews in Molecular, Cellular and Developmental Biology* **23**:831–840. DOI: https://doi.org/10.1002/bies.1118, PMID: 11536295

Li L, Liu H, Krout M, Richmond JE, Wang Y, Bai J, Weeratunga S, Collins BM, Ventimiglia D, Yu Y, Xia J, Tang J, Liu J, Hu Z. 2021. A novel dual Ca2+ sensor system regulates Ca2+-dependent neurotransmitter release. *Journal of Cell Biology* **220**:202008121. DOI: https://doi.org/10.1083/jcb.202008121

Lin K-H, Taschenberger H, Neher E. 2017. Dynamics of volume-averaged intracellular Ca^{2+} in a rat CNS nerve terminal during single and repetitive voltage-clamp depolarizations . *The Journal of Physiology* **595**:3219–3236. DOI: https://doi.org/10.1113/JP272773

Liu H, Bai H, Hui E, Yang L, Evans CS, Wang Z, Kwon SE, Chapman ER. 2014. Synaptotagmin 7 functions as a Ca^{2+}-sensor for synaptic vesicle replenishment. *eLife* **3**:e01524. DOI: https://doi.org/10.7554/eLife.01524, PMID: 24569478

Llinás R, Sugimori M, Silver RB. 1992. Microdomains of high calcium concentration in a presynaptic terminal. *Science* **256**:677–679. DOI: https://doi.org/10.1126/science.1350109, PMID: 1350109

Lou X, Scheuss V, Schneggenburger R. 2005. Allosteric modulation of the presynaptic Ca^{2+} sensor for vesicle fusion. *Nature* **435**:497–501. DOI: https://doi.org/10.1038/nature03568, PMID: 15917809

Lou X, Korogod N, Brose N, Schneggenburger R. 2008. Phorbol esters modulate spontaneous and Ca^{2+}-evoked transmitter release via acting on both Munc13 and protein kinase C. *The Journal of Neuroscience* **28**:8257–8267. DOI: https://doi.org/10.1523/JNEUROSCI.0550-08.2008, PMID: 18701688

Luo F, Südhof TC. 2017. Synaptotagmin-7-Mediated asynchronous release boosts High-Fidelity synchronous transmission at a central synapse. *Neuron* **94**:826–839. DOI: https://doi.org/10.1016/j.neuron.2017.04.020, PMID: 28521135

Magleby KL. 1987. Short-term changes in synaptic efficacy. In: Edelman G. M, Gall W. E, Cowan W. M (Eds). *Synaptic Function.* New York: John Wiley & Son. p. 21–56.

Mahfooz K, Singh M, Renden R, Wesseling JF. 2016. A Well-Defined readily releasable pool with fixed capacity for storing vesicles at Calyx of held. *PLOS Computational Biology* **12**:e1004855. DOI: https://doi.org/10.1371/journal.pcbi.1004855, PMID: 27035349

Malagon G, Miki T, Tran V, Gomez LC, Marty A. 2020. Incomplete vesicular docking limits synaptic strength under high release probability conditions. *eLife* **9**:e52137. DOI: https://doi.org/10.7554/eLife.52137, PMID: 32228859

Markram H, Roth A, Helmchen F. 1998. Competitive calcium binding: implications for dendritic calcium signaling. *Journal of Computational Neuroscience* **5**:331–348. DOI: https://doi.org/10.1023/a:1008891229546, PMID: 9663555

Matthews G. 2000. Vesicle fiesta at the synapse. *Nature* **406**:835–836. DOI: https://doi.org/10.1038/35022674, PMID: 10972270

Maus L, Lee C, Altas B, Sertel SM, Weyand K, Rizzoli SO, Rhee J, Brose N, Imig C, Cooper BH. 2020. Ultrastructural correlates of presynaptic functional heterogeneity in hippocampal synapses. *Cell Reports* **30**:3632–3643. DOI: https://doi.org/10.1016/j.celrep.2020.02.083, PMID: 32187536

Meinrenken CJ, Borst JG, Sakmann B. 2002. Calcium secretion coupling at Calyx of held governed by nonuniform channel-vesicle topography. *The Journal of Neuroscience* **22**:1648–1667. DOI: https://doi.org/10.1523/JNEUROSCI.22-05-01648.2002, PMID: 11880495

Miki T, Malagon G, Pulido C, Llano I, Neher E, Marty A. 2016. Actin- and Myosin-Dependent vesicle loading of presynaptic docking sites prior to exocytosis. *Neuron* **91**:808–823. DOI: https://doi.org/10.1016/j.neuron.2016.07.033, PMID: 27537485

Miki T, Nakamura Y, Malagon G, Neher E, Marty A. 2018. Two-component latency distributions indicate two-step vesicular release at simple glutamatergic synapses. *Nature Communications* **9**:3943. DOI: https://doi.org/10.1038/s41467-018-06336-5, PMID: 30258069

Miki T, Midorikawa M, Sakaba T. 2020. Direct imaging of rapid tethering of synaptic vesicles accompanying exocytosis at a fast central synapse. *PNAS* **117**:14493–14502. DOI: https://doi.org/10.1073/pnas.2000265117, PMID: 32513685

Millar AG, Zucker RS, Ellis-Davies GC, Charlton MP, Atwood HL. 2005. Calcium sensitivity of neurotransmitter release differs at Phasic and tonic synapses. *The Journal of Neuroscience* **25**:3113–3125. DOI: https://doi.org/10.1523/JNEUROSCI.4717-04.2005, PMID: 15788768

Müller M, Goutman JD, Kochubey O, Schneggenburger R. 2010. Interaction between facilitation and depression at a large CNS synapse reveals mechanisms of short-term plasticity. *The Journal of Neuroscience* **30**:2007–2016. DOI: https://doi.org/10.1523/JNEUROSCI.4378-09.2010, PMID: 20147529

Nakamura Y, Harada H, Kamasawa N, Matsui K, Rothman JS, Shigemoto R, Silver RA, DiGregorio DA, Takahashi T. 2015. Nanoscale distribution of presynaptic $ca^{(2+)}$ channels and its impact on vesicular release during development. *Neuron* **85**:145–158. DOI: https://doi.org/10.1016/j.neuron.2014.11.019, PMID: 25533484

Neef J, Urban NT, Ohn TL, Frank T, Jean P, Hell SW, Willig KI, Moser T. 2018. Quantitative optical nanophysiology of Ca^{2+} signaling at inner hair cell active zones. *Nature Communications* **9**:290. DOI: https://doi.org/10.1038/s41467-017-02612-y, PMID: 29348575

Neher E. 1998. Vesicle pools and $Ca2+$ microdomains: new tools for understanding their roles in neurotransmitter release. *Neuron* **20**:389–399. DOI: https://doi.org/10.1016/s0896-6273(00)80983-6, PMID: 9539117

Neher E, Brose N. 2018. Dynamically primed synaptic vesicle states: key to understand synaptic Short-Term plasticity. *Neuron* **100**:1283–1291. DOI: https://doi.org/10.1016/j.neuron.2018.11.024, PMID: 30571941

Neher E, Lux HD. 1973. Rapid changes of potassium concentration at the outer surface of exposed single neurons during membrane current flow. *Journal of General Physiology* **61**:385–399. DOI: https://doi.org/10.1085/jgp.61.3.385

Neher E, Sakaba T. 2008. Multiple roles of calcium ions in the regulation of neurotransmitter release. *Neuron* **59**:861–872. DOI: https://doi.org/10.1016/j.neuron.2008.08.019, PMID: 18817727

Nusser Z. 2018. Creating diverse synapses from the same molecules. *Current Opinion in Neurobiology* **51**:8–15. DOI: https://doi.org/10.1016/j.conb.2018.01.001, PMID: 29353084

Pan B, Zucker RS. 2009. A general model of synaptic transmission and short-term plasticity. *Neuron* **62**:539–554. DOI: https://doi.org/10.1016/j.neuron.2009.03.025, PMID: 19477155

Pulido C, Marty A. 2017. Quantal fluctuations in central mammalian synapses: functional role of vesicular docking sites. *Physiological Reviews* **97**:1403–1430. DOI: https://doi.org/10.1152/physrev.00032.2016, PMID: 28835509

Rebola N, Reva M, Kirizs T, Szoboszlay M, Lőrincz A, Moneron G, Nusser Z, DiGregorio DA. 2019. Distinct nanoscale calcium channel and synaptic vesicle topographies contribute to the diversity of synaptic function. *Neuron* **104**:693–710. DOI: https://doi.org/10.1016/j.neuron.2019.08.014, PMID: 31558350

Rhee JS, Betz A, Pyott S, Reim K, Varoqueaux F, Augustin I, Hesse D, Südhof TC, Takahashi M, Rosenmund C, Brose N. 2002. Beta phorbol ester- and diacylglycerol-induced augmentation of transmitter release is mediated by Munc13s and not by PKCs. *Cell* **108**:121–133. DOI: https://doi.org/10.1016/s0092-8674(01)00635-3, PMID: 11792326

Ritzau-Jost A, Delvendahl I, Rings A, Byczkowicz N, Harada H, Shigemoto R, Hirrlinger J, Eilers J, Hallermann S. 2014. Ultrafast action potentials mediate kilohertz signaling at a central synapse. *Neuron* **84**:152–163. DOI: https://doi.org/10.1016/j.neuron.2014.08.036, PMID: 25220814

Ritzau-Jost A, Jablonski L, Viotti J, Lipstein N, Eilers J, Hallermann S. 2018. Apparent calcium dependence of vesicle recruitment. *The Journal of Physiology* **596**:4693–4707. DOI: https://doi.org/10.1113/JP275911

Rothman JS, Kocsis L, Herzog E, Nusser Z, Silver RA. 2016. Physical determinants of vesicle mobility and supply at a central synapse. *eLife* **5**:e15133. DOI: https://doi.org/10.7554/eLife.15133, PMID: 27542193

Sabatini BL, Oertner TG, Svoboda K. 2002. The life cycle of ca(2+) ions in dendritic spines. *Neuron* **33**:439–452. DOI: https://doi.org/10.1016/s0896-6273(02)00573-1, PMID: 11832230

Sakaba T, Stein A, Jahn R, Neher E. 2005. Distinct kinetic changes in neurotransmitter release after SNARE protein cleavage. *Science* **309**:491–494. DOI: https://doi.org/10.1126/science.1112645, PMID: 16020741

Sakaba T. 2008. Two Ca^{2+}-dependent steps controlling synaptic vesicle fusion and replenishment at the cerebellar basket cell terminal. *Neuron* **57**:406–419. DOI: https://doi.org/10.1016/j.neuron.2007.11.029, PMID: 18255033

Sakaba T, Neher E. 2001a. Calmodulin mediates rapid recruitment of fast-releasing synaptic vesicles at a calyx-type synapse. *Neuron* **32**:1119–1131. DOI: https://doi.org/10.1016/s0896-6273(01)00543-8, PMID: 11754842

Sakaba T, Neher E. 2001b. Quantitative relationship between transmitter release and calcium current at the Calyx of held synapse. *The Journal of Neuroscience* **21**:462–476. DOI: https://doi.org/10.1523/JNEUROSCI.21-02-00462.2001

Saviane C, Silver RA. 2006. Fast vesicle reloading and a large pool sustain high bandwidth transmission at a central synapse. *Nature* **439**:983–987. DOI: https://doi.org/10.1038/nature04509, PMID: 16496000

Schlüter OM, Basu J, Südhof TC, Rosenmund C. 2006. Rab3 superprimes synaptic vesicles for release: implications for short-term synaptic plasticity. *The Journal of Neuroscience* **26**:1239–1246. DOI: https://doi.org/10.1523/JNEUROSCI.3553-05.2006, PMID: 16436611

Schneggenburger R. 2005. Ca^{2+} uncaging in nerve terminals. In: Yuste R, Konnerth A (Eds). *Imaging in Neuroscience and Development: A Laboratory Manual*. New York: Cold Spring Harbor Laboratory Press. p. 415–419.

Schneggenburger R, Neher E. 2000. Intracellular calcium dependence of transmitter release rates at a fast central synapse. *Nature* **406**:889–893. DOI: https://doi.org/10.1038/35022702, PMID: 10972290

Shin OH, Lu J, Rhee JS, Tomchick DR, Pang ZP, Wojcik SM, Camacho-Perez M, Brose N, Machius M, Rizo J, Rosenmund C, Südhof TC. 2010. Munc13 C2B domain is an activity-dependent Ca2+ regulator of synaptic exocytosis. *Nature Structural & Molecular Biology* **17**:280–288. DOI: https://doi.org/10.1038/nsmb.1758, PMID: 20154707

Silva M, Tran V, Marty A. 2021. Calcium-dependent docking of synaptic vesicles. *Trends in Neurosciences* **44**:579–592. DOI: https://doi.org/10.1016/j.tins.2021.04.003, PMID: 34049722

Simon SM, Llinás RR. 1985. Compartmentalization of the submembrane calcium activity during calcium influx and its significance in transmitter release. *Biophysical Journal* **48**:485–498. DOI: https://doi.org/10.1016/S0006-3495(85)83804-2, PMID: 2412607

Straub I, Witter L, Eshra A, Hoidis M, Byczkowicz N, Maas S, Delvendahl I, Dorgans K, Savier E, Bechmann I, Krueger M, Isope P, Hallermann S. 2020. Gradients in the mammalian cerebellar cortex enable Fourier-like transformation and improve storing capacity. *eLife* **9**:e51771. DOI: https://doi.org/10.7554/eLife.51771, PMID: 32022688

Südhof TC. 2004. The synaptic vesicle cycle. *Annual Review of Neuroscience* **27**:509–547. DOI: https://doi.org/10.1146/annurev.neuro.26.041002.131412, PMID: 15217342

Südhof TC. 2013. Neurotransmitter release: the last millisecond in the life of a synaptic vesicle. *Neuron* **80**:675–690. DOI: https://doi.org/10.1016/j.neuron.2013.10.022, PMID: 24183019

Sugita S, Shin OH, Han W, Lao Y, Südhof TC. 2002. Synaptotagmins form a hierarchy of exocytotic Ca^{2+} sensors with distinct Ca^{2+} affinities. *The EMBO Journal* **21**:270–280. DOI: https://doi.org/10.1093/emboj/21.3.270, PMID: 11823420

Sun J, Pang ZP, Qin D, Fahim AT, Adachi R, SÃ¼dhof TC, Südhof TC. 2007. A dual-Ca^{2+}-sensor model for neurotransmitter release in a central synapse. *Nature* **450**:676–682. DOI: https://doi.org/10.1038/nature06308

Taschenberger H, Woehler A, Neher E. 2016. Superpriming of synaptic vesicles as a common basis for intersynapse variability and modulation of synaptic strength. *PNAS* **113**:E4548–E4557. DOI: https://doi.org/10.1073/pnas.1606383113

Taschenberger H, von Gersdorff H. 2000. Fine-tuning an auditory synapse for speed and fidelity: developmental changes in Presynaptic Waveform, EPSC kinetics, and synaptic plasticity. *The Journal of Neuroscience* **20**:9162–9173. DOI: https://doi.org/10.1523/JNEUROSCI.20-24-09162.2000, PMID: 11124994

Thoreson WB, Rabl K, Townes-Anderson E, Heidelberger R. 2004. A highly $^{Ca2+}$-sensitive pool of vesicles contributes to linearity at the rod photoreceptor ribbon synapse. *Neuron* **42**:595–605. DOI: https://doi.org/10.1016/S0896-6273(04)00254-5, PMID: 15157421

Tran V, Park MCH, Stricker C. 2018. An improved measurement of the Ca^{2+}-binding affinity of fluorescent Ca^{2+} indicators. *Cell Calcium* **71**:86–94. DOI: https://doi.org/10.1016/j.ceca.2018.01.001, PMID: 29604967

Valera AM, Doussau F, Poulain B, Barbour B, Isope P. 2012. Adaptation of granule cell to Purkinje cell synapses to high-frequency transmission. *Journal of Neuroscience* **32**:3267–3280. DOI: https://doi.org/10.1523/JNEUROSCI.3175-11.2012, PMID: 22378898

Vandael D, Borges-Merjane C, Zhang X, Jonas P. 2020. Short-Term plasticity at hippocampal mossy fiber synapses is induced by natural activity patterns and associated with vesicle pool engram formation. *Neuron* **107**:509–521. DOI: https://doi.org/10.1016/j.neuron.2020.05.013, PMID: 32492366

Vevea JD, Kusick GF, Chen E, Courtney KC, Watanabe S, Chapman ER. 2021. Synaptotagmin 7 is enriched at the plasma membrane through γ-secretase processing to promote vesicle docking and control synaptic plasticity in mouse hippocampal neurons. *bioRxiv*. DOI: https://doi.org/10.1101/2021.02.09.430404

Voets T. 2000. Dissection of three Ca^{2+}-dependent steps leading to secretion in chromaffin cells from mouse adrenal slices. *Neuron* **28**:537–545. DOI: https://doi.org/10.1016/S0896-6273(00)00131-8, PMID: 11144362

Wadel K, Neher E, Sakaba T. 2007. The coupling between synaptic vesicles and Ca^{2+} channels determines fast neurotransmitter release. *Neuron* **53**:563–575. DOI: https://doi.org/10.1016/j.neuron.2007.01.021, PMID: 17296557

Walter AM, Pinheiro PS, Verhage M, Sørensen JB. 2013. A sequential vesicle pool model with a single release sensor and a $Ca^{(2+)}$-dependent priming catalyst effectively explains $Ca^{(2+)}$-dependent properties of neurosecretion. *PLOS Computational Biology* **9**:e1003362. DOI: https://doi.org/10.1371/journal.pcbi.1003362, PMID: 24339761

Wang LY, Neher E, Taschenberger H. 2008. Synaptic vesicles in mature calyx of Held synapses sense higher nanodomain calcium concentrations during action potential-evoked glutamate release. *Journal of Neuroscience* **28**:14450–14458. DOI: https://doi.org/10.1523/JNEUROSCI.4245-08.2008, PMID: 19118179

Wang LY, Kaczmarek LK. 1998. High-frequency firing helps replenish the readily releasable pool of synaptic vesicles. *Nature* **394**:384–388. DOI: https://doi.org/10.1038/28645, PMID: 9690475

Wölfel M, Lou X, Schneggenburger R. 2007. A mechanism intrinsic to the vesicle fusion machinery determines fast and slow transmitter release at a large CNS synapse. *Journal of Neuroscience* **27**:3198–3210. DOI: https://doi.org/10.1523/JNEUROSCI.4471-06.2007, PMID: 17376981

Yamada WM, Zucker RS. 1992. Time course of transmitter release calculated from simulations of a calcium diffusion model. *Biophysical Journal* **61**:671–682. DOI: https://doi.org/10.1016/S0006-3495(92)81872-6, PMID: 1354503

Yasuda R, Nimchinsky EA, Scheuss V, Pologruto TA, Oertner TG, Sabatini BL, Svoboda K. 2004. Imaging calcium concentration dynamics in small neuronal compartments. *Science's STKE : signal transduction knowledge environment* **2004**:pl5. DOI: https://doi.org/10.1126/stke.2192004pl5, PMID: 14872098

Zhai RG, Bellen HJ. 2004. The architecture of the active zone in the presynaptic nerve terminal. *Physiology* **19**:262–270. DOI: https://doi.org/10.1152/physiol.00014.2004, PMID: 15381754

Zucker RS. 1992. Effects of photolabile calcium chelators on fluorescent calcium indicators. *Cell Calcium* **13**:29–40. DOI: https://doi.org/10.1016/0143-4160(92)90027-P, PMID: 1540986

Zucker RS, Regehr WG. 2002. Short-term synaptic plasticity. *Annual Review of Physiology* **64**:355–405. DOI: https://doi.org/10.1146/annurev.physiol.64.092501.114547, PMID: 11826273

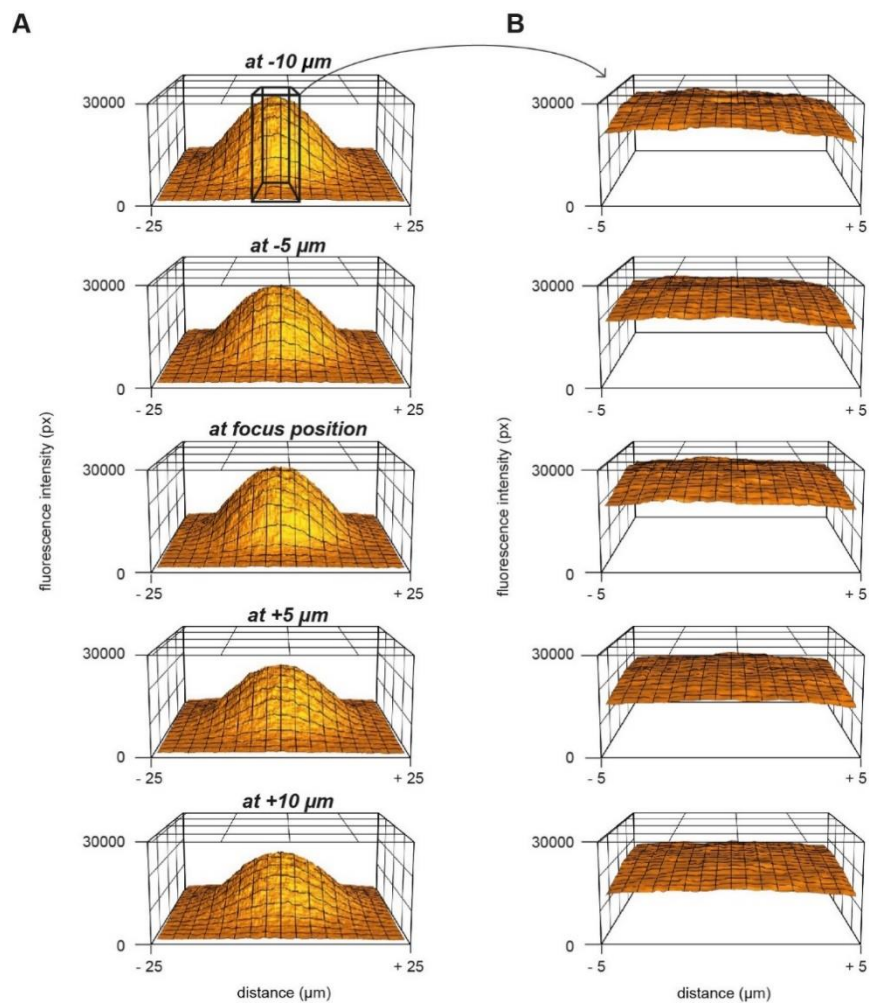**Supplementary figures of Eshra et al., 2021**

Figure 2 - figure supplement 1

Measurement of the UV energy profile with caged fluorescein
(A) 3D plot of the fluorescence profile in response to UV uncaging of caged-fluorescein at different z-positions.
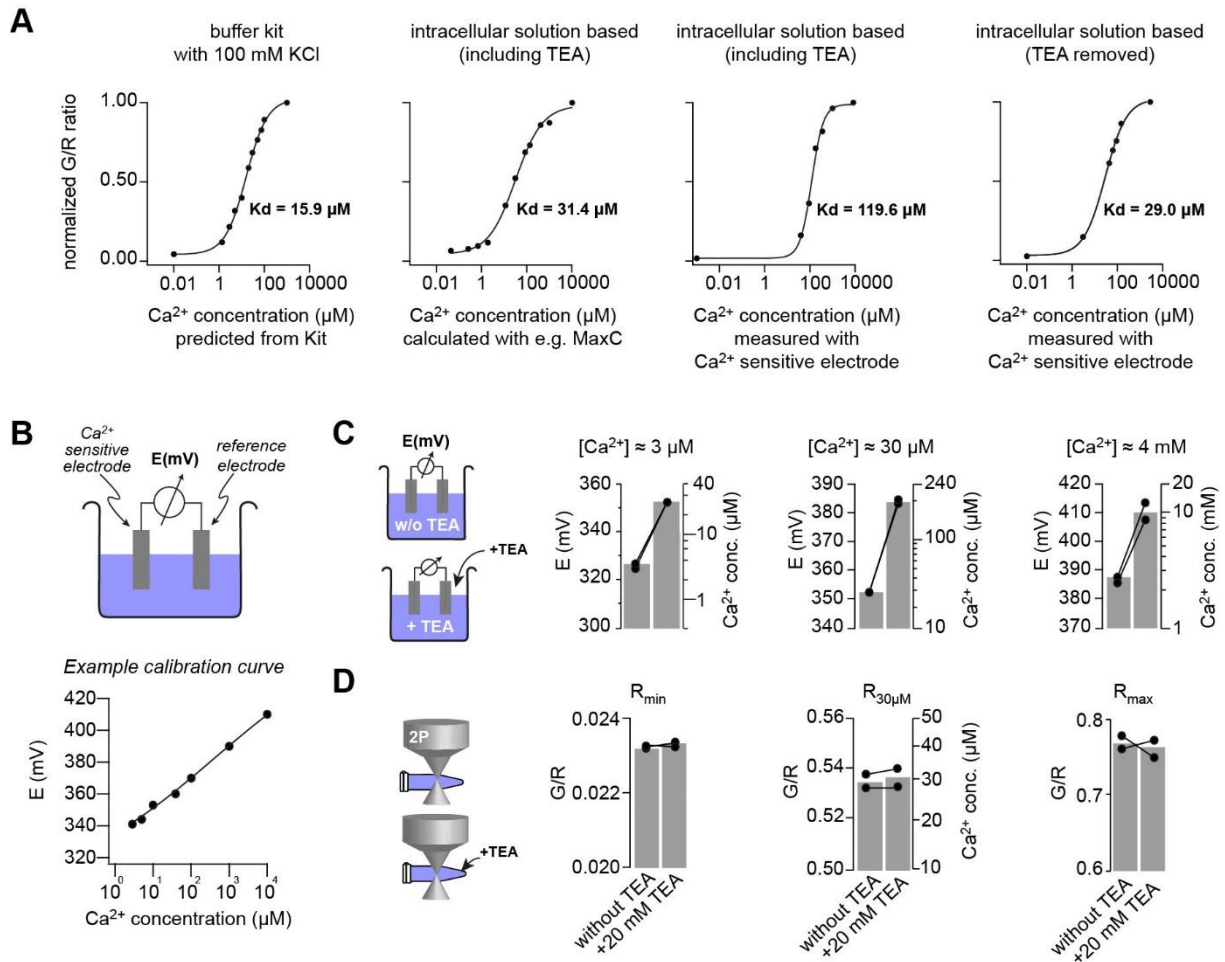(B) Magnification of the middle part in panel (A) over a range of 10 μm.

Figure 3 - figure supplement 1

Measuring the K_D of the Ca^{2+} sensitive dyes

(A) Green (OGB-5N) over red (Atto594) fluorescence ratio for different Ca^{2+} concentrations, measured using either a Ca^{2+} calibration buffered kit or by clamping the free Ca^{2+} using EGTA in the intracellular patching solution. The free Ca^{2+} concentration was predicted from the kit, calculated with software like Maxchelator (MaxC) or measured by potentiometry using a Ca^{2+}-sensitive electrode. The indicated K_D values were obtained from superimposed fits with Hill equations. (B) *Top:* illustration of the Ca^{2+}-sensitive electrode. *Bottom:* Example of a calibration curve of the Ca^{2+}-sensitive electrode fitted with a straight line. (C) Effect of Tetraethylammonium (TEA) on the Ca^{2+}-sensitive electrode at different Ca^{2+} concentrations. 20 mM TEA induced ~10-fold increase in the potential (left axis) and thus the read-out Ca^{2+} concentration (right axis) of intracellular solutions which had free Ca^{2+} concentrations clamped by EGTA to 3 μM, 30 μM, or 4 mM (pH was kept constant; bargraphs represent the mean; line-connected circles represent two independent repetitions). (D) Effect of TEA on G/R fluorescence ratio. The ratio of the intracellular solution containing only 10 mM EGTA (R$_{min}$), free Ca^{2+} clamped with EGTA to 30 μM (R$_{30μM}$), or 10 mM Ca^{2+} (R$_{max}$) did not change upon adding 20 mM TEA indicating that TEA is not contaminated with Ca^{2+} but instead TEA specifically interferes with the Ca^{2+}-sensitive electrode.
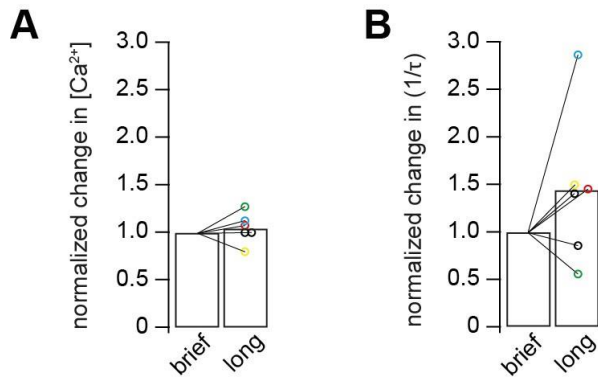
Figure 3 - figure supplement 2

Comparison of brief versus long UV illumination to rule out fast Ca^{2+} overshoots
(A) Post-flash Ca^{2+} concentration obtained from long flashes of 1 ms duration and 10% UV intensity, normalized to post-flash Ca^{2+} concentration obtained from brief flashes of 0.1 ms duration and 100% UV intensity. Two consecutive weak flashes (brief and long) were applied on each cell (n = 6 paired cells). (B) Release rates obtained from long flashes of 1 ms duration and 10% UV intensity, normalized to release rates obtained from brief flashes of 0.1 ms duration and 100% UV intensity. Color code matches the data in A and B. Two consecutive weak flashes (brief and long) were applied on each cell (n = 6 paired cells).

Figure 3 - figure supplement 3

Correction for the post-flash changes in the fluorescent properties of the intracellular solution
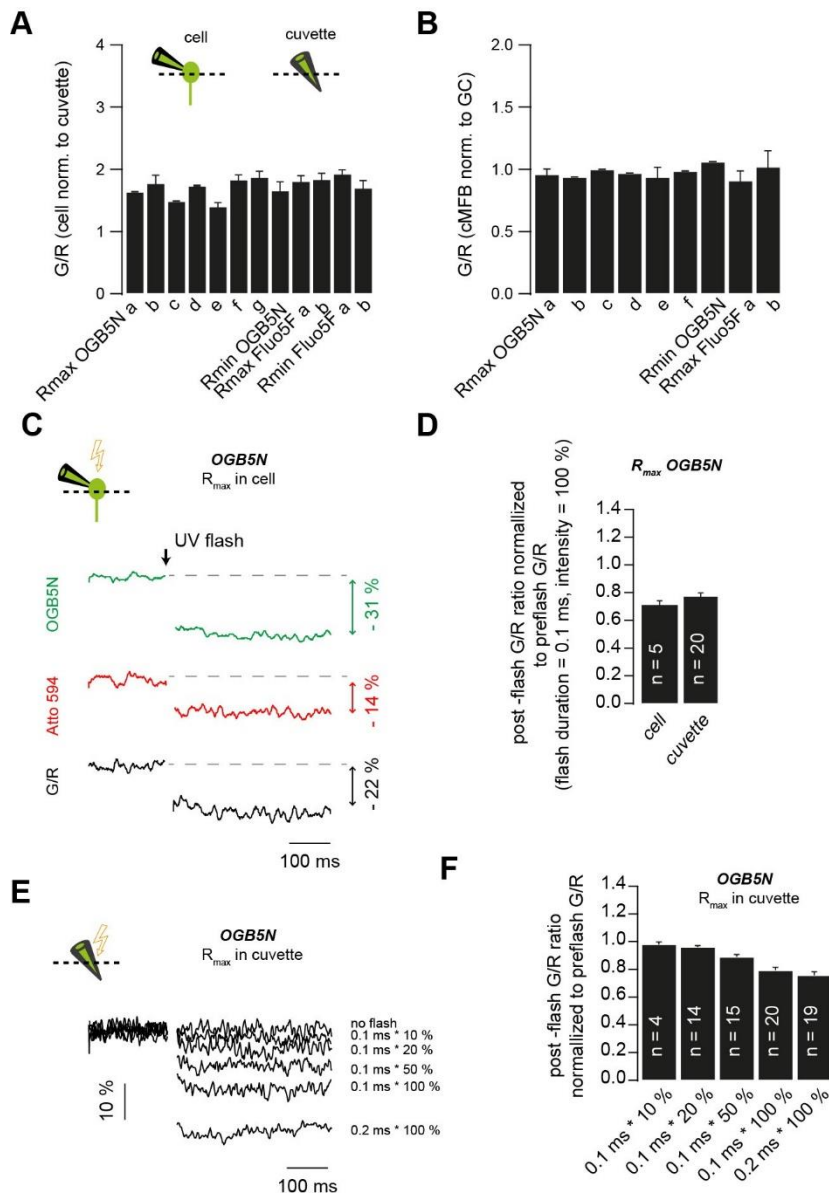(A) Green over red fluorescence (G/R) ratios measured in situ normalized to G/R ratios measured in cuvettes. Data represent the different solutions used throughout the study. (a–g) represent measurements obtained from different solutions prepared using different pre-stocks of the fluorescent indicators or a different DMn/Ca^{2+} concentration. (B) Green over red fluorescence (G/R) ratios measured in cMFBs normalized to G/R ratios measured in GCs. Data represent different solutions used throughout the study. (a–f) represent measurements obtained from different solutions prepared using different pre-stocks of the fluorescent indicators or a different DMn/Ca^{2+} concentration. (C) Example traces of in situ post-flash alterations in the green fluorescence, in the red fluorescence, and the overall drop in the G/R ratio (in black) in response to a UV flash of 0.1 ms duration and 100% intensity. (D) Comparison of the UV-flash-induced bleaching of fluorescent indicators measured in cells to the UV-flash-induced bleaching of fluorescent indicators measured in cuvettes, in response to a UV flash of 0.1 ms duration and 100% intensity. (E) Example traces of UV-flash-induced changes occurring in cuvettes in response to UV flashes of different intensities or duration. (F) Average UV-flash-induced changes occurring in cuvettes in response to UV flashes of different intensities or duration.

48
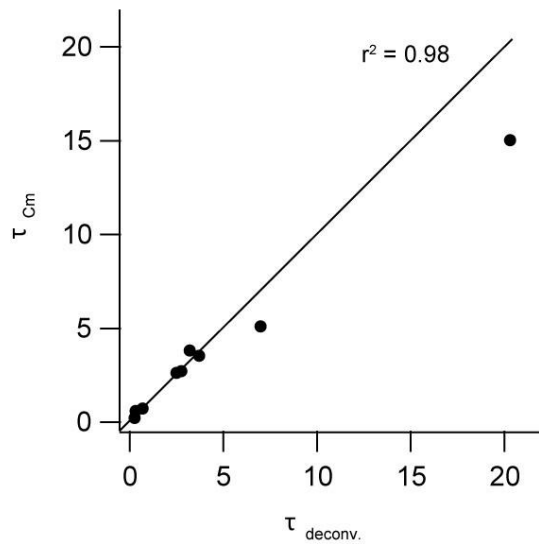
Figure 3 - figure supplement 4

Comparison of the time constants obtained from presynaptic capacitance measurements (τ_{Cm}) and analysis of postsynaptic current recordings (τ_{deconv})

The time constants were obtained from the initial fast component of exponential fits of the capacitance trace and the cumulative release trace obtained from the deconvolution analysis of the simultaneously recorded postsynaptic current. The line represents the identity relation ($r^2 = 0.98$; n = 9 paired cMFB-GC recordings).

3. Publication 2

Title: **Gradients in the mammalian cerebellar cortex enable Fourier-like transformation and improve storing capacity**

Journal: eLife

DOI: 10.7554/eLife.51771

Year: 2020

Authors: Isabelle Straub*****, Laurens Witter*****, Abdelmoneim Eshra*****, Miriam Hoidis*****, Niklas Byczkowicz, Sebastian Maas, Igor Delvendahl, Kevin Dorgans, Elise Savier, Ingo Bechmann, Martin Krueger, Philippe Isope, Stefan Hallermann

Pages: 51 - 86

(* indicates equal contribution)

Gradients in the mammalian cerebellar cortex enable Fourier-like transformation and improve storing capacity

Isabelle Straub[1†], Laurens Witter[1,2†], Abdelmoneim Eshra[1†], Miriam Hoidis[1†], Niklas Byczkowicz[1], Sebastian Maas[1], Igor Delvendahl[1‡], Kevin Dorgans[3§], Elise Savier[3#], Ingo Bechmann[4], Martin Krueger[4], Philippe Isope[3], Stefan Hallermann[1*]

[1]Carl-Ludwig-Institute for Physiology, Medical Faculty, Leipzig University, Leipzig, Germany; [2]Department of Integrative Neurophysiology, Center for Neurogenomics and Cognitive Research (CNCR), VU University, Amsterdam, Netherlands; [3]Institut des Neurosciences Cellulaires et Intégratives, CNRS, Université de Strasbourg, Strasbourg, France; [4]Institute of Anatomy, Medical Faculty, Leipzig University, Leipzig, Germany

*For correspondence:
stefan_jens.hallermann@uni-leipzig.de

[†]These authors contributed equally to this work

Present address: [‡]Institute of Molecular Life Sciences, University of Zurich, Zurich, Switzerland; [§]Okinawa Institute of Science and Technology, Graduate University, Okinawa, Japan; [#]Biology and Psychology Department, University of Virginia, Charlottesville, United States

Abstract Cerebellar granule cells (GCs) make up the majority of all neurons in the vertebrate brain, but heterogeneities among GCs and potential functional consequences are poorly understood. Here, we identified unexpected gradients in the biophysical properties of GCs in mice. GCs closer to the white matter (inner-zone GCs) had higher firing thresholds and could sustain firing with larger current inputs than GCs closer to the Purkinje cell layer (outer-zone GCs). Dynamic Clamp experiments showed that inner- and outer-zone GCs preferentially respond to high- and low-frequency mossy fiber inputs, respectively, enabling dispersion of the mossy fiber input into its frequency components as performed by a Fourier transformation. Furthermore, inner-zone GCs have faster axonal conduction velocity and elicit faster synaptic potentials in Purkinje cells. Neuronal network modeling revealed that these gradients improve spike-timing precision of Purkinje cells and decrease the number of GCs required to learn spike-sequences. Thus, our study uncovers biophysical gradients in the cerebellar cortex enabling a Fourier-like transformation of mossy fiber inputs.

Introduction

Digital audio compression (e.g. 'MP3'; *Jayant et al., 1993*) and image compression (e.g. 'JPEG'; *Wallace, 1992*) rely on Fourier transformations, which decompose a signal (e.g. sound amplitude as a function of time or image intensity as a function of space) into its frequency components (power as a function of frequency). By storing these frequency components with different precision depending on psychophysical demands of hearing and seeing, the overall storage capacity can be increased dramatically. In principle, neuronal networks consisting of neurons with varied electrophysiological properties could be suitable for Fourier-like transformations of information. This could benefit processing in neuronal circuits by increasing the signal-to-noise ratio of input signals or by selecting only relevant spectral components of a signal. Interestingly, there are indications that for example pyramidal neurons in the visual cortex and in the hippocampus are tuned to different inputs or different input strengths (*Cembrowski and Spruston, 2019*; *Fletcher and Williams, 2019*; *Soltesz and Losonczy, 2018*). However, whether these neuronal networks perform a Fourier-like transform of their inputs remains unknown.

eLife digest The timing of movements such as posture, balance and speech are coordinated by a region of the brain called the cerebellum. Although this part of the brain is small, it contains a huge number of tiny nerve cells known as granule cells. These cells make up more than half the nerve cells in the human brain. But why there are so many is not well understood.

The cerebellum receives signals from sensory organs, such as the ears and eyes, which are passed on as electrical pulses from nerve to nerve until they reach the granule cells. These electrical pulses can have very different repetition rates, ranging from one pulse to a thousand pulses per second. Previous studies have suggested that granule cells are a uniform population that can detect specific patterns within these electrical pulses. However, this would require granule cells to identify patterns in signals that have a range of different repetition rates, which is difficult for individual nerve cells to do.

To investigate if granule cells are indeed a uniform population, Straub, Witter, Eshra, Hoidis et al. measured the electrical properties of granule cells from the cerebellum of mice. This revealed that granule cells have different electrical properties depending on how deep they are within the cerebellum. These differences enabled the granule cells to detect sensory signals that had specific repetition rates: signals that contained lots of repeats per second were relayed by granule cells in the lower layers of the cerebellum, while signals that contained fewer repeats were relayed by granule cells in the outer layers.

This ability to separate signals based on their rate of repetition is similar to how digital audio files are compressed into an MP3. Computer simulations suggested that having granule cells that can detect specific rates of repetition improves the storage capacity of the brain.

These findings further our understanding of how the cerebellum works and the cellular mechanisms that underlie how humans learn and memorize the timing of movement. This mechanism of separating signals to improve storage capacity may apply to other regions of the brain, such as the hippocampus, where differences between nerve cells have also recently been reported.

Controlling the timing and precision of movements is considered to be one of the main functions of the cerebellum. In the cerebellum, the firing frequency of Purkinje cells (PCs) (*Heiney et al., 2014*; *Herzfeld et al., 2015*; *Hewitt et al., 2011*; *Medina and Lisberger, 2007*; *Payne et al., 2019*; *Sarnaik and Raman, 2018*; *Witter et al., 2013*) or the timing of spikes (*Brown and Raman, 2018*; *Sarnaik and Raman, 2018*) have been shown to be closely related to movement. Indeed, cerebellar pathology impairs precision in motor learning tasks (*Gibo et al., 2013*; *Martin et al., 1996*) and timing of rhythmic learning tasks (*Keele and Ivry, 1990*). These functions are executed by a remarkably simple neuronal network architecture. Inputs from mossy fibers (MFs) are processed by GCs and transmitted via their parallel fiber (PF) axons to PCs, which provide the sole output from the cerebellar cortex. GCs represent the first stage in cerebellar processing and have been proposed to provide pattern separation and conversion of the MF input into a sparser representation (recently reviewed by *Cayco-Gajic and Silver, 2019*). These MF inputs show a wide variety of signaling frequencies, ranging from slow modulating activity to kilohertz bursts of activity (*Arenz et al., 2008*; *Rancz et al., 2007*; *Ritzau-Jost et al., 2014*; *van Kan et al., 1993*). Interestingly, in most cellular models of the cerebellum, each MF is considered to be either active or inactive with little consideration for this wide range of frequencies (*Albus, 1971*; *Marr, 1969*). Furthermore, in these models, GCs are generally considered as a uniform population of neurons.

Here, we show that the biophysical properties of GCs differ according to their vertical position in the GC layer. GCs located close to the white matter (inner-zone) preferentially transmit high-frequency MF inputs, have shorter action potentials, and a higher voltage threshold to fire an action potential compared with GCs close to the PC layer (outer-zone). These gradients in properties of GCs enable a Fourier-like transformation of the MF input, where inner-zone GCs convey the high-frequency, and outer-zone GCs the low-frequency components of the MF input. The different Fourier-like components are sent to PCs by specialized downstream signaling pathways, which differ in PF axon diameters, action potential conduction velocity, and PC excitatory postsynaptic potential

(EPSP) kinetics. Computational simulations show that the biophysical gradients in the GC and molecular layer significantly reduce the number of GCs required to learn a sequence of firing frequencies and reduce the time needed to switch between firing frequencies.

Results

Gradients in the biophysical properties of inner- to outer-zone GCs

To investigate whether GCs are tuned for different frequencies, we first investigated the intrinsic membrane properties of GCs from different depths within the GC layer in lobule V of the cerebellum of P21-30 mice. We divided the GC layer into three zones and performed whole-cell current-clamp recordings from inner- (closest to the white matter), middle- and outer-zone GCs (closest to PCs) (*Figure 1A,B*). Upon current injection, inner-zone GCs were less excitable compared with outer-zone GCs (*Figure 1C*). On average, the relationship between the frequency of action potentials and the injected current was surprisingly different for inner- and outer-zone GCs (*Figure 1D*): inner-zone GCs needed higher current injections to fire an action potential (inner: 56.8 ± 2.6 pA vs. middle: 51.2 ± 2.0 pA vs. outer: 39.4 ± 2.0 pA; n = 38, 25, and 37, respectively; $P_{Kruskal-Wallis}$ <0.0001; *Figure 1E*) and to achieve the maximum firing rate compared with middle- and outer-zone GCs (inner: 224.6 ± 9.8 pA vs. middle: 190.8 ± 9.6 pA vs. outer: 174.3 ± 9.0 pA, respectively; $P_{Kruskal-Wallis}$ = 0.002; *Figure 1F*). Consistently, inner-zone GCs had a more depolarized threshold for action potential generation compared with middle- and outer-zone GCs (−38.0 ± 0.7 mV vs. −38.2 ± 0.8 mV vs. −41.4 ± 0.6 mV; $P_{Kruskal-Wallis}$ = 0.003; *Figure 1G*) and a lower input resistance (486 ± 27 MΩ vs. 494 ± 27 MΩ vs. 791 ± 63 MΩ; $P_{Kruskal-Wallis}$ = <0.0001; *Figure 1H*). Furthermore, the capacitance of inner-zone GCs was significantly larger compared with outer-zone GCs (inner: 5.8 ± 0.2 pF vs. middle: 5.8 ± 0.2 pF vs. outer: 4.6 ± 0.1 pF; $P_{Kruskal-Wallis}$ = <0.0001 *Figure 1I*). In agreement with these findings, we observed depolarization block in inner-zone GCs at higher current inputs than for outer-zone GCs (*Figure 1C,D*). Furthermore, a larger delay of the first spike was observed in inner- compared with outer-zone GCs (*Figure 1J*; $P_{Kruskal-Wallis}$ = 0.0001; *Figure 1K*). The delay with 60 pA current injection was 48 ± 6 ms for inner-, 38 ± 4 ms for middle-, and 23 ± 2 ms for outer-zone GCs (n = 32, 25, and 37, respectively; note that 6 out of 38 inner-zone GCs did not fire an action potential at 60 pA). Finally, the action potential half-width of GCs differed significantly between the three zones (inner: 122 ± 2 μs vs. middle: 137 ± 4 μs vs. outer: 143 ± 4 μs; $P_{Kruskal-Wallis}$ = 0.0001; *Figure 1L*). The distribution of the raw data (*Figure 1—figure supplement 1*) suggests a gradual change in the average cell parameters along the depth axis of the GC layer, but two populations of neurons (*salt and pepper* distribution), or three populations of neurons (inner-, middle-, and outer-zone) cannot fully be ruled out.

To test whether these gradients are specific to lobule V, we investigated GCs in lobule IX. Here, we observed very similar gradients to lobule V (*Figure 1—figure supplement 2*). In short, outer-zone GCs were more excitable and had broader spikes compared with inner-zone GCs. Interestingly, the absolute values between lobule V and IX differed (*Figure 1—figure supplement 2*), consistent with previously described differences in, for example the firing frequency in vivo between these two lobules (*Witter and De Zeeuw, 2015a*; *Zhou et al., 2014*) and in the differential density of K_v4 and Ca_v3 channel expression in GCs across different lobules (*Heath et al., 2014*; *Rizwan et al., 2016*; *Serôdio and Rudy, 1998*). Taking the large functional difference between spino- and vestibulo-cerebellum into account (*Witter and De Zeeuw, 2015b*), these data suggest that different biophysical properties of GCs are likely a conserved mechanism throughout the entire cerebellar cortex, potentially tuning GCs to different frequencies.

Development can have large effects on the physiology of neurons, and GCs in particular undergo profound changes during development (*Dhar et al., 2018*; *Lackey et al., 2018*). To exclude confounding effects of the developmental stage, we tested whether these gradients were also present in more adult mice. Recordings obtained from GCs in lobule V in animals between 80 and 100 days of age revealed very similar gradients to those observed in young animals (*Figure 1—figure supplement 3*). Together, these data show prominent gradients in the electrophysiological properties of GCs over the depth of the GC layer, and that these gradients can consistently be found across different lobules and ages.
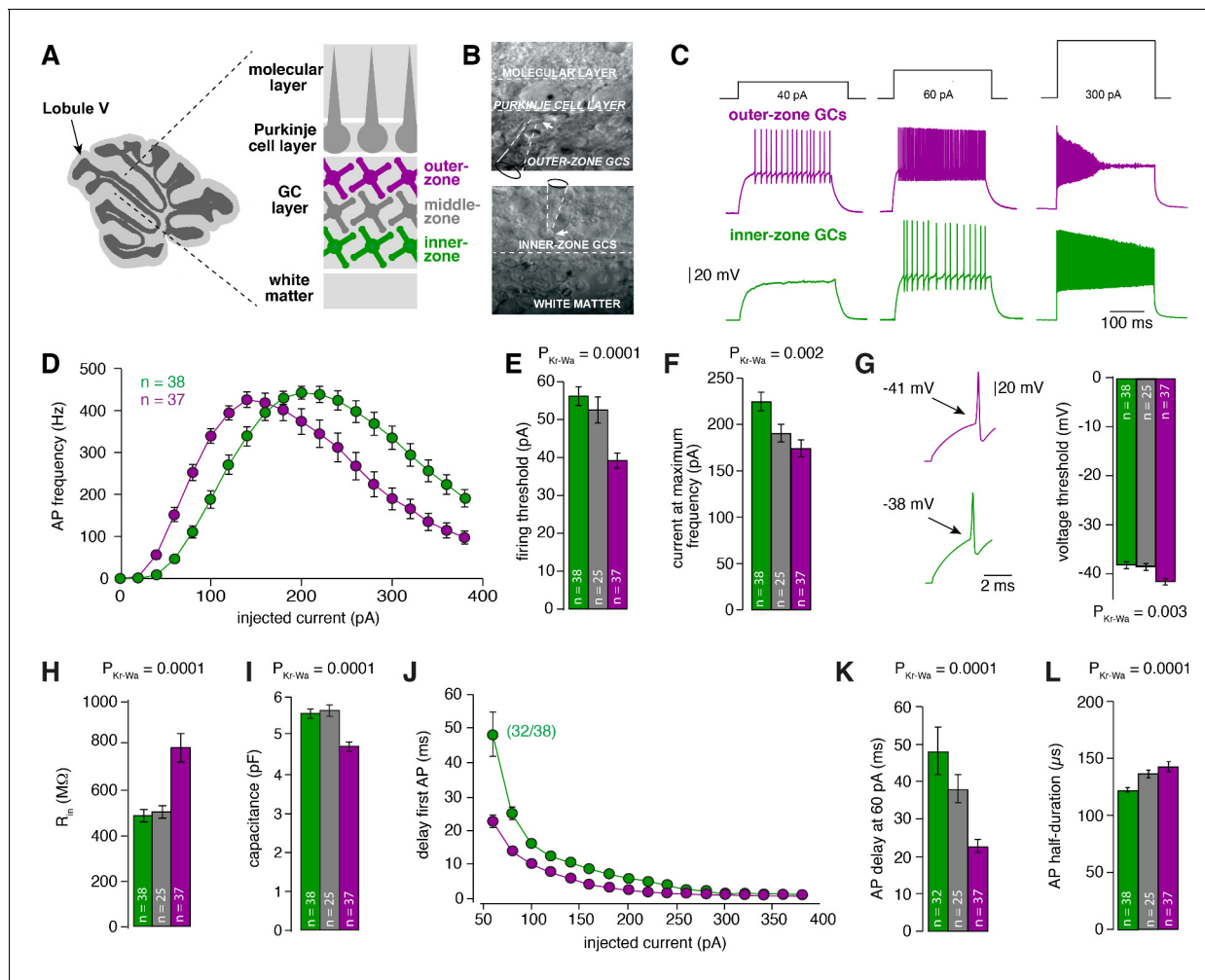
Figure 1. Gradients in the biophysical properties of inner- to outer-zone GCs. (**A**) Scheme of a parasagittal slice from the cerebellar cortex where lobule V is indicated by an arrow. Enlargement shows a schematic representation of the white matter, the GC, PC and molecular layer of the cerebellar cortex. Throughout the manuscript, inner-zone GCs (close to the white matter) are depicted in green, the middle-zone GCs in gray, and the outer-zone GC (close to the PCs) in magenta. (**B**) Example differential-interference-contrast (DIC) microscopic images of acute cerebellar slices during recordings from outer- (top) and an inner-zone GCs (bottom). The pipette is indicated with a dashed line. (**C**) Example current-clamp recordings from an outer-zone GC (magenta, top) and an inner-zone GC (green, bottom) after injection of increasing currents (40 pA, 60 pA and 300 pA). (**D**) Average action potential frequency from inner- (green, n = 38) and outer- (magenta, n = 37) zone GCs plotted against the injected current. Note that the maximum frequency is similar but outer-zone GCs achieved the maximum firing rate with a lower current injection (error bars represent SEM). (**E**) Average current threshold for action potential firing of inner-, middle- and outer-zone GCs ($P_{Dunns} = 0.0001$ for inner- vs outer-zone GCs). All bar graphs represent mean and SEM. (**F**) Average current needed to elicit maximum firing frequency for inner-, middle- and outer-zone GCs ($P_{Dunns} = 0.001$ for inner- vs outer-zone GCs). (**G**) Left: example action potentials from an inner- and outer-zone GC with the indicated (arrows) mean voltage-threshold for firing action potentials. Right: Comparison of the average voltage threshold for action potential firing ($P_{Dunns} = 0.006$ for inner- vs outer-zone GCs). (**H**) Average input resistance of inner-, middle- and outer-zone GCs ($P_{Dunns} = 0.0001$ for inner- vs outer-zone GCs). (**I**) Average capacitance of inner-, middle- and outer-zone GCs ($P_{Dunns} = 0.0001$ for inner- vs outer-zone GCs). (**J**) Delay time of the first action potential plotted against injected current. Note that only 32 of 38 inner-zone GCs fired action potentials at a current injection of 60 pA. (**K**) Delay of the first action potential of inner-, middle- and outer-zone GCs at a current injection of 60 pA ($P_{Dunns} = 0.0001$ for inner- vs outer-zone GCs). (**L**) Average action potential half-duration of inner-, middle- and outer-zone GCs ($P_{Dunns} = 0.0001$ for inner- vs outer-zone GCs).

The online version of this article includes the following figure supplement(s) for figure 1:

Figure supplement 1. Raw data of the bar graphs from *Figure 1*.
Figure supplement 2. Gradients in the biophysical properties of GCs and PFs are preserved throughout the cerebellar cortex.
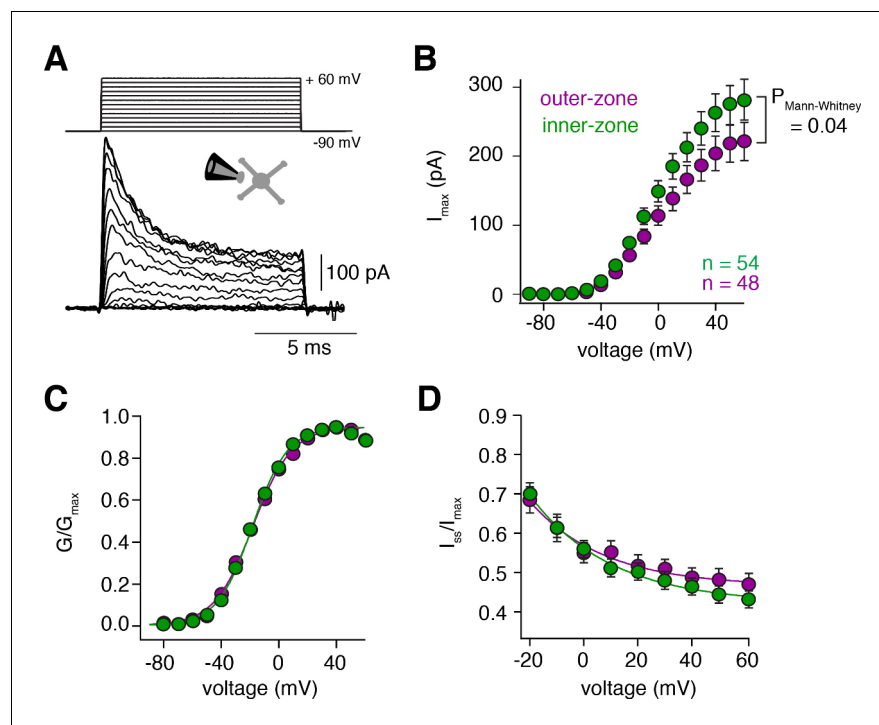**Figure supplement 3.** Gradients in the biophysical properties of GCs and PFs are also found in 3-month-old animals.

54

Figure 2. Voltage-gated potassium currents are larger at inner-zone GCs. (**A**) Example potassium currents from outside-out patches of cerebellar GCs evoked by voltage steps from −90 to +60 mV in 10 mV increments with a duration of 10 ms. All recordings were made in the presence of 1 µM TTX and 150 µM CdCl$_2$ to block voltage-gated sodium and calcium channels, respectively. (**B**) Average peak potassium current (I$_{max}$) plotted versus step potential of inner (green) and outer-zone (magenta) GCs. Significance level was tested with a Mann-Whitney *U* Test for the value at +60 mV and the p value is indicated in the figure. (**C**) Average normalized peak potassium conductance (G/G$_{max}$) versus step potential of inner (green) and outer-zone (magenta) GCs. (**D**) Average steady-state current (I$_{ss}$, mean current of the last 2 ms of the 10 ms depolarization) normalized to the peak current (I$_{max}$) versus step potential of inner (green) and outer-zone GCs (magenta).

The online version of this article includes the following figure supplement(s) for figure 2:

Figure supplement 1. Raw data of the amplitude of potassium currents at 60 pA current injection.
Figure supplement 2. Steady-state activation and inactivation are similar for inner and outer GCs.

Voltage-gated potassium currents are larger at inner-zone GCs

To investigate possible biophysical causes for the gradients in the biophysical properties, we investigated voltage-gated potassium (K$_v$) currents by performing voltage-clamp recordings in outside-out patches from somata of inner- and outer-zone GCs in lobule V (*Figure 2A*). The maximum K$_v$ current at -60 mV was significantly higher in inner-zone GCs (282 ± 29 pA, n = 48) compared with outer-zone GCs (221 ± 28 pA, n = 54, P$_{Mann-Whitney}$ = 0.04; *Figure 2B*; *Figure 2—figure supplement 1*). Neither the steady-state activation curve (*Figure 2C*) nor the degree of inactivation (*Figure 2D*) was different between the two GC populations. Furthermore, steady-state inactivation, which was investigated with different holding potentials, was similar between inner- and outer-zone GCs (*Figure 2—figure supplement 2*). These data suggest that inner- and outer-zone GCs have a similar composition of K$_v$ channels, but inner-zone GCs have a higher K$_v$ channel density. The larger K$_v$ currents in inner-zone GCs are consistent with the short action potential duration of inner-zone GCs (cf. *Figure 1*). Thus, our data provide a biophysical explanation for the observed gradients in GC properties.

MF inputs are differentially processed by inner- and outer-zone GCs

The gradients within the GC layer create an optimal range of input strengths for each GC. To test how these gradients impact the processing of synaptic MF inputs, we performed Dynamic Clamp experiments (*Desai et al., 2017*) and investigated whether different MF input frequencies
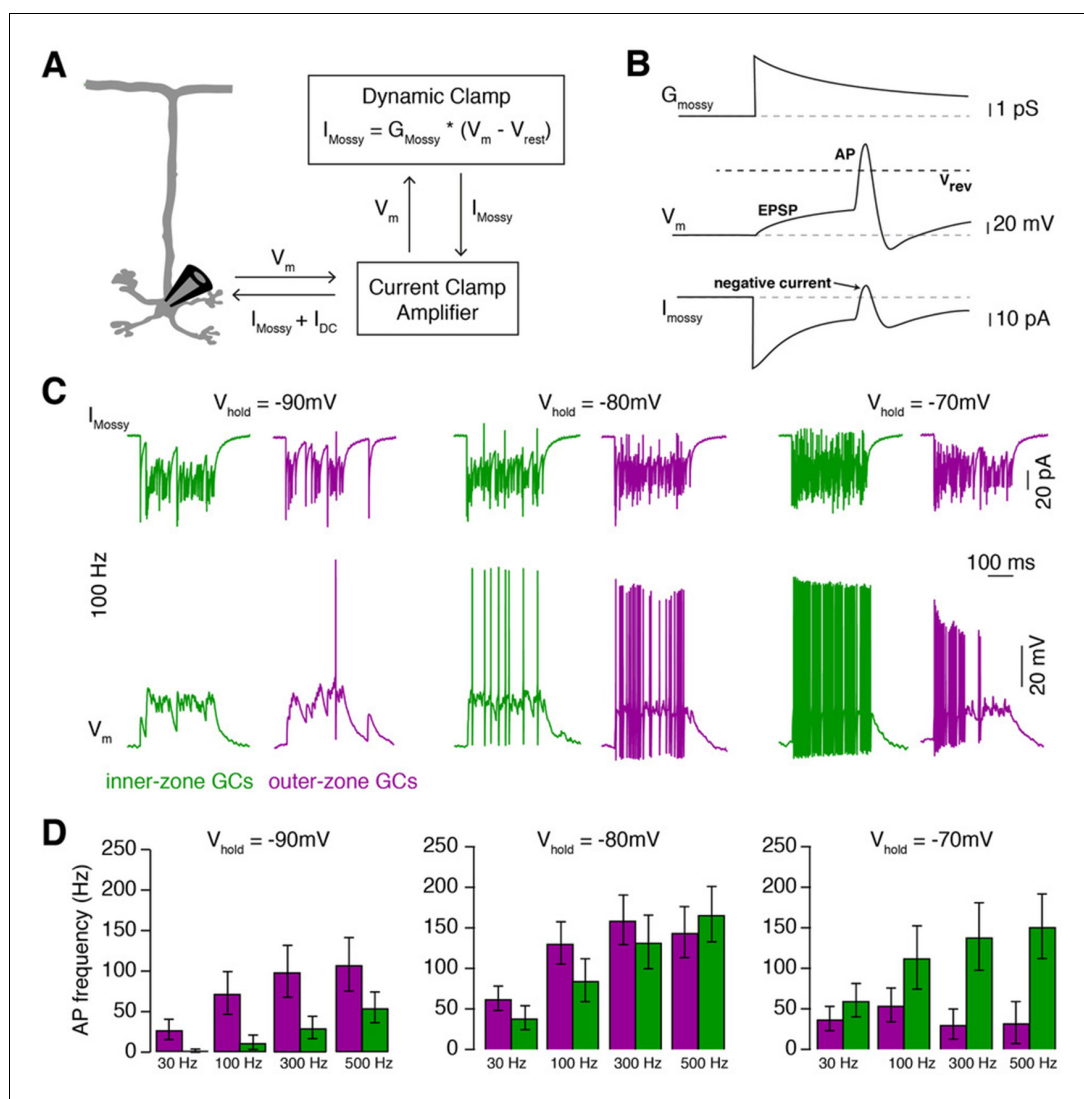
Figure 3. MF inputs are differentially processed by inner- and outer-zone GCs. (A) Schematic representation of the Dynamic Clamp system. (B) Illustration of MF conductance (G_{mossy}), GC membrane potential (V_m), and MF current (I_{mossy}) for the Dynamic Clamp technique. Note the prediction of a negative current during an action potential as apparent in the experimental traces in panel C. (C) Example Dynamic Clamp recordings of inner- (green) and outer-zone (magenta) GCs at different holding potentials (−90 mV left; −80 mV middle and −70 mV right) at a stimulation frequency of 100 Hz. Upper traces represent poisson-distributed MF currents. Lower traces show the measured corresponding membrane potential with EPSPs and action potentials. (D) Average firing frequency of inner- and outer-zone GCs during MF- like inputs at different frequencies and at the indicated holding potentials. The online version of this article includes the following figure supplement(s) for figure 3:

Figure supplement 1. MF input is similar for inner- and outer-zone GCs.
Figure supplement 2. Raw data of the bar graphs from *Figure 3*. Same data as in *Figure 3D*, but shown as box plots (median and interquartile range with whiskers) superimposed with single data points.

differentially affect spiking in inner- and outer-zone GCs (*Figure 3A and B*). We first recorded excitatory postsynaptic currents (EPSC) from GCs in inner- and outer-zones of lobule V after single MF stimulation. We found no significant differences in the amplitude or kinetics of EPSCs in inner- and outer-zone GCs (*Figure 3—figure supplement 1*).

Individual MFs span the entire depth of the GC layer, contacting both inner- and outer-zone GCs (*Krieger et al., 1985*; *Palay and Chan-Palay, 1974*). Furthermore, GCs are electronically extremely compact neurons and can be considered as a single compartment (*D'Angelo et al., 1993*;

56

Therefore, we could use the Dynamic Clamp technique to implement the conductance of identical MF signals in inner- and outer-zone GCs based on the measured EPSC kinetics. We first applied input of a single MF with Poisson-distributed firing-frequencies ranging between 30 and 500 Hz for 300 ms duration while changing the resting membrane potential to simulate the large variability of membrane potential observed in GCs in vivo (*Chadderton et al., 2004*). In line with the gradients in the electrophysiological properties of GCs, inner-zone GCs fired fewer action potentials compared with outer-zone GCs in response to low-frequency MF inputs at a membrane potential of approximately –90 mV (*Figure 3C and D*; *Figure 3— figure supplement 2*). In contrast, inner-zone GCs fired more action potentials compared with outer-zone GCs in response to high-frequency MF inputs at a membrane potential of approximately –70 mV. In vivo, such a depolarization would be caused by reduced inhibition and/or simultaneous activation of multiple MF inputs. These data suggest that outer- and inner-zone GCs are specialized to process low- and high-frequency MF inputs, respectively.

Fourier-like transformation of MF input frequency

To further test whether inner- and outer-zone GCs can extract different frequency components from a MF input signal, which would resemble a Fourier-transformation, we varied the MF input frequency sinusoidally between 30 and 300 Hz, representing a range of in-vivo-like tonic firing behaviour (*Figure 4A*; *Arenz et al., 2008*; *van Kan et al., 1993*). At a holding potential of -70 mV, commonly occurring in vivo (*Chadderton et al., 2004*), inner-zone GCs responded preferentially to high-frequency MF inputs up to 300 Hz, while outer-zone GCs responded preferentially to low-frequency inputs up to 100 Hz (*Figure 4B*; *Figure 4—figure supplement 1*). To estimate the optimal frequency at which inner- and outer-zone GCs preferentially fire action potentials, we calculated the phase angle (see Materials and methods, *Equation 3*). The mean phase angle, at which GC preferentially fired, was $162 \pm 8°$ for inner-zone (n = 10) and $100 \pm 20°$ for outer-zone GCs (n = 7; $P_{Mann-Whitney} = 0.02$; *Figure 4C*), representing an average firing frequency of 284 and 116 Hz for inner- and outer-zone GCs, respectively (cf. *Equation 2*). Thus, the gradients in the biophysical properties enable the cerebellar GC layer to split incoming MF signals into different frequency bands and thereby to perform a Fourier-like transformation of the compound MF input signal.

The position of PFs is correlated with the position of GC somata

A Fourier-like transformation in the GC layer (i.e. a separation of the spectral components of MF signals) could be particularly relevant if downstream pathways are specialized for these spectral components. Early silver-stainings and drawings from Ramón y Cajal indicate that inner-zone GCs give rise to PFs close to the PC layer and outer-zone GCs give rise to PFs close to the pia (*Eccles et al., 1967*; *Cajal, 1911* but see *Espinosa and Luo, 2008*; *Wilms and Häusser, 2015*). To test this possibility, we examined the axons of GCs. First, we investigated whether there is a correlation between the relative positions of the PF in the molecular layer and the GC somata in the GC layer. DiI was injected in vivo into the GC layer to label GCs and their axons. Several GCs were clearly stained 24 hr after DiI injection (*Figure 5A*), and the position of their soma and PF in the cerebellar cortex could be measured (*Figure 5B–D*). Even though the length of the ascending GC axon showed considerable variation (196 ± 5.5 μm, range: 144 to 291 μm, n = 39 axons in n = 6 mice), after normalization for the thickness of the molecular and GC layers, the GC soma position was significantly correlated with the position of the bifurcation in the GC axon (*Figure 5C,D*; R = –0.86, p<0.001). These data show that inner-zone GCs preferentially give rise to PF located near the PC layer (inner-zone PFs) and outer-zone GC give rise to PF near the surface of the cerebellar cortex (outer-zone PFs).

Inner-zone PFs have larger diameter and higher action potential conduction velocity

Next, we tested whether PFs, like GCs, have different properties depending on their position within the molecular layer. First, we compared the PF diameters in electron microscopic images of parasagittal sections of lobule V of mouse cerebellum and found significantly larger diameters for inner-zone PFs compared with middle- and outer-zone PFs (182 ± 2.6 nm, n = 703 vs. 159 ± 2.0 nm, n = 819 vs. 145 ± 1.7 nm, n = 1024 *Figure 6A–C*; $P_{Kruskal-Wallis} < 0.0001$), which is in agreement with

previous investigations reported in cat (*Eccles et al., 1967*), monkey (*Fox and Barnard, 1957*), rat (*Pichitpornchai et al., 1994*), and mouse (*Wyatt et al., 2005*).

The axonal diameter is usually correlated with conduction velocity (*Jack et al., 1983*). We therefore recorded compound action potentials of PFs in lobule V and compared their conduction velocity in the inner-, middle-, and outer-zone of the molecular layer (*Figure 6D–F*). We detected a significantly higher velocity in inner-zone PFs compared with middle- or outer-zone PFs (0.334 ± 0.003 m*s^{-1}, n = 8 vs. 0.303 ± 0.004 m*s^{-1}, n = 6 vs. 0.287 ± 0.007 m*s^{-1}, n = 8; *Figure 6F*; P$_{Kruskal-Wallis}$ <0.0001). The absolute velocity and the gradient in the velocity from inner- to outer-zone PFs agree well with previous studies (*Baginskas et al., 2009*; *Vranesic et al., 1994*). These results suggest that inner-zone PFs are specialized for fast signaling, which is consistent with the concept that inner-zone GCs are tuned for high-frequency inputs (cf. *Figures 1* and *2*).

In addition to the above results obtained from lobule V, similar gradients in both axon diameter and axon conduction velocity were found in lobule IX (*Figure 6—figure supplement 1*). This suggests that gradients in axon diameter and axon conduction speed are general features of the cerebellar cortex.

A possible confounder of our results could be an over-representation of large-diameter Lugaro cell axons within inner-zone PFs (*Dieudonné and Dumoulin, 2000*). However, this would predict that the histograms of the axon diameters show two peaks with varying amplitude. Instead, we observed a single bell-shaped distribution in each zone (*Figure 6—figure supplement 2*), arguing that the
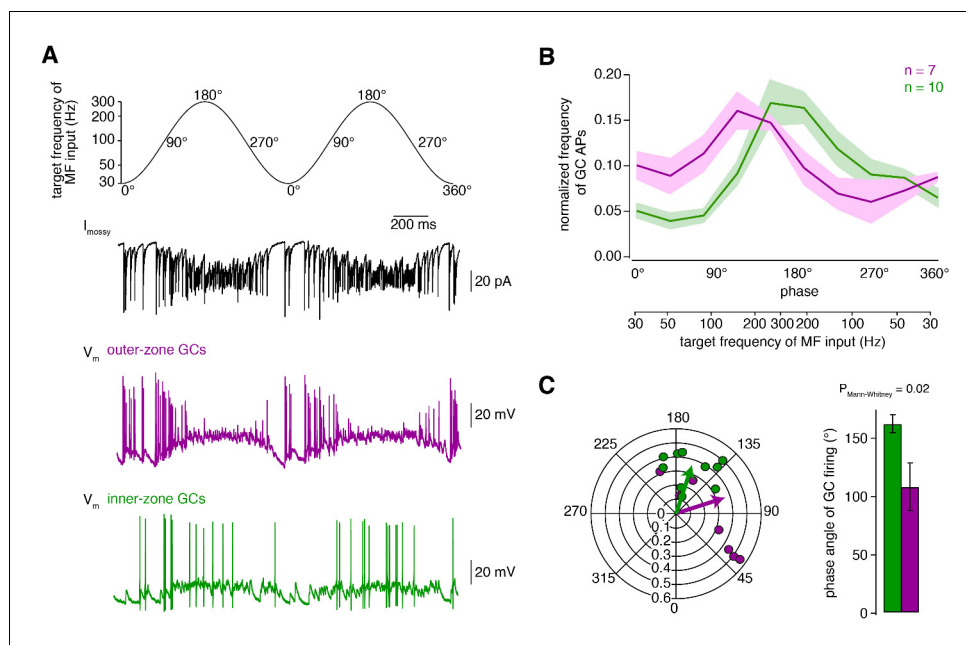
Figure 4. Fourier-like transformation of MF input frequency. (**A**) Target frequency of the Dynamic Clamp MF-like inputs during two cycles. The frequencies varied sinusoidally on a logarithmic scale between 30 to 300 Hz and the cycle duration was 1 s (*Equation 2*). The degree values denote the phase angle. *Black:* example trace of poisson-distributed MF-like inputs. *Magenta and green:* example membrane potential during Dynamic Clamp experiments of an outer- and an inner-zone GC, respectively, at a holding potential of approximately −70 mV. (**B**) Average normalized frequency of action potentials (APs) fired by inner- and outer-zone GCs (green and magenta, respectively) versus the phase angle and the target MF-like frequency within one cycle (for each cell, the integral of the spike histogram was normalized to 1; see *Figure 4—figure supplement 1* for absolute frequency). The light green and magenta areas represent the SEM. (**C**) Polar plot of phase angle and vector strength of the preferred firing frequency according to *Equation 3* from inner- (green) and outer-zone (magenta) GCs (*dots:* single cells; *arrows:* average). Bar graph of the average phase angle at which inner- and outer-zone GCs preferentially fired action potentials.

The online version of this article includes the following figure supplement(s) for figure 4:

Figure supplement 1. Raw data of the traces shown in *Figure 4B*.

Figure 5. The position of PFs is correlated with the position of GC somata. (**A**) Example of GCs labeled with DiI 24 hr post injection. Numerous GCs from inner-, middle-, and outer-zone were labeled. (**B**) Exa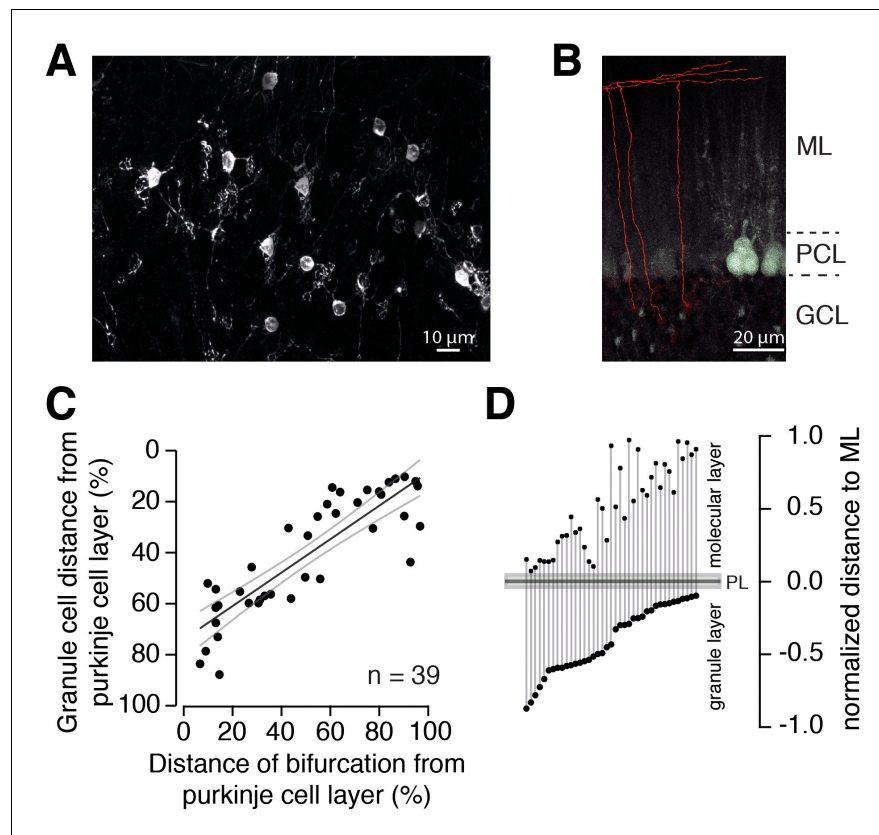mple of traced axons from different GCs from the outer zone. The axon was traced (red) from the cell soma to the bifurcation site in the molecular layer. Stained cell bodies of GCs are also visible (white). *ML:* molecular layer; *PCL:* Purkinje cell layer; *GCL:* granule cell layer. (**C**) The distance between labeled GCs and the PC layer strongly correlated with the distance between the axon bifurcation and the PC layer (Pearson's correlation coefficient R = –0.86; p<0.001). Solid black line depicts the linear interpolation and the gray lines represent SEM of the fit. The number of GCs (n) is indicated. (**D**) Position of the GC somata within the GC layer of each traced cell linked to the position of the bifurcation site in the molecular layer. The distances were normalized to the height of the corresponding layers.

measured differences between axon diameters were not due to varying contributions from Lugaro cell axons, but reflect the differences between inner-, middle-, and outer-zone PFs.

PCs process inner-, middle-, and outer-zone PF inputs differentially

Our data thus far indicate that GCs and PFs are adapted to different MF input frequencies and conduction velocities, respectively. This arrangement could in principle provide PFs with functionally segregated information streams that are differentially processed in PCs. To investigate this possibility, we made whole-cell current-clamp recordings from PCs in sagittal slices of the cerebellar vermis. PCs were held at a hyperpolarized voltage to prevent spiking and to isolate excitatory inputs. Electrical stimulation of PFs was performed at inner-, middle-, and outer-zones of the molecular layer and the stimulation intensity was adjusted to obtain similar EPSP amplitudes in all zones (*Figure 7A,B*). Stimulation of inner-zone PFs resulted in EPSPs (*Barbour, 1993*; *Roth and Häusser, 2001*) with shorter rise and decay times compared with EPSPs obtained from stimulating outer-zone PFs (rise$_{20-80}$: inner: 0.57 ± 0.04 ms, n = 12; middle: 0.93 ± 0.17 ms, n = 4; outer: 1.83 ± 0.33 ms, n = 12; $P_{Kruskal-Wallis}$ = 0.0001; decay: inner: 21.9 ± 1.5 ms, middle: 39.7 ± 1.1 ms outer: 40.8 ± 4.1 ms; $P_{Kruskal-Wallis}$ = 0.0004, *Figure 7C*; *Figure 7—figure supplement 1*). These results suggest that inner-zone PF inputs undergo less dendritic filtering in PCs compared with outer-zone PF inputs (*De Schutter and Bower, 1994a*; *Roth and Häusser, 2001* but see *De Schutter and Bower, 1994b*). To investigate high-frequency inputs to PCs, we elicited five EPSPs at 100 Hz and 500 Hz (*Figure 7D,E*).
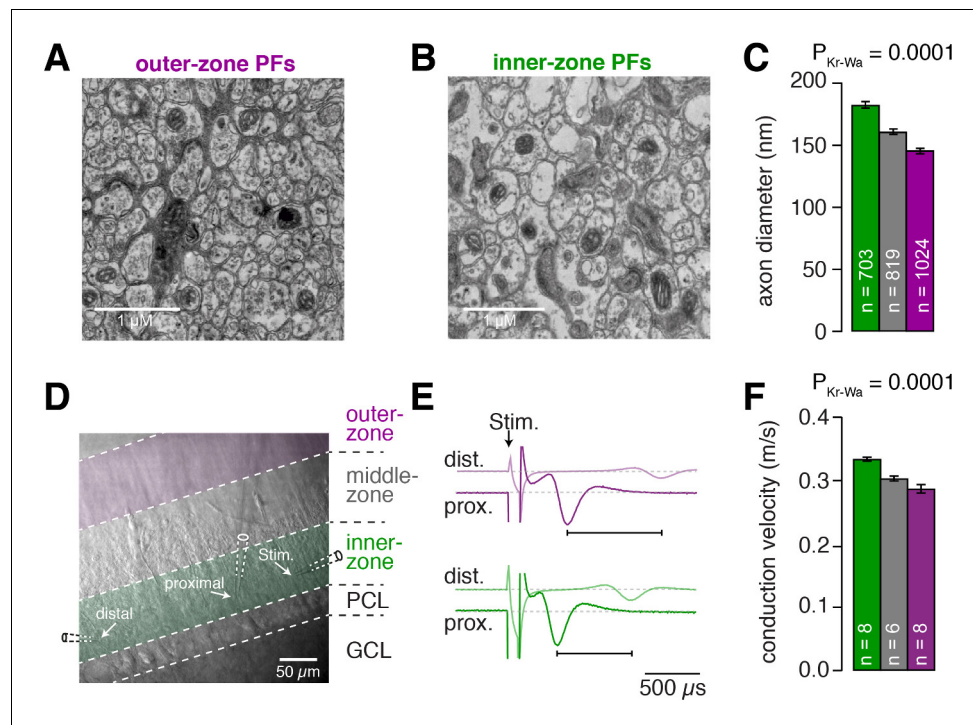
Figure 6. Inner-zone PFs have larger diameter and higher action potential conduction velocity. (A) Electron microscopic image of the outer (A) and inner zone (B) of sagittal sections through the molecular layer. (C) Summary of axon diameters in the inner- (green), middle- (gray), and outer-zone (magenta) of the molecular layer (P_{Dunns} = 0.0001 for inner- vs outer-zone GCs). (D) DIC image of the molecular layer superimposed with a schematic illustration of the experimental setup to measure compound action potentials from PFs. Compound action potentials were evoked by a stimulus electrode (right) and recorded by a proximal and distal recording electrode (middle, left). (E) Example traces used to determine the conduction velocity of inner- and outer-zone PFs. The time difference between the compound action potential arriving at the proximal electrode (solid traces) and the distal electrode (light traces) was used to determine the velocity. The time was shorter for inner-zone PFs (green) compared with outer-zone PFs (magenta). (F) Summary of conduction velocity in inner-, middle- and outer-zones (P_{Dunns} = 0.0007 for inner- vs outer-zone GCs).
The online version of this article includes the following figure supplement(s) for figure 6:

Figure supplement 1. Differences in axon diameter and conduction velocity are also found in lobule IX.
Figure supplement 2. Histogram of the axon diameters.

Individual EPSPs evoked from inner-zone PFs showed clear individual rising phases and peaks between each stimulus and less summation compared with outer-zone PFs (*Figure 7D–F*; *Figure 7— figure supplement 1*). These results suggest that inner-zone PFs can transmit timing information more faithfully compared with outer-zone PFs and thus control spike timing of PCs more precisely.

The observed neuronal gradients increase storing capacity and improve temporal precision of PC spiking

Thus far we have described prominent gradients in the electrophysiological properties of GCs over the depth of the GC layer that enable inner- and outer-zone GCs to preferentially respond to high- and low-frequency inputs, respectively. The different frequency components are transferred via specialized PFs, which enable PCs to interpret high-frequency signals rapidly at the base of their dendritic trees and low-frequency signals slowly at more distal parts of their dendritic trees (*Figure 8A*).

To address the functional implications of these gradients in the GC and molecular layer, we performed computational modeling of a neuronal network of the cerebellar cortex with integrate-and-fire neurons. The model consisted of one PC and a varying number of GCs and MFs (*Figure 8A*). GCs received randomly determined MF inputs with either tonic (*Arenz et al., 2008*; *van Kan et al., 1993*) or bursting (*Rancz et al., 2007*) in-vivo-like spiking sequences. MF inputs were randomly
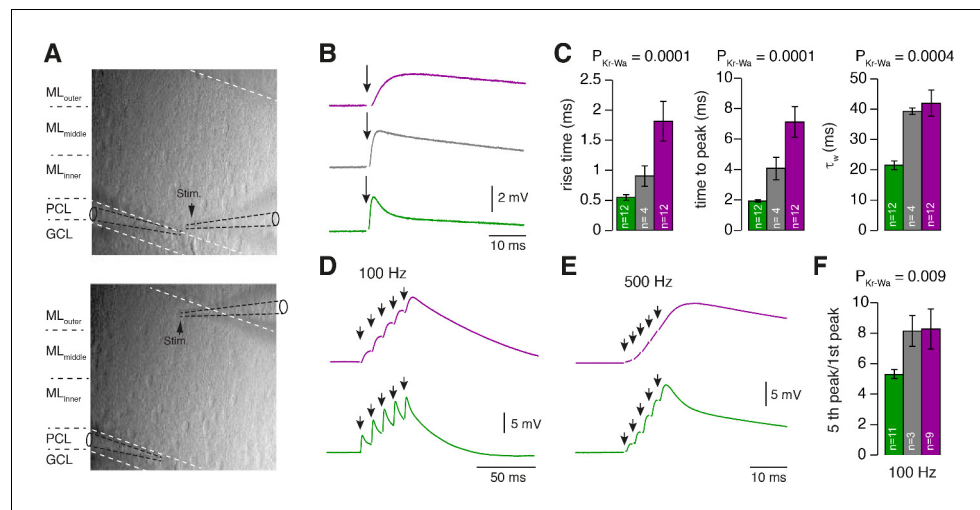
Figure 7. PCs differentially process inner-, middle-, and outer-zone PF inputs. (**A**) DIC image of the molecular layer superimposed with a schematic illustration of PC recordings while stimulating inner- (top) and outer-zone PFs (bottom). Shown are the GC layer (GCL), PC layer (PCL) and molecular layer (ML). (**B**) EPSPs measured at the PC soma after stimulation (1 Hz) of inner- (green), middle- (gray), and outer-zone PFs (magenta). (**C**) Average 20% to 80% rise time, time to peak and weighted decay time-constant of PC EPSPs after stimulation of inner- (green; n = 12), middle- (gray; n = 4) and outer-zone PFs (magenta; n = 12) as shown in B (P_{Dunns} = 0.0001; P_{Dunns} = 0.0001; P_{Dunns} = 0.0009 for inner- vs outer-zone GCs, respectively). Note, one cell out of 12 had a monoexponentiell decay. (**D-E**) Example traces of EPSPs from a PC after five impulses to inner- (green) and outer-zone PFs (magenta) at 100 Hz (**D**) and 500 Hz (**E**). (**F**) Average paired-pulse ratio measured in PCs after five 100 Hz stimuli at inner- (green; n = 11), middle- (gray, n = 3) and outer- zone PFs (magenta, n = 8; P_{Dunns} = 0.04 for inner- vs outer-zone GCs).

The online version of this article includes the following figure supplement(s) for figure 7:

Figure supplement 1. Raw data of the bar graphs from *Figure 7*.

distributed across layers, consistent with MFs having rosettes throughout the depth of the granule cell layer (*Krieger et al., 1985*; *Palay and Chan-Palay, 1974*). By changing the synaptic weights of the GC to PC synapses, the PC had to acquire a target spiking sequence with regular 80-, 40- and 120 Hz firing (*Figure 8B*). The algorithm for changing the synaptic weights was a combination of a learning algorithm based on climbing-fiber-like punishments and an unbiased minimization algorithm (see Materials and methods).

We first compared a model without gradients, where the parameters were set at the average of the experimentally determined values, with a model including all experimentally determined gradients (black and red, respectively, throughout *Figure 8*). To measure the difference between the final PC spiking and the target sequence, we calculated van Rossum errors using a time constant of 30 ms (*van Rossum, 2001*; *Figure 8C–E*). With an increasing number of GCs, the final PC spiking sequence resembled the target sequences increasingly better, as illustrated by an average spiking histogram from many repetitions with different random sets of MF inputs for models consisting of 100 and 1000 GCs (*Figure 8B*). As expected, the average minimal van Rossum error (for many repetitions with different random sets of MF inputs) decreased with increasing number of GCs (*Figure 8C*). For all sizes of the GC population, the average minimal van Rossum error was significantly smaller in the model containing all the experimentally determined gradients compared with the model without any gradients. For example, to obtain the spiking precision of the model containing 400 GCs with all gradients, the model without gradients required 800 GCs (cf. red arrows in *Figure 8C*). This indicates that for a cerebellum exploiting gradients, the number of GCs can at least be halved while obtaining a certain temporal precision compared with a cerebellum containing no gradients.

To investigate the relative contribution of each of the gradients, we tested models containing single gradients in isolation, resulting in intermediate van Rossum errors (blue, yellow, and green in *Figure 8C,D*). The average relative differences between the models across all sizes of the GC
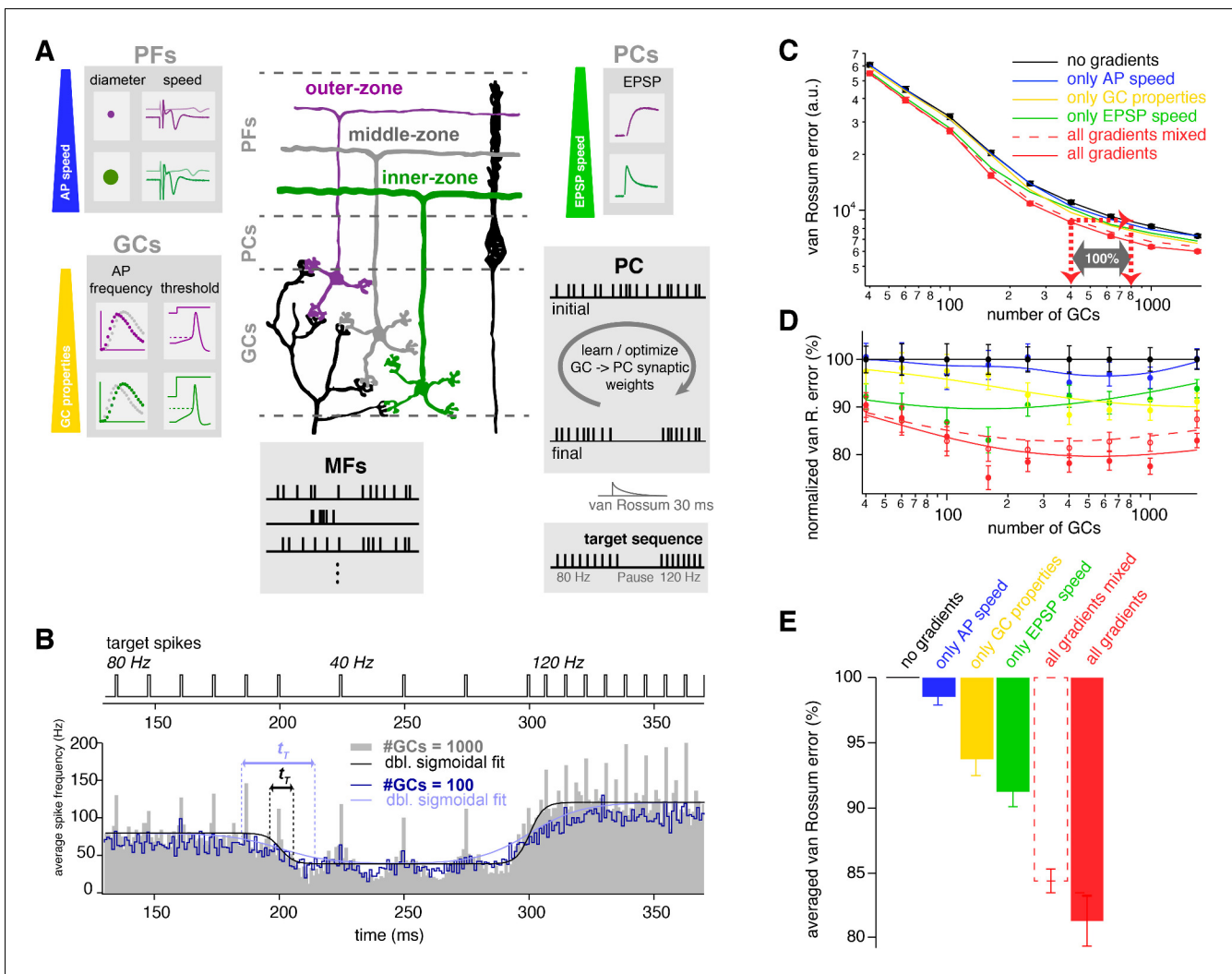
Figure 8. The observed neuronal gradients increase storing capacity and improve temporal precision of PC spiking. (A) Schematic illustration of the network model of the cerebellar cortex as explained in the main text. (B) Average spiking histogram for models consisting of 100 and 1000 GCs, superimposed with double sigmoidal fits constrained to 80, 40 and 120 Hz. The target spiking sequence is indicated above. t_T indicates the transition time of the sigmoidal fit for the respective number of GCs. (C) Double logarithmic plot of the average minimal van Rossum error plotted against the number of GCs for models with no gradients (black), with only gradually varied PF conduction velocity (blue), GC parameters (yellow),)and EPSP kinetics (green), and with all gradients (red). Furthermore, all parameters were gradually varied but the connectivity between GC, PF and EPSPs was random (all gradients mixed; dashed red). Red dashed lines with arrows indicate the number of GCs needed to obtain the same van Rossum error with all gradients compared to no gradients. With no gradients, twice as many GCs are needed to obtain the same van Rossum error. (D) Average van Rossum error as shown in panel C but normalized to values obtaned from the model without gradients, superimposed with a smoothing spline interpolation. (E) Average of the relative differences shown in panel D.

The online version of this article includes the following figure supplement(s) for figure 8:

Figure supplement 1. The observed neuronal gradients reduce the temporal error and improve rate coding of PC spikes.

populations suggest an almost additive behavior of the individual gradients to the overall performance (*Figure 8E*).

To further investigate the interplay of the different gradients, we investigated a model containing all gradients, but the connectivity between GCs, PF action potential conduction velocity, and PC EPSP kinetics were randomly intermixed (red dashed lines in *Figure 8C–E*). The network benefits

from these intermixed gradients, but maximum optimization can only be obtained with correct connectivity (*Figure 8E*).

The time constant to calculate the van Rossum error can be decreased or increased to investigate spike timing or slower changes in firing rate, respectively. The impact of the gradients increased with increasing time constant (*Figure 8—figure supplement 1A,B*), indicating that rate coded signaling especially benefits from the here described gradients. To specifically test the effect of gradients on the cerebellum's ability to switch between firing frequencies, we made sigmoid fits around the times of firing rate changes. The transition time (t_T; see Materials and methods) from these fits showed that models with all gradients showed on average about 30% faster 'frequency-switching' than models without any gradients (*Figure 8—figure supplement 1C–F*).

Finally, we repeated the modeling experiments but used a target sequence with a firing pause (i.e. 80, 0, and 120 Hz instead of 80, 40, and 120 Hz) resulting in similar conclusions regarding the van Rossum errors and transition times (*Figure 8—figure supplement 1G–M*). A pause in firing enabled us to quantify the temporal error at the beginning and the end of the pause (*Figure 8—figure supplement 1N–Q*). These spike times have been proposed to be of particular relevance for behavior (*Hong et al., 2016*). Analysis of the temporal error in the beginning and the end of the pause revealed similar results compared with the van Rossum error and the transition time. Thus, our modeling results show that the experimentally determined gradients improve the spiking precision, accelerate 'frequency-switching', and increase the storing capacity of the cerebellar cortex.

Discussion

In this study, we describe gradients in the biophysical properties of superficial to deep GCs, which enables the GC layer to perform a Fourier-like transformation of the MF input. Furthermore, we show that the downstream pathways from GCs to PCs are specialized for transmitting the frequency band for which the corresponding GCs are tuned to. Finally, computational modeling demonstrates that both the gradients in the GC layer and the specialized downstream pathways improve the spiking precision, accelerate the switching between firing frequencies of PCs, and increase storing capacity in the cerebellar cortex.

Fourier-like transformation in the cerebellar cortex

Our data demonstrate that outer-zone GCs preferentially fire during MF input with low frequency ('low-frequency' GCs, magenta in *Figure 9A*), whereas inner-zone GCs preferentially fire during MF input with high frequency ('high-frequency' GCs, green in *Figure 9A*). The separation of a signal into its frequency components resembles a Fourier transformation (*Figure 9B*). The analogy with a Fourier transformation has the limitations that (1) the separation is only partial with overlapping ranges of preferred frequency, (2) a single MF cannot transmit two frequencies simultaneously but only separated in time (as illustrated in *Figure 9A*) and (3) concurrent inputs from two MFs with different frequencies synapsing onto a single GC cannot be separated. Yet, our data indicate that the entire GC layer with several MFs sending various frequencies to numerous GCs can execute a Fourier-like transformation. In analogy to the dispersion of white light into its spectral components by an optical prism, the broadband MF signal is separated into its spectral components with inner- to outer-zone GCs preferentially transmitting the high- to low-frequency components, respectively.

Such a partial separation offers the chance to differentially process high- and low-frequency components. Indeed, in the molecular layer, the high-frequency components of the MF signal are sent via rapidly conducting axons to proximal parts of the PC dendritic tree. This allows fast (phasic) signals to have a strong and rapid impact on PC firing. On the other hand, low-frequency components of the MF signal are conducted more slowly and elicit slower EPSPs, allowing slow (tonic) signals to have a modulatory impact on PC firing. Our data indicate that, in analogy to the increased storing capacity of digital audio and image compression (*Jayant et al., 1993*; *Wallace, 1992*), the combination of a Fourier-like transformation in the GC layer and specialized downstream signaling pathways in the molecular layer dramatically reduce the number of required GCs for precise PC spiking (*Figure 8*). Furthermore, our data support the 'adaptive filter' theory of the cerebellum, where broadband MF input is differentially filtered by GCs (*Dean et al., 2010*; *Fujita, 1982*; *Singla et al., 2017*). Within this framework, our data indicate gradients in the band-pass filtering properties of GCs. Furthermore, our data could provide an additional explanation for the improvement in motor learning
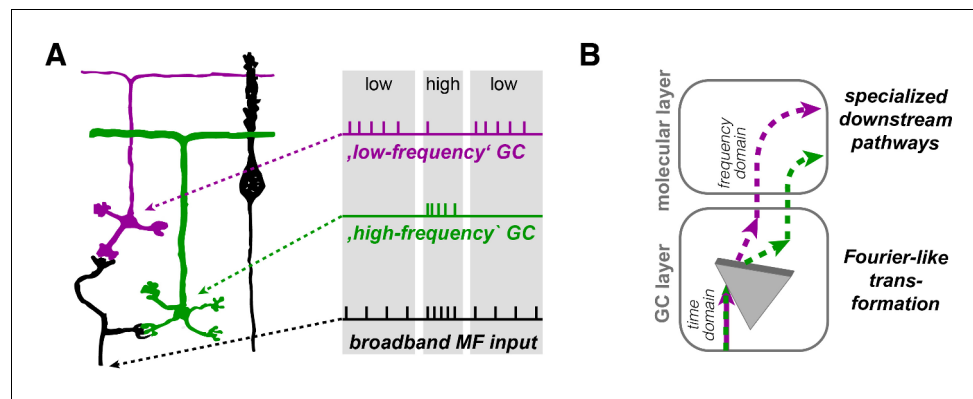
Figure 9. Illustration of the concept of Fourier-like transformation in the cerebellar cortex. (**A**) Illustration of a broadband MF input conveying a sequence of low, high, and low firing frequency. Inner-zone GCs will preferentially fire during high-frequency inputs ('high-frequency' GC) and outer-zone GCs during low-frequency inputs ('low-frequency' GC). (**B**) Schematic illustration of the signal flow through the cerebellar cortex. The Fourier-like transformation in the GC layer is illustrated as an optical prism separating the spectral components on the MF input. Thereby, the MF signal in the time domain is partially transformed into the frequency domain and sent to PCs via specialized signaling pathways in the molecular layer.

when elevating background activity of MFs (*Albergaria et al., 2018*): the elevated MF activity will help to overcome the high threshold of inner-zone GCs, which rapidly and effectively impact PCs via fast conducting PFs at the proximal dendrite.

Axes of frequency specialization in the cerebellum

There are at least two axes of heterogeneity in the cerebellar cortex. First, Zebrin stripes can be observed as parasagittal zones ('medio-lateral' axis) in cerebellar cortex (*Apps et al., 2018*). Firing rate, firing regularity, synaptic connectivity and synaptic plasticity seems to differ between PCs in zebrin positive and negative zones (*Valera et al., 2016*; *Wadiche and Jahr, 2005*; *Xiao et al., 2014*; *Zhou et al., 2014*). Second, there is a lobular organization ('rostro-caudal' axis) as shown here by the functional differences between lobules V and IX (*Figure 1—figure supplement 1*). GCs in lobule IX are tuned to lower frequencies than GCs in lobule V. These findings are largely in line with previous investigations (*Heath et al., 2014*; *Witter and De Zeeuw, 2015a*; *Zhou et al., 2014*), where the anterior cerebellum was identified to process high-frequency or bursting signals, while the vestibulocerebellum mainly processed lower frequency or slowly-modulating inputs. Furthermore, the optimal time intervals for introduction of spike timing dependent plasticity differ between the vermis and the flocculus (*Suvrathan et al., 2016*).

In addition to these two known axes of heterogeneity, we described an axis that is orthogonal to the surface of the cerebellar cortex. This 'depth' axis causes inner-zone GCs to be tuned to higher frequencies than outer-zone GCs. The frequency gradients along the 'depth'-axes are in line with recently described connections of nucleo-cortical MFs and PC, which specifically target GCs close to the PC layer (*Gao et al., 2016*; *Guo et al., 2016*). These connections send slow feedback signals to the outer-zone GCs, which — according to our framework — are ideally suited to process such slow modulatory signals. Independent of these specialized feedback pathways, MFs exhibit heterogeneity (*Chabrol et al., 2015*; *Bengtsson and Jörntell, 2009*). Consistent with MFs having rosettes throughout the depth of the granule cell layer (*Krieger et al., 1985*; *Palay and Chan-Palay, 1974*), our data indicate that each type of the heterogeneous MF inputs is split into its frequency components along the depth axis. A preference of some MFs to specific zones could furthermore contributes to the frequency separation (*Quy et al., 2011*; *Jörntell and Ekerot, 2006*).

Our results predict that superficial GCs, such as the ones imaged recently in the investigation of eye-blink conditioning and reward representation in the cerebellar cortex (*Giovannucci et al., 2017*;

64

Wagner et al., 2017), would preferentially convey low-frequency signals to PCs and might not be representative for the full range of frequencies present over the depth of the GC layer. Recently, diverse adaptation of GCs to 2-s-lasting current injections has been described (Masoli et al., 2019), but it remains unknown to which extent this form of adaptation exhibits a gradient along the depth axis. The genetic reasons for the here-observed gradients in cerebellar cortex are currently not known. Due to a large variability within each zone, our data cannot rule out a *salt and pepper* distribution of two populations of neurons (Espinosa and Luo, 2008). However, neurons in the medial vestibular nucleus exhibit a graded tuning of the capacity for fast-spiking by expression levels of specific ion channels (Kodama et al., 2020). Thus, including this new 'depth' axis, there are three orthogonal axes along which the cerebellar cortex is tuned for preferred frequency, indicating the importance of proper frequency tuning of the circuitry.

The role of inhibition

In the current study we did not investigate molecular layer interneurons, which can have a large impact on PC spiking (Blot et al., 2016; Dizon and Khodakhah, 2011; Gaffield and Christie, 2017; Mittmann et al., 2005; Sudhakar et al., 2017). However, the spatial arrangement of stellate and basket cell interneurons is consistent with our framework. Although the dendrites of molecular layer interneurons can span the entire molecular layer, the dendrites of basket cells seem to be preferentially located at the inner-zone of the molecular layer (Palkovits et al., 1971; Rakic, 1972), which positions them ideally to receive rapid high-frequency signals of inner-zone PFs. Consistently, they impact PC firing rapidly and efficiently via their pinceaus (Blot and Barbour, 2014). Furthermore, the dendrites of a subset of stellate cells (with their somata located in the outer-zone molecular layer) are preferentially located at the outer-zone molecular layer (Palkovits et al., 1971; Rakic, 1972), which positions them ideally to receive modulatory low-frequency signals and elicit slow IPSPs in PCs. Furthermore, molecular layer interneurons seem to represent a continuum along the vertical axis, with a correlation between the vertical location of the soma, axonal boutons, and dendrite location (Sultan and Bower, 1998), which is consistent with the here-described continuum of biophysical properties along the vertical axis of the cortex. Incorporating molecular layer interneurons, their synaptic plasticity and their potential gradients into the frequency-dispersion framework may show a further increase in the dynamic range of frequency separation within the cerebellar cortex c what we have described here (Gao et al., 2012).

Functional implications for the cerebellum

MF firing frequencies range from <1 to ~1000 Hz (Arenz et al., 2008; Chadderton et al., 2004; Jörntell and Ekerot, 2006; Rancz et al., 2007; van Kan et al., 1993). Many previous modeling studies investigating cerebellar function considered the activity of each MF as a constant digital value (Albus, 1971; Babadi and Sompolinsky, 2014; Brunel et al., 2004; Clopath et al., 2012; Marr, 1969), a constant analog value (Chabrol et al., 2015; Clopath and Brunel, 2013), or spike sequences with constant frequency (Billings et al., 2014; Cayco-Gajic et al., 2017; Steuber et al., 2007). We focused on the time-varying aspects of MF integration in GCs, and therefore implemented a model with a corresponding large range of MF input frequencies that could change over time. It would be interesting to elucidate whether models with more uniform MF inputs, such as those found in many previous models, would benefit from the here-observed biophysical gradients.

To implement these gradients in a model, we used a simplified cerebellar circuitry that does not consider active dendrites (Llinás and Sugimori, 1980) or the tonic activity of PCs (Raman and Bean, 1997). It will therefore be interesting to investigate if the here-observed gradients in the GC and molecular layer improve the performance of more complex models of the cerebellar cortex (De Schutter and Bower, 1994a; Garrido et al., 2013; Masoli et al., 2015; Medina et al., 2000; Rössert et al., 2015; Spanne and Jörntell, 2013; Steuber et al., 2007; Sudhakar et al., 2017; Walter and Khodakhah, 2009; Yamazaki and Tanaka, 2007). Furthermore, it remains to be investigated whether gradients in the GC layer also improve models that aim to explain tasks such as eyeblink conditioning (Mauk and Buonomano, 2004) and vestibulo-ocular reflexes (Lac et al., 1995).

Our model simulated the learning that PCs undergo to acquire specific firing frequencies in response to GC input. PC firing rate and spiking precision have been shown to be closely related to movement (Brown and Raman, 2018; Sarnaik and Raman, 2018). Our results show that the same

temporal spiking precision or the same frequency switching speed can be obtained with approximately half the number of GCs when GC gradients are implemented (*Figure 8*). Taking into account the large number of cerebellar GCs in the brain (*Herculano-Houzel, 2009*; *Williams and Herrup, 1988*), a significant reduction in the number of GCs could represent an evolutionary advantage to minimize neuronal maintenance energy (*Howarth et al., 2012*; *Isler and van Schaik, 2006*). Therefore, the dramatic increase in storing capacity for precise PC spiking provides an evolutionary explanation for the emergence of gradients in the neuronal properties.

Functional implications for other neural networks

Based on the described advantages of the Fourier transformation for rapid and storing-efficient information processing, we hypothesize that other neural networks also perform Fourier-like transformations and use segregated frequency-specific signaling pathways. To our knowledge, this has rarely been shown explicitly, but similar mechanisms might operate, for example, in the spinal cord network: descending motor commands from the pyramidal tract send broadband signals to motoneurons with different input resistances resulting from differences in size. This enables small motoneurons to fire during low-frequency inputs and large motoneurons only during high-frequency inputs (*Henneman et al., 1965*). Furthermore, specialized efferent down-stream signaling pathways innervate specific types of muscles with specialized short-term plasticity of the corresponding neuromuscular junctions (*Wang and Brehm, 2017*).

In the hippocampus, frequency preferences of hippocampal neurons are well established in enabling segregation of compound oscillatory input into distinct frequency components (*Pike et al., 2000*). Furthermore, there is increasing evidence that what has been considered a homogeneous population of neurons exhibit gradients in the neuronal properties (*Cembrowski and Spruston, 2019*), such as the intrinsic electrical properties and synaptic connectivity in CA3 pyramidal neurons (*Galliano et al., 2013*). The here reported heterogeneity furthermore enables functional segregation of information streams for example in CA1 pyramidal neurons (*Soltesz and Losonczy, 2018*). Additionally, gradients in biophysical properties of neurons in the entorhinal cortex might serve to generate functional outcomes relevant for the generation of grid cell sizes (*Giocomo et al., 2007*; *Schmidt-Hieber and Nolan, 2017*; *Orchard et al., 2013*). Finally, in the neocortex, gradients in anatomical and biophysical properties were recently uncovered (*Fletcher and Williams, 2019*).

In summary, our findings contribute to the growing body of evidence that the neurons of a cell layer can exhibit systematic functional heterogeneities with differential tuning of neurons along gradients. Our data furthermore suggest that such gradients facilitate complex transformation of information, such as Fourier-like transformations, to cope with a broad temporal diversity of signals in the central nervous system.

Materials and methods

Electrophysiology

Parasagittal 300-µm-thick cerebellar slices were prepared from P21–P30 (young animals) or from P80– P100 (old animals) C57BL/6 mice of either sex as described previously (*Ritzau-Jost et al., 2014*; *Delvendahl et al., 2015*). Animals were treated in accordance with the German and French Protection of Animals Act and with the guidelines for the welfare of experimental animals issued by the European Communities Council Directive. The extracellular solution for the whole-cell measurements contained (in mM): NaCl 125, $NaHCO_3$ 25, glucose 20, KCl 2.5, $CaCl_2$ 2, NaH_2PO_4 1.25, $MgCl_2$1 (310 mOsm, pH 7.3 when bubbled with Carbogen (95%O_2/5%CO_2)). For outside-out measurements of potassium currents (*Figure 2*), 150 µM $CdCl_2$ and 1 µM TTX were added to the external solution to block voltage-gated calcium channels and sodium channels, respectively. The intracellular solution contained in mM: K-Gluconate 150, NaCl 10, K-Hepes 10, Mg-ATP 3, Na-GTP 0.3, EGTA 0.05 (305 mOsm, pH 7.3). A liquid junction potential of +13 mV was corrected for. All electrophysiological measurements were performed with a HEKA EPC10 amplifier (HEKA Elektronik, Lambrecht/ Pfalz, Germany) under control of the Patchmaster software. All measurements were performed at 34–37°C.

Current clamp recordings in GCs

Action potentials were evoked in current-clamp mode by current pulses (amplitude 20–400 pA, duration 300 ms). To determine the input resistance, subthreshold current pulses were applied from −20 to + 20 pA in 2 pA steps. The resistance of the solution-filled patch-pipettes was between 6 and 12 MΩ . Data were sampled at 200 kHz.

Outside-out recordings in GCs

To reliably clamp potassium currents from the soma of GCs (*Figure 2*), potassium currents were measured in outside-out patches pulled from the soma of inner and outer GCs by applying 10-ms voltage steps from −90 to +60 mV with 10 mV increments at an intersweep interval of 1 s. The intersweep holding potential was −90 mV. Data were sampled at 100 kHz.

Compound action potentials in PFs

For the detection of compound action potentials in PFs, two pipettes (tip resistances 1–4 MΩ) filled with extracellular solution and connected to the patch-clamp amplifier were positioned within the molecular layer of horizontally cut slices of the cerebellar vermis. The average distance between two recording electrodes was 143 ± 5 μm. Compound action potentials were evoked by voltage stimulation (100 V) for 100 μs with a third pipette connected to an accumulator powered stimulation device (ISO-Pulser ISOP1, AD-Elektronik, Buchenbach, Germany). 40 to 80 stimulations delivered at 1 Hz were averaged and analyzed.

Excitatory postsynaptic potentials in PC

Excitatory postsynaptic potentials (EPSPs) in PC were elicited by voltage stimulation of the PFs within the inner, middle or outer third of the molecular layer from horizontally cut cerebellar slices (*Figure 7*). 10 μM SR95531 was added to the external solution to block GABA$_A$ receptors. The stimulation pipette was filled with extracellular solution, and the voltage was adjusted between 6 to 25 V to elicit EPSPs with amplitudes between 1 and 2 mV. EPSPs were measured after a single 100 μs voltage stimulation or five stimulations (100 μs duration) at a frequency of 100 and 500 Hz. Averages of 30 trains per stimulation protocol were used for data analysis.

Excitatory postsynaptic currents in GCs

To measure evoked EPSCs from GCs (*Figure 3—figure supplement 1*), 90–100 days-old mice were used. GCs from inner- or outer-zone from lobule V were held at resting conditions and MF axons were stimulated at 1 Hz with a second pipette. The average stimulation voltage was 36 ± 3 V for outer-zone GCs and 37 ± 3 V for inner-zone GCs.

Dynamic Clamp of MF conductance in GCs

In order to analyze the response of GCs on in vivo-like MF inputs, we used a Dynamic Clamp implemented with the microcontroller Teensy 3.6 (https://www.pjrc.com) as described by *Desai et al. (2017)*. The Teensy was programmed using the Arduino integrated development environment with the code provided by *Desai et al. (2017)* and modified for our need as described in the following.

The time course of MF conductance was

$$G_{EPSC}(t) = G_{max} A_{norm} \left(-e^{-\frac{t}{\tau_r}} + \sum_{i=1}^{3} a_i e^{-\frac{t}{\tau_i}} \right) \tag{1}$$

where the exponential rise time (τ_r) was 0.1 ms, the decay time constants (τ_1, τ_2, and τ_3) were 0.3, 8, and 40 ms, respectively, and the relative amplitude of the decay components (a_1, a_2, and a_3) were 0.7, 0.26, and 0.04, respectively. The peak conductance (G_{max}) was 1 nS (*Hallermann et al., 2010*) and the normalization factor (A_{norm}) was 0.518, which was numerically calculated to obtain a peak amplitude of 1. The kinetics of the MF conductance were chosen to reproduce the measured mixed AMPA and NMDA EPSC kinetics of single EPSCs (*Figure 3—figure supplement 1*) and trains of EPSCs (*Baade et al., 2016*). The short-term plasticity during Poisson sequence of spikes was implemented by changing G_{max} according to a simple phenomenological model (*Tsodyks and Markram,*

1997) assuming a release probability p_{r0} of 0.4 (*Ritzau-Jost et al., 2014*). Facilitation was implemented as an increase in the release probability according to $p_r = p_r + 0.2*(1- p_r)$ and decaying back to p_{r0} with a time constant of 12 ms (*Saviane and Silver, 2006*). Depression was implemented according to a recovery process with a time constant of 25 ms, which approximates a biexponential recovery process of 12 ms and 2 s (*Hallermann et al., 2010*; *Saviane and Silver, 2006*). The resulting short-term plasticity reproduced previously obtained data with regular spiking ranging from 20 to 1000 Hz (*Baade et al., 2016*; *Hallermann et al., 2010*; *Ritzau-Jost et al., 2014*).

The microcontroller was programmed to implement the MF conductance and its short-term plasticity with Poisson distributed spike times with a constant frequency ranging from 30 to 500 Hz for 300 ms (*Figure 3*). In each cell, each frequency was applied five times.

To investigate the response to sinusoidally varying input frequencies (*Figure 4*), the target frequency of the Poisson process (F) was varied on a logarithmic scale according to:

$$F(t) = exp(\log(F_{min}) + (\log(F_{max}) - \log(F_{min}))(0.5 - 0.5 \, cos(2\pi t/T))) \tag{2}$$

where the minimal and maximal frequency (F_{min} and F_{max}) were 30 and 300 Hz, respectively, and the duration of the sine wave cycle (T) was 1 s. In each cell, 10 cycles were applied consecutively for at least four times (interval >30 s). The histogram of the spike times (*Figure 4B*) was averaged across the last four cycles of all cells. The vector strength and phase angle (*van Kan et al., 1993*) were calculated as the absolute value and the argument of the complex number ρ ($i = \sqrt{-1}$):

$$\rho = \frac{1}{N}\sum_{n=1}^{N} e^{i2\pi\frac{t_n}{T}} \tag{3}$$

where t_n are the spike times of all N spikes per experiment and T the cycle duration (1 s). To increase statistical validity, only those cells that fired more than 100 action potentials during the analyzed cycles were included in the analysis. This criterion resulted in the exclusion of 3 out of 13 and 2 out of 9 cells for inner- and outer-zone GCs, respectively. However, inclusion of these cells in the analysis resulted in similar preference for MF firing frequency [phase angle along the cycle: 146 ± 10° for inner-zone (n = 13) and 103 ± 18° for outer-zone GCs (n = 9; $P_{Mann-Whitney}$= 0.06), representing an average firing frequency of 246 and 123 Hz for inner- and outer-zone GCs, respectively].

Electron microscopy

Four C57BL/6 mice of either sex with an age between P23–P28 were sacrificed, followed by transcardial perfusion with saline and consecutively a fixative containing 4% paraformaldehyde and 2% glutaraldehyde in phosphate-buffered saline (PBS). After removal of the brain, the tissue was allowed to post-fix over night at 4°C and sagittal sections of the cerebellum were prepared at a thickness of 60 µm using a Leica microtome (Leica Microsystems, Wetzlar, Germany). The sections were stained in 0.5% osmium tetroxide in PBS for 30 min followed by dehydration in graded alcohol and another staining step with 1% uranyl acetate in 70% ethanol. After further dehydration, the tissue was embedded in durcupan (Sigma-Aldrich), which was allowed to polymerize for 48 hr at 56°C between coated microscope slides and cover glasses. Regions of interest were identified by light microscopy, cut and transferred onto blocks of durcupan to obtain ultra-thin sections using an Ultramicrotome (Leica Microsystems). Ultra-thin sections were transferred onto formvar-coated copper grids and stained with lead citrate. Ultrastructural analysis was performed using a Zeiss SIGMA electron microscope (Zeiss NTS, Oberkochen, Germany) equipped with a STEM detector and ATLAS software.

Measurement of parallel-fiber axon diameter

Electron micrographs were manually analyzed in a blind manner (numbered by masked randomization) and each micrograph was divided into eight identically sized fields. The diameter of each parallel-fiber axon was measured as the longest chord in one or two of these fields. Cross sections with visible active zones or mitochondria were excluded from analysis.

DiI injections and GC tracking

Six P20 CD1 mice were anesthetized with isoflurane (4%). An incision of the skin to expose the skull was made and a hole was manually drilled using a 25G needle above the desired injection site.

Injections of small amounts of DiI (1,1-dioctadecyl-3,3,3,3 tetramethylindocarbocyanine perchlorate, ThermoFisher Scientific, 10% in N,N-dimethylformamide) were performed using a broken glass pipette connected to a picospritzer II (Parker Instrumentation). 24 hr after injection, animals were sacrificed and transcardially perfused with 4% paraformaldehyde in PBS. The cerebellum was dissected, fixed overnight, and embedded in 4% agarose in PBS. 150 µm thick sections were then cut in the transverse or sagittal plane using a vibratome (VT1000, Leica microsystems). Z-Stacks (1 µm steps) were acquired using a confocal microscope (Leica SP5 II, 63x objective). GCs were traced from their soma to the axonal bifurcation of PFs. (Average stack depth: 84 ± 20 µm). GC axons were reconstructed using the 'Simple Neurite Tracer' plugin (*Longair et al., 2011*) in Fiji (ImageJ, NIH, USA). This plugin allowed us to assess the continuity of axons between several cross-sections. GC ascending axons were then fully traced and measured within the Z-limits of image sections. The size of the different layers of cerebellar cortex was reconstructed in each Z-stack. To avoid variability, all distances were normalized to the corresponding molecular layer height.

Data analysis

Current-clamp data were analyzed using custom-written procedures in Igor Pro software (WaveMetrics, Oregon, USA) as previously described (*Eshra et al., 2019*). Intrinsic properties of GCs were determined from the injected currents that elicited the largest number of action potentials. The action potential threshold was defined as the membrane voltage at which the first derivative exceeded 100 V s^{-1}, the minimal action potential peak was set at −20 mV and the minimal amplitude at 20 mV. All action potentials with a half-width shorter than 50 µs and longer than 500 µs were excluded. Action potential voltage threshold and half-width were calculated from the average of the first five action potentials. If a trace contained less than five action potentials, only the first action potential was considered. The action potential frequency was determined by dividing the number of action potentials during the 300-ms-lasting current injection by 300 ms. Membrane capacitance, resting membrane potential and series resistance were read from the amplifier software (HEKA) after achieving the whole-cell configuration. Input resistance (R_{in}) was analyzed from alternating subthreshold current injections from −20 to 20 pA (2 pA steps). The resulting voltage was plotted against the injected current and a spline interpolation was performed to obtain the slope at the holding membrane potential (0 pA current injection).

The peak-current from outside-out patches was determined from voltage steps (−90 to +60 mV) with Fitmaster software (HEKA). Steady-state inactivation was determined from the last 2 ms of the respective sweep. Cells were only included if 50 pA $<I_{max} < 1$ nA to exclude potential whole-cell measurements and membrane-vesicles.

EPSP measurements from PCs and EPSC measurements from GCs were analyzed with the Fitmaster software (HEKA). For PC EPSPs, 20–80% rise time and time to peak were determined from the average of 30 individual single EPSPs. GCs EPSCs were averaged from 25 traces. To obtain the decay kinetics, single EPSPs/EPSCs were fitted with either one or two exponentials. The weighted time constant was calculated as:

$$\tau_{w} = \frac{A_{slow}\tau_{slow} + A_{fast}\tau_{fast}}{A_{slow} + A_{fast}} \tag{4}$$

Paired-pulse ratio was determined between the first and the 5th EPSP after stimulation with 100 Hz trains. Single EPSCs from inner- and outer-zone GCs were averaged and fitted with two exponentials. The decay kinetics and amplitude of the grand-average was used to implement the MF EPSCs for the Dynamic Clamp.

Neuronal networking modeling

The neuronal network consisted of varying numbers of MF inputs, GCs, and one PC and was implemented in Matlab (The MathWorks, Inc, Natick, Massachusetts, R2017a). For each simulation, a random set of MF inputs was generated. This input was then fed to a layer of integrate-and-fire GCs. An integrate-and-fire PC received the output of the GCs as EPSPs with delays based on PF conduction velocity. The PF-to-PC synaptic weights were optimized with the aim to make the PC spiking sequence similar to the target sequence. In the following, each component of the model is explained in detail.

69

MF inputs

To simulate in vivo-like MF firing patterns, half of the MFs fired tonically (*van Kan et al., 1993*) and the other half fired bursts (*Rancz et al., 2007*). All MF spike trains were modeled first by generating a 'threshold trace'. For tonically firing MFs, this threshold trace was a Gaussian function with a peak and standard deviation chosen from uniform distributions ranging between 10 and 100 Hz and 0.2 and 0.5 s respectively, and a peak time point between 0 and 0.5 s. For burst firing MFs, the threshold trace was an exponential function with a peak randomly chosen between 600 and 1200 Hz, a decay time constant of 30 ms and a peak between 0 and 0.5 s. The threshold trace was then evaluated against random numbers from a uniform distribution to determine the occurrence of a spike. To accelerate the simulations, the sampling time interval was adjusted to 1 ms.

GC properties

GCs were implemented as integrate and fire models with the following parameters: membrane resistance linearly varied between 450 MΩ for inner GCs to 800 MΩ for outer GCs (*Figure 1H*) and the threshold linearly varied between −37 mV for inner GCs to −42 mV for outer GCs (*Figure 1G*). For the models without the GC gradient, these values were set to the mean of the values for the inner and outer GC (i.e. 625 MΩ and −39 mV). The reset potential was set to −90 mV and the membrane potential to −80 mV.

PF properties

To simulate a different action potential conduction velocity, the GC spike times were delayed by a value linearly varied between 0 for inner and 3 ms for outer GCs. The delay was calculated as the difference in conduction time required to travel 5 mm with a speed of 0.28 and 0.33 m s^{-1} (*Figure 4F*). Even with this anatomically rather too large PF length (*Harvey and Napper, 1991*), the PF conduction speed had only a small impact on the model performance (see e.g. blue lines and bars in *Figure 7C–E*), arguing against a big impact of PF conduction delays (*Braitenberg et al., 1997*) at least in our model approach.

Synaptic connections and properties

Each MF was connected to 10 GCs and each GC received 2 MF inputs, that is, the number of MF was 1/5 of the number of GCs. Since our model consists only of 'active' MFs, we chose only 2 and not 4 MFs per GCs (*Billings et al., 2014*). The MF to GC synapse was implemented as a model with one pool of vesicles with a release probability of 0.5 and a vesicle recruitment time constant of 13 ms (*Hallermann et al., 2010*). Synaptic facilitation was implemented by increasing the release probability after each spike by 0.2 decaying to the resting release probability with a time constant of 12 ms (*Saviane and Silver, 2006*). The synaptic conductance had exponential rise and decay time constants of 0.1 and 2 ms, respectively, and a peak amplitude of 1.9 nS (*Silver et al., 1992*). Correspondingly, the GC to PC synapse was implemented as a model with one pool of vesicles with a release probability (p_{r0}) of 0.4 and a vesicle recruitment time constant of 50 ms. Synaptic facilitation was implemented by increasing the release probability after each spike by 0.2 decaying to the resting release probability with a time constant of 50 ms (*Doussau et al., 2017*; *Isope and Barbour, 2002*; *Valera et al., 2012*). The synaptic conductance had an exponential rise time constant between 0.5 and 2 ms and a decay time constant between 17.5 and 70 ms for inner- and outer-zone GCs, respectively (*Figure 6*). The peak amplitude was adjusted to equalize the charge of the EPSC and to generate an approximately correct number of PC spikes (with the initial start values, that is, all GC to PC synaptic weight factors = 1) by linearly varying between 0.5 and 0.15 nS for inner- and outer-zone GCs, respectively.

PC properties

The PC was implemented as an integrate and fire model with a membrane resistance of 15 MΩ, resting membrane potential of −50 mV, and a firing threshold of −45 mV. Spontaneous firing of PCs (*Raman and Bean, 1997*) was not implemented, and the only inputs to drive PCs to threshold were the GC-to-PC EPSCs.

Target sequence and van Rossum error

Based on in vivo firing patterns (**Witter and De Zeeuw, 2015a**), an arbitrary target firing sequence of 80, 40, and 120 Hz for 300, 100, and 100 ms, respectively, was chosen. The distance between the PC and the target spiking sequence was quantified with the van Rossum error (**van Rossum, 2001**). Both spiking sequences were convolved with an exponential kernel with a decay time constant of 30 ms (or values ranging from 2 to 300 ms in (**Figure 8—figure supplement 1A,B**). The van Rossum error was defined as the integral of the square of the difference between these two convolved traces. We also tested another algorithm to calculate the van Rossum error (**Houghton and Kreuz, 2012**), C++ code taken from http://pymuvr.readthedocs.io/ and incorporated into Matlab via the MEX function and results were comparable.

Learning and minimization algorithm

For each random set of MF inputs, the GC to PC synaptic weights were changed according to the following algorithm with the aim to minimize the van Rossum error between the PC spiking sequence and the target sequence. The initial values of the synaptic weights were 1, and values were allowed to change between 0 and 100. First, an algorithm was used that was based on supervised learning (**Raymond and Medina, 2018**) to punish the GCs that have spikes that precede unwanted PC spikes. Subsequently, an unbiased optimization of the GC to PC synaptic weight was performed using the patternsearch() algorithm of Matlab to minimize the van Rossum error. To increase the chance that a global (and not local) minimum was found, the minimization of the routine was repeated several times with random starting values. Other optimization routines such as a simplex [(fminsearch() of Matlab) or a genetic algorithm (ga() of Matlab)] revealed similar results. To exclude the possibility that the differences in the minimal van Rossum error between models with and without gradients were due to a bias in our learning algorithm, we performed a set of simulations with networks consisting of less than 100 GCs, in which we skipped the learning algorithm and only used an unbiased minimization algorithm. This resulted in similar difference in the minimal van Rossum error between models with and without gradients, indicating that the learning algorithm was not biased toward one type of model. For networks consisting of more than 100 GCs the pre-learning was required to facilitate the finding of the global minimum.

300 different sets of random MF inputs were used to determine 300 statistically independent minimal van Rossum values for each of the models with a different number of GCs and a different number of implemented gradients (illustrated as mean ± SEM in **Figure 8C**). Comparing different models with the same set of MF input (using the nonparametric paired Wilcoxon signed-rank statistical test) the difference was significant (p<0.001) for all of the models and all number of GCs. The van Rossum errors were then normalized to the mean of the error of the model without gradients (**Figure 8D**). The values in **Figure 8D** were fitted with cubic spline interpolation using the logarithm of the number of GCs as abscissa.

To quantify the transition time between two target frequencies of the PC, the spike histogram was fitted with the equation

$$f(t) = 80 + \frac{-80 + 40}{1 + e^{-(t-200)/t_T}} + \frac{-40 + 120}{1 + e^{-(t-300)/t_T}} \tag{5}$$

where f is the spike frequency in Hz and t the time in ms. The transition time t_T corresponds to the 23% to 77% decay and rise time for the transition from 80 to 40 Hz and from 40 to 120 Hz, respectively.

Sensitivity of model parameters

We verified that our conclusions do not critically depend on specific parameters of the model. For example, decreasing the simulation time interval from 1 ms to 100 µs, resulted in a difference of the best van Rossum error of 21% between models with and without gradients consisting of 100 GC, compared with a difference of 17% between the corresponding models with the default simulation time interval of 1 ms (cf. **Figure 8D**). With 4 MFs per GC (not 2) the difference of the best van Rossum error was 15% between models with and without gradients consisting of 100 GC (17% with 2 MF per GC). With a membrane resistance of the PC of 100 MΩ (not 15 MΩ) the difference of the best van Rossum error was 23% between models with and without gradients consisting of 100 GCs

71

(17% with 15 MΩ). Finally, changing the target sequence to 80, 0, and 120 Hz (not 80, 40, and 120 Hz) resulted in very similar results as obtained with the original target (compare *Figure 8C–E* with *Figure 8—figure supplement 1H–J* and *Figure 8—figure supplement 1D–F* with *Figure 8—figure supplement 1K–M*).

Code

The Matlab scripts used to reproduce the model results in *Figure 8* are available at: https://github.com/HallermannLab/2019_GC_heterogen (*Straub, 2019*; copy archived at https://github.com/elifes-ciences-publications/2019_GC_heterogen/settings).

Statistical testing

Data are expressed as mean ± SEM or as box plots with median and interquartile range. The number of analyzed cells is indicated in the figures. To test for statistically significant differences, we performed Kruskal-Wallis (for three groups) or Mann-Whitney U tests (for two groups) and provide the p values (P_{Kr-Wa}, or $P_{Mann-Whitney}$) above the bar-graphs. In case of three groups, we performed non-parametric Dunn's multiple comparisons post-hoc tests and provide the p values in the figure legends (P_{Dunn}). Results were considered statistically significant if $p < 0.05$.

Acknowledgements

Additional information

Author contributions

Isabelle Straub, Conceptualization, Data curation, Software, Supervision, Investigation, Visualization, Methodology, Writing - original draft, Writing - review and editing; Laurens Witter, Data curation, Software, Investigation, Visualization, Methodology, Writing - original draft, Writing - review and editing; Abdelmoneim Eshra, Data curation, Software, Investigation, Visualization, Methodology, Writing - review and editing; Miriam Hoidis, Niklas Byczkowicz, Data curation, Investigation, Visualization; Sebastian Maas, Data curation, Software, Investigation; Igor Delvendahl, Data curation, Software, Writing - review and editing; Kevin Dorgans, Data curation, Software, Investigation, Writing - review and editing; Elise Savier, Martin Krueger, Data curation, Investigation, Writing - review and editing; Ingo Bechmann, Philippe Isope, Data curation, Supervision, Investigation, Writing - review and editing; Stefan Hallermann, Conceptualization, Software, Supervision, Visualization, Methodology, Writing - original draft, Writing - review and editing

Author ORCIDs

Isabelle Straub https://orcid.org/0000-0003-1152-5542
Laurens Witter https://orcid.org/0000-0003-2357-0578
Niklas Byczkowicz http://orcid.org/0000-0002-6517-287X
Igor Delvendahl https://orcid.org/0000-0002-6151-2363
Kevin Dorgans http://orcid.org/0000-0003-1724-6384
Elise Savier https://orcid.org/0000-0001-7512-1630
Stefan Hallermann https://orcid.org/0000-0001-9376-7048

Ethics

Animal experimentation: All experiments were approved in advance by the Institutional Ethics Committees and animals were treated in accordance with the European (EU Directive 2010/63/EU, Annex IV for animal experiments), National, and Leipzig University guidelines.

Additional files

Supplementary files

• Transparent reporting form

Data availability

All data generated or analysed during this study are included in the manuscript and supporting files. The Matlab scripts used to reproduce the model results in Figure 8 is available at: https://github.com/HallermannLab/2019_GC_heterogen (copy archived at https://github.com/elifesciences-publications/2019_GC_heterogen).

References

Albergaria C, Silva NT, Pritchett DL, Carey MR. 2018. Locomotor activity modulates associative learning in mouse cerebellum. *Nature Neuroscience* **21**:725–735. DOI: https://doi.org/10.1038/s41593-018-0129-x, PMID: 29662214

Albus JS. 1971. A theory of cerebellar function. *Mathematical Biosciences* **10**:25–61. DOI: https://doi.org/10.1016/0025-5564(71)90051-4

Apps R, Hawkes R, Aoki S, Bengtsson F, Brown AM, Chen G, Ebner TJ, Isope P, Jörntell H, Lackey EP, Lawrenson C, Lumb B, Schonewille M, Sillitoe RV, Spaeth L, Sugihara I, Valera A, Voogd J, Wylie DR, Ruigrok TJH. 2018. Cerebellar modules and their role as operational cerebellar processing units. *The Cerebellum* **17**:654–682. DOI: https://doi.org/10.1007/s12311-018-0952-3

Arenz A, Silver RA, Schaefer AT, Margrie TW. 2008. The contribution of single synapses to sensory representation in vivo. *Science* **321**:977–980. DOI: https://doi.org/10.1126/science.1158391, PMID: 18703744

Baade C, Byczkowicz N, Hallermann S. 2016. NMDA receptors amplify mossy fiber synaptic inputs at frequencies up to at least 750 hz in cerebellar granule cells. *Synapse* **70**:269–276. DOI: https://doi.org/10.1002/syn.21898, PMID: 26887562

Babadi B, Sompolinsky H. 2014. Sparseness and expansion in sensory representations. *Neuron* **83**:1213–1226. DOI: https://doi.org/10.1016/j.neuron.2014.07.035, PMID: 25155954

Baginskas A, Palani D, Chiu K, Raastad M. 2009. The H-current secures action potential transmission at high frequencies in rat cerebellar parallel fibers. *European Journal of Neuroscience* **29**:87–96. DOI: https://doi.org/10.1111/j.1460-9568.2008.06566.x, PMID: 19087162

Barbour B. 1993. Synaptic currents evoked in purkinje cells by stimulating individual granule cells. *Neuron* **11**:759–769. DOI: https://doi.org/10.1016/0896-6273(93)90085-6

Bengtsson F, Jörntell H. 2009. Sensory transmission in cerebellar granule cells relies on similarly coded mossy fiber inputs. *PNAS* **106**:2389–2394. DOI: https://doi.org/10.1073/pnas.0808428106, PMID: 19164536

Billings G, Piasini E, Lőrincz A, Nusser Z, Silver RA. 2014. Network structure within the cerebellar input layer enables lossless sparse encoding. *Neuron* **83**:960–974. DOI: https://doi.org/10.1016/j.neuron.2014.07.020, PMID: 25123311

Blot A, de Solages C, Ostojic S, Szapiro G, Hakim V, Léna C. 2016. Time-invariant feed-forward inhibition of Purkinje cells in the cerebellar cortex *in vivo*. *The Journal of Physiology* **594**:2729–2749. DOI: https://doi.org/10.1113/JP271518

Blot A, Barbour B. 2014. Ultra-rapid axon-axon ephaptic inhibition of cerebellar purkinje cells by the pinceau. *Nature Neuroscience* **17**:289–295. DOI: https://doi.org/10.1038/nn.3624, PMID: 24413696

Braitenberg V, Heck D, Sultan F. 1997. The detection and generation of sequences as a key to cerebellar function: experiments and theory. *Behavioral and Brain Sciences* **20**:229–245. DOI: https://doi.org/10.1017/S0140525X9700143X, PMID: 10096998

Brown ST, Raman IM. 2018. Sensorimotor integration and amplification of reflexive whisking by well-timed spiking in the cerebellar corticonuclear circuit. *Neuron* **99**:564–575. DOI: https://doi.org/10.1016/j.neuron.2018.06.028

Brunel N, Hakim V, Isope P, Nadal JP, Barbour B. 2004. Optimal information storage and the distribution of synaptic weights: perceptron versus purkinje cell. *Neuron* **43**:745–757. DOI: https://doi.org/10.1016/j.neuron.2004.08.023, PMID: 15339654

Cajal R. 1911. *Histologie Du Système Nerveux De l'Homme Et Des Vertébrés*. Paris: Maloine.

Cayco-Gajic NA, Clopath C, Silver RA. 2017. Sparse synaptic connectivity is required for decorrelation and pattern separation in feedforward networks. *Nature Communications* **8**:1116. DOI: https://doi.org/10.1038/s41467-017-01109-y, PMID: 29061964

Cayco-Gajic NA, Silver RA. 2019. Re-evaluating Circuit Mechanisms Underlying Pattern Separation. *Neuron* **101**:584–602. DOI: https://doi.org/10.1016/j.neuron.2019.01.044

Cembrowski MS, Spruston N. 2019. Heterogeneity within classical cell types is the rule: lessons from hippocampal pyramidal neurons. *Nature Reviews Neuroscience* **20**:193–204. DOI: https://doi.org/10.1038/s41583-019-0125-5, PMID: 30778192

Chabrol FP, Arenz A, Wiechert MT, Margrie TW, DiGregorio DA. 2015. Synaptic diversity enables temporal coding of coincident multisensory inputs in single neurons. *Nature Neuroscience* **18**:718–727. DOI: https://doi.org/10.1038/nn.3974, PMID: 25821914

Chadderton P, Margrie TW, Häusser M. 2004. Integration of quanta in cerebellar granule cells during sensory processing. *Nature* **428**:856–860. DOI: https://doi.org/10.1038/nature02442, PMID: 15103377

Clopath C, Nadal J-P, Brunel N. 2012. Storage of correlated patterns in standard and bistable purkinje cell models. *PLOS Computational Biology* **8**:e1002448. DOI: https://doi.org/10.1371/journal.pcbi.1002448

Clopath C, Brunel N. 2013. Optimal properties of analog perceptrons with excitatory weights. *PLOS Computational Biology* **9**:e1002919. DOI: https://doi.org/10.1371/journal.pcbi.1002919, PMID: 23436991

D'Angelo E, Rossi P, Taglietti V. 1993. Different proportions of N-methyl-D-aspartate and non-N-methyl-D-aspartate receptor currents at the mossy fibre-granule cell synapse of developing rat cerebellum. *Neuroscience* **53**:121–130. DOI: https://doi.org/10.1016/0306-4522(93)90290-V, PMID: 8097019

De Schutter E, Bower JM. 1994a. An active membrane model of the cerebellar purkinje cell II. simulation of synaptic responses. *Journal of Neurophysiology* **71**:401–419. DOI: https://doi.org/10.1152/jn.1994.71.1.401, PMID: 8158238

De Schutter E, Bower JM. 1994b. Simulated responses of cerebellar purkinje cells are independent of the dendritic location of granule cell synaptic inputs. *PNAS* **91**:4736–4740. DOI: https://doi.org/10.1073/pnas.91.11.4736, PMID: 8197127

Dean P, Porrill J, Ekerot C-F, Jörntell H. 2010. The cerebellar microcircuit as an adaptive filter: experimental and computational evidence. *Nature Reviews Neuroscience* **11**:30–43. DOI: https://doi.org/10.1038/nrn2756

Delvendahl I, Straub I, Hallermann S. 2015. Dendritic patch-clamp recordings from cerebellar granule cells demonstrate electrotonic compactness. *Frontiers in Cellular Neuroscience* **9**:93. DOI: https://doi.org/10.3389/fncel.2015.00093, PMID: 25852483

Desai NS, Gray R, Johnston D. 2017. A dynamic clamp on every rig. *Eneuro* **4**:ENEURO.0250-17.2017. DOI: https://doi.org/10.1523/ENEURO.0250-17.2017, PMID: 29085905

Dhar M, Hantman AW, Nishiyama H. 2018. Developmental pattern and structural factors of dendritic survival in cerebellar granule cells in vivo. *Scientific Reports* **8**:17561. DOI: https://doi.org/10.1038/s41598-018-35829-y, PMID: 30510282

Dieudonné S, Dumoulin A. 2000. Serotonin-driven long-range inhibitory connections in the cerebellar cortex. *The Journal of Neuroscience* **20**:1837–1848. DOI: https://doi.org/10.1523/JNEUROSCI.20-05-01837.2000, PMID: 10684885

Dizon MJ, Khodakhah K. 2011. The role of interneurons in shaping purkinje cell responses in the cerebellar cortex. *Journal of Neuroscience* **31**:10463–10473. DOI: https://doi.org/10.1523/JNEUROSCI.1350-11.2011, PMID: 21775592

Doussau F, Schmidt H, Dorgans K, Valera AM, Poulain B, Isope P. 2017. Frequency-dependent mobilization of heterogeneous pools of synaptic vesicles shapes presynaptic plasticity. *eLife* **6**:e28935. DOI: https://doi.org/10.7554/eLife.28935, PMID: 28990927

Eccles JC, Ito M, Szentagothai J. 1967. *The Cerebellum as a Neuronal Machine.* Berlin: Springer-Verlag.

Eshra A, Hirrlinger P, Hallermann S. 2019. Enriched environment shortens the duration of action potentials in cerebellar granule cells. *Frontiers in Cellular Neuroscience* **13**. DOI: https://doi.org/10.3389/fncel.2019.00289, PMID: 31379501

Espinosa JS, Luo L. 2008. Timing neurogenesis and differentiation: insights from quantitative clonal analyses of cerebellar granule cells. *Journal of Neuroscience* **28**:2301–2312. DOI: https://doi.org/10.1523/JNEUROSCI.5157-07.2008, PMID: 18322077

Fletcher LN, Williams SR. 2019. Neocortical topology governs the dendritic integrative capacity of layer 5 pyramidal neurons. *Neuron* **101**:76–90. DOI: https://doi.org/10.1016/j.neuron.2018.10.048, PMID: 30472076

Fox CA, Barnard JW. 1957. A quantitative study of the purkinje cell dendritic branchlets and their relationship to afferent fibres. *Journal of Anatomy* **91**:299–313. PMID: 13448989

Fujita M. 1982. Adaptive filter model of the cerebellum. *Biological Cybernetics* **45**:195–206. DOI: https://doi.org/10.1007/BF00336192, PMID: 7171642

Gaffield MA, Christie JM. 2017. Movement rate is encoded and influenced by widespread, coherent activity of cerebellar molecular layer interneurons. *The Journal of Neuroscience* **37**:4751–4765. DOI: https://doi.org/10.1523/JNEUROSCI.0534-17.2017, PMID: 28389475

Galliano E, Gao Z, Schonewille M, Todorov B, Simons E, Pop AS, D'Angelo E, van den Maagdenberg AM, Hoebeek FE, De Zeeuw CI. 2013. Silencing the majority of cerebellar granule cells uncovers their essential role in motor learning and consolidation. *Cell Reports* **3**:1239–1251. DOI: https://doi.org/10.1016/j.celrep.2013.03.023, PMID: 23583179

Gao Z, van Beugen BJ, De Zeeuw CI. 2012. Distributed synergistic plasticity and cerebellar learning. *Nature Reviews Neuroscience* **13**:619–635. DOI: https://doi.org/10.1038/nrn3312, PMID: 22895474

Gao Z, Proietti-Onori M, Lin Z, Ten Brinke MM, Boele HJ, Potters JW, Ruigrok TJ, Hoebeek FE, De Zeeuw CI. 2016. Excitatory cerebellar nucleocortical circuit provides internal amplification during associative conditioning. *Neuron* **89**:645–657. DOI: https://doi.org/10.1016/j.neuron.2016.01.008, PMID: 26844836

Garrido JA, Ros E, D'Angelo E. 2013. Spike timing regulation on the millisecond scale by distributed synaptic plasticity at the cerebellum input stage: a simulation study. *Frontiers in Computational Neuroscience* **7**:64. DOI: https://doi.org/10.3389/fncom.2013.00064, PMID: 23720626

Gibo TL, Criscimagna-Hemminger SE, Okamura AM, Bastian AJ. 2013. Cerebellar motor learning: are environment dynamics more important than error size? *Journal of Neurophysiology* **110**:322–333. DOI: https://doi.org/10.1152/jn.00745.2012, PMID: 23596337

Giocomo LM, Zilli EA, Fransén E, Hasselmo ME. 2007. Temporal frequency of subthreshold oscillations scales with entorhinal grid cell field spacing. *Science* **315**:1719–1722. DOI: https://doi.org/10.1126/science.1139207, PMID: 17379810

Giovannucci A, Badura A, Deverett B, Najafi F, Pereira TD, Gao Z, Ozden I, Kloth AD, Pnevmatikakis E, Paninski L, De Zeeuw CI, Medina JF, Wang SS. 2017. Cerebellar granule cells acquire a widespread predictive feedback signal during motor learning. *Nature Neuroscience* **20**:727–734. DOI: https://doi.org/10.1038/nn.4531, PMID: 28319608

Guo C, Witter L, Rudolph S, Elliott HL, Ennis KA, Regehr WG. 2016. Purkinje cells directly inhibit granule cells in specialized regions of the cerebellar cortex. *Neuron* **91**:1330–1341. DOI: https://doi.org/10.1016/j.neuron.2016.08.011, PMID: 27593180

Hallermann S, Fejtova A, Schmidt H, Weyhersmüller A, Silver RA, Gundelfinger ED, Eilers J. 2010. Bassoon speeds vesicle reloading at a central excitatory synapse. *Neuron* **68**:710–723. DOI: https://doi.org/10.1016/j.neuron.2010.10.026, PMID: 21092860

Harvey RJ, Napper RM. 1991. Quantitative studies on the mammalian cerebellum. *Progress in Neurobiology* **36**:437–463. DOI: https://doi.org/10.1016/0301-0082(91)90012-P, PMID: 1947173

Heath NC, Rizwan AP, Engbers JD, Anderson D, Zamponi GW, Turner RW. 2014. The expression pattern of a Cav3-Kv4 complex differentially regulates spike output in cerebellar granule cells. *Journal of Neuroscience* **34**:8800–8812. DOI: https://doi.org/10.1523/JNEUROSCI.0981-14.2014, PMID: 24966380

Heiney SA, Wohl MP, Chettih SN, Ruffolo LI, Medina JF. 2014. Cerebellar-dependent expression of motor learning during eyeblink conditioning in head-fixed mice. *Journal of Neuroscience* **34**:14845–14853. DOI: https://doi.org/10.1523/JNEUROSCI.2820-14.2014, PMID: 25378152

Henneman E, Somjen G, Carpenter DO. 1965. Excitability and inhibitability of motoneurons of different sizes. *Journal of Neurophysiology* **28**:599–620. DOI: https://doi.org/10.1152/jn.1965.28.3.599, PMID: 5835487

Herculano-Houzel S. 2009. The human brain in numbers: a linearly scaled-up primate brain. *Frontiers in Human Neuroscience* **3**:31. DOI: https://doi.org/10.3389/neuro.09.031.2009, PMID: 19915731

Herzfeld DJ, Kojima Y, Soetedjo R, Shadmehr R. 2015. Encoding of action by the purkinje cells of the cerebellum. *Nature* **526**:439–442. DOI: https://doi.org/10.1038/nature15693, PMID: 26469054

Hewitt AL, Popa LS, Pasalar S, Hendrix CM, Ebner TJ. 2011. Representation of limb kinematics in purkinje cell simple spike discharge is conserved across multiple tasks. *Journal of Neurophysiology* **106**:2232–2247. DOI: https://doi.org/10.1152/jn.00886.2010, PMID: 21795616

Hong S, Negrello M, Junker M, Smilgin A, Thier P, De Schutter E. 2016. Multiplexed coding by cerebellar purkinje neurons. *eLife* **5**:e13810. DOI: https://doi.org/10.7554/eLife.13810, PMID: 27458803

Houghton C, Kreuz T. 2012. On the efficient calculation of Van Rossum distances. *Network: Computation in Neural Systems* **23**:48–58. DOI: https://doi.org/10.3109/0954898X.2012.673048

Howarth C, Gleeson P, Attwell D. 2012. Updated energy budgets for neural computation in the neocortex and cerebellum. *Journal of Cerebral Blood Flow & Metabolism* **32**:1222–1232. DOI: https://doi.org/10.1038/jcbfm.2012.35

Isler K, van Schaik CP. 2006. Metabolic costs of brain size evolution. *Biology Letters* **2**:557–560. DOI: https://doi.org/10.1098/rsbl.2006.0538, PMID: 17148287

Isope P, Barbour B. 2002. Properties of unitary granule cell–>purkinje cell synapses in adult rat cerebellar slices. *The Journal of Neuroscience* **22**:9668–9678. DOI: https://doi.org/10.1523/JNEUROSCI.22-22-09668.2002, PMID: 12427822

Jack JJB, Noble D, Tsien RW. 1983. *Electric Current Flow in Excitable Cells*. Oxford: Clarendon Press.

Jayant N, Johnston J, Safranek R. 1993. Signal compression based on models of human perception. *Proceedings of the IEEE* **81**:1385–1422. DOI: https://doi.org/10.1109/5.241504

Jörntell H, Ekerot C-F. 2006. Properties of somatosensory synaptic integration in cerebellar granule cells in *vivo* . *Journal of Neuroscience* **26**:11786–11797. DOI: https://doi.org/10.1523/JNEUROSCI.2939-06.2006

Keele SW, Ivry R. 1990. Does the cerebellum provide a common computation for diverse tasks? A timing hypothesis. *Annals of the New York Academy of Sciences* **608**:179–211. DOI: https://doi.org/10.1111/j.1749-6632.1990.tb48897.x, PMID: 2075953

Kodama T, Gittis AH, Shin M, Kelleher K, Kolkman KE, McElvain L, Lam M, du Lac S. 2020. Graded coexpression of ion channel, neurofilament, and synaptic genes in Fast-Spiking vestibular nucleus neurons. *The Journal of Neuroscience* **40**:496–508. DOI: https://doi.org/10.1523/JNEUROSCI.1500-19.2019, PMID: 31719168

Krieger C, Shinoda Y, Smith AM. 1985. Labelling of cerebellar mossy fiber afferents with intra-axonal horseradish peroxidase. *Experimental Brain Research* **59**:414–417. DOI: https://doi.org/10.1007/BF00230923, PMID: 2411585

Lac S, Raymond JL, Sejnowski TJ, Lisberger SG. 1995. Learning and memory in the vestibulo-ocular reflex. *Annual Review of Neuroscience* **18**:409–441. DOI: https://doi.org/10.1146/annurev.ne.18.030195.002205

Lackey EP, Heck DH, Sillitoe RV. 2018. Recent advances in understanding the mechanisms of cerebellar granule cell development and function and their contribution to behavior. *F1000Research* **7**:1142. DOI: https://doi.org/10.12688/f1000research.15021.1, PMID: 30109024

Llinás R, Sugimori M. 1980. Electrophysiological properties of in vitro purkinje cell dendrites in mammalian cerebellar slices. *The Journal of Physiology* **305**:197–213. DOI: https://doi.org/10.1113/jphysiol.1980.sp013358, PMID: 7441553

Longair MH, Baker DA, Armstrong JD. 2011. Simple neurite tracer: open source software for reconstruction, visualization and analysis of neuronal processes. *Bioinformatics* **27**:2453–2454. DOI: https://doi.org/10.1093/bioinformatics/btr390

Marr D. 1969. A theory of cerebellar cortex. *The Journal of Physiology* **202**:437–470. DOI: https://doi.org/10.1113/jphysiol.1969.sp008820, PMID: 5784296

Martin TA, Keating JG, Goodkin HP, Bastian AJ, Thach WT. 1996. Throwing while looking through prisms. I. focal olivocerebellar lesions impair adaptation. *Brain* **119 (Pt 4**:1183–1198. DOI: https://doi.org/10.1093/brain/119.4.1183, PMID: 8813282

Masoli S, Solinas S, D'Angelo E. 2015. Action potential processing in a detailed purkinje cell model reveals a critical role for axonal compartmentalization. *Frontiers in Cellular Neuroscience* **9**:47. DOI: https://doi.org/10.3389/fncel.2015.00047, PMID: 25759640

Masoli S, Tognolina M, Laforenza U, Moccia F, D'Angelo E. 2019. Parameter tuning differentiates granule cell subtypes enriching the repertoire of retransmission properties at the cerebellum input stage. *bioRxiv*. DOI: https://doi.org/10.1101/638247

Mauk MD, Buonomano DV. 2004. The neural basis of temporal processing. *Annual Review of Neuroscience* **27**:307–340. DOI: https://doi.org/10.1146/annurev.neuro.27.070203.144247, PMID: 15217335

Medina JF, Garcia KS, Nores WL, Taylor NM, Mauk MD. 2000. Timing mechanisms in the cerebellum: testing predictions of a large-scale computer simulation. *The Journal of Neuroscience* **20**:5516–5525. PMID: 10884335

Medina JF, Lisberger SG. 2007. Variation, signal, and noise in cerebellar sensory-motor processing for smooth-pursuit eye movements. *Journal of Neuroscience* **27**:6832–6842. DOI: https://doi.org/10.1523/JNEUROSCI.1323-07.2007, PMID: 17581971

Mittmann W, Koch U, Häusser M. 2005. Feed-forward inhibition shapes the spike output of cerebellar purkinje cells. *The Journal of Physiology* **563**:369–378. DOI: https://doi.org/10.1113/jphysiol.2004.075028, PMID: 15613376

Orchard J, Yang H, Ji X. 2013. Does the entorhinal cortex use the fourier transform? *Frontiers in Computational Neuroscience* **7**:179. DOI: https://doi.org/10.3389/fncom.2013.00179, PMID: 24376415

Palay SM, Chan-Palay V. 1974. *Cerebellar Cortex: Cytology and Organization*. Berlin: Springer.

Palkovits M, Magyar P, Szentágothai J. 1971. Quantitative histological analysis of the cerebellar cortex in the cat. 3. structural organization of the molecular layer. *Brain Research* **34**:1–18. DOI: https://doi.org/10.1016/0006-8993(71)90347-7, PMID: 5124919

Payne HL, French RL, Guo CC, Nguyen-Vu TB, Manninen T, Raymond JL. 2019. Cerebellar purkinje cells control eye movements with a rapid rate code that is invariant to spike irregularity. *eLife* **8**:e37102. DOI: https://doi.org/10.7554/eLife.37102, PMID: 31050648

Pichitpornchai C, Rawson JA, Rees S. 1994. Morphology of parallel fibres in the cerebellar cortex of the rat: an experimental light and electron microscopic study with biocytin. *The Journal of Comparative Neurology* **342**:206–220. DOI: https://doi.org/10.1002/cne.903420205, PMID: 8201032

Pike FG, Goddard RS, Suckling JM, Ganter P, Kasthuri N, Paulsen O. 2000. Distinct frequency preferences of different types of rat hippocampal neurones in response to oscillatory input currents. *The Journal of Physiology* **529 Pt 1**:205–213. DOI: https://doi.org/10.1111/j.1469-7793.2000.00205.x, PMID: 11080262

Quy PN, Fujita H, Sakamoto Y, Na J, Sugihara I. 2011. Projection patterns of single mossy fiber axons originating from the dorsal column nuclei mapped on the aldolase C compartments in the rat cerebellar cortex. *The Journal of Comparative Neurology* **519**:874–899. DOI: https://doi.org/10.1002/cne.22555, PMID: 21280042

Rakic P. 1972. Extrinsic cytological determinants of basket and stellate cell dendritic pattern in the cerebellar molecular layer. *The Journal of Comparative Neurology* **146**:335–354. DOI: https://doi.org/10.1002/cne.901460304

Raman IM, Bean BP. 1997. Resurgent sodium current and action potential formation in dissociated cerebellar purkinje neurons. *The Journal of Neuroscience* **17**:4517–4526. DOI: https://doi.org/10.1523/JNEUROSCI.17-12-04517.1997, PMID: 9169512

Rancz EA, Ishikawa T, Duguid I, Chadderton P, Mahon S, Häusser M. 2007. High-fidelity transmission of sensory information by single cerebellar mossy fibre boutons. *Nature* **450**:1245–1248. DOI: https://doi.org/10.1038/nature05995

Raymond JL, Medina JF. 2018. Computational principles of supervised learning in the cerebellum. *Annual Review of Neuroscience* **41**:233–253. DOI: https://doi.org/10.1146/annurev-neuro-080317-061948, PMID: 29986160

Ritzau-Jost A, Delvendahl I, Rings A, Byczkowicz N, Harada H, Shigemoto R, Hirrlinger J, Eilers J, Hallermann S. 2014. Ultrafast action potentials mediate kilohertz signaling at a central synapse. *Neuron* **84**:152–163. DOI: https://doi.org/10.1016/j.neuron.2014.08.036, PMID: 25220814

Rizwan AP, Zhan X, Zamponi GW, Turner RW. 2016. Long-Term potentiation at the mossy fiber–granule cell relay invokes postsynaptic second-messenger regulation of Kv4 channels. *The Journal of Neuroscience* **36**:11196–11207. DOI: https://doi.org/10.1523/JNEUROSCI.2051-16.2016

Rössert C, Dean P, Porrill J. 2015. At the edge of Chaos: how cerebellar granular layer network dynamics can provide the basis for temporal filters. *PLOS Computational Biology* **11**:e1004515. DOI: https://doi.org/10.1371/journal.pcbi.1004515, PMID: 26484859

76

Roth A, Häusser M. 2001. Compartmental models of rat cerebellar purkinje cells based on simultaneous somatic and dendritic patch-clamp recordings. *The Journal of Physiology* **535**:445–472. DOI: https://doi.org/10.1111/j.1469-7793.2001.00445.x, PMID: 11533136

Sarnaik R, Raman IM. 2018. Control of voluntary and optogenetically perturbed locomotion by spike rate and timing of neurons of the mouse cerebellar nuclei. *eLife* **7**:e29546. DOI: https://doi.org/10.7554/eLife.29546

Saviane C, Silver RA. 2006. Fast vesicle reloading and a large pool sustain high bandwidth transmission at a central synapse. *Nature* **439**:983–987. DOI: https://doi.org/10.1038/nature04509, PMID: 16496000

Schmidt-Hieber C, Nolan MF. 2017. Synaptic integrative mechanisms for spatial cognition. *Nature Neuroscience* **20**:1483–1492. DOI: https://doi.org/10.1038/nn.4652, PMID: 29073648

Serôdio P, Rudy B. 1998. Differential expression of Kv4 K+ channel subunits mediating subthreshold transient K$^+$ (A-type) currents in rat brain. *Journal of Neurophysiology* **79**:1081–1091. DOI: https://doi.org/10.1152/jn.1998.79.2.1081, PMID: 9463463

Silver RA, Traynelis SF, Cull-Candy SG. 1992. Rapid-time-course miniature and evoked excitatory currents at cerebellar synapses in situ. *Nature* **355**:163–166. DOI: https://doi.org/10.1038/355163a0, PMID: 1370344

Singla S, Dempsey C, Warren R, Enikolopov AG, Sawtell NB. 2017. A cerebellum-like circuit in the auditory system cancels responses to self-generated sounds. *Nature Neuroscience* **20**:943–950. DOI: https://doi.org/10.1038/nn.4567, PMID: 28530663

Soltesz I, Losonczy A. 2018. CA1 pyramidal cell diversity enabling parallel information processing in the Hippocampus. *Nature Neuroscience* **21**:484–493. DOI: https://doi.org/10.1038/s41593-018-0118-0

Spanne A, Jörntell H. 2013. Processing of multi-dimensional sensorimotor information in the spinal and cerebellar neuronal circuitry: a new hypothesis. *PLOS Computational Biology* **9**:e1002979. DOI: https://doi.org/10.1371/journal.pcbi.1002979, PMID: 23516353

Steuber V, Mittmann W, Hoebeek FE, Silver RA, De Zeeuw CI, Häusser M, De Schutter E. 2007. Cerebellar LTD and pattern recognition by purkinje cells. *Neuron* **54**:121–136. DOI: https://doi.org/10.1016/j.neuron.2007.03.015

Straub I. 2019. 2019_GC_heterogen. *GitHub*. fd237fc. https://github.com/HallermannLab/2019_GC_heterogen

Sudhakar SK, Hong S, Raikov I, Publio R, Lang C, Close T, Guo D, Negrello M, De Schutter E. 2017. Spatiotemporal network coding of physiological mossy fiber inputs by the cerebellar granular layer. *PLOS Computational Biology* **13**:e1005754. DOI: https://doi.org/10.1371/journal.pcbi.1005754, PMID: 28934196

Sultan F, Bower JM. 1998. Quantitative golgi study of the rat cerebellar molecular layer interneurons using principal component analysis. *The Journal of Comparative Neurology* **393**:353–373. DOI: https://doi.org/10.1002/(SICI)1096-9861(19980413)393:3<353::AID-CNE7>3.0.CO;2-0, PMID: 9548555

Suvrathan A, Payne HL, Raymond JL. 2016. Timing rules for synaptic plasticity matched to behavioral function. *Neuron* **92**:959–967. DOI: https://doi.org/10.1016/j.neuron.2016.10.022, PMID: 27839999

Tsodyks MV, Markram H. 1997. The neural code between neocortical pyramidal neurons depends on neurotransmitter release probability. *PNAS* **94**:719–723. DOI: https://doi.org/10.1073/pnas.94.2.719, PMID: 9012851

Valera AM, Doussau F, Poulain B, Barbour B, Isope P. 2012. Adaptation of granule cell to purkinje cell synapses to high-frequency transmission. *Journal of Neuroscience* **32**:3267–3280. DOI: https://doi.org/10.1523/JNEUROSCI.3175-11.2012, PMID: 22378898

Valera AM, Binda F, Pawlowski SA, Dupont JL, Casella JF, Rothstein JD, Poulain B, Isope P. 2016. Stereotyped spatial patterns of functional synaptic connectivity in the cerebellar cortex. *eLife* **5**:e09862. DOI: https://doi.org/10.7554/eLife.09862, PMID: 26982219

van Kan PL, Gibson AR, Houk JC. 1993. Movement-related inputs to intermediate cerebellum of the monkey. *Journal of Neurophysiology* **69**:74–94. DOI: https://doi.org/10.1152/jn.1993.69.1.74, PMID: 8433135

van Rossum MC. 2001. A novel spike distance. *Neural Computation* **13**:751–763. DOI: https://doi.org/10.1162/089976601300014321, PMID: 11255567

Vranesic I, Iijima T, Ichikawa M, Matsumoto G, Knöpfel T. 1994. Signal transmission in the parallel fiber-Purkinje cell system visualized by high-resolution imaging. *PNAS* **91**:13014–13017. DOI: https://doi.org/10.1073/pnas.91.26.13014, PMID: 7809165

Wadiche JI, Jahr CE. 2005. Patterned expression of purkinje cell glutamate transporters controls synaptic plasticity. *Nature Neuroscience* **8**:1329–1334. DOI: https://doi.org/10.1038/nn1539, PMID: 16136036

Wagner MJ, Kim TH, Savall J, Schnitzer MJ, Luo L. 2017. Cerebellar granule cells encode the expectation of reward. *Nature* **544**:96–100. DOI: https://doi.org/10.1038/nature21726, PMID: 28321129

Wallace GK. 1992. The JPEG still picture compression standard. *IEEE Transactions on Consumer Electronics* **38**:xviii–xxxiv. DOI: https://doi.org/10.1109/30.125072

Walter JT, Khodakhah K. 2009. The advantages of linear information processing for cerebellar computation. *PNAS* **106**:4471–4476. DOI: https://doi.org/10.1073/pnas.0812348106, PMID: 19234116

Wang WC, Brehm P. 2017. A gradient in synaptic strength and plasticity among motoneurons provides a peripheral mechanism for locomotor control. *Current Biology* **27**:415–422. DOI: https://doi.org/10.1016/j.cub.2016.12.010, PMID: 28111148

Williams RW, Herrup K. 1988. The control of neuron number. *Annual Review of Neuroscience* **11**:423–453. DOI: https://doi.org/10.1146/annurev.ne.11.030188.002231, PMID: 3284447

Wilms CD, Häusser M. 2015. Reading out a spatiotemporal population code by imaging neighbouring parallel fibre axons in vivo. *Nature Communications* **6**:6464. DOI: https://doi.org/10.1038/ncomms7464, PMID: 25751648

77

Witter L, Canto CB, Hoogland TM, de Gruijl JR, De Zeeuw CI. 2013. Strength and timing of motor responses mediated by rebound firing in the cerebellar nuclei after purkinje cell activation. *Frontiers in Neural Circuits* **7**: 133. DOI: https://doi.org/10.3389/fncir.2013.00133, PMID: 23970855

Witter L, De Zeeuw CI. 2015a. In vivo differences in inputs and spiking between neurons in lobules VI/VII of neocerebellum and lobule X of archaeocerebellum. *The Cerebellum* **14**:506–515. DOI: https://doi.org/10.1007/s12311-015-0654-z, PMID: 25735968

Witter L, De Zeeuw CI. 2015b. Regional functionality of the cerebellum. *Current Opinion in Neurobiology* **33**: 150–155. DOI: https://doi.org/10.1016/j.conb.2015.03.017, PMID: 25884963

Wyatt KD, Tanapat P, Wang SS. 2005. Speed limits in the cerebellum: constraints from myelinated and unmyelinated parallel fibers. *European Journal of Neuroscience* **21**:2285–2290. DOI: https://doi.org/10.1111/j.1460-9568.2005.04053.x, PMID: 15869526

Xiao J, Cerminara NL, Kotsurovskyy Y, Aoki H, Burroughs A, Wise AK, Luo Y, Marshall SP, Sugihara I, Apps R, Lang EJ. 2014. Systematic regional variations in purkinje cell spiking patterns. *PLOS ONE* **9**:e105633. DOI: https://doi.org/10.1371/journal.pone.0105633, PMID: 25144311

Yamazaki T, Tanaka S. 2007. A spiking network model for passage-of-time representation in the cerebellum. *European Journal of Neuroscience* **26**:2279–2292. DOI: https://doi.org/10.1111/j.1460-9568.2007.05837.x

Zhou H, Lin Z, Voges K, Ju C, Gao Z, Bosman LW, Ruigrok TJ, Hoebeek FE, De Zeeuw CI, Schonewille M. 2014. Cerebellar modules operate at different frequencies. *eLife* **3**:e02536. DOI: https://doi.org/10.7554/eLife.02536, PMID: 24843004
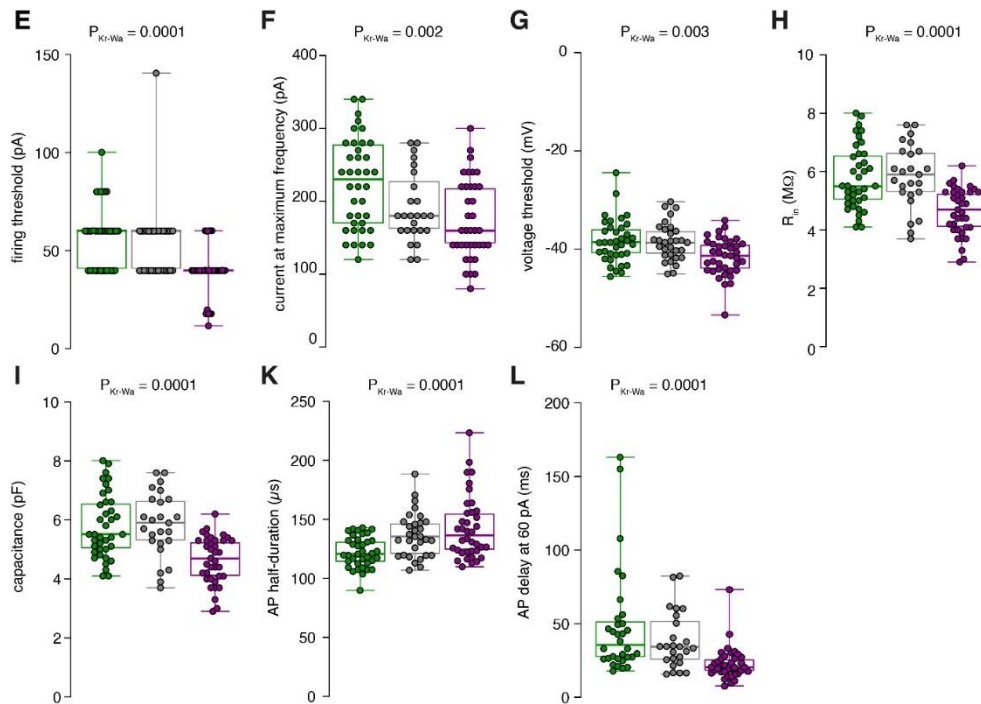
Figure 1 - figure supplement 1

Raw data of the bar graphs from Figure 1
The panels of Figure 1 containing bar graphs are shown as box plots (median and interquartile range with whiskers indicating the entire range) superimposed with the single data points. The same color code as in Figure 1 is used for inner- (green), middle- (gray) and outer-zone (magenta) GCs.
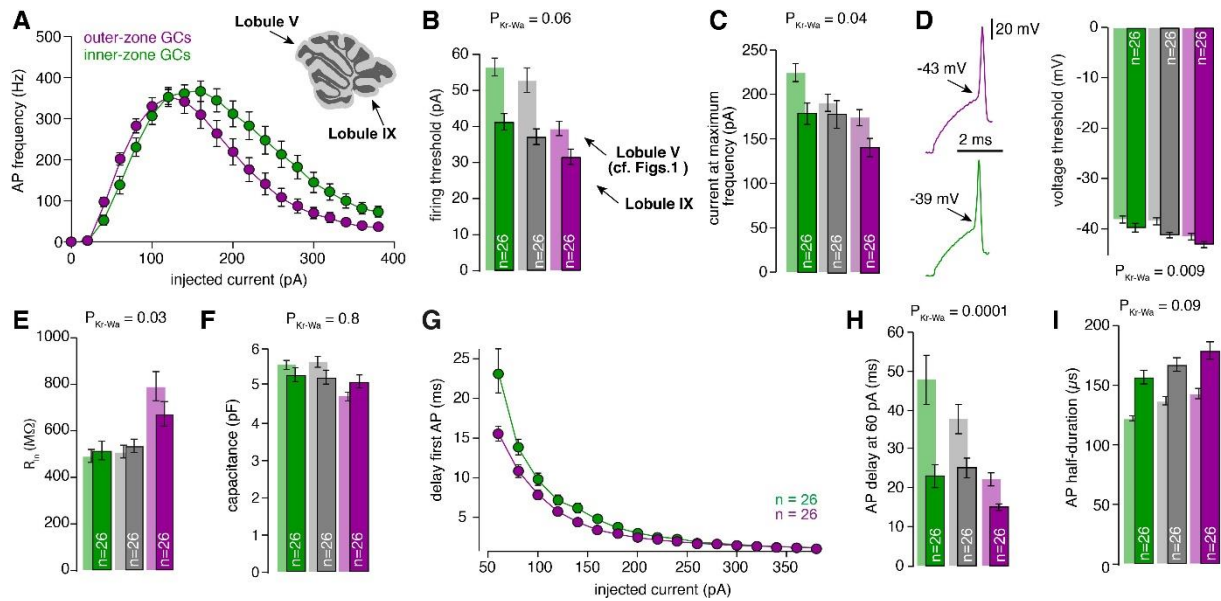
Figure 1 - figure supplement 2

Gradients in the biophysical properties of GCs and PFs are preserved throughout the cerebellar cortex
(A) Average action potential frequency from inner (green) and outer-zone GCs (magenta) plotted against the injected current. Inset: An image of a cerebellar slice indicating lobule V and lobule IX by arrows. (B) Bar graphs represent the firing threshold of GCs from inner (dark-green), middle (dark-gray) and outer-zone (dark-magenta). The light-colored bar graphs in the background are the data from lobule V shown in Figure 1. Firing threshold is higher in inner- compared to outer-zone GCs from lobule IX, and with the same current injection, GCs from lobule IX fire action potentials faster compared to lobule V. The numbers of recorded GCs for lobule IX (n) are indicated (P_{Dunns} = 0.06 for inner- vs outer-zone GCs). (C) Average current needed to elicit the maximum number of action potentials for of inner- (green), middle- (gray) and outer-zone GCs (magenta) (P_{Dunns} = 0.06 for inner- vs outer-zone GCs). (D) Left: example action potentials from an inner- and outer-zone GC with the indicated (arrows) mean voltage threshold for firing action potentials. Right: Average voltage threshold to elicit action potentials in inner-, middle- and outer-zone GCs from lobule IX compared with data from lobule V. Voltage threshold for outer-zone GCs is lower compared to inner-zone GCs from lobule IX (P_{Dunns} = 0.009 for inner- vs outer-zone GCs). (E) Input resistance of GCs from outer-zone of lobule IV is higher compared to inner- and middle-zone GCs but there is no difference between the input resistance of GCs from lobule V and IX (P_{Dunns} = 0.03 for inner-vs outer-zone GCs). (F) Average capacitance of inner-, middle- and outer-zone GCs. In contrary to lobule V, there is no difference in the capacitance of GC from inner-, middle, or outer-zone (P_{Dunns} = 0.8 for inner- vs outer-zone GCs). (G) Delay of the first action potential plotted against the injected current. (H) Delay of the first action potential after a current injection of 60 pA from inner-, middle- and outer-zone GCs from lobule IX compared to lobule V (P_{Dunns} = 0.01 for inner- vs outer-zone GCs). (I) The action potential half-duration of inner-zone (dark-green) GCs from lobule IX is shorter compared to middle (dark-gray)- and outer-zone (dark-magenta) GCs (P_{Dunns} = 0.09 for inner- vs outer-zone GCs). Compared to lobule V (light-colored bar graphs), the GCs from lobule IX showed a broader action potential half-width.
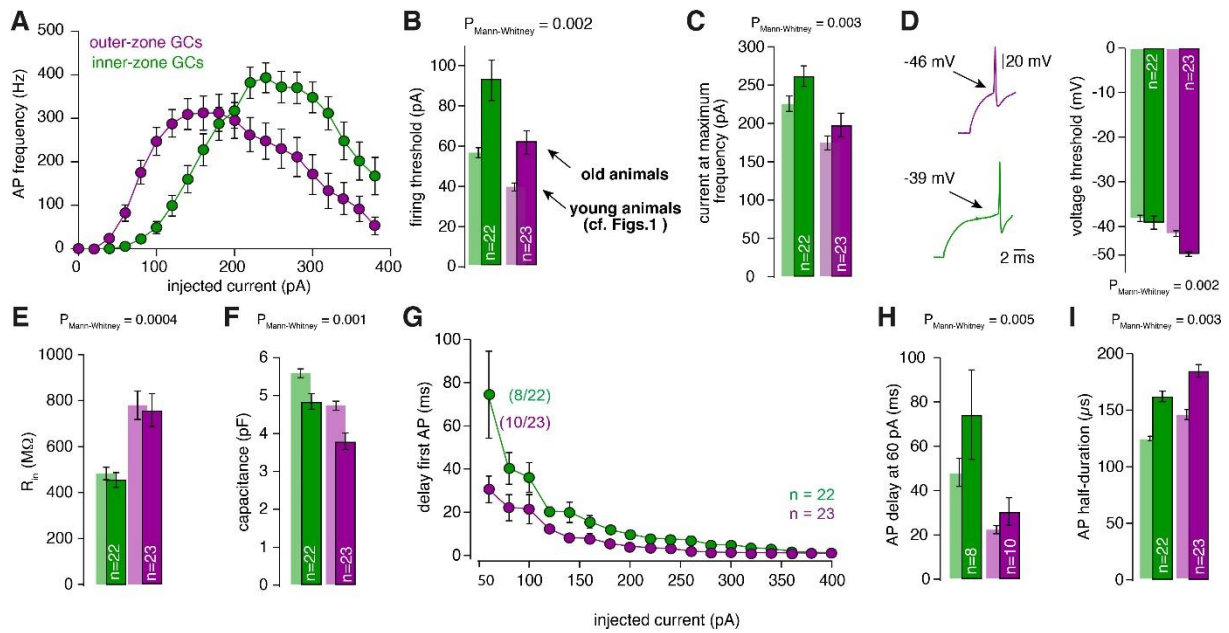
Figure 1 - figure supplement 3

Gradients in the biophysical properties of GCs and PFs are also found in 3-month-old animals
(A) Average action potential frequency from inner (green) and outer (magenta) zone GCs plotted against the injected current for 3-month-old animals. For all these measurements GCs from lobule V were used. (B) Bar graphs represent the firing threshold of GCs from inner (dark-green) and outer-zone (dark-magenta). The light-colored bar graphs in the background are the data from lobule V in young (21–30 days-old) animals shown in Figure 1. Firing threshold is higher in inner- compared with outer-zone GCs from old animals. (C) Average current needed to elicit the maximum number of action potentials for of inner- (green) and outer-zone GCs (magenta). (D) Left: example action potentials from an inner- and outer-zone GC with the indicated (arrows) mean voltage-threshold for firing action potentials. Right: Average voltage threshold to elicit action potentials in inner and outer-zone GCs from old animals compared with data from young animals. (E) Input resistance of GCs from outer-zone is higher compared to inner-zone GCs. But there is no difference between the input resistance of GCs from young and old animals. (F) Average capacitance of inner- and outer-zone GCs. In agreement with the data from the young animals, inner-zone GCs have a higher capacitance compared to outer-zone GCs. (G) Delay of the first action potential plotted against the injected current. Since the mean current threshold is higher compared to young animals only 8 out of 22 GCs from inner- and 10 out of 23 GCs from outer-zone already fired action potentials at a current injection of 60 pA. (H) Delay of the first action potential after a current injection of 60 pA from inner-, middle- and outer-zone GCs from old animals compared to young animals. (I) The action potential half-duration of inner-zone (dark-green) GCs from old animals is shorter compared with outer-zone (dark-magenta) GCs.
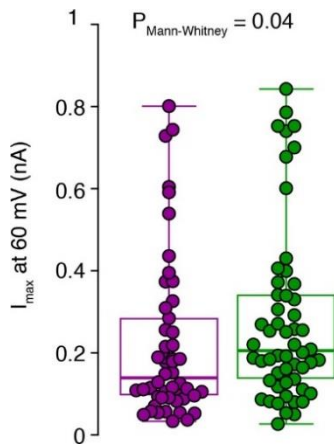
81

Figure 2 - figure supplement 1

Raw data of the amplitude of potassium currents at 60 pA current injection
Peak amplitudes of single-cell potassium currents from inner-(green) and outer-zone CGs (magenta) after 60 pA current injection are shown together with box plots (median and interquartile range with whiskers).
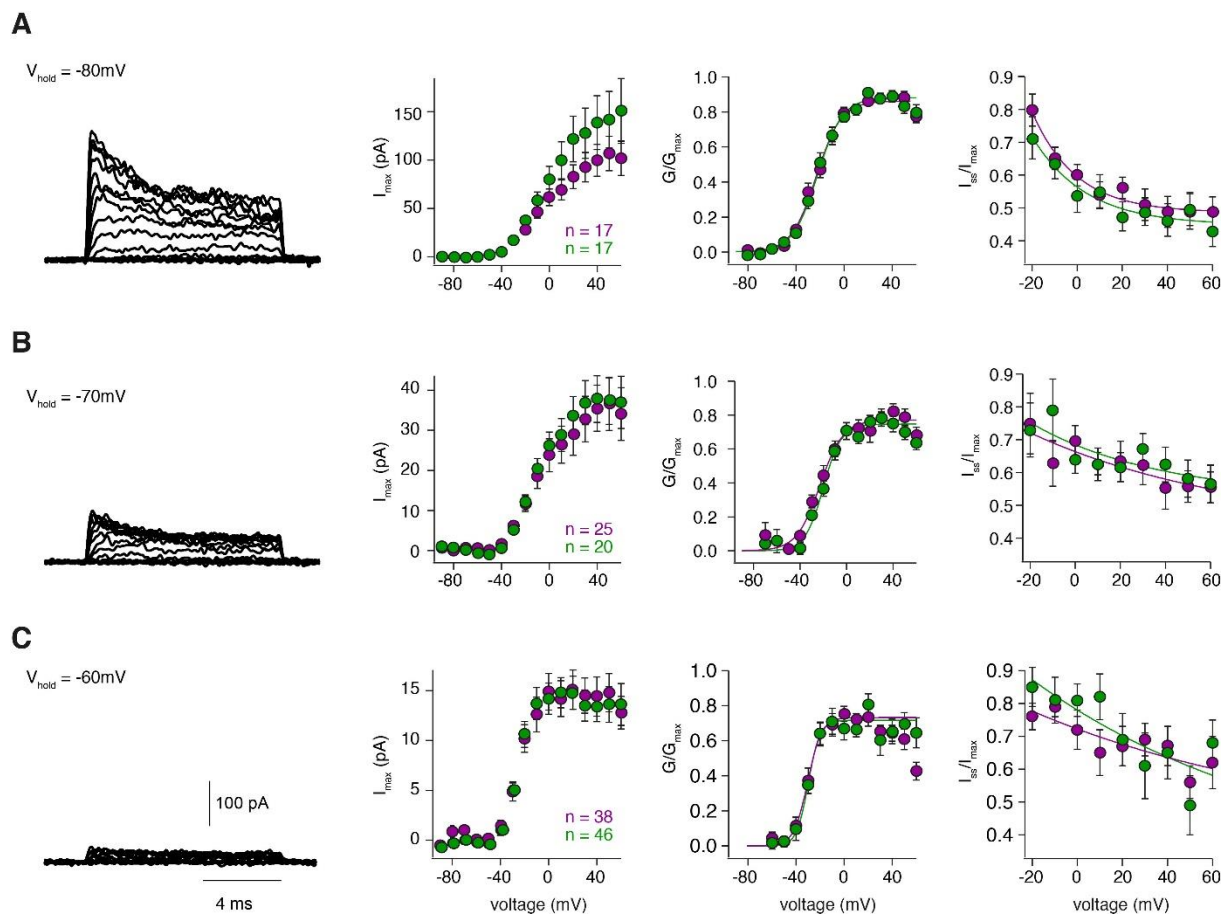
Figure 2 - figure supplement 2

Steady-state activation and inactivation are similar for inner and outer GCs
(A – C) left: Example potassium currents from outside-out patches of cerebellar GCs evoked by voltage steps from −90 to +60 mV in 10 mV increments with a duration of 10 ms. The intersweep holding potential varied between −80 mV (A), −70 mV (B) and −60 mV (C). Panels show the corresponding current-voltage relationship (first panel) of inner- (green) and outer-zone GCs (magenta), the normalized conductance (second panel) and the normalized inactivation behavior (third panel). The number of measured cells is indicated in the figure.
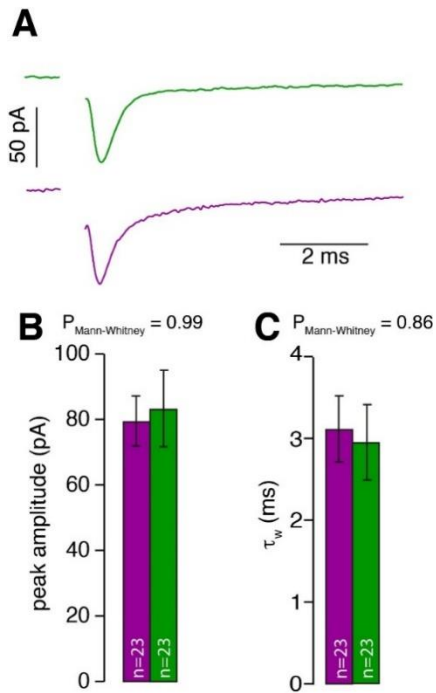
Figure 3 - figure supplement 1

MF input is similar for inner- and outer-zone GCs
(A) Examples of single EPSCs measured from inner- (green) and outer-zone GCs (magenta) after 1 Hz stimulation of MF axons. Stimulation artifacts were removed. (B) Average amplitude of EPSCs from inner- (green) and outer-zone GCs. (C) Weighted decay time (Equation 4) of EPSCs from inner- (green) and outer-zone GCs (magenta).
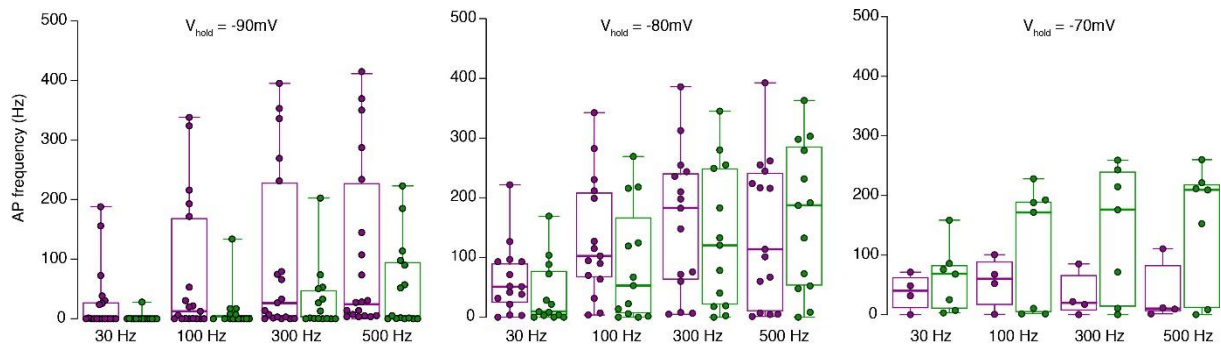
Figure 3 - figure supplement 2

Raw data of the bar graphs from Figure 3. Same data as in Figure 3D, but shown as box plots (median and interquartile range with whiskers) superimposed with single data points
The same color code as in Figure 3 is used for inner- (green) and outer-zone (magenta) GCs.

Figure 4 - figure supplement 1

Raw data of the traces shown in Figure 4B
Data of Figure 4B are shown as single cell data (each cell is one line) superimposed with the median (circles) and interquartile range (error bars). Upper graph: inner-zone GCs in green, lower graph: outer-zone GCs in magenta.
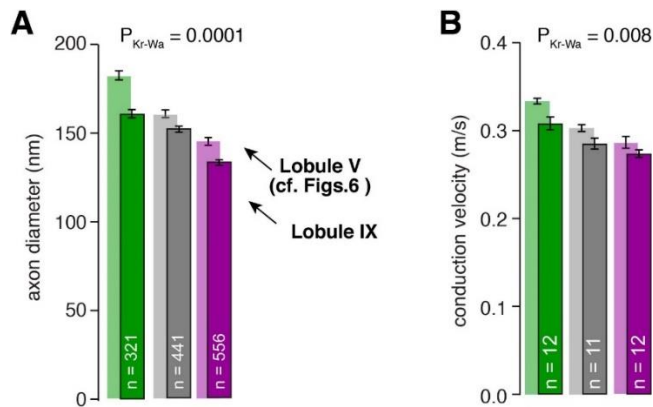
Figure 6 - figure supplement 1

Differences in axon diameter and conduction velocity are also found in lobule IX
(A) Summary of axon diameters in the inner- (green), middle- (gray), and outer-zone (magenta) of the molecular layer (P_{Dunns} = 0.0001 for inner- vs outer-zone GCs). The light-colored bar graphs in the background are the data from lobule V shown in Figure 6. (B) Summary of conduction velocity in the inner-, middle- and outer-zone of of the molecular layer of lobule IX (P_{Dunns} = 0.007 for inner- vs outer-zone).
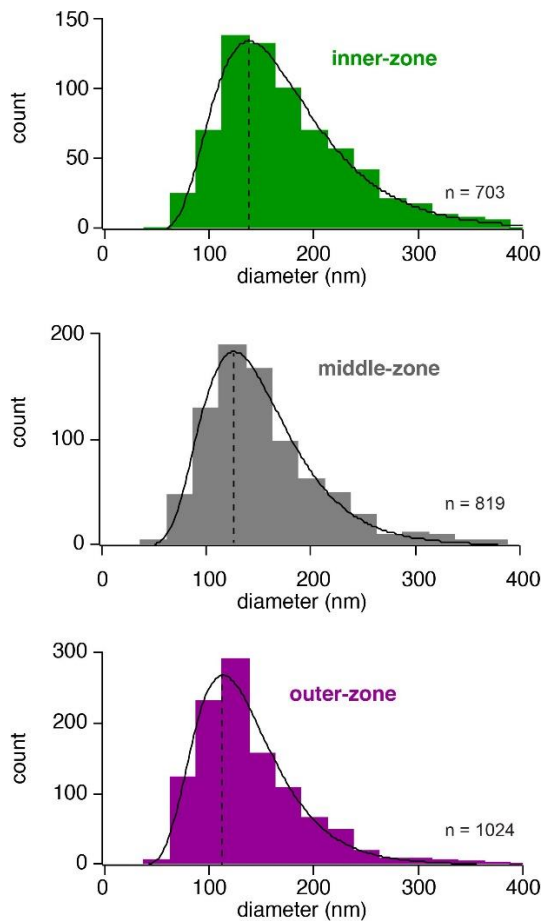
Figure 6 - figure supplement 2

Histogram of the axon diameters
Histograms of the diameter of inner-, middle- and outer-zone axons in the molecular layer. Data were fit with a skewed Gaussian function: $a\, e^{\left[-\log(2)\left(\left(\log\left(1+2b\frac{d-d0}{ds}\right)/b\right)^2\right)\right]}$, where a is the amplitude, d the diameter, and $d0$ the diameter at the peak. ds and b represent parameters related to the width and the skewness, respectively. The peak is indicated by a vertical line.
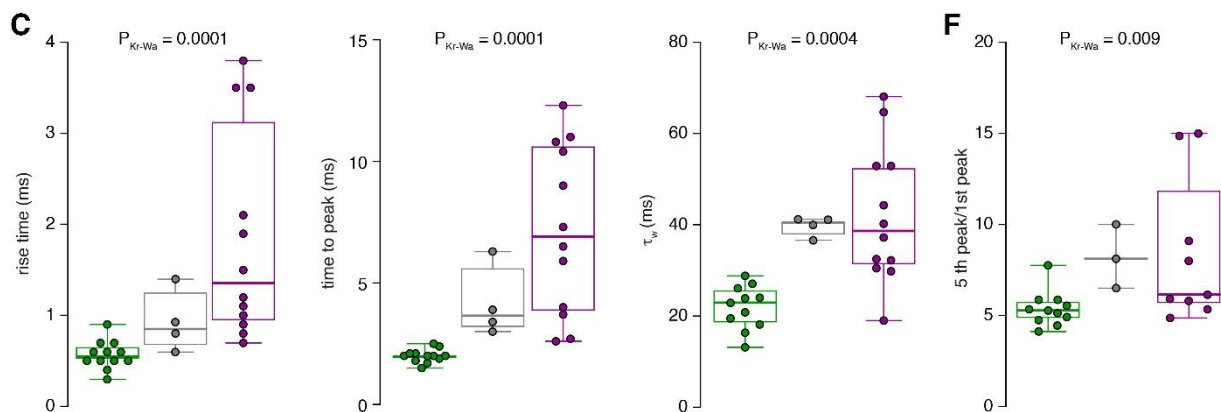
Figure 7 - figure supplement 1

Raw data of the bar graphs from Figure 7

The data from panels of Figure 7 with bar graphs are shown as box plots (median and interquartile range with whiskers indicating the entire range) superimposed with the single data points. The same color code as in Figure 7 is used for inner- (green), middle- (gray) and outer-zone (magenta) GCs, respectively.
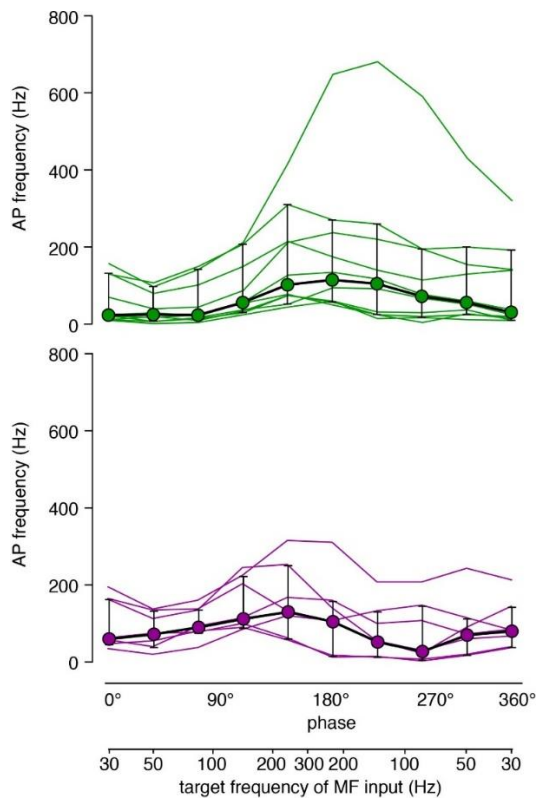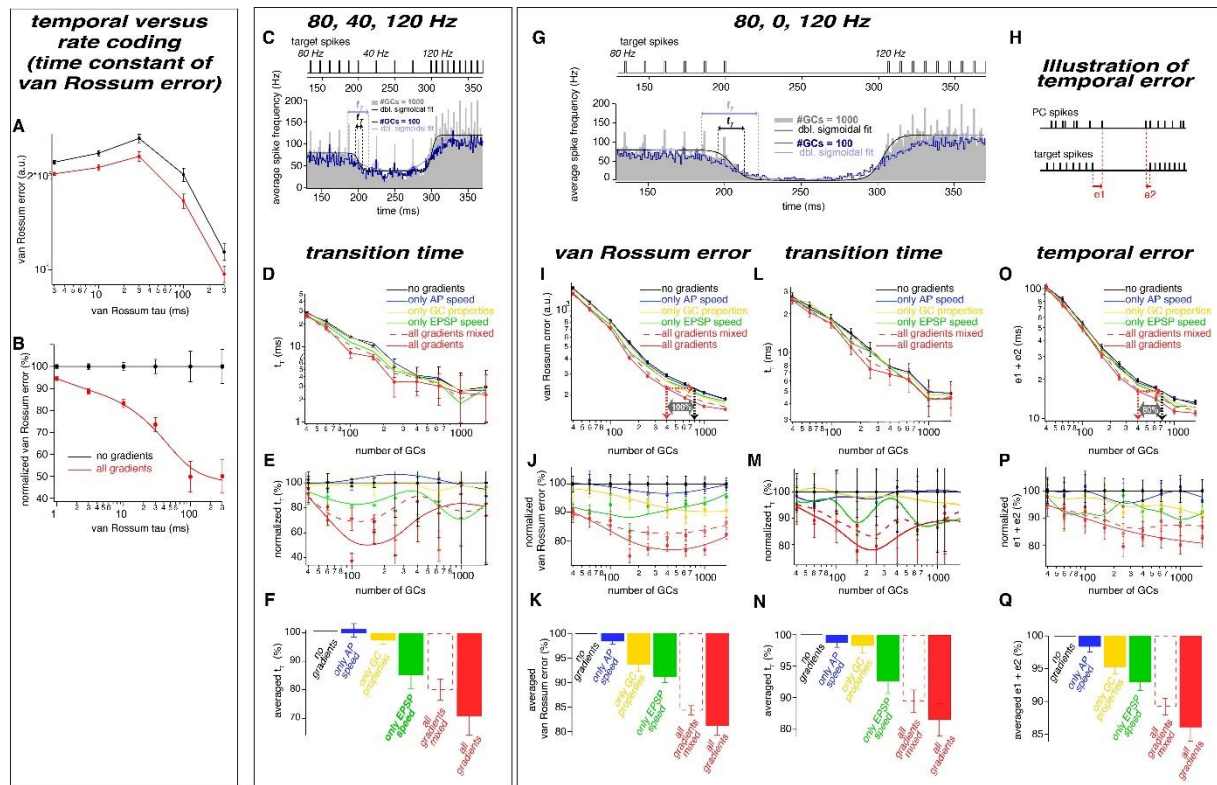

Figure 8 - figure supplement 1

The observed neuronal gradients reduce the temporal error and improve rate coding of PC spikes
(A) Double logarithmic plot of the van Rossum error of models with 300 GCs without (black) and with all gradients (red) plotted versus the time constant of the van Rossum kernel ranging from 2 to 300 ms. (B) Data as in panel A normalized to the model without gradients. (C) Average spiking histogram for models consisting of 100 and 1000 GCs, superimposed with double sigmoidal fits constrained to 80, 40 and 120 Hz. The target spiking sequence is indicated above. The data is reproduced from Fig. 8B for direct comparison with panel G. (D) Double logarithmic plot of the transition time (t_T) of the double exponential fits as illustrated in panel C. To minimize the impact of outliers caused by unstable conversion of double exponential fits, the data presented as median and the error bars represent 95% confidence intervals. (E) Transition time (t_T) as shown in panel D but normalized to the value of the model without gradients, superimposed with a smoothing spline interpolation. (F) Average of the relative differences shown in panel E. (G) Average spiking histogram for models consisting of 100 and 1000 GCs, superimposed with double sigmoidal fits constrained to 80, 0 and 120 Hz. The target spiking sequence with 80, 0, and 120 Hz is indicated above. (H) Illustration of the temporal error (e1 and e2) of the spikes defining the beginning and the end of the pause. (I-Q) Analyses for the 80, 0, 120 Hz target sequence including the van Rossum error (I-K), the transition time (t_T) (L-N) and the temporal error (O-Q).

4. Publication 3

Title: **Enriched environment shortens the duration of action potentials in cerebellar granule cells**

Enriched Environment Shortens the Duration of Action Potentials in Cerebellar Granule Cells

Abdelmoneim Eshra[1], Petra Hirrlinger[2] and Stefan Hallermann[1]*

[1] Medical Faculty, Carl-Ludwig-Institute for Physiology, Leipzig University, Leipzig, Germany, [2] Medical Faculty, Medizinisch-Experimentelles Zentrum, Leipzig University, Leipzig, Germany

Environmental enrichment for rodents is known to enhance motor performance. Structural and molecular changes have been reported to be coupled with an enriched environment, but functional alterations of single neurons remain elusive. Here, we compared mice raised under control conditions and an enriched environment. We tested the motor performance on a rotarod and subsequently performed whole-cell patch-clamp recordings in cerebellar slices focusing on granule cells of lobule IX, which is known to receive vestibular input. Mice raised in an enriched environment were able to remain on an accelerating rotarod for a longer period of time. Electrophysiological analyses revealed normal passive properties of granule cells and a functional adaptation to the enriched environment, manifested in faster action potentials (APs) with a higher depolarized voltage threshold and larger AP overshoot. Furthermore, the maximal firing frequency of APs was higher in mice raised in an enriched environment. These data show that enriched environment causes specific alterations in the biophysical properties of neurons. Furthermore, we speculate that the ability of cerebellar granule cells to generate higher firing frequencies improves motor performance.

Keywords: enriched environment, action potential, granule cell, cerebellum, electrophysiology

INTRODUCTION

Environmental enrichment (EE) refers to refined conditions for housing animals, which result in enhanced motor, social, sensory and cognitive performances (Nithianantharajah and Hannan, 2006). In the 1940s, Donald Hebb used EE and showed that rats, which were raised in his home, had superior problem solving abilities compared to laboratory-raised rats (Hebb, 1947, 1949). In addition, EE has been reported to improve motor performance when checked with assays such as rotarod, eyeblink conditioning, grid walking, rope suspension, footfault, and walk initiation tests (Madroñal et al., 2010; Horvath et al., 2013; Lee et al., 2013).

On the anatomical level, EE leads to thicker regions in the cerebellar cortex (Diamond et al., 1966) and altered dendritic and spine morphology (Volkmar and Greenough, 1972; Restivo et al., 2005). EE robustly induces neurogenesis in the hippocampus (Kempermann et al., 1997) and cell proliferation in the amygdala (Okuda et al., 2009) as well as gliogenesis, manifested in an increase in the number of new astrocytes in the visual cortex (Sirevaag and Greenough, 1987), the motor cortex (Ehninger and Kempermann, 2003) and the hippocampus (Kronenberg et al., 2007). Furthermore, EE increases the number of myelin-forming oligodendrocytes (Szeligo and Leblond, 1977; Sirevaag and Greenough, 1987) and the number of myelinated fibers in the cerebral white matter (Yang et al., 2013).

88

On the molecular level, EE has been extensively studied. A change in the expression level of many genes involved in neuronal structure, synaptic plasticity, and neurotransmission have been reported (Rampon et al., 2000; Barak et al., 2013). Moreover, the expression levels of brain-derived neurotrophic factor (BDNF) and nerve growth factor (NGF) were found to be increased in association with EE (Torasdotter et al., 1998; Rossi et al., 2006).

Granule cells are the most abundant neurons in the brain (Williams and Herrup, 1988), representing the input layer, which translates mossy fiber signals into parallel fiber signals that project to Purkinje cells (Eccles et al., 1967). Granule cells seem to have various functional roles for sensory processing (Chadderton et al., 2004), locomotion (Powell et al., 2015), and reward predictions (Wagner et al., 2017). To gain a better understanding of the improvement of motor performance induced by EE on a cellular level, we here focused on the biophysical properties of granule cells in a specific region of the cerebellum, lobule IX, which receives vestibular sensory signals (Barmack, 2003) and is involved in motor tasks such as the rotarod test (Ruediger et al., 2011). We found that EE changed fundamental biophysical parameters of granule cells, such as the duration of action potentials.

MATERIALS AND METHODS

Animals and Housing

Mice were bred and treated in accordance with the German Protection of Animals Act and with the guidelines for the welfare of experimental animals issued by the European Communities Council Directive. Mice were housed in either EE or control conditions from birth (pre-weaning) until the age of P70-80 before testing. The EE cages were designed to be bigger (height: 140 and 150 mm, for control and EE, respectively; bottom: 252 × 167 and 427 × 267 mm, for control and EE, respectively) and contained climbing ladders, plastic tubes, tunnels and small boxes as well as a variety of other toys like igloos and saucer wheels (**Figure 1A**). Groups of mice designated to the EE cohort were housed in larger groups (∼5 and ∼9, for control and EE, respectively) to allow more social interactions. The configuration of the EE was changed approximately twice per week by rearranging the position of the toys and by adding and removing toys to provide novelty, complexity, and different opportunities for learning. Both mice groups, EE and controls, were housed under an appropriate temperature (21–23°C) and humidity (40–60%) in a controlled atmosphere with a 12 h/12 h light/dark cycle, and had free access to both water and food.

Preparation and Electrophysiology

Acute cerebellar slices were prepared from mature (P70–80) C57BL/6 mice of either sex. Mice were lightly anaesthetized with isoflurane and killed rapidly by decapitation. The cerebellar vermis was removed quickly and then placed in a chamber filled with ice-cold extracellular solution. Parasagittal slices of 300 μm were cut using a Leica VT1200 microtome (Leica Microsystems, Wetzlar, Germany), transferred to an incubation chamber at ∼35°C for 30 min, and subsequently stored at room temperature.

The extracellular solution for slice preparation, storage, and electrophysiological recordings contained (in mM) the following: NaCl 125, NaHCO$_3$ 25, glucose 20, KCl 2.5, CaCl$_2$ 2, NaH$_2$PO$_4$ 1.25 and MgCl$_2$ 1 [310 mOsm, pH 7.3 when bubbled with Carbogen (5% (vol/vol) O$_2$ and 95% (vol/vol) CO$_2$)].

Cerebellar granule cells were visualized after mounting a slice into a recording chamber placed on the stage of a Nikon upright microscope equipped with infrared differential interference contrast. Slices were continuously superfused with extracellular solution and the temperature in the center of the recording chamber was set to 36°C using a TC-324B perfusion heat controller (Warner Instruments, Hamden, CT, United States). Patch pipettes were pulled from borosilicate glass (Science Products, Hofheim, Germany) using a DMZ Puller (Zeitz-Instruments, Munich, Germany). Patch pipettes had open-tip resistances of 6–8 MΩ (when filled with intracellular solution). The intracellular solution contained the following (in mM): K-gluconate 150, NaCl 10, K-HEPES 10, MgATP 3 and Na-GTP 0.3 (300–305 mOsm, pH adjusted to 7.3 with KOH). Whole-cell patch-clamp recordings from granule cells were made using a HEKA EPC10/2 amplifier (HEKA Elektronik, Lambrecht, Germany) operated by the corresponding software PatchMaster (HEKA Elektronik), running on a personal computer. Recordings were performed in the middle region of the granule cell layer of lobule IX of the cerebellar vermis. Measurements were corrected for a liquid junction potential of +13 mV. Series resistance was typically <40 MΩ. Experiments with series resistance >40 MΩ were excluded. Action potentials were evoked in current-clamp mode by injecting brief current pulses (amplitude 10–500 pA; duration 300 ms). Recordings from neurons of mice raised in an enriched environment and the corresponding control, of the same gender, were done in the same day in an interleaved manner.

Rotarod Test

Before testing began, mice were given a trial in order to familiarize them with the procedure. Mice were placed on the rotarod (Panlab, Harvard apparatus) at a constant acceleration from 4 to 40 rounds per minute for a total of 120 s so that the longer the mouse remained on the rod, the faster it had to move to maintain balance. Each time the mouse fell, it was immediately returned to the rod and the process was restarted for ∼10 trials per mouse. EE and control mice were compared on an animal-to-animal basis by averaging the latencies per mouse (**Figure 1B**) and on a trial-to-trial basis by averaging the latencies per trial number (**Figure 1C**). Motor assessment of each EE mouse and the corresponding control, having the same gender, was done on the same day, and both were later sacrificed to be used for electrophysiological recordings.

Analysis of Action Potential Parameters

Data were analyzed using custom-made procedures in Igor Pro software (WaveMetrics, Tigard, OR, United States). The parameters of the action potentials (APs) were determined in the trace at current threshold, the trace with 60-pA-current injection, and the trace with most APs elicited. In each of these three traces the analysis was restricted to the first AP, average of the first five

FIGURE 1 | Enriched environment improves motor performance. **(A)** Example photographs of EE cage showing different items placed during the housing of the mice. **(B)** Left: Bar graphs showing comparison of the absolute latency on the rotarod per animal (animal-to-animal basis). Right: Bar graph of the average latency on the rotarod assessment test for EE and control mice, $n = 14$ and 14 mice, respectively; Student's t-test was used to measure statistical significance, $P_{t-test} = 0.007$. **(C)** Left: Bar graphs showing comparison of the absolute latency on the rotarod per trial number (trial-to-trial basis). Right: Bar graph of the grand average of the latency on the rotarod, $n = 123$ and 123 trials, for control and EE mice, respectively; $P_{t-test} = 5 \times 10^{-6}$.

APs at the beginning of the current injection, and average of all APs. In traces with less than five APs, the value for the first five APs was the average of those up to four APs. In four and one out of 299 cells in control and EE mice, respectively, the current threshold was above 60 pA, and accordingly the numbers of cells for the 60-pA-current trace were 295 and 298 for control and EE mice, respectively. The half duration of AP was measured at half maximum amplitude. The amplitude was measured from threshold to peak. The threshold was defined as the membrane voltage at which the first derivative exceeded 100 V/s. Action potentials with a peak smaller than −20 mV, an amplitude smaller than 20 mV, and a half duration smaller than 50 μs or larger than 500 μs were excluded. These exclusion criteria were chosen to ensure that only proper APs are analyzed. For example, the distribution of AP duration is well within the 50 and 500 μs borders (**Supplementary Figure S2B**).

Statistics

Data are presented as mean ± SEM. To provide a simple measure of the statistical difference of the shown comparisons, the P-value of the Student's t-test is provided for each bar graph (using Microsoft Excel or Igor Pro software). In addition, a four-way ANOVA test with the following four factors was used: (1) AP parameters (half-duration, amplitude, overshoot and threshold), (2) trace per cell (trace at current threshold, trace with 60 pA, and trace with maximal number of APs), (3) APs per trace (first AP, first five APs, and average of all APs), and (4) animal group (control and EE). For the comparison of control vs. EE mice (4th factor), the P-value was 0.0002. However, the significance level of the four-way ANOVA is most likely

an overestimation, because the investigated parameters are not completely independent. We therefore focused on the P-values of the t-test (P_{t-test}). For each of the four AP parameters, there was the same trend between control and enriched conditions in the various analyzed APs. In addition, we addressed the statistical significance of the difference of the AP half duration not only on a neuron-to-neuron but also on a mouse-to-mouse basis (i.e., the average value for each mouse). To address the significance of the correlations (**Figure 4D** and **Supplementary Figures S3A,B**), we provided the Pearson correlation coefficient ($R_{Pearson}$) and the corresponding P-value ($P_{Pearson}$) as well as the P-value of the Spearman rank correlation coefficient ($P_{Spearman\ Rank}$). T-tests were calculated with Microsoft Excel and the other statistical tests with built-in functions of Mathematica 10 (Wolfram Research, Champaign, IL, United States).

RESULTS

Enriched Environment Improves Motor Performance

To investigate the effect of continuous long-term EE (**Figure 1A**) on the motor performance of mice, we used the rotarod test. The performance of mice raised in an EE (referred to as EE mice in the following) was significantly better on the rotating rod than the corresponding control mice. This was manifested in a significantly longer latency to fall from the rotarod in the case of EE mice than for the corresponding controls, both for animal-to-animal overall performance (38.7 ± 2.1 and 53.2 ± 4.5 s for control and EE mice, $n = 14$ and 14 mice, respectively;

FIGURE 2 | Action potentials of EE mice have shorter half duration. (A) Example voltage traces upon injecting current of increasing amplitudes (orange: trace at current threshold; cyan: trace with 60-pA-current injection; red: trace with maximum APs fired; green: trace with highest current injection and decrease in APs number). (B) Top: Magnification of the shaded part in panel (A) showing an example of APs. Bottom: Corresponding magnification showing a single AP. (C) Average AP half duration for control and EE mice (orange: trace at current threshold, n = 299 and 299 cells; cyan: trace with 60-pA-current injection, n = 295 and 298 cells; red: trace with maximum APs fired, n = 299 and 299 cells). From left to right, analysis of first AP, first five APs, and average of all APs. All the P-values shown are from Student's t-test.

P_{t-test} = 0.007; **Figure 1B**) and for trial-to-trial basis (38.1 ± 0.9 and 51.3 ± 1.4 s for control and enriched animals, n = 123 and 123 trials, respectively; P_{t-test} = 5 × 10^{-6}; **Figure 1C**). This is consistent with previous findings where EE was reported to have a direct effect on motor functions when assessed with different motor coordination assays (Madroñal et al., 2010; Horvath et al., 2013; Lee et al., 2013). These data indicate that EE mice have improved motor capabilities as evaluated by the rotarod test.
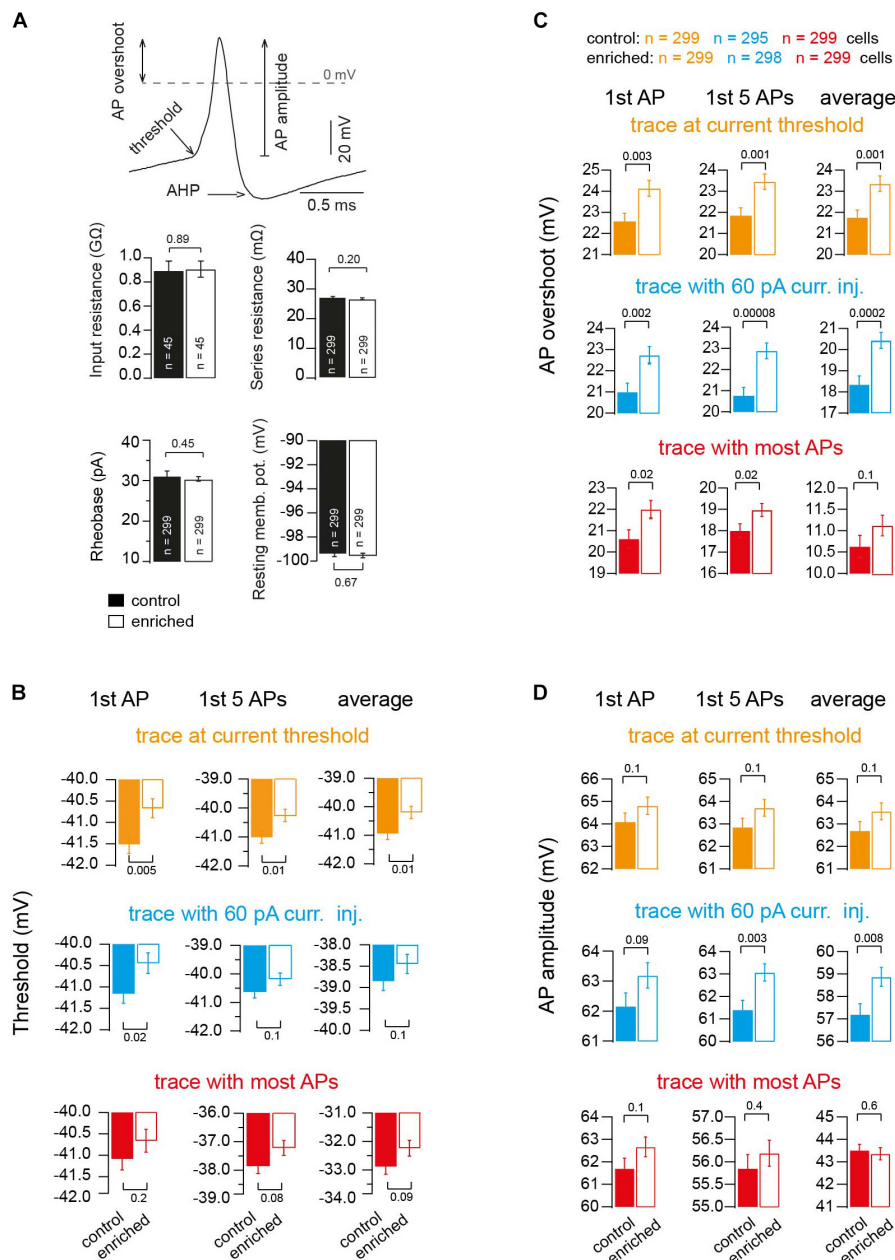
Action Potentials of EE Mice Have Shorter Half Duration

To test if and how these improvements in motor skills go along with alterations of the biophysical parameters of single neurons, we performed whole-cell current-clamp recordings from granule cells and measured the excitability of the neurons and the properties of the APs. We analyzed 90,750 APs, in 600 neurons in 30 mice, elicited by injection of depolarizing current of different amplitudes (10–500 pA; **Figure 2A**). Due to several reasons (like AP broadening and amplitude reduction), which can change the AP shape over the duration of injected current, and in order to properly compare the APs in both conditions, we focused on three traces to be representative for all the APs fired per neuron: (1) the trace with lowest current injection and at least one AP (current threshold), (2) the trace where APs were elicited upon 60 pA current injection, and (3) the trace where the highest number of APs appeared. Within each of these three traces, we analyzed the first AP, the average of the first five APs, and the average of all APs (**Figure 2B**). The half duration of the AP of neurons of EE mice

was found to be significantly shorter than the half duration of APs of neurons of control mice (e.g., first AP in the traces at a current threshold: 166.1 ± 1.6 and 159.7 ± 1.5 μs for control and EE mice, n = 299 and 299, respectively; P_{t-test} = 0.002; **Figure 2C**). The analysis of other APs in other traces revealed similar results (**Figure 2C**). To further test the observed effect of EE on AP half duration, we compared the AP half duration on a mouse-to-mouse basis (i.e., the average value for each mouse). We found a tendency toward faster APs in EE compared to control mice (P_{t-test} ≈ 0.1; **Supplementary Figure S1**), indicating that a trend with a significance level of 10% exists even on a mouse-to-mouse basis. In order to test the robustness of our measurements, we compared the AP half duration of control mice of different ages from P20 to 1 year, and found that the AP half duration did not change significantly between different age groups (**Supplementary Figure S2A**), indicating that our technique allows precise and reliable determination of AP parameters. The AP seems to be a constant parameter throughout development between the age of P20 and 1 year. Despite this developmental constancy, our data demonstrate that the AP half duration of cerebellar granule cells of mice raised in an EE environment is shorter compared to the corresponding control mice.

Alteration in Threshold, Overshoot, and Amplitude of Action Potentials Upon Enrichment

To gain insight into the different biophysical properties of APs of EE mice, we first compared the input resistance by injecting

FIGURE 3 | Alteration in threshold, overshoot and amplitude of action potentials upon enrichment. **(A)** Example of an AP illustrating the criteria of measuring AP threshold, AP overshoot and AP amplitude. Bar graphs showing the average of resting membrane potential, $n = 299$ and 299 cells; input resistance, $n = 45$ and 45 cells; rheobase, $n = 299$ and 299 cells; and series resistance, $n = 299$ and 299 cells, of neurons of control and EE mice, respectively. **(B)** Average voltage threshold of APs of neurons of control and EE mice (orange: trace at current threshold, $n = 299$ and 299 cells; cyan: trace with 60-pA-current injection, $n = 295$ and 298 cells; red: trace with maximum APs fired, $n = 299$ and 299 cells). From left to right, analysis of first AP, first five APs and average of all APs, respectively. **(C)** Corresponding average AP overshoot. **(D)** Corresponding average AP amplitude. All the P-values shown are from Student's t-test.

current of low amplitude into a subset of granule cells (∼3) from each animal of either the EE or control groups, and observed no significant change (0.88 ± 0.08 and 0.90 ± 0.07 GΩ, for control and EE mice, $n = 45$ and 45, respectively; $P_{t-\text{test}} = 0.89$; **Figure 3A**). Other passive parameters of neurons were similar, too (series resistance: 27.4 ± 0.4 and 26.7 ± 0.4 MΩ, for control and EE mice, $n = 299$ and 299, respectively; $P_{t-\text{test}} = 0.2$;

rheobase: 31.3 ± 1.1 and 30.4 ± 0.5 pA; $P_{t-\text{test}} = 0.45$; and resting membrane potential: -99.4 ± 0.3 and -99.5 ± 0.2 mV; $P_{t-\text{test}} = 0.67$; **Figure 3A**).

In order to gain more mechanistic insights, we focused on additional parameters of the APs and found that the threshold potential of the APs of EE mice had a more depolarized voltage than the APs of control mice (e.g., first AP in the traces at current

threshold: -41.5 ± 0.21 and -40.67 ± 0.22 mV for control and EE mice, $n = 299$ and 299, respectively; $P_{t-test} = 0.005$). The analysis of other APs in other traces revealed similar results (**Figure 3B**). The maximum peak of the voltage overshoot reached during the AP was higher in EE compared to control mice (e.g., first AP in the traces at current threshold 22.58 ± 0.36 and 24.13 ± 0.37 mV, for control and EE mice, $n = 299$ and 299, respectively, $P_{t-test} = 0.003$). The analysis of other APs in other traces revealed similar results (**Figure 3C**). Furthermore, there was also a tendency for the absolute amplitude of APs to be higher in the case of EE mice compared to control mice (e.g., first AP in the traces at current threshold 64.09 ± 0.38 and 64.8 ± 0.38 mV, for control and EE mice, $n = 299$ and 299, respectively, $P_{t-test} = 0.1$). The analysis of other APs in other traces revealed similar results (**Figure 3D**).

Interestingly, when analyzing the after-hyperpolarizing (AHP) component of the APs, there was no significant difference between EE and control mice. For the trace at current threshold, the delay between the peak (maximum) of the AP and the peak (minimum) of the AHP was not different between EE and control mice groups (402.6 ± 3.3 and 401.9 ± 3.4 μs for control and EE mice, $n = 299$ and 299, respectively; $P_{t-test} = 0.89$), and the AHP voltage did not change either (e.g., first AP in the traces at current threshold: -64.9 ± 0.2 and -64.8 ± 0.2 mV for control and EE mice, $n = 299$ and 299, respectively; $P_{t-test} = 0.85$). The analysis of other APs in other traces revealed similar results, indicating that channels responsible for the after-hyperpolarization of APs were not altered. Thus, these data indicate that several fundamental parameters of APs are altered in EE mice compared to control mice.

Enriched Environment Tunes Neurons for Firing at Higher Frequencies

The shortening of the AP half duration suggests that neurons are able to fire at higher frequencies after EE. We analyzed the maximum firing frequency of the first two APs (instantaneous frequency), the average of the first five APs, and average of all APs of the trace where most APs occurred (**Figure 4A**), and found that neurons of EE mice were able to reach higher firing frequencies than neurons of control mice (e.g., instantaneous frequency of 495.5 ± 9.8 and 521.6 ± 9.4 Hz, for control and EE mice, $n = 299$ and 299, respectively; $P_{t-test} = 0.05$; **Figure 4B**). We also analyzed the maximum firing frequency on a mouse-to-mouse basis corresponding to the analysis of the AP half duration in **Supplementary Figure S1**. Again, the maximum firing frequency showed a tendency to be larger in EE compared to control mice ($P_{t-test} \approx 0.1$; **Figure 4C**). Finally, we observed a correlation between the maximum firing frequency per animal (i.e., the average from ~20 granule cells) and the motor performance of the same animal measured on the same day (i.e., average latency of ~10 trials on the rotarod; **Figure 4D**). In addition, there was an inverse correlation between maximum firing frequency and AP half duration (**Supplementary Figure S3A**). As a result, there was also a tendency of an inverse correlation between the latency on the rotarod and the AP half duration (**Supplementary Figure S3B**; see last paragraph of the discussion for a cautious interpretation of the correlations described here). These data indicate that the maximal firing frequency of granule cells is higher in EE compared to control mice.
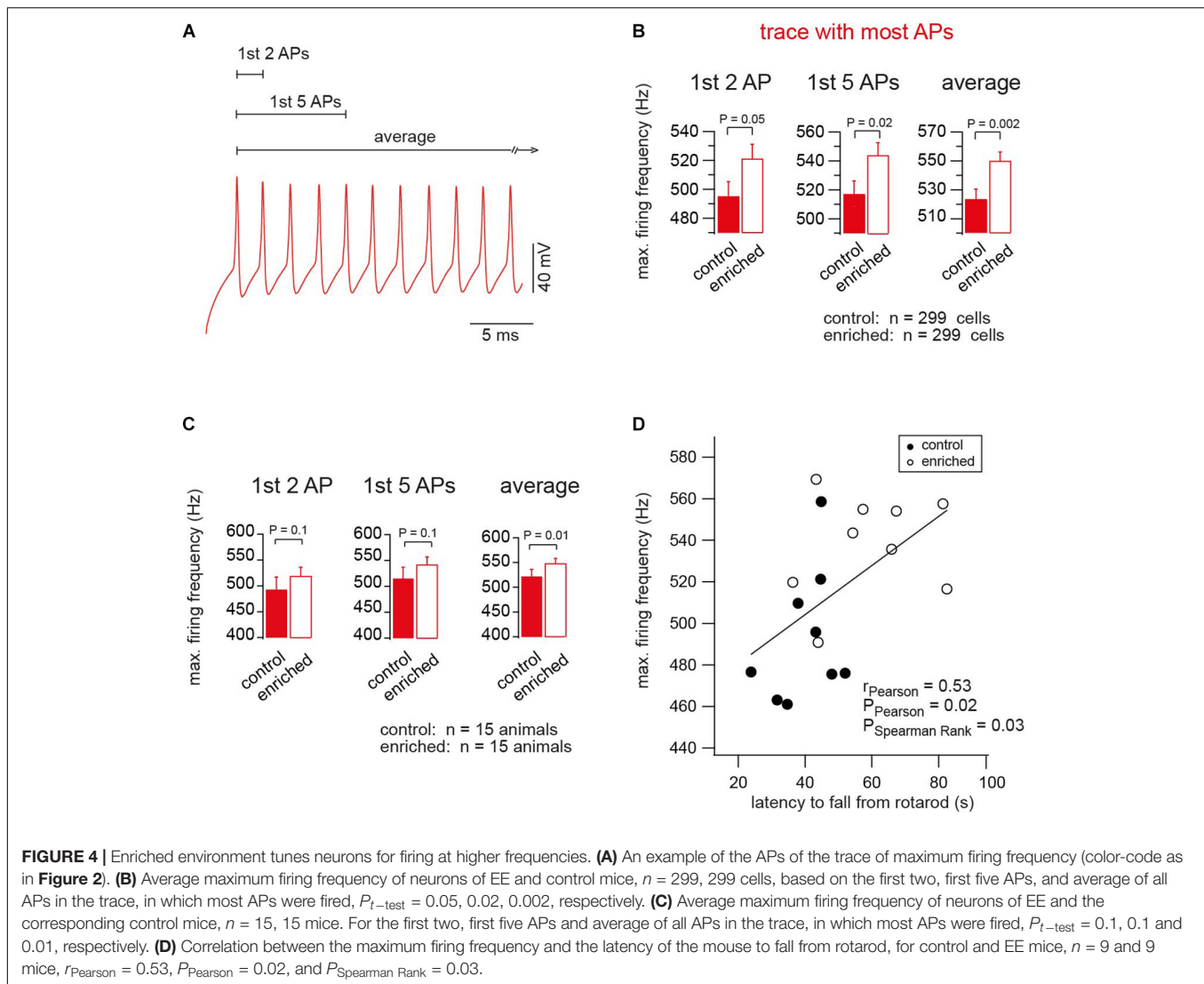
DISCUSSION

Our data show that, upon EE, cerebellar granule cells of lobule IX of the cerebellum have altered AP parameters and can fire APs at higher frequencies. Thus, fundamental biophysical parameters of the neurons are influenced by the environment. Furthermore, the maximal firing frequency of granule cells correlated with the motor performance of the mice. This correlation does not provide a causal relationship between firing rate and behavior, but it is tempting to speculate that higher firing frequencies of cerebellar granule cells are beneficial for rapid sensory-motor integration.

EE-Induced Changes in Action Potentials

We found that EE shortened the half-duration, increased the overshoot, and increased the threshold of APs. The observed effect is likely due to an alteration induced by EE on ion channels, so that voltage-gated potassium channels (K_v) and sodium channels (Na_v) have different densities and/or different properties (Keyvani et al., 2004). The observed shortening in the AP half duration could be explained by faster activating K_v channels. In fact, a regulatory effect of EE on potassium channels and particularly the regulatory subunit $K_v\beta1$ has been reported (Need et al., 2003). The observed increase in the amplitude and the threshold of APs could be linked to a change in the density or properties of Na_v channels. Interestingly, an effect of EE on sodium channel $Na_v1.6$ has been reported, in which EE decreased the amplitude of the ramp-induced persistent sodium current of the medium spiny neurons in the nucleus accumbens (Scala et al., 2018). Our data showing that the input resistance and the resting membrane potential were not altered upon EE is consistent with other work showing constant passive cell parameters during intrinsic homeostatic plasticity of cortical pyramidal neurons (Desai et al., 1999). Thus, the changes in ion channel properties and/or density upon EE are specific to channels shaping the AP and do not extend to channels setting the passive neuronal properties.

Our finding that EE alters AP properties adds to the emerging idea that AP properties are dynamically regulated. For example, it was recently shown that a direct modulation of presynaptic K_v channels in hippocampal mossy fiber boutons mediates a form of synaptic plasticity by activity-dependent release of arachidonic acid from the postsynaptic CA3 neurons (Carta et al., 2014). In addition, prominent alterations of AP half duration were observed during homeostatic plasticity induced in fast spiking interneurons (Miller et al., 2011). Furthermore, the AP half-duration of specific neurons in the amygdala and the cochlear nucleus was changed by fear extinction and noise exposure, respectively (Senn et al., 2014; Ngodup et al., 2015). Finally, altered neuronal activity in avian brainstem auditory neurons (Kuba et al., 2010) or hippocampal neurons (Grubb and Burrone, 2010) causes a rearrangement of the Na_v channels in the axon initial segment, contributing to the excitability and firing patterns

93

FIGURE 4 | Enriched environment tunes neurons for firing at higher frequencies. **(A)** An example of the APs of the trace of maximum firing frequency (color-code as in **Figure 2**). **(B)** Average maximum firing frequency of neurons of EE and control mice, $n = 299$, 299 cells, based on the first two, first five APs, and average of all APs in the trace, in which most APs were fired, $P_{t-test} = 0.05$, 0.02, 0.002, respectively. **(C)** Average maximum firing frequency of neurons of EE and the corresponding control mice, $n = 15$, 15 mice. For the first two, first five APs and average of all APs in the trace, in which most APs were fired, $P_{t-test} = 0.1$, 0.1 and 0.01, respectively. **(D)** Correlation between the maximum firing frequency and the latency of the mouse to fall from rotarod, for control and EE mice, $n = 9$ and 9 mice, $r_{Pearson} = 0.53$, $P_{Pearson} = 0.02$, and $P_{Spearman\ Rank} = 0.03$.

of neurons (Evans et al., 2015; Kole and Brette, 2018). Our results are thus consistent with a scenario, in which EE alters neuronal activity, which in turn induces plastic alterations in ion channels responsible for shaping the AP waveform.

Relation of Motor Performance and Firing Rate

Information can be coded as the average firing rate or as the temporal correlation of the exact time of the APs (Rieke et al., 1997). For example, vestibular, proprioceptive, and somatosensory information (Van Kan et al., 1993; Jörntell and Ekerot, 2006; Arenz et al., 2008) as well as the control of muscles (Adrian and Bronk, 1929) relies on rate coding. Our finding that improved motor performance correlates with AP frequency is therefore consistent with the idea that an increased bandwidth of firing accelerates information processing (reviewed in Delvendahl and Hallermann, 2016). Particularly, the increase in firing frequency of granule cells guarantees the precision of

information transfer from the granule cell level to the Purkinje cell level, assuring a more precise pace-making role for Purkinje cells, which is critical in motor coordination (Walter et al., 2006).

We observed both a shortening of the AP half duration and an increase in the maximal firing frequency upon EE. There was an inverse correlation between maximum firing frequency and AP half duration (**Supplementary Figure S3A**). Such inverse correlation has also been observed within vestibular nucleus neurons (Gittis et al., 2010), across cell types (Carter and Bean, 2009), and across different species (Wang et al., 2016). As expected from the correlation between the latency on the rotarod and the maximal firing frequency (**Figure 4D**), we therefore also observed a tendency for an inverse correlation between the latency on the rotarod and the AP half duration (**Supplementary Figure S3B**).

Thus, our data provide support to the idea that the duration of the AP and the maximum frequency of firing are related to the speed of sensory-motor information processing. Interestingly, action potential kinetics were recently shown to correlate with

another behavioral parameter (the intelligence quotient; IQ) in humans (Goriounova et al., 2018). However, several caveats should be considered regarding the relation between behavior and biophysical properties of neurons. (1) The correlations, which we observed here between performance on the rotarod and AP firing in granule cells, is statistically significant but not very strong. (2) The correlations do not imply causal relationships. (3) Our results were obtained in acute brain slices and future studies in freely behaving animals need to confirm the correlation between behavior and neuronal firing patterns *in vivo*. (4) Several other neuronal factors changing upon EE could contribute to the improved motor performance, such as myelination (Szeligo and Leblond, 1977; McKenzie et al., 2014), neuronal density (Kempermann et al., 1997), and dendritic and spine morphology (Volkmar and Greenough, 1972; Restivo et al., 2005). (5) Other parts of the nervous system (e.g., other types of neurons, other cerebellar lobules, the motor cortex, and the vestibular and proprioceptive systems) could change and cause the improved motor performance. (6) Factors independent of the nervous system (e.g., muscle strength and body weight) could underlie the improved rotarod performance. Yet, independent of the difficult question of the relation between behavior and neuronal biophysical properties, our data convincingly demonstrate that fundamental parameters such as AP duration and maximum firing frequency are influenced by the environment.

ETHICS STATEMENT

All experiments were approved in advance by the Institutional Ethics Committees and animals were treated in accordance with the European (EU Directive 2010/63/EU, Annex IV for animal experiments), national, and Leipzig University guidelines.

AUTHOR CONTRIBUTIONS

AE and SH designed the study, analyzed the data, and wrote the manuscript. AE performed the experiments. All authors approved the final version of the manuscript.

SUPPLEMENTARY MATERIAL

The Supplementary Material for this article can be found online at: https://www.frontiersin.org/articles/10.3389/fncel.2019.00289/full#supplementary-material

FIGURE S1 | Statistical analysis of AP half duration considering the average value for each mouse instead of the average value for each cell. The average AP half duration of 15 EE and 15 control mice is shown; (orange: trace at current threshold; cyan: trace with 60-pA-current injection; red: trace with maximum APs fired). From left to right, analysis of first AP, first five APs, and average of all APs, respectively. All the P-values shown are from Student's t-test.

FIGURE S2 | Constancy of action potential half duration between different age groups. **(A)** Average AP half duration of control mice of different age groups (n refers to the number of cells). **(B)** Histogram showing the distribution of the half duration of all APs recorded.

FIGURE S3 | Correlation between behavior and electrophysiology. **(A)** Correlation between maximum firing frequency and AP half duration, for control and EE mice, $n = 9$, 9 mice, $r_{Pearson} = 0.70$, $P_{Pearson} = 0.0007$, $P_{Spearman\ Rank} = 0.0002$. **(B)** Correlation between AP half duration and latency to fall from rotarod, for control and EE mice, $n = 9$, 9 mice, $r_{Pearson} = 0.43$, $P_{Pearson} = 0.07$, $P_{Spearman\ Rank} = 0.04$.

REFERENCES

Adrian, E. D., and Bronk, D. W. (1929). The discharge of impulses in motor nerve fibres: part II. The frequency of discharge in reflex and voluntary contractions. *J. Physiol.* 67, 119–151. doi: 10.1113/jphysiol.1929.sp002557

Arenz, A., Silver, R. A., Schaefer, A. T., and Margrie, T. W. (2008). The contribution of single synapses to sensory representation *in vivo*. *Science* 321, 977–980. doi: 10.1126/science.1158391

Barak, B., Shvarts-Serebro, I., Modai, S., Gilam, A., Okun, E., Michaelson, D. M., et al. (2013). Opposing actions of environmental enrichment and Alzheimer's disease on the expression of hippocampal microRNAs in mouse models. *Transl. Psychiatry* 3:e304. doi: 10.1038/tp.2013.77

Barmack, N. H. (2003). Central vestibular system: vestibular nuclei and posterior cerebellum. *Brain Res. Bull.* 60, 511–541. doi: 10.1016/S0361-9230(03)00055-8

Carta, M., Lanore, F., Rebola, N., Szabo, Z., Da Silva, S. V., Lourenço, J., et al. (2014). Membrane lipids tune synaptic transmission by direct modulation of presynaptic potassium channels. *Neuron* 81, 787–799. doi: 10.1016/j.neuron.2013.12.028

Carter, B. C., and Bean, B. P. (2009). Sodium entry during action potentials of mammalian neurons: incomplete inactivation and reduced metabolic efficiency in fast-spiking neurons. *Neuron* 64, 898–909. doi: 10.1016/j.neuron.2009.12.011

Chadderton, P., Margrie, T. W., and Häusser, M. (2004). Integration of quanta in cerebellar granule cells during sensory processing. *Nature* 428, 856–860. doi: 10.1038/nature02442

Delvendahl, I., and Hallermann, S. (2016). The cerebellar mossy fiber synapse as a model for high-frequency transmission in the mammalian CNS. *Trends Neurosci.* 39, 722–737. doi: 10.1016/j.tins.2016.09.006

Desai, N. S., Rutherford, L. C., and Turrigiano, G. G. (1999). Plasticity in the intrinsic excitability of cortical pyramidal neurons. *Nat. Neurosci.* 2, 515–520. doi: 10.1038/9165

Diamond, M. C., Law, F., Rhodes, H., Lindner, B., Rosenzweig, M. R., Krech, D., et al. (1966). Increases in cortical depth and glia numbers in rats subjected to enriched environment. *J. Comp. Neurol.* 128, 117–125. doi: 10.1002/cne.901280110

Eccles, J. C., Ito, M., and Szentagothai, J. (1967). *The Cerebellum as a Neuronal Machine*. Berlin: Springer.

Ehninger, D., and Kempermann, G. (2003). Regional effects of wheel running and environmental enrichment on cell genesis and microglia proliferation in the adult murine neocortex. *Cereb. Cortex* 13, 845–851. doi: 10.1093/cercor/13.8.845

Evans, M. D., Dumitrescu, A. S., Kruijssen, D. L. H., Taylor, S. E., and Grubb, M. S. (2015). Rapid modulation of axon initial segment length influences repetitive spike firing. *Cell Rep.* 13, 1233–1245. doi: 10.1016/j.celrep.2015.09.066

Gittis, A. H., Moghadam, S. H., and du Lac, S. (2010). Mechanisms of sustained high firing rates in two classes of vestibular nucleus neurons: differential contributions of resurgent Na, Kv3, and BK currents. *J. Neurophysiol.* 104, 1625–1634. doi: 10.1152/jn.00378.2010

Goriounova, N. A., Heyer, D. B., Wilbers, R., Verhoog, M. B., Giugliano, M., Verbist, C., et al. (2018). Large and fast human pyramidal neurons associate with intelligence. *eLife* 7:e41714. doi: 10.7554/eLife.41714

Grubb, M. S., and Burrone, J. (2010). Activity-dependent relocation of the axon initial segment fine-tunes neuronal excitability. *Nature* 465, 1070–1074. doi: 10.1038/nature09160

Hebb, D. (1947). The effects of early experience on problem solving at maturity. *Am. Psychol.* 2, 306–307.

Hebb, D. (1949). *The Organization of Behavior*. New York, NY: John Wiley & Sons.

Horvath, G., Reglodi, D., Vadasz, G., Farkas, J., and Kiss, P. (2013). Exposure to enriched environment decreases neurobehavioral deficits induced by neonatal glutamate toxicity. *Int. J. Mol. Sci.* 14, 19054–19066. doi: 10.3390/ijms140919054

Jörntell, H., and Ekerot, C.-F. (2006). Properties of somatosensory synaptic integration in cerebellar granule cells *in vivo*. *J. Neurosci.* 26, 11786–11797. doi: 10.1523/JNEUROSCI.2939-06.2006

Kempermann, G., Kuhn, H. G., and Gage, F. H. (1997). More hippocampal neurons in adult mice living in an enriched environment. *Nature* 386, 493–495. doi: 10.1038/386493a0

Keyvani, K., Sachser, N., Witte, O. W., and Paulus, W. (2004). Gene expression profiling in the intact and injured brain following environmental enrichment. *J. Neuropathol. Exp. Neurol.* 63, 598–609. doi: 10.1093/jnen/63.6.598

Kole, M. H., and Brette, R. (2018). The electrical significance of axon location diversity. *Curr. Opin. Neurobiol.* 51, 52–59. doi: 10.1016/j.conb.2018.02.016

Kronenberg, G., Wang, L. P., Geraerts, M., Babu, H., Synowitz, M., Vicens, P., et al. (2007). Local origin and activity-dependent generation of nestin-expressing protoplasmic astrocytes in CA1. *Brain Struct. Funct.* 212, 19–35. doi: 10.1007/s00429-007-0141-5

Kuba, H., Oichi, Y., and Ohmori, H. (2010). Presynaptic activity regulates Na^+ channel distribution at the axon initial segment. *Nature* 465, 1075–1078. doi: 10.1038/nature09087

Lee, M. Y., Yu, J. H., Kim, J. Y., Seo, J. H., Park, E. S., Kim, C. H., et al. (2013). Alteration of synaptic activity-regulating genes underlying functional improvement by long-term exposure to an enriched environment in the adult brain. *Neurorehabil. Neural Repair* 27, 561–574. doi: 10.1177/1545968313481277

Madroñal, N., López-Aracil, C., Rangel, A., del Río, J. A., Delgado-García, J. M., and Gruart, A. (2010). Effects of enriched physical and social environments on motor performance, associative learning, and hippocampal neurogenesis in mice. *PLoS One* 5:e11130. doi: 10.1371/journal.pone.0011130

McKenzie, I. A., Ohayon, D., Li, H., De Faria, J. P., Emery, B., Tohyama, K., et al. (2014). Motor skill learning requires active central myelination. *Science* 346, 318–322. doi: 10.1126/science.1254960

Miller, M. N., Okaty, B. W., Kato, S., and Nelson, S. B. (2011). Activity-dependent changes in the firing properties of neocortical fast-spiking interneurons in the absence of large changes in gene expression. *Dev. Neurobiol.* 71, 62–70. doi: 10.1002/dneu.20811

Need, A. C., Irvine, E. E., and Giese, K. P. (2003). Learning and memory impairments in Kvβ1.1-null mutants are rescued by environmental enrichment or ageing. *Eur. J. Neurosci.* 18, 1640–1644. doi: 10.1046/j.1460-9568.2003.02889.x

Ngodup, T., Goetz, J. A., Mcguire, B. C., Sun, W., Lauer, A. M., and Xu-Friedman, M. A. (2015). Activity-dependent, homeostatic regulation of neurotransmitter release from auditory nerve fibers. *Proc. Natl. Acad. Sci. U.S.A.* 112, 6479–6484. doi: 10.1073/pnas.1420885112

Nithiananantharajah, J., and Hannan, A. J. (2006). Enriched environments, experience-dependent plasticity and disorders of the nervous system. *Nat. Rev. Neurosci.* 7, 697–709. doi: 10.1038/nrn1970

Okuda, H., Tatsumi, K., Makinodan, M., Yamauchi, T., Kishimoto, T., and Wanaka, A. (2009). Environmental enrichment stimulates progenitor cell proliferation in the amygdala. *J. Neurosci. Res.* 87, 3546–3553. doi: 10.1002/jnr.22160

Powell, K., Mathy, A., Duguid, I., and Häusser, M. (2015). Synaptic representation of locomotion in single cerebellar granule cells. *eLife* 4:e07290. doi: 10.7554/elife.07290

Rampon, C., Jiang, C. H., Dong, H., Tang, Y.-P., Lockhart, D. J., Schultz, P. G., et al. (2000). Effects of environmental enrichment on gene expression in the brain. *Proc. Natl. Acad. Sci. U.S.A.* 97, 12880–12884. doi: 10.1073/pnas.97.23.12880

Restivo, L., Ferrari, F., Passino, E., Sgobio, C., Bock, J., Oostra, B. A., et al. (2005). Enriched environment promotes behavioral and morphological recovery in a mouse model for the fragile X syndrome. *Proc. Natl. Acad. Sci. U.S.A.* 102, 11557–11562. doi: 10.1073/pnas.0504984102

Rieke, F., Warland, D., de Ruyter Van Steveninck, R. R., and Bialek, W. (1997). "Spikes: exploring the neural code," in *Computational Neuroscience*, ed. K. Robertson (Cambridge, MA: MIT Press).

Rossi, C., Angelucci, A., Costantin, L., Braschi, C., Mazzantini, M., Babbini, F., et al. (2006). Brain-derived neurotrophic factor (BDNF) is required for the enhancement of hippocampal neurogenesis following environmental enrichment. *Eur. J. Neurosci.* 24, 1850–1856. doi: 10.1111/j.1460-9568.2006.05059.x

Ruediger, S., Vittori, C., Bednarek, E., Genoud, C., Strata, P., Sacchetti, B., et al. (2011). Learning-related feedforward inhibitory connectivity growth required for memory precision. *Nature* 473, 514–518. doi: 10.1038/nature09946

Scala, F., Nenov, M. N., Crofton, E. J., Singh, A. K., Folorunso, O., Zhang, Y., et al. (2018). Environmental enrichment and social isolation mediate neuroplasticity of medium spiny neurons through the GSK3 pathway. *Cell Rep.* 23, 555–567. doi: 10.1016/j.celrep.2018.03.062

Senn, V., Wolff, S. B. E., Herry, C., Grenier, F., Ehrlich, I., Gründemann, J., et al. (2014). Long-range connectivity defines behavioral specificity of amygdala neurons. *Neuron* 81, 428–437. doi: 10.1016/j.neuron.2013.11.006

Sirevaag, A. M., and Greenough, W. T. (1987). Differential rearing effects on rat visual cortex synapses. III. neuronal and glial nuclei, boutons, dendrites, and capillaries. *Brain Res.* 424, 320–332. doi: 10.1016/0006-8993(87)91477-6

Szeligo, F., and Leblond, C. P. (1977). Response of the three main types of glial cells of cortex nad corpus callosum in rats handled during suckling or exposed to enriched, control and impoverished environments following weaning. *J. Comp. Neurol.* 172, 247–263. doi: 10.1002/cne.901720205

Torasdotter, M., Metsis, M., Henriksson, B. G., Bengt, W., and Mohammed, A. H. (1998). Environmental enrichment results in higher levels of nerve growth factor mRNA in the rat visual cortex and hippocampus. *Behav. Brain Res.* 93, 83–90. doi: 10.1016/S0166-4328(97)00142-3

Van Kan, P. L., Gibson, A. R., and Houk, J. C. (1993). Movement-related inputs to intermediate cerebellum of the monkey. *J. Neurophysiol.* 69, 74–94. doi: 10.1152/jn.1993.69.1.74

Volkmar, F. R., and Greenough, W. T. (1972). Rearing complexity affects branching of dendrites in the visual cortex of the rat. *Science* 176, 1445–1447. doi: 10.1126/science.176.4042.1445

Wagner, M. J., Kim, T. H., Savall, J., Schnitzer, M. J., and Luo, L. (2017). Cerebellar granule cells encode the expectation of reward. *Nature* 544, 96–100. doi: 10.1038/nature21726

Walter, J. T., Alviña, K., Womack, M. D., Chevez, C., and Khodakhah, K. (2006). Decreases in the precision of purkinje cell pacemaking cause cerebellar dysfunction and ataxia. *Nat. Neurosci.* 9, 389–397. doi: 10.1038/nn1648

Wang, B., Ke, W., Guang, J., Chen, G., Yin, L., Deng, S., et al. (2016). Firing frequency maxima of fast-spiking neurons in human, monkey, and mouse neocortex. *Front. Cell. Neurosci.* 10:239. doi: 10.3389/fncel.2016.00239

Williams, R. W., and Herrup, K. (1988). The control of neuron number. *Annu. Rev. Neurosci.* 11, 423–453. doi: 10.1146/annurev.neuro.11.1.423

Yang, S., Li, C., Qiu, X., Zhang, L., Lu, W., Chen, L., et al. (2013). Effects of an enriched environment on myelin sheaths in the white matter of rats during normal aging: a stereological study. *Neuroscience* 234, 13–21. doi: 10.1016/j.neuroscience.2013.01.003

96

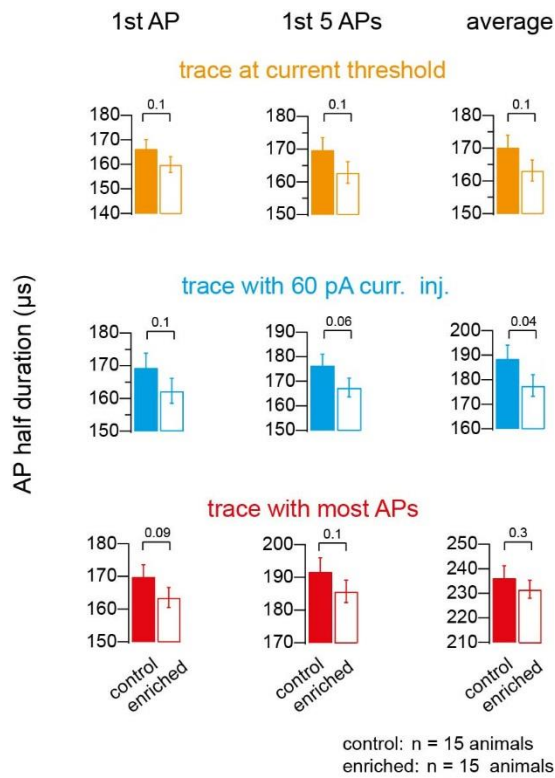**Supplementary figures of Eshra et al., 2019**

FIGURE S1

Statistical analysis of AP half duration considering the average value for each mouse instead of the average value for each cell. The average AP half duration of 15 EE and 15 control mice is shown; (orange: trace at current threshold; cyan: trace with 60-pA-current injection; red: trace with maximum APs fired). From left to right, analysis of first AP, first five APs, and average of all APs, respectively. All the P-values shown are from Student's t-test.
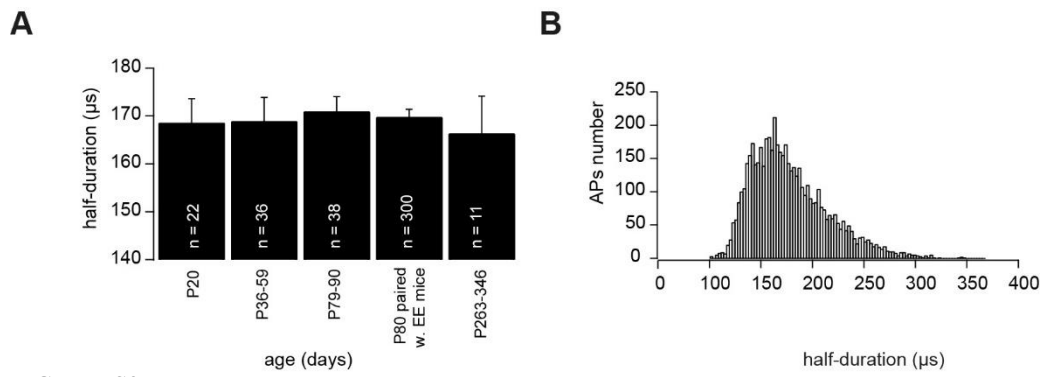
FIGURE S2

Constancy of action potential half duration between different age groups.
(A) Average AP half duration of control mice of different age groups (n refers to the number of cells). (B) Histogram showing the distribution of the half duration of all APs recorded.

FIGURE S3

Correlation between behavior and electrophysiology.
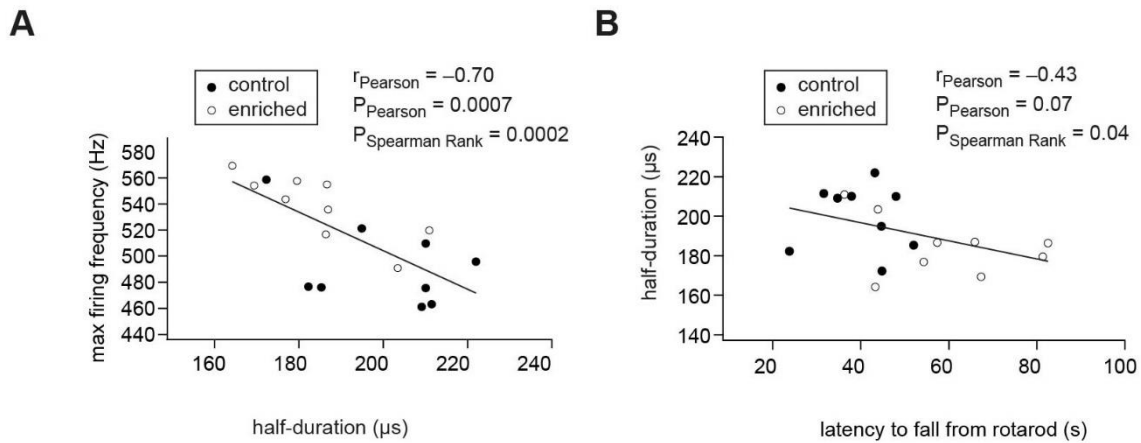(A) Correlation between maximum firing frequency and AP half duration, for control and EE mice, n = 9, 9 mice, $r_{Pearson}$ = 0.70, $P_{Pearson}$ = 0.0007, $P_{SpearmanRank}$ = 0.0002. (B) Correlation between AP half duration and latency to fall from rotarod, for control and EE mice, n = 9, 9 mice, $r_{Pearson}$ = 0.43, $P_{Pearson}$ = 0.07, $P_{SpearmanRank}$ = 0.04.

5. Summary

Dissertation for obtaining the academic degree PhD (Dr. rer. nat.)

Functional analysis of a high fidelity cerebellar synapse

Submitted by: Abdelmoneim Eshra

           Carl Ludwig Institute of Physiology
           Medical School of the University of Leipzig

Supervised by: Prof. Dr. med. Stefan Hallermann

Submitted in: February 2022

The function of the CNS depends on efficient processing of neuronal signals. High frequency signaling accelerates the process of information transfer and expands the coding capacity. In this work, I addressed the following three questions: (1) How is the presynaptic release machinery tuned to perform fast synaptic release? (2) How do fast neuronal signals propagate along the network? (3) Is the neuronal ability, to perform high frequency signaling, a plastic parameter that could be directly altered via experiences? I used the cMFB-GC synapse to address these questions. This synapse represents an ideal system to study high frequency signaling in the CNS, because mossy fiber axons carry broad-bandwidth signals to the cerebellum with firing frequencies up to 1.2 kHz *in vivo* (Jörntell & Ekerot, 2006; Rancz et al., 2007). Therefore, I studied high frequency signaling at the cMFB-GC synapse from (1) the synaptic, (2) the neuronal network, and (3) the behavioral perspectives. In the following sections, I present a short summary of the three publications of this cumulative dissertation and future perspectives of the obtained results.

5.1. Ca^{2+} dependence of neurotransmitter release at the cMFBs

The mechanisms of neurotransmitter release and especially the Ca^{2+} dependence is still surprisingly poorly understood. It is particularly unclear, how synapses can release neurotransmitter at high frequencies. In this work, a mechanistic analysis of synaptic release at the cMFBs was provided (Eshra et al., 2021). The cMFB-GC synapse is a high fidelity central synapse and represent one of the few synaptic terminals where direct recordings can be performed in brain tissue of mature mice.

AP-evoked responses were found to be critically dependent on basal Ca^{2+} levels (below 200 nM), indicating a high affinity Ca^{2+} sensor for vesicle priming. The strong Ca^{2+} dependence of vesicle priming resulted in an increased size of the RRP upon elevating the residual Ca^{2+} level. Therefore, these results contribute to better mechanistic understanding of synaptic facilitation. In order to understand the Ca^{2+} dependence of vesicle fusion, I implemented Ca^{2+} uncaging to avoid the issue of different Ca^{2+} domains (Figure 2B), occurring during the AP-triggered opening of VGCCs, that cannot be differentiated experimentally. Combining Ca^{2+} uncaging with quantitative two-photon Ca^{2+} imaging and electrophysiology (Figure 5A), I was able to obtain the relationship between the kinetics of vesicle fusion and the Ca^{2+} concentration. The obtained dose-response curves show significant release in the low Ca^{2+} range (below 5 µM). The intracellular Ca^{2+} dependence of the vesicular release rate was surprisingly shallow and did not show any signs of saturations up to a Ca^{2+} concentration of 50 µM, hence indicating a low affinity sensor for vesicle fusion. Analysis of the mechanisms of fusion of the RRP showed the existence of at least two distinct kinetic steps contributing to release within the first 10 ms. Quantitative functional analysis of this data indicated very rapid vesicle replenishment which occurred via sequential (Figure 5B) or parallel vesicle pools (Figure 5C). The Ca^{2+} dependence of vesicle replenishment, occurring within the first 100 ms after Ca^{2+} uncaging, showed very little Ca^{2+} dependence indicating either a Ca^{2+} independent process or an apparent Ca^{2+} independence in the relevant Ca^{2+} range due to an almost saturated high-affinity Ca^{2+} sensor.
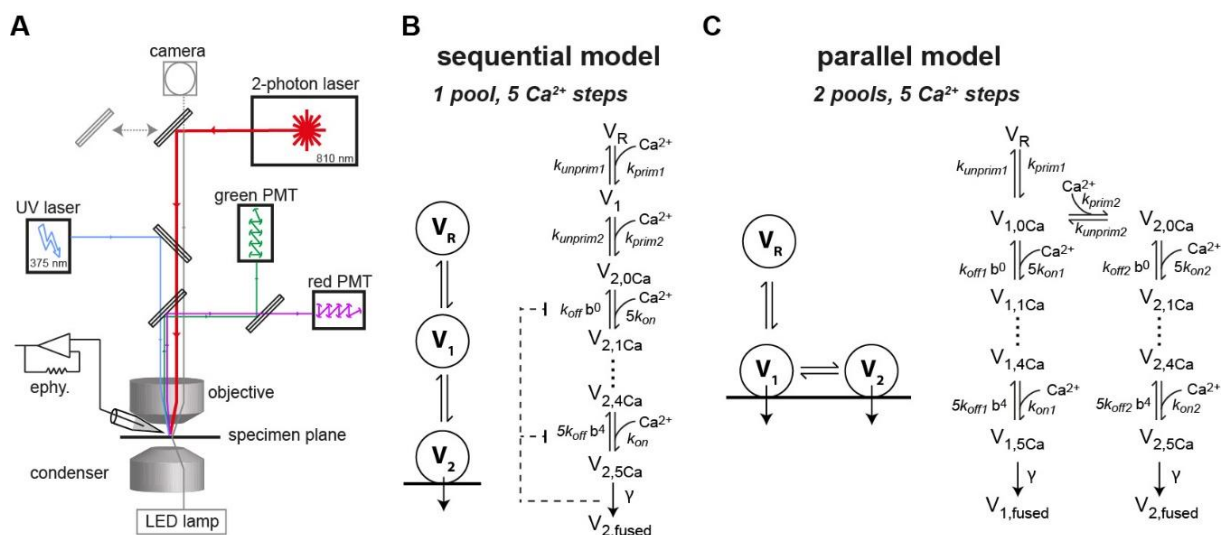

Figure 5: Kinetic models which explain synaptic release at the cMFBs

(A) Illustration of the experimental setup which was used in Eshra et al. (2021) showing the establishment of UV-induced Ca^{2+} uncaging and two-photon quantitative Ca^{2+} imaging together with electrophysiology (adopted from Eshra et al., 2021). (B) A sequential model where the release of the release-ready pool of vesicles (RRP) occurs from two subpools of vesicles (V_1, V_2). One subpool represents the docked vesicles (V_2) and the other represents a replacement pool (V_1) which can undergo rapid docking and fusion. Therefore, this model describes two

sequential kinetic steps of release (adopted from Eshra et al., 2021). (C) A parallel model where the release of the RRP occurs from two subpools of vesicles (V_1, V_2), where both types of vesicles can fuse but with different Ca^{2+} sensitivity. Therefore, this model describes two parallel kinetic steps of release (adopted from Eshra et al., 2021).

Therefore, my data reveal the presence of two types of Ca^{2+} sensors having high and low affinities that mediate synaptic release at the cMFB. The co-existence of multiple sensors could represent an evolutionary adaptation, that prevents the depletion of the RRP at medium Ca^{2+} concentrations, to allow maintaining high frequency neurotransmission with high fidelity.

5.2. Functional heterogeneity among GCs

How are high frequency input signals from the cMFBs processed at the postsynaptic level? Most previous models of the cerebellar network assumed that GCs represent a homogenous population of neurons that are functionally uniform. Here, I used whole-cell recording from GCs located in different positions in the cerebellar cortex and contributed to the description of prominent functional differences among GCs (Straub et al., 2020). My recordings and recordings from other coworkers in the laboratory revealed the existence of biophysical heterogeneity along the depth axis of the cerebellar cortex. My recordings showed that deep GCs (close to the white matter) fired APs with shorter half duration compared to more superficial GCs (close to the Purkinje cells). Deep GCs had higher threshold for firing APs compared to more superficial GCs and were able to reach higher AP firing frequencies (Figure 6). Additional data from my coworkers revealed the presence of: (1) a Fourier-like transformation of mossy fiber input into its frequency components in the GC layer, (2) functional and anatomical differences in different parallel fiber layers, and (3) differential processing of inputs from different parallel fiber layers to the Purkinje cells. Therefore, the ability of a GC to process the mossy fiber inputs differentially, based on its spatial properties, represents a critical mechanism to control information processing in the cerebellum.
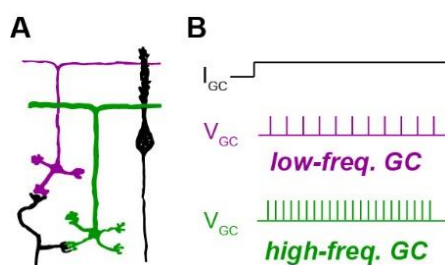

Figure 6: Spatio-functional heterogeneity of cerebellar GCs

(A) Illustration of the GCs along the depth axes (modified from Straub et al., 2020). (B) In response to small current injections (I_{GC}), GCs close to the white matter (green) were able to fire APs at higher frequencies than GCs close to the Purkinje cells (magenta; modified from Straub et al., 2020).

In addition, I investigated the heterogeneity along the rostro-caudal axis. Rostral GCs (in lobule V of the cerebellum) also showed functional and biophysical heterogeneity when compared to caudal GCs (lobule IX). GCs of lobule V had higher threshold for firing APs compared to the

more caudal GCs of lobule IX. Moreover, GCs of lobule V fired APs with shorter half duration, and could reach higher firing frequencies than GCs of lobule IX. The here-described rostro-caudal axis is largely in line with previous studies (Colin Heath et al., 2014; Witter & de Zeeuw, 2015; Zhou et al., 2014), where the anterior cerebellum was shown to process high-frequency bursting signals, while the vestibulo-cerebellum mainly processed lower frequency inputs. The here-reported two axes of biophysical heterogeneity, the depth axis and the rostro-caudal axis, contribute to the growing body of evidence for the functional differences within the cerebellar cortex (Apps et al., 2018). The existence of these functional gradients might facilitate information processing in the cerebellum via the frequency dispersion of input signals in the cerebellar cortex (Straub et al., 2020).

5.3. Environmental enrichment alters the biophysical properties of single neurons

After describing mechanisms of high frequency neuronal signaling in the context of neurotransmitter release and processing of input signals, I aimed to investigate whether the neuronal intrinsic ability, to reach maximal firing frequency, can be altered via environmental inputs. One of the core functions of the cerebellum is the fine coordination of timing and precision of motor functions. In the cerebellar network, the cMFB-GC synapse represents the first processing station which distributes sensory inputs to a huge number of GCs. Enriched environment is an effective tool that improves the motor performance of animals (Horvath et al., 2013; Lee et al., 2013; Madroñal et al., 2010). At the cerebellar glomerulus, motor learning induced prominent structural plasticity (Figure 4C; Ruediger et al., 2011), however, the occurrence of functional adaptations to the improved motor performance remains unclear. In this work, I demonstrated direct functional alterations of cerebellar GCs in response to enriched environment (Eshra et al., 2019). First, the improvement in motor skills induced via environmental enrichment was confirmed via the rotarod assay. Next, whole-cell recordings were used to describe the biophysical adaptations occurring to GCs of environmentally enriched animals. APs of GCs of environmentally enriched animals had shorter half duration, more depolarized voltage threshold, and larger overshoot (Figure 7A). On the other hand, the passive properties of GCs did not change upon environmental enrichment. Therefore, the enriched environment-induced changes are likely to be specific to the densities or properties of the ion channels which shape the AP waveform but do not extend to the channels responsible for setting the passive properties of neurons. GCs of environmentally enriched animals were able to reach higher firing frequencies than GCs of control animals (Figure 7B), suggesting an increased ability of signal processing at the cMFB-GC. Furthermore, a significant (although

weak) correlation was found between the maximum firing frequency and the motor performance on the rotarod. This correlation does not provide any causal relationship between firing rate and motor skills, but it is tempting to speculate that rapid sensory-motor integration benefits from the ability of GCs to reach higher firing frequencies. Taken together, these results demonstrate that maximum firing frequency is a plastic parameter that can adapt to sensory inputs from the environment.
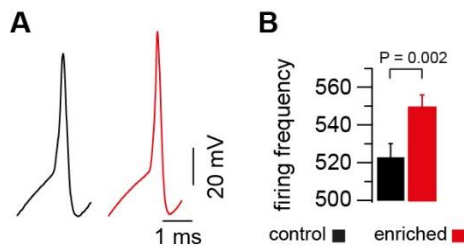

Figure 7: Effect of environmental enrichment on the firing properties of cerebellar GCs

(A) APs recorded from GCs of control (black) or environmentally enriched (red) animals. GCs of environmentally enriched animals fired APs with shorter half duration and larger overshoot compared to GCs of control animals (modified from Eshra et al., 2019). (B) Comparison of the AP firing frequency of GCs of animals grown in control (black) or enriched (red) conditions. GCs of environmentally enriched animals were able to fire APs at higher frequencies compared to GCs of control animals (adopted from Eshra et al., 2019).

5.4. Outlook

Towards understanding the mechanisms of high frequency signaling, my work provided more insights into how the release machinery of a fast synapse performs high fidelity neurotransmitter release. The results raise several exciting questions, for example, whether the here-described model of synaptic release is exclusive to cMFBs. This is the first study to investigate the release kinetics at a relatively mature central synapse. Since synaptic fidelity has been shown to increase with age, it would therefore be interesting to study the Ca^{2+} dependence of synaptic release during development. Furthermore, the exact molecular identity and expression level of the here-described Ca^{2+} sensors remain ambiguous.

This work described heterogeneity in the biophysical properties of GCs that were previously considered functionally homogenous. Similar mechanisms could exist in other brain regions which could have important implications on the functional understanding of the neuronal network. Finally, it would be interesting to check if the design of artificial neural networks profits from the implementation of neuronal heterogeneities.

How does growing in a different environment affect the computational power of single neurons? Revealing the ability of GCs to reach high firing frequencies, upon environmental enrichment, raises two important questions: (1) whether the here-reported increase in firing frequencies is beneficial for the integration of sensory motor functions and (2) if this effect extends to other types of neurons in the brain.

6. References

Albus, J. S. (1971). A theory of cerebellar function. Mathematical Biosciences *10*, 25–61. https://doi.org/10.1016/0025-5564(71)90051-4

Apps, R., Hawkes, R., Aoki, S., Bengtsson, F., Brown, A. M., Chen, G., Ebner, T. J., Isope, P., Jörntell, H., Lackey, E. P., Lawrenson, C., Lumb, B., Schonewille, M., Sillitoe, R. V., Spaeth, L., Sugihara, I., Valera, A., Voogd, J., Wylie, D. R., & Ruigrok, T. (2018). Cerebellar modules and their role as operational cerebellar processing units: a consensus paper [corrected]. The Cerebellum *17*, 654–682. https://doi.org/10.1007/s12311-018-0952-3

Atwood, H. L., & Karunanithi, S. (2002). Diversification of synaptic strength: presynaptic elements. Nature Reviews Neuroscience *3*, 497–516. https://doi.org/10.1038/nrn876

Barak, B., Shvarts-Serebro, I., Modai, S., Gilam, A., Okun, E., Michaelson, D. M., Mattson, M. P., Shomron, N., & Ashery, U. (2013). Opposing actions of environmental enrichment and Alzheimer's disease on the expression of hippocampal microRNAs in mouse models. Translational Psychiatry *3*, e304. https://doi.org/10.1038/tp.2013.77

Beutner, D., Voets, T., Neher, E., & Moser, T. (2001). Calcium dependence of exocytosis and endocytosis at the cochlear inner hair cell afferent synapse. Neuron *29*, 681–690. https://doi.org/10.1016/s0896-6273(01)00243-4

Bornschein, G., & Schmidt, H. (2019). Synaptotagmin Ca^{2+} sensors and their spatial coupling to presynaptic Ca_v channels in central cortical synapses. Frontiers in molecular neuroscience *11*, 494. https://doi.org/10.3389/fnmol.2018.00494

Brose, N., Petrenko, A. G., Südhof, T. C., & Jahn, R. (1992). Synaptotagmin: a calcium sensor on the synaptic vesicle surface. Science *256*, 1021–1025. https://doi.org/10.1126/science.1589771

Chadderton, P., Margrie, T. W., & Häusser, M. (2004). Integration of quanta in cerebellar granule cells during sensory processing. Nature *428*, 856–860. https://doi.org/10.1038/nature02442

Heath, N. C., Rizwan, A. P., Engbers, J. D., Anderson, D., Zamponi, G. W., & Turner, R. W. (2014). The expression pattern of a Cav3-Kv4 complex differentially regulates spike output in cerebellar granule cells. The Journal of Neuroscience *34*, 8800–8812. https://doi.org/10.1523/JNEUROSCI.0981-14.2014

DeFelipe J. (2006). Brain plasticity and mental processes: Cajal again. Nature Reviews Neuroscience *7*, 811–817. https://doi.org/10.1038/nrn2005

Delvendahl, I., & Hallermann, S. (2016). The cerebellar mossy fiber synapse as a model for high-frequency transmission in the mammalian CNS. Trends in Neurosciences *39*, 722–737. https://doi.org/10.1016/j.tins.2016.09.006

Delvendahl, I., Jablonski, L., Baade, C., Matveev, V., Neher, E., & Hallermann, S. (2015). Reduced endogenous Ca^{2+} buffering speeds active zone Ca^{2+} signaling. Proceedings of the National Academy of Sciences of the United States of America *112*, 3075–3084. https://doi.org/10.1073/pnas.1508419112

Diamond, M. C., Law, F., Rhodes, H., Lindner, B., Rosenzweig, M. R., Krech, D., & Bennett, E. L. (1966). Increases in cortical depth and glia numbers in rats subjected to enriched environment. The Journal of Comparative Neurology *128*, 117–126. https://doi.org/10.1002/cne.901280110

DiPolo, R., & Beaugé, L. (1983). The calcium pump and sodium-calcium exchange in squid axons. Annual Review of Physiology *45*, 313–324. https://doi.org/10.1146/annurev.ph.45.030183.001525

Dodge, F. A., Jr, & Rahamimoff, R. (1967). Co-operative action of calcium ions in transmitter release at the neuromuscular junction. The Journal of Physiology *193*, 419–432. https://doi.org/10.1113/jphysiol.1967.sp008367

Eccles, J. C., Ito, M., & Szentágothai, J. (1967). The cerebellum as a neuronal machine. In The Cerebellum as a Neuronal Machine. https://doi.org/10.1007/978-3-662-13147-3

Ehninger, D., & Kempermann, G. (2003). Regional effects of wheel running and environmental enrichment on cell genesis and microglia proliferation in the adult murine neocortex. Cerebral cortex *13*, 845–851. https://doi.org/10.1093/cercor/13.8.845

Eshra, A., Hirrlinger, P., & Hallermann, S. (2019). Enriched environment shortens the duration of action potentials in cerebellar granule cells. Frontiers in Cellular Neuroscience *13*, 289. https://doi.org/10.3389/fncel.2019.00289

Eshra, A., Schmidt, H., Eilers, J., & Hallermann, S. (2021). Calcium dependence of neurotransmitter release at a high fidelity synapse. eLife *10*, e70408. https://doi.org/10.7554/eLife.70408

Espinosa, J. S., & Luo, L. (2008). Timing neurogenesis and differentiation: insights from quantitative clonal analyses of cerebellar granule cells. The Journal of Neuroscience *28*, 2301–2312. https://doi.org/10.1523/JNEUROSCI.5157-07.2008

Fukaya, R., Maglione, M., Sigrist, S. J., & Sakaba, T. (2021). Rapid Ca^{2+} channel accumulation contributes to cAMP-mediated increase in transmission at hippocampal mossy

fiber synapses. Proceedings of the National Academy of Sciences of the United States of America *118*, e2016754118. https://doi.org/10.1073/pnas.2016754118

Gabbiani, F., Midtgaard, J., & Knöpfel, T. (1994). Synaptic integration in a model of cerebellar granule cells. Journal of Neurophysiology *72*, 999–1009. https://doi.org/10.1152/jn.1994.72.2.999

Garwicz, M., Jörntell, H., & Ekerot, C. F. (1998). Cutaneous receptive fields and topography of mossy fibres and climbing fibres projecting to cat cerebellar C3 zone. The Journal of Physiology *512*, 277–293. https://doi.org/10.1111/j.1469-7793.1998.277bf.x

Hallermann, S., Fejtova, A., Schmidt, H., Weyhersmüller, A., Silver, R. A., Gundelfinger, E. D., & Eilers, J. (2010). Bassoon speeds vesicle reloading at a central excitatory synapse. Neuron *68*, 710–723. https://doi.org/10.1016/j.neuron.2010.10.026

Hebb, D. (1947). The effects of early experience on problem solving at maturity. American Psychologist *2*, 306–307.

Hebb, D. (1949). The Organization of Behavior. New York, NY: John Wiley & Sons.

Heidelberger, R., Heinemann, C., Neher, E., & Matthews, G. (1994). Calcium dependence of the rate of exocytosis in a synaptic terminal. Nature *371*, 513–515. https://doi.org/10.1038/371513a0

Heuser, J. E., & Reese, T. S. (1973). Evidence for recycling of synaptic vesicle membrane during transmitter release at the frog neuromuscular junction. The Journal of Cell Biology *57*, 315–344. https://doi.org/10.1083/jcb.57.2.315

Hodgkin, A. L., & Huxley, A. F. (1952). A quantitative description of membrane current and its application to conduction and excitation in nerve. The Journal of Physiology *117*, 500–544. https://doi.org/10.1113/jphysiol.1952.sp004764

Horvath, G., Reglodi, D., Vadasz, G., Farkas, J., & Kiss, P. (2013). Exposure to enriched environment decreases neurobehavioral deficits induced by neonatal glutamate toxicity. International Journal of Molecular Sciences *14*, 19054–19066. https://doi.org/10.3390/ijms140919054

Imig, C., Min, S. W., Krinner, S., Arancillo, M., Rosenmund, C., Südhof, T. C., Rhee, J., Brose, N., & Cooper, B. H. (2014). The morphological and molecular nature of synaptic vesicle priming at presynaptic active zones. Neuron *84*, 416–431. https://doi.org/10.1016/j.neuron.2014.10.009

Ito M. (1970). Neurophysiological aspects of the cerebellar motor control system. International Journal of Neurology *7*, 162–176.

Jakab, R. L., & Hámori, J. (1988). Quantitative morphology and synaptology of cerebellar glomeruli in the rat. Anatomy and Embryology *179*, 81–88. https://doi.org/10.1007/BF00305102

Jörntell, H., & Ekerot, C. F. (2006). Properties of somatosensory synaptic integration in cerebellar granule cells in vivo. The Journal of Neuroscience *26*, 11786–11797. https://doi.org/10.1523/JNEUROSCI.2939-06.2006

Kaeser, P. S., & Regehr, W. G. (2017). The readily releasable pool of synaptic vesicles. Current Opinion in Neurobiology *43*, 63–70. https://doi.org/10.1016/j.conb.2016.12.012

Kempermann, G., Kuhn, H. G., & Gage, F. H. (1997). More hippocampal neurons in adult mice living in an enriched environment. Nature *386*, 493–495. https://doi.org/10.1038/386493a0

Kochubey, O., Lou, X., & Schneggenburger, R. (2011). Regulation of transmitter release by Ca^{2+} and synaptotagmin: insights from a large CNS synapse. Trends in Neurosciences *34*, 237–246. https://doi.org/10.1016/j.tins.2011.02.006

Krieger, C., Shinoda, Y., & Smith, A. M. (1985). Labelling of cerebellar mossy fiber afferents with intra-axonal horseradish peroxidase. Experimental Brain Research *59*, 414–417. https://doi.org/10.1007/BF00230923

Lee, M. Y., Yu, J. H., Kim, J. Y., Seo, J. H., Park, E. S., Kim, C. H., Kim, H., & Cho, S. R. (2013). Alteration of synaptic activity-regulating genes underlying functional improvement by long-term exposure to an enriched environment in the adult brain. Neurorehabilitation and Neural Repair *27*, 561–574. https://doi.org/10.1177/1545968313481277

Leggio, M. G., Mandolesi, L., Federico, F., Spirito, F., Ricci, B., Gelfo, F., & Petrosini, L. (2005). Environmental enrichment promotes improved spatial abilities and enhanced dendritic growth in the rat. Behavioural Brain Research *163*, 78–90. https://doi.org/10.1016/j.bbr.2005.04.009

Llinás, R., Sugimori, M., & Silver, R. B. (1992). Microdomains of high calcium concentration in a presynaptic terminal. Science *256*, 677–679. https://doi.org/10.1126/science.1350109

Madroñal, N., López-Aracil, C., Rangel, A., del Río, J. A., Delgado-García, J. M., & Gruart, A. (2010). Effects of enriched physical and social environments on motor performance,

associative learning, and hippocampal neurogenesis in mice. PLoS One *5*, e11130. https://doi.org/10.1371/journal.pone.0011130

Marr D. (1969). A theory of cerebellar cortex. The Journal of Physiology *202*, 437–470. https://doi.org/10.1113/jphysiol.1969.sp008820

Miki, T., Midorikawa, M., & Sakaba, T. (2020). Direct imaging of rapid tethering of synaptic vesicles accompanying exocytosis at a fast central synapse. Proceedings of the National Academy of Sciences of the United States of America *117*, 14493–14502. https://doi.org/10.1073/pnas.2000265117

Neher, E., & Sakaba, T. (2008). Multiple roles of calcium ions in the regulation of neurotransmitter release. Neuron *59*, 861–872. https://doi.org/10.1016/j.neuron.2008.08.019

Nusser Z. (2018). Creating diverse synapses from the same molecules. Current Opinion in Neurobiology *51*, 8–15. https://doi.org/10.1016/j.conb.2018.01.001

Ramón y Cajal, S. (1911). Histologie du systeme nerveux de l'homme et des vertebres. Paris Maloine, 2.

Rampon, C., Jiang, C. H., Dong, H., Tang, Y. P., Lockhart, D. J., Schultz, P. G., Tsien, J. Z., & Hu, Y. (2000). Effects of environmental enrichment on gene expression in the brain. Proceedings of the National Academy of Sciences of the United States of America *97*, 12880–12884. https://doi.org/10.1073/pnas.97.23.12880

Rancz, E. A., Ishikawa, T., Duguid, I., Chadderton, P., Mahon, S., & Häusser, M. (2007). High-fidelity transmission of sensory information by single cerebellar mossy fibre boutons. Nature *450*, 1245–1248. https://doi.org/10.1038/nature05995

Restivo, L., Ferrari, F., Passino, E., Sgobio, C., Bock, J., Oostra, B. A., Bagni, C., & Ammassari-Teule, M. (2005). Enriched environment promotes behavioral and morphological recovery in a mouse model for the fragile X syndrome. Proceedings of the National Academy of Sciences of the United States of America *102*, 11557–11562. https://doi.org/10.1073/pnas.0504984102

Ritzau-Jost, A., Delvendahl, I., Rings, A., Byczkowicz, N., Harada, H., Shigemoto, R., Hirrlinger, J., Eilers, J., & Hallermann, S. (2014). Ultrafast action potentials mediate kilohertz signaling at a central synapse. Neuron *84*, 152–163. https://doi.org/10.1016/j.neuron.2014.08.036

Rosenzweig, M. R., Bennett, E. L., Hebert, M., & Morimoto, H. (1978). Social grouping cannot account for cerebral effects of enriched environments. Brain Research *153*, 563–576. https://doi.org/10.1016/0006-8993(78)90340-2

Rossi, C., Angelucci, A., Costantin, L., Braschi, C., Mazzantini, M., Babbini, F., Fabbri, M. E., Tessarollo, L., Maffei, L., Berardi, N., & Caleo, M. (2006). Brain-derived neurotrophic factor (BDNF) is required for the enhancement of hippocampal neurogenesis following environmental enrichment. The European Journal of Neuroscience *24*, 1850–1856. https://doi.org/10.1111/j.1460-9568.2006.05059.x

Ruediger, S., Vittori, C., Bednarek, E., Genoud, C., Strata, P., Sacchetti, B., & Caroni, P. (2011). Learning-related feedforward inhibitory connectivity growth required for memory precision. Nature *473*, 514–518. https://doi.org/10.1038/nature09946

Sakaba T. (2008). Two Ca^{2+}-dependent steps controlling synaptic vesicle fusion and replenishment at the cerebellar basket cell terminal. Neuron *57*, 406–419. https://doi.org/10.1016/j.neuron.2007.11.029

Saviane, C., & Silver, R. A. (2006). Fast vesicle reloading and a large pool sustain high bandwidth transmission at a central synapse. Nature *439*, 983–987. https://doi.org/10.1038/nature04509

Schneggenburger, R., & Neher, E. (2000). Intracellular calcium dependence of transmitter release rates at a fast central synapse. Nature *406*, 889–893. https://doi.org/10.1038/35022702

Schwaller B. (2020). Cytosolic Ca^{2+} buffers are inherently Ca^{2+} signal modulators. Cold Spring Harbor Perspectives in Biology *12*, a035543. https://doi.org/10.1101/cshperspect.a035543

Silva, M., Tran, V., & Marty, A. (2021). Calcium-dependent docking of synaptic vesicles. Trends in Neurosciences *44*, 579–592. https://doi.org/10.1016/j.tins.2021.04.003

Simon, S. M., & Llinás, R. R. (1985). Compartmentalization of the submembrane calcium activity during calcium influx and its significance in transmitter release. Biophysical Journal *48*, 485–498. https://doi.org/10.1016/S0006-3495(85)83804-2

Straub, I., Witter, L., Eshra, A., Hoidis, M., Byczkowicz, N., Maas, S., Delvendahl, I., Dorgans, K., Savier, E., Bechmann, I., Krueger, M., Isope, P., & Hallermann, S. (2020). Gradients in the mammalian cerebellar cortex enable Fourier-like transformation and improve storing capacity. eLife *9*, e51771. https://doi.org/10.7554/eLife.51771

Südhof T. C. (2004). The synaptic vesicle cycle. Annual Review of Neuroscience *27*, 509–547. https://doi.org/10.1146/annurev.neuro.26.041002.131412

Sun, J. Y., Wu, X. S., & Wu, L. G. (2002). Single and multiple vesicle fusion induce different rates of endocytosis at a central synapse. Nature *417*, 555–559. https://doi.org/10.1038/417555a

Ramón y Cajal, S. (1894). The Croonian lecture. La fine structure des centres nerveux. Proceedings of the Royal Society of London *55*, 331–335. https://doi.org/10.1098/rspl.1894.0063

Thoreson, W. B., Rabl, K., Townes-Anderson, E., & Heidelberger, R. (2004). A highly Ca^{2+}-sensitive pool of vesicles contributes to linearity at the rod photoreceptor ribbon synapse. Neuron *42*, 595–605. https://doi.org/10.1016/s0896-6273(04)00254-5

Torasdotter, M., Metsis, M., Henriksson, B. G., Winblad, B., & Mohammed, A. H. (1998). Environmental enrichment results in higher levels of nerve growth factor mRNA in the rat visual cortex and hippocampus. Behavioural Brain Research *93*, 83–90. https://doi.org/10.1016/s0166-4328(97)00142-3

Tran, V., & Stricker, C. (2018). Diffusion of Ca^{2+} from small boutons en passant into the axon shapes AP-evoked Ca^{2+} transients. Biophysical Journal *115*, 1344–1356. https://doi.org/10.1016/j.bpj.2018.07.018

van Kan, P. L., Gibson, A. R., & Houk, J. C. (1993). Movement-related inputs to intermediate cerebellum of the monkey. Journal of Neurophysiology *69*, 74–94. https://doi.org/10.1152/jn.1993.69.1.74

van Praag, H., Kempermann, G., & Gage, F. H. (2000). Neural consequences of environmental enrichment. Nature Reviews Neuroscience *1*, 191–198. https://doi.org/10.1038/35044558

Volkmar, F. R., & Greenough, W. T. (1972). Rearing complexity affects branching of dendrites in the visual cortex of the rat. Science *176*, 1445–1447. https://doi.org/10.1126/science.176.4042.1445

Wang, L. Y., Neher, E., & Taschenberger, H. (2008). Synaptic vesicles in mature calyx of Held synapses sense higher nanodomain calcium concentrations during action potential-evoked glutamate release. The Journal of Neuroscience *28*, 14450–14458. https://doi.org/10.1523/JNEUROSCI.4245-08.2008

Williams, R. W., & Herrup, K. (1988). The control of neuron number. Annual Review of Neuroscience *11*, 423–453. https://doi.org/10.1146/annurev.ne.11.030188.002231

Wilms, C. D., & Häusser, M. (2015). Reading out a spatiotemporal population code by imaging neighbouring parallel fibre axons in vivo. Nature Communications *6*, 6464. https://doi.org/10.1038/ncomms7464

Witter, L., & De Zeeuw, C. I. (2015). In vivo differences in inputs and spiking between neurons in lobules VI/VII of neocerebellum and lobule X of archaeocerebellum.   The Cerebellum 14, 506–515. https://doi.org/10.1007/s12311-015-0654-z
Zhai, R. G., & Bellen, H. J. (2004). The architecture of the active zone in the presynaptic nerve terminal. Physiology *19*, 262–270. https://doi.org/10.1152/physiol.00014.2004

Zhou, H., Lin, Z., Voges, K., Ju, C., Gao, Z., Bosman, L. W., Ruigrok, T. J., Hoebeek, F. E., De Zeeuw, C. I., & Schonewille, M. (2014). Cerebellar modules operate at different frequencies. eLife *3*, e02536. https://doi.org/10.7554/eLife.02536

7. Appendix

7.1. Presentation of my own contribution

This dissertation is based on results which led to the Publication of the following original research articles:

(1)

Eshra A, Schmidt H, Eilers J, and Hallermann S (2021). Calcium dependence of neurotransmitter release at a high fidelity synapse. ELife, 10: e70408.

(2)

Straub I*****, Witter L*****, **Eshra A***, Hoidis M*****, Byczkowicz N, Maas S, Delvendahl I, Dorgans K, Savier E, Bechmann I, Krueger M, Isope P, and Hallermann S (2020). Gradients in the mammalian cerebellar cortex enable Fourier-like transformation and improve storing capacity. ELife, 9: e51771.

(3)

Eshra A, Hirrlinger P, and Hallermann S (2019). Enriched environment shortens the duration of action potentials in cerebellar granule cells. Frontiers in Cellular Neuroscience, 13: 289.

(* indicates equal contribution)

Contribution to Eshra et al., 2021

Together with Prof. Hallermann, I initiated the project, developed the hypothesis, designed the study, and established the methods. I performed and analyzed all experiments shown in (Figures 1 – 7, all supplementary figures). Simulations of the release schemes based on the experimental data were performed by Prof. Hallermann (Figures 6C – E, 7D). Prof. Schmidt and Prof. Eilers performed the modeling of the Ca^{2+} transients (Figure 6A, B). The manuscript was mainly written by me and Prof. Hallermann.

Declaration by all authors

Abdelmoneim Eshra: Conceptualization, Data curation, Investigation, Visualization, Methodology, Writing - original draft, Writing - review and editing

Hartmut Schmidt: Investigation, Visualization, Methodology, Writing - original draft, Writing - review and editing

Jens Eilers: Methodology, Writing - review and editing

Stefan Hallermann: Conceptualization, Software, Investigation, Methodology, Writing - original draft, Writing - review and editing

Abdelmoneim Eshra   Hartmut Schmidt   Jens Eilers   Stefan Hallermann

Contribution to Straub et al., 2020

I performed and analyzed the patch-clamp recordings at lobule V and lobule IX shown in (Figure 1 and Figure 1 supplements). I performed the analysis using a script that was originally written by Prof. Hallermann in Igor Pro and later modified by me. Moreover, I proposed to study whether the functional and structural heterogeneity along the depth axis, which was observed in lobule V, extends to lobule IX. This would allow more general conclusions about frequency specialization within the cerebellar cortex, because previously published *in vivo* data showed different firing rates between lobules V and IX (Witter & De Zeeuw 2015). Therefore, I performed the slice electrophysiology in the two lobules, which supported a global heterogeneity in the biophysical properties of GCs. Dr. Straub and Prof. Hallermann wrote the original version of the manuscript and I was involved in the editing and writing of the manuscript.

Declaration by all authors

Isabelle Straub: Conceptualization, Data curation, Software, Supervision, Investigation, Visualization, Methodology, Writing - original draft, Writing - review and editing

Laurens Witter: Data curation, Software, Investigation, Visualization, Methodology, Writing - original draft, Writing - review and editing

Abdelmoneim Eshra: Data curation, Software, Investigation, Visualization, Methodology, Writing - review and editing

Miriam Hoidis: Data curation, Investigation, Visualization

Niklas Byczkowicz: Data curation, Investigation, Visualization

Sebastian Maas: Data curation, Software, Investigation

Igor Delvendahl: Data curation, Software, Writing - review and editing

Kevin Dorgans: Data curation, Software, Writing - review and editing

Elise Savier: Data curation, Investigation, Writing - review and editing

Ingo Bechmann: Data curation, Supervision, Investigation, Writing - review and editing

Martin Krueger: Data curation, Investigation, Writing - review and editing

Philippe Isope: Data curation, Supervision, Investigation, Writing - review and editing

Stefan Hallermann: Conceptualization, Software, Supervision, Visualization, Methodology, Writing - original draft, Writing - review and editing

Isabelle Straub   Laurens Witter   Abdelmoneim Eshra   Miriam Hoidis

Niklas Byczkowicz   Sebastian Maas   Igor Delvendahl   Kevin Dorgans

Elise Savier   Ingo Bechmann   Martin Krueger   Philippe Isope

Stefan Hallermann

Contribution to Eshra et al., 2019

Together with Prof. Hallermann, I initiated the project, developed the hypothesis, and designed the study. The code used in Igor Pro to analyze the action potentials was initially written by Prof. Hallermann and later modified by me. I performed all electrophysiology experiments and behavioral assessment. The establishment of the enriched environment housing conditions was done by Dr. Petra Hirrlinger. I and Prof. Hallermann wrote the manuscript.

Declaration by all authors

Abdelmoneim Eshra:	Project idea and conceptualization
	Investigation: electrophysiology and behavioral experiments
	Analysis, interpretation, and visualization of data
	Writing of the publication
Petra Hirrlinger:	establishment of enriched environment housing conditions
Stefan Hallermann:	Project idea and conceptualization
	Analysis, interpretation, and visualization of data
	Acquisition of financial support
	Writing of the publication

Abdelmoneim Eshra   Petra Hirrlinger   Stefan Hallermann

7.2. Declaration of authorship

Hiermit erkläre ich, dass ich die vorliegende Arbeit selbstständig und ohne unzulässige Hilfe oder Benutzung anderer als der angegebenen Hilfsmittel angefertigt habe. Ich versichere, dass Dritte von mir weder unmittelbar noch mittelbar eine Vergütung oder geldwerte Leistungen für Arbeiten erhalten haben, die im Zusammenhang mit dem Inhalt der vorgelegten Dissertation stehen, und dass die vorgelegte Arbeit weder im Inland noch im Ausland in gleicher oder ähnlicher Form einer anderen Prüfungs-behörde zum Zweck einer Promotion oder eines anderen Prüfungsverfahrens vorgelegt wurde. Alles aus anderen Quellen und von anderen Personen übernommene Material, das in der Arbeit verwendet wurde oder auf das direkt Bezug genommen wird, wurde als solches kenntlich gemacht. Insbesondere wurden alle Personen genannt, die direkt an der Entstehung der vorliegenden Arbeit beteiligt waren. Die aktuellen gesetzlichen Vorgaben in Bezug auf die Zulassung der klinischen Studien, die Bestimmungen des Tierschutzgesetzes, die Bestimmungen des Gentechnikgesetzes und die allgemeinen Datenschutzbestimmungen wurden eingehalten. Ich versichere, dass ich die Regelungen der Satzung der Universität Leipzig zur Sicherung guter wissenschaftlicher Praxis kenne und eingehalten habe.

I hereby declare that I have completed the present work independently and without unauthorized help or the use of aids other than those specified. I affirm that third parties have neither directly nor indirectly received remuneration or monetary benefits from me for work related to the content of the submitted dissertation, and that the submitted work has not been submitted neither domestically nor abroad in the same or a similar form to another examination authority for the purpose of a doctorate or another examination procedure. All materials adopted from other sources and from other persons that were used in the work or that is directly referred to has been marked as such. In particular, all persons who were directly involved in the creation of the present work were named. The current legal requirements with regard to the approval of clinical studies, the provisions of the Animal Welfare Act, the provisions of the Genetic Engineering Act and the general data protection provisions have been complied with. I assure you that I know the regulations of the statutes of the University of Leipzig to ensure good scientific practice and that I have complied with them.

Date: 01.02.2022   Signature:

7.3. Curriculum Vitae

7.4. Scientific publications and talks

Publications

Eshra A, Hirrlinger P, and Hallermann S (2019). Enriched environment shortens the duration of action potentials in cerebellar granule cells. Frontiers in Cellular Neuroscience, 13: 289

Byczkowicz N, **Eshra A**, Montanaro J, Trevisiol A, Hirrlinger J, Kole M H P, Shigemoto R, and Hallermann S (2019). HCN channel-mediated neuromodulation can control action potential velocity and fidelity in central axons. eLife, 8: e42766.

Straub I*****, Witter L *****, **Eshra A***, Hoidis M *****, Byczkowicz N, Maas S, Delvendahl I, Dorgans K, Savier E, Bechmann I, Krueger M, Isope P, and Hallermann S (2020). Gradients in the mammalian cerebellar cortex enable Fourier-like transformation and improve storing capacity. eLife, 9: e51771

Eshra A, Schmidt H, Eilers J, and Hallermann S (2021). Calcium dependence of neurotransmitter release at a high fidelity synapse. eLife, 10: e70408

Conferences and symposia

Straub I*****, Witter L *****, **Eshra A***, Hoidis M *****, Byczkowicz N, Maas S, Delvendahl I, Dorgans K, Savier E, Bechmann I, Krueger M, Isope P, and Hallermann S. Separate pathways for high and low frequency signals in the cerebellar cortex. Meeting of the German Neuroscience Society, 2017, Göttingen, Germany

Straub I*****, Witter L *****, **Eshra A***, Hoidis M *****, Byczkowicz N, Maas S, Delvendahl I, Dorgans K, Savier E, Bechmann I, Krueger M, Isope P, and Hallermann S. Fourier-like transformation in the cerebellar cortex. 11th FENS Forum of Neuroscience, 2018, Berlin, Germany

Eshra A, Hirrlinger P, and Hallermann S. Enriched environment accelerates action potentials. Meeting of the German Neuroscience Society, 2019, Göttingen, Germany

Eshra A, Hirrlinger P, and Hallermann S. Enriched Environment Shortens the Duration of Action Potentials in Cerebellar Granule Cells. Annual meeting of the Society for Neuroscience, 2019, Chicago, USA

Eshra A and Hallermann S. Calcium dependence of vesicle priming and fusion at a high frequency synapse. Japanese Society for the Promotion of Science/ core-to-core program, 2020, Berlin, Germany

Eshra A, and Hallermann S. Calcium dependence of neurotransmitter release at a mature central synapse. Japanese Society for the Promotion of Science/core-to-core program, 2021, virtual

(* indicates equal contribution)

7.5. Acknowledgments